PRODUCTION AND CHARACTERIZATION OF CERAMIC COMPONENTS VIA CURRENT SINTERING TECHNIQUES

A Thesis Submitted to
the Graduate School of Engineering and Sciences of
İzmir Institute of Technology
in Partial Fulfillment of the Requirements for the Degree of

DOCTOR OF PHILOSOPHY

in Materials Science and Engineering

by
Levent KARACASULU

December 2023
İZMİR

We approve the thesis of **Levent KARACASULU**

Examining Committee Members:

Prof. Dr. Çekdar Vakıf AHMETOĞLU
Materials Science and Engineering, İzmir Institute of Technology

Assoc. Prof. Dr. Fatih TOPTAN
Materials Science and Engineering, İzmir Institute of Technology

Prof. Dr. Ender SUVACI
Materials Science and Engineering, Eskişehir Technical University

Prof. Dr. Yaşar AKDOĞAN
Materials Science and Engineering, İzmir Institute of Technology

Assist. Prof. Dr. Mattia BIESUZ
Industrial Engineering, University of Trento

04 December 2023

Prof. Dr. Çekdar Vakıf AHMETOĞLU
Supervisor, Materials Science and Engineering,
İzmir Institute of Technology

Assoc. Prof. Dr. Umut ADEM
Co-Supervisor, Materials Science and Engineering,
İzmir Institute of Technology

Prof. Dr. Yaşar AKDOĞAN
Head of the Department of Materials Science and Engineering

Prof. Dr. Mehtap EANES
Dean of the Graduate School of Engineering and Sciences

ACKNOWLEDGMENTS

I would like to express my sincere gratitude to the following individuals and institutions whose invaluable contributions and support made this doctoral thesis possible.

First and foremost, I extend my deepest appreciation to my advisor, Prof. Dr. Çekdar Vakıf Ahmetoğlu, for his guidance and endless support throughout this research journey. I am also grateful to Prof. Dr. Ender Suvacı and Assoc. Prof. Dr. Fatih Toptan for their patience, constructive feedback, and guidance during this research journey and for being a thesis progress committee and a jury member. I would like to express my appreciation to Assist. Prof. Dr. Mattia Biesuz for his feedback and critical discussion during my thesis progress and for being a jury member by arriving in Türkiye. I am also thankful to Prof. Dr. Yaşar Akdoğan for evaluating my thesis and being a jury member.

From the bottom of my heart, I would also like to thank my colleagues, especially current and former team members of Inorganic solid materials group, Öykü İçin Erdemir, Cerem Pişkin, Esin Karataş, Ezgi Oğur, Furkan Çapraz, Ecem Özmen Tunç, Uğur Kartal, Nazlıcan Uza, and Dr. Tuğçe Semerci for their support.

For my visiting research journey at the University of Trento in Italy, I acknowledge the financial support of JECS Trust which led to the beginning of the story. I would like to thank Prof. Vincenzo M. Sglavo and Prof. Gian D. Sorarù who welcomed me into their laboratories during my doctoral research period in Italy. Furthermore, I extend my thanks to my colleagues and friends in Italy, Dr. Emanuele De Bona, Dr. Andrea Zambotti, Dr. Damandeep Kaur, Dr. Rajat Chaudhary, Dr. Michele Cassetta, Dr. Marco Zago, Sonia Marin Cortés, Justyna Ignaczak, Adane Muche Abebe, Angela Bruni, Alessandro Tomasini, Fabio Torazzi, Albina Abdurakhmanova, Dr. Matteo Cristinelli, Andrea Marchet, and Anıl Osman Tur for their endless support.

I would also like to acknowledge the individuals with whom I collaborated closely, whose expertise and collaboration significantly enriched this study. Many people have also contributed their expertise during this research journey. Therefore, I would like to thank my co-advisor, Assoc. Prof. Dr. Umut Adem, Dr. Merve Günnar Karakaya, and Melike Tokkan for their input on the measurements of electrical properties; Prof. Claude Estournès and Dr. Thomas Hérisson de Beauvoir for their input on EIS measurements;

Dr. Mauro Bortolotti for his input on detailed XRD studies throughout my thesis. I would also like to thank the team of the Center for Materials Research (CMR) at IZTECH.

I have special thanks to my beloved friends; Melek Umay Tüz, Ezgi Şatıroğlu, Sinan Ozan Özel, Berkay Yazırlı, Yonca Yazırlı, Yunus Emre Kılıç, Çetin Meriç Güvenç, and Tuğçe Aybüke Arıca Güvenç, Büşra Molacı, Sümeyra Çiğdem Sözer, and Mutlu Devrim Yaman for their endless support, understanding, and compassion. I would like to express my gratitude to my relative Gözde Özbey and her husband Nevzat Özbey for supporting my work abroad. Lastly, but most importantly, I want to express my deepest appreciation to my family.

Throughout my PhD study, I would like to gratefully acknowledge the supports of TUBITAK (The Scientific and Technological Research Council of Türkiye) within 1001 - The Scientific and Technological Research Projects Funding program (Project Grant No:218M342) and 2214-A - International Research Fellowship Program for PhD students.

ABSTRACT

PRODUCTION AND CHARACTERIZATION OF CERAMIC COMPONENTS VIA CURRENT SINTERING TECHNIQUES

This dissertation aims to utilize contemporary advanced sintering techniques such as cold sintering, reactive hydrothermal liquid phase densification, fast firing, flash sintering, and ultrafast high-temperature sintering for sintering of various ceramic materials. The ceramics produced through these methods are compared with their traditional counterparts in terms of processing-structure-property relationships.

In the first section, a brief overview of the advanced sintering techniques used is provided. Chapters 2-7 give a review study on low-temperature densification techniques, and the studies conducted using the cold sintering process and reactive hydrothermal liquid phase densification process, namely cold sintering techniques, which allow densification below 400 °C. Chapters 8&9 presents research related to ceramic materials produced via the fast-firing technique with rapid heating rates compared to conventional sintering, widely employed in the industry. Chapters 10-12 cover sintering studies conducted utilizing joule heating based sintering techniques allowing very fast heating rates such as flash sintering and ultrafast high-temperature sintering. Chapter 13 presents a comparison of current sintering techniques used in terms of applicability, equipment, materials, and so on. The pros and cons of such techniques were explained.

In conclusion, there may be no guarantee that every ceramic material will yield successful results in all sintering processes. It is essential to recognize that each sintering process occurs within distinct sintering mechanisms. The selection of the appropriate advanced sintering method and conditions should be based on an assessment of the specific material's characteristics and the desired properties in the final product.

ÖZET

GÜNCEL SİNTERLEME TEKNİKLERİ İLE SERAMİK BİLEŞENLERİNİN ÜRETİMİ VE KARAKTERİZASYONU

Bu tez, çeşitli seramik malzemelerin sinterlenmesi için soğuk sinterleme, reaktif hidrotermal sıvı faz yoğunlaştırma, hızlı pişirme, flaş sinterleme ve ultra hızlı yüksek sıcaklıkta sinterleme gibi çağdaş ileri sinterleme tekniklerini kullanmayı amaçlamaktadır. Bu yöntemlerle üretilen seramikler, işleniş-yapı-özellik ilişkileri açısından geleneksel muadilleriyle karşılaştırılmaktadır.

Birinci bölümde, kullanılan ileri sinterleme tekniklerine kısa bir genel bakış sunulmaktadır. 2.-7. bölümde, düşük sıcaklıkta yoğunlaşma teknikleri üzerine bir derleme çalışması ile 400 °C'nin altında yoğunlaştırmaya olanak sağlayan soğuk sinterleme prosesi ve reaktif hidrotermal sıvı fazda yoğunlaştırma prosesi yani soğuk sinterleme teknikleri kullanılarak yapılan çalışmalar anlatılmaktadır. 8. ve 9. bölümde, endüstride yaygın olarak kullanılan geleneksel sinterleme ile karşılaştırıldığında hızlı ısıtma hızına sahip hızlı pişirme tekniği ile üretilen seramik malzemelere ilişkin araştırmalar sunulmaktadır. 10.-12. Bölümde çok hızlı ısınma oranlarına olanak sağlayan flaş sinterleme ve ultra hızlı yüksek sıcaklıkta sinterleme gibi joule ısıtma bazlı sinterleme teknikleri kullanılarak yapılan sinterleme çalışmaları anlatılmaktadır. 13.Bölüm, uygulanabilirlik, ekipman, malzeme vb. açısından kullanılan mevcut sinterleme tekniklerinin bir karşılaştırmasını sunmaktadır. Bu tekniklerin artıları ve eksileri açıklanmıştır.

Sonuç olarak her seramik malzemenin tüm sinterleme işlemlerinde başarılı sonuçlar vereceğinin garantisi olmayabilir. Her sinterleme işleminin farklı sinterleme mekanizmaları içerisinde gerçekleştiğini bilmek önemlidir. Uygun ileri sinterleme yönteminin ve koşullarının seçimi, malzemenin kendine has karakterinin belirlenmesine ve nihai üründe istenen özelliklerin değerlendirilmesine dayanmalıdır.

Dedicated to
those striving for Reason and Science
in the path of M. K. ATATÜRK
on the 100th anniversary
of the Republic of Türkiye....

TABLE OF CONTENTS

LIST OF FIGURES

Figure **Page**

Figure **Page**

Figure **Page**

Figure **Page**

Figure **Page**

Figure **Page**

Figure **Page**

Figure **Page**

Figure **Page**

Figure **Page**

LIST OF TABLES

Table **Page**

Table **Page**

LIST OF ABBREVIATIONS

CS	Conventional sintering
CSP	Cold sintering process
EDX	Energy dispersive X-ray spectroscopy
EIS	Electrochemical impedance spectroscopy
FF	Fast-firing
FS	Flash sintering
FTIR	Fourier transform infrared spectroscopy
HHP	Hydrothermal hot pressing
HRS	Hydrothermal reaction sintering
ICP-OES	Inductively coupled plasma-Optical emission spectrometry
KNN	Potassium sodium niobate
rHLPD	Reactive hydrothermal liquid phase densification
RTD	Room-temperature densification
SEM	Scanning electron microscope
TEM	Transmission electron microscope
TGA	Thermogravimetric analysis
UHS	Ultrafast high-temperature sintering
WP	Warm Press
XPS	X-ray photoelectron spectroscopy
XRD	X-ray diffraction
YSZ	Yttria-stabilized zirconia

CHAPTER 1

INTRODUCTION

The present PhD dissertation is written as cumulative comprising five peer-reviewed publications as listed below:

1. L. Karacasulu, E. Ogur, C. Piskin, C. Vakifahmetoglu, 2021. Cold sintering of soda-lime glass. Scr. Mater. 192, 111–114.
2. L. Karacasulu, D. Karl, A. Gurlo, C. Vakifahmetoglu, Cold sintering as a promising ISRU technique: A case study of Mars regolith simulant, Icarus. 389 (2023) 115270.
3. L. Karacasulu, C. Vakifahmetoglu, Cold sintering assisted two-step sintering of potassium sodium niobate (KNN) ceramics, Materials Science and Engineering: B. 297 (2023) 116709.
4. L. Karacasulu, M. Tokkan, M. Bortolotti, G. Ischia, U. Adem, C. Vakifahmetoglu, Electrical characteristics of low temperature densified barium titanate, Ceram. Int. 46 (2020) 16670–16676.
5. L. Karacasulu, U. Kartal, O. Icin, M. Bortolotti, M. Biesuz, C. Vakifahmetoglu, Formation of monolithic $SrTiO_3$-TiO_2 ceramic heterostructures by reactive hydrothermal sintering, J. Eur. Ceram. Soc. 43 (2023) 6982–6988.

Besides the manuscripts listed above, I have also contributed to the following publications related to the topic of this thesis.

1. C. Vakifahmetoglu, L. Karacasulu, Cold sintering of ceramics and glasses: A review, Curr. Opin. Solid State Mater. Sci. 24 (2020) 100807.
2. M. Biesuz, L. Karacasulu, C. Vakifahmetoglu, V.M. Sglavo, On the temperature measurement during ultrafast high-temperature sintering (UHS): Shall we trust metal-shielded thermocouples?, J. Eur. Ceram. Soc. (2023) in press.

1.1. General overview

The process of bonding, densifying, and/or recrystallizing powder compacts—that is, transforming a green body into a stronger monolith—is essentially what is meant to be understood by the term "sintering".[1–5] For thousands of years, ceramics have been consolidated by sintering process. Typically, a powder compact is heated to elevated temperatures at rates ranging from a fraction to a few °C per minute.[6] However, whereas ceramic objects found in archeological locations point out sintering practice even 26000 years ago, the first steps towards the establishment of sintering theory were only taken in the early 1900s.[3,7]

For sintering to occur, there must be a reduction of the total interfacial energy between the two particles to be sintered toward the thermodynamic minimum.[3,8] Driving forces for sintering are the terms used to describe the sources that result in this reduction of free energy. Typically, there are three potential driving forces for sintering: i) curvature of particle surfaces, ii) externally applied pressure, and iii) chemical reactions. (Please see Chapter 2 later for more detailed information).[2,3] Sintering is motivated by the driving forces, but it also requires the transport of the matter, which in crystalline solids takes place through a process of diffusion involving species i.e., atoms, ions, or molecules. The structure of crystalline solids is not ideal. They have various imperfections, which are called defects, at any temperature. These defects are what enable diffusional mass transport to occur. Defects regulate the rate of matter transport, which controls the rates of processes like sintering, grain growth, and creep.[3] Generally, diffusion in ceramics is mediated by point defects (e.g., interstitials or, more commonly, vacancies). Changes in composition, temperature, and even atmosphere (e.g., a controlled oxygen partial pressure) can have a large impact on the concentrations of the defects. It is worth noting that compared to simpler solids i.e. metals and covalent semiconductors, the transport properties of ceramics are much more complex.[3,9]

In addition to conventional sintering, i.e., pressureless sintering, there are several pressure-assisted sintering techniques such as hot pressing (HP), hot isostatic pressing (HIP), sinter/hot and gas forging, and so on. In these techniques, externally applied pressure as a driving force may contribute to densification. Besides, as known, control of microstructure in ceramics can be controlled by optimizing each of the production process steps from powder to sintering [10]. But for the sintering step, conventional sintering has

limitations for effectively controlling microstructure. For example, grain growth that occurs in conventional sintering may not be desirable [6]. This issue is addressed by some advanced sintering techniques such as spark plasma sintering (SPS) [11,12], microwave sintering [13–15], and flash sintering [16,17].

1.2. Current sintering techniques

In this section, advanced or unconventional sintering techniques currently used within the scope of the dissertation are briefly mentioned for the reader's understanding. The mentioned techniques have been categorized into three main groups: Cold sintering techniques, fast firing, and joule heating based sintering techniques.

1.2.1. Cold sintering techniques

Although scientists have been making efforts to sinter ceramics at low temperatures under different techniques since the 1970s, cold sintering process was brought back to the agenda by turning it into a simple system by researchers at Penn State University in 2016.[5] Cold sintering process (CSP) enables densification of ceramic and glass materials under high pressures (below 1 GPa) and low temperatures (< 400 °C) with the aid of purposely introduced additives such as water, acidic/basic solutions, salts (and their solutions), and the components that can form a eutectic.[5,18–24] In Cold sintering process, the starting powder is mixed with the additives mentioned above. Then the obtained mixture is constantly compressed by using a uniaxial press. The heating process is carried out utilizing a resistance jacket wrapped around the die.[25] Although there have been several reports related to the plausible mechanism that takes place during CSP, it is still unknown what standardized diffusion mechanism could be in the process.[26,27] However, it is possible to say that the formation of a supersaturated liquid is necessary for densification and that this can also be achieved by dissolving the starting particles in acidic or basic solutions or simply by preloading the liquid phase with the relevant chemical groups, i.e. by adding water-soluble salts instead of changing the

acidity/basicity.[5] Additionally, Jabr et al.[28] showed that the way to extend CSP for industrial applications is feasible.

Reactive hydrothermal liquid phase densification (rHLPD) process is a patented technique with a different low-temperature densification concept compared to the typical cold sintering process based on the hydrothermal reaction, infiltration, reactive crystallization, and liquid phase sintering principles.[29,30] Thus, rHLPD allows the densification of ceramics simultaneously in one pot by combining the synthesis and densification at temperatures below 400°C. In rHLPD process (Figure 1.1), there is no application of suitable pressure (e.g., uniaxial pressure) aiding densification, therefore; the center of the particles does not approach one another by the effect of external pressure as in the cold sintering process. However, there is a high requirement for hydrothermal crystallization reaction that can transform into final products with greater molar volume compared to green body.[30,31] Relevant detailed information regarding techniques given or not mentioned here is provided in detail in Chapter 2.

Figure 1.1. Schematic representation of rHLPD process using acid digestion vessel.

1.2.2. Fast firing

As an unconventional sintering technique, fast firing (FF) process also known as rapid sintering, fast sintering, rapid-rate sintering, or rapid pressureless sintering was proposed at the beginning of the 80s to enhance densification of ceramics and suppress

grain growth. Fast firing enables densification by utilizing a much faster heating rate (10^2-10^3 °C/min) and a higher sintering temperature with a shorter dwell time.[6,32,33] In fast-firing process, a fast heating rate has a key role to enhance densification and grain growth control. This knowledge accomplished from the fast firing process lays the foundation for many other novel sintering methods such as spark-plasma sintering, microwave sintering, and flash sintering.[6] For the same density, fast fired samples have grains with smaller sizes, besides preventing pore boundary separation, compared to conventional sintering.[6,34]

Basically, fast firing process involves quickly introducing green samples into the hot zone of a furnace so that the samples quickly reach higher temperatures with a relatively faster heating rate where the activation energy for densification, Q_r, is higher than the activation energy for grain growth, Q_g, (i.e., densification rate vs. Grain growth rate) as shown in Figure 1.2. [32,35,36] In addition, it is a quite useful technique, especially for the industry. Since the 1970s, this method has been commonly used to sinter both conventional and advanced ceramics, and shown to operate in both lab and large-scale furnaces. Ceramics can be sintered quickly in an intermittent resistive box or tube furnaces as well as continuous zone sintering furnaces.[37] Hence, fast firing has been proposed in the literature for several materials systems, including traditional ceramics such as tiles and sanitaryware [38–40], technical ceramics such as alumina [41–44], barium titanate [33,45–47], ferrites [48], indium tin oxide [49], lanthanum gallate [50], lead magnesium niobate [51,52], lead zirconia titanate [53,54], zirconia [34,44,55–57], and even composites.[58]

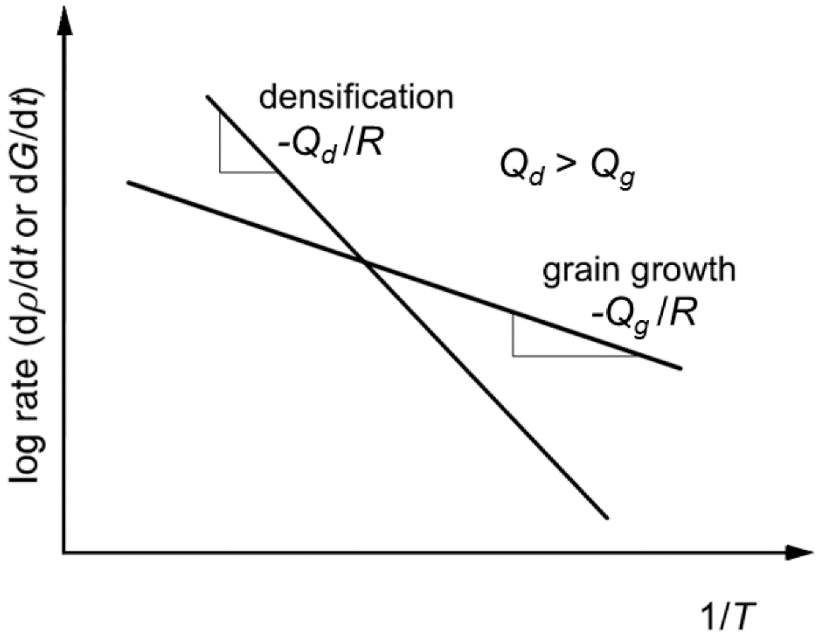

Figure 1.2. Dependency on temperature of densification and grain growth rate for a material where the activation energy for densification, Qr, is higher than the activation energy for grain growth, Qg.

(Source: Kang, 2020)[36]

1.2.3. Joule heating based sintering techniques

1.2.3.1. Flash sintering

Among Flash sintering (FS) is an electric field-assisted sintering technique, explored in 2010 by researchers at the University of Colorado.[59] In this advanced sintering technique, an electric field is applied directly to the prepared ceramic body and current is forced to flow through the body. At a specific onset combination of electric field and furnace temperature, densification is triggered by flash sintering in an extremely short time (usually a few seconds to a few minutes). In this system, however, the sample must be of specific dimensions and geometries for proper bonding to the electrodes and for a homogeneous current distribution. Three types of sample geometries are generally used in flash sintering experiments (Figure 1.3). The first flash sintering experiments were

carried out using dog bone shape specimens with two holes on the opposite side of the sample where the electrodes were placed.[17]

Although the dog bone shape appears to be the most useful geometry for electrical conductivity processes due to its thin cross-section for the flash sintering process, practical applications for such shapes are very limited. Similar to the dog bone, sintering can be performed by appropriately wrapping electrodes around the ends of samples produced in rod geometries. In specimens produced with such geometries, the electric current and field are homogeneous only in the central region of the specimens. In cylindrical pellets, another sample geometry used, the electrodes consist of metallic disks or grid-shaped structures (specially prepared) pressed on the flat surfaces of the sample. Conductive pastes (e.g. silver paste) can also be used to increase electrical conductivity.[17] In this context, the best electric field and current density can only be achieved under certain geometrical conditions.[60] Pellets smaller than 10 mm in diameter are usually used in flash sintering experiments. However, the height-diameter ratio of such pellets is also important. Samples with relatively short heights can cause heterogeneous structures by increasing the formation of hot spots while minimizing gradients between the center and the electrode.[61]

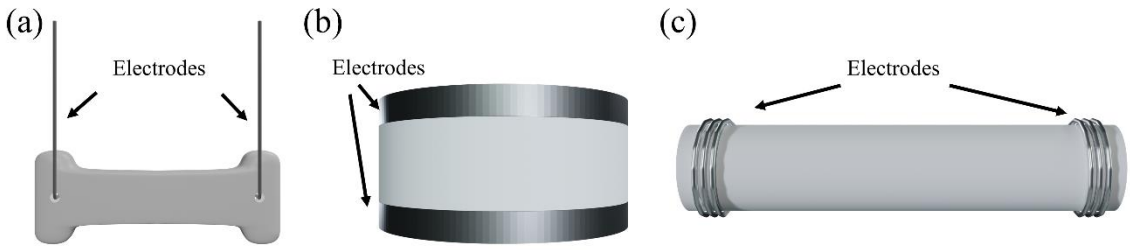

Figure 1.3. Schematic representation of typical sample geometries used in flash sintering experiments; a) dog bone, b) pellet, c) rod.

1.2.3.2. Ultrafast high-temperature sintering

Wang et al. [62] introduced a novel contemporary sintering technique in 2020, which is called Ultra-fast High-temperature Sintering (UHS). As shown in Figure 1.4., UHS enables the densification of monolithic ceramics by radiative heating (10^3-10^4 K/min)

usually under an inert atmosphere such as argon in extremely short times (10-300s).[62] This is attained by wrapping the green body within graphite felts which are quickly Joule-heated by an electric current passage. To date, several materials systems have been processed by UHS, including zirconia [63], tricalcium phosphate [64], silicon nitride [65], alumina [66], and various zirconates.[67,68] Also, the recently emerged UHS has been used to prevent undesired Li loss during sintering. $Li_{1.3}Al_{0.3}Ti_{1.7}(PO_4)_3$ (LATP) was sintered up to a relative density of 90.2% within 100 s, compared to the relative density of 85.4% reached for conventional sintering.[69] Similar to LATP which contains lithium, $Li_7La_3Zr_2O_{12}$ (LLZO) was densified using the same method because the short exposure time to high temperatures decreases Li loss by evaporation.[70] Furthermore, in contrast to flash sintering, it allows the rapid synthesis and sintering of a wide range of ceramic materials by separating the intrinsic properties of the material (electrical response) from the process. Compared to other advanced sintering techniques (spark plasma sintering (SPS), cold sintering, flash sintering), this technique allows multiple materials to be sintered simultaneously (e.g. 100 5 mm diameter ceramic samples in 20 columns and 5 rows). Besides, since in the UHS technique the ceramics can pass quickly through the heating strips, it provides a great potential for sintering products in a way that can be scaled up from laboratory scale to industrial scale.[62]

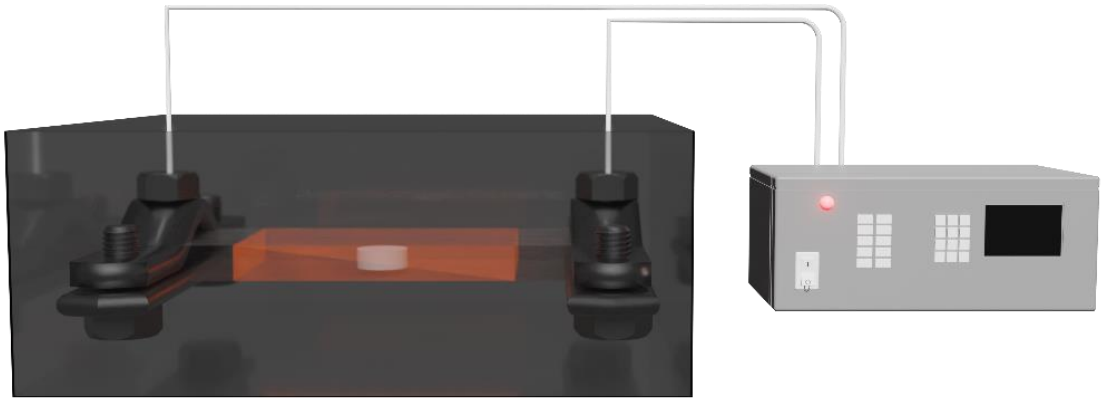

Figure 1.4. Schematic image of the ultra-fast high temperature sintering process.

1.3. Sintering mechanisms of current sintering techniques

1.3.1. Effect of hydrothermal conditions

As previously mentioned, the cold sintering process requires the simultaneous combination of a liquid phase, external pressure, and temperature. This promotes a localized dissolution of the ceramic at the neck center, ion diffusion through the liquid, and precipitation at the neck surface as shown in Figure 1.5.[71] As the die for cold sintering process can be heated to a temperature below 400 °C, heat is transferred from the heating jacket to the sample by conduction, similar to hydrothermal hot-pressing.[72] As dissolution at particle contact points plays a crucial role in cold sintering, the ceramic must have a high solubility in the selected fluid phase and preferably have congruent dissolution.

The mass transport is indeed activated by a gradient in the chemical potential induced by the external pressure. Actually, the chemical potential gradient with respect to the pressure (p) of the "i" (μ_i) component of the system can be written as:

$$\frac{\partial \mu_i}{\partial p} = \Omega + p \frac{\partial \Omega}{\partial p} \tag{1.1}$$

Here Ω is the atomic volume. Assuming that the atomic volume gradient with respect to pressure is modest than, we can deduce that

$$\frac{\partial \mu_i}{\partial p} \approx \Omega > 0. \tag{1.2}$$

In other words, the chemical potential of the high-stressed contact at solid-liquid-solid interface (μ_1) is higher than that of and low-stressed free pore region (μ_2), causing mass transport from the neck center to its surface.[71,73–75]

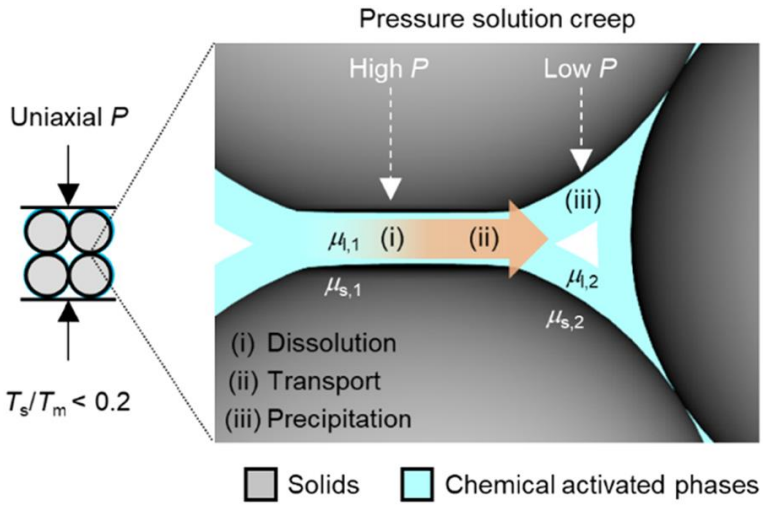

Figure 1.5. Schematic illustration of the mass transport during cold sintering process.

(Source: Sada, T. et al., 2021)[71]

In rHLPD, there are no major mass transport processes that occur in sintering, bringing the particle centers closer together and causing volumetric shrinkage. rHLPD enables a hydrothermal chemical reaction between the solute in the solvent and the porous matrix to crystallize and cause grain growth by filling the pores.[30] Similar to hydrothermal conversion principles, the transformation of a porous body to a densified body can take place via either in situ transformation or dissolution-reprecipitation mechanisms.[76] Additionally, heat can be transferred by conduction and convection.

1.3.2. Effect of heating rate

Different mass transport mechanisms contribute to sintering at different temperatures. The major transport mechanisms that occur during sintering are lattice, grain boundary, and surface diffusion. When compared, the required activation energy values, in ascending order, correspond to surface diffusion, grain boundary diffusion, and volume diffusion, respectively. Accordingly, surface diffusion governs mass transport during sintering at low temperatures, enhancing neck growth, while grain boundary diffusion at intermediate temperatures and lattice diffusion (from the grain boundaries) at high temperatures dominates transport during sintering, resulting in densification (Figure

1.6). Therefore, the driving force through the early stages of sintering is provided by the curvature radii of the surface. Consequently, any neck growth during this stage causes a decrease in the driving force for sintering. High heating rates reduce this loss of driving force by minimizing the time spent at lower temperatures, where surface diffusion i.e., neck growth dominates. In the UHS process, where high heating rates are used, the same mass transport mechanisms are considered to exist as in the fast-firing technique.[62,77]

Other mechanisms have been proposed by Todd and co-workers. These include the formation of a thinner and less-coordinated pore structure in rapid sintering (probably related to the suppression of surface diffusion).[78] Additionally, they suggested that the grain boundaries formed by rapid sintering might possess an out-of-equilibrium structure and diffusion coefficients different from those obtained conventionally.[57,79]

From the heat transport point of view, conduction and convection heat transfer mechanisms are not usually sufficient for sintering techniques with high heating rates. It was shown that heat transfer by radiation plays a more important role in such rapid sintering techniques.[66,80] When considering UHS and fast firing (direct sintering) the heat is always absorbed in the sample surface as the sample is exposed to intense IR radiation (with also some contribution at the visible wavelength). Other rapid sintering techniques like flash sintering make use of internal heat generation by the Joule effect, this results in a thermal gradient within the sample which is opposite to what is typically observed in fast firing and UHS: in flash the sample surface is colder due to the heat losses by radiation.[81] In addition, microwave sintering presents somehow an intermediate behavior depending on the dielectric loss factor of the ceramic. If the ceramic is lossy there is bulk dielectric heating, otherwise, the sample is heated by absorbing the IR radiation emitted by a susceptor. Often, ceramics become lossy at high temperatures thus combining the two mechanisms. To some extent, this condition appears “ideal” as it reduces the thermal gradients combining both external and internal heating. A similar behavior takes place in flash spark plasma sintering where the heat is first absorbed by conduction from a graphite element in contact with the sample and then, once a critical temperature is reached, internal Joule heating starts.[82]

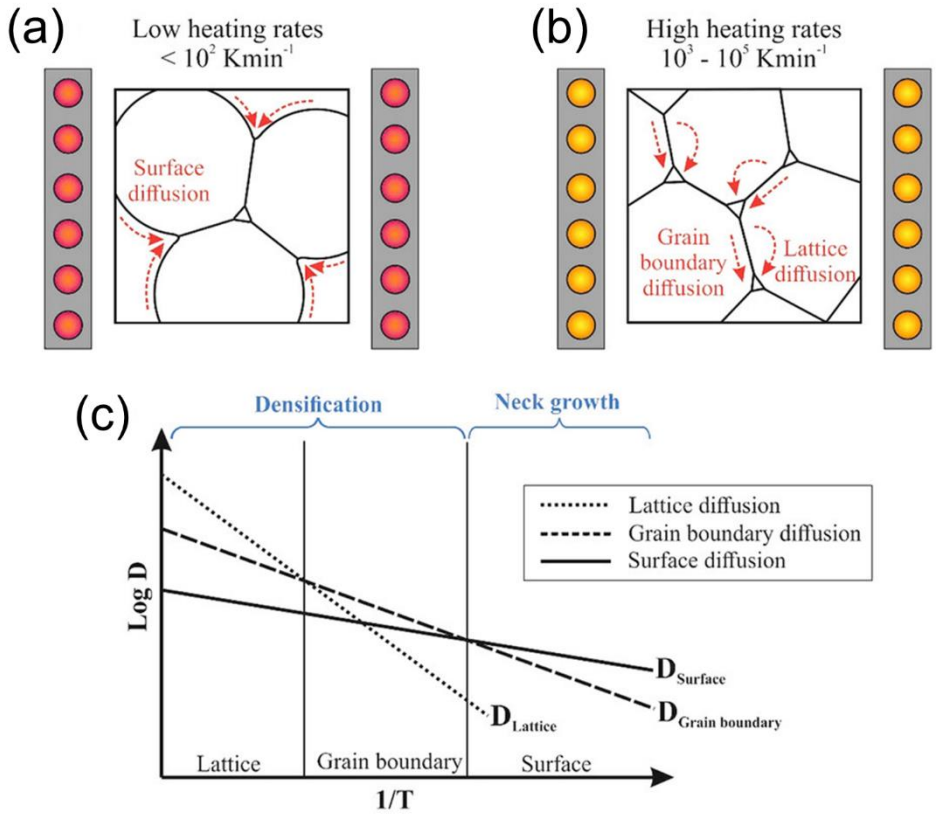

Figure 1.6. Influence of heating rate on sintering; (a) low heating rate, (b) high heating rate, (c) diffusion coefficients as a function of 1/T.

(Source: Guillon, O. et al., 2023)[77]

1.3.3. Effect of electric current and field

Describing plausible phenomena caused by electric current and field on the material during sintering is complex (Figure 1.7). These complex phenomena depend on several factors such as composition, environment, field type, temperature, and time. Even low electric fields within the sample cause an increase in shrinkage.[83] Joule heating takes place with current flow, increasing the temperature by several hundreds of degrees compared to the furnace temperature.[77] Indeed, different mechanisms have been proposed to explain densification related to heating rates, localized overheating of the grain boundaries, population of defects, defects mobility, and driving force for diffusion.[17]

From the perspective of defect chemistry, point defects must be sufficiently mobile and exist in high enough concentrations for ion transport to occur.[77,84] Defect formation under electric fields has been suggested by Raj and co workers as a possible cause of increased sintering kinetics under electrical loading.[59] When Frenkel pairs are generated, an ion typically shifts from its lattice site to an interstitial site, creating a vacancy. However, from a view of thermodynamic aspects, it has been revealed that forming these defect pairs within the crystal lattice demands exceedingly high fields—well beyond the magnitudes employed in sintering experiments.[77] As such, the underlying mechanisms of this complicated defect formation still remain elusive within the realm of current scientific understanding. Besides, chromatic alteration is observed in samples produced under such conditions because while oxygen ions are transported to the anode side, migration of positively charged oxygen vacancies accumulated on the cathode side occurs.[77] The reduction of the oxide induced by the electric current might also play a role also on sintering, it has been for instance reported that reducing conditions decrease the energy barrier for cation diffusion in fluorites.[85]

Cationic diffusion drags grain boundary migration. Since cationic diffusion usually depends on the partial pressure of oxygen, the drag effect of segregation relies on the reduction state. The electrical field impacts grain growth behavior by changing oxygen vacancy concentration.[77] Such thoughts regarding defect chemistry can also be seen in UHS process because reducing the atmosphere used with a presence of carbon felt may provide defect formation at elevated temperatures, which might affect the densification and grain growth.[86]

Localized overheating or even melting of the grain boundary (due to the reduced section for current flow and the localized higher resistivity as a result of the space charge region), has been widely discussed as a flash sintering mechanism[87,88], however numerical simulations seem to discredit this hypothesis.[89] While the thermal gradients could be extremely high ($\approx 10^6$ K/m) the absolute temperature difference is modest as the scale of the particles is usually in the order of 1 μm or even below.

In flash sintering, about 90% of the total energy input is heat loss by radiation while conduction and convection losses can be assumed to be negligible.[81,90] In contrast to flash sintering, in spark plasma sintering the heat is generated by the Joule effect and transferred to the sample by conduction. In UHS, heat is mainly transferred from carbon felt by radiation (with a small amount of conduction as well).[62]

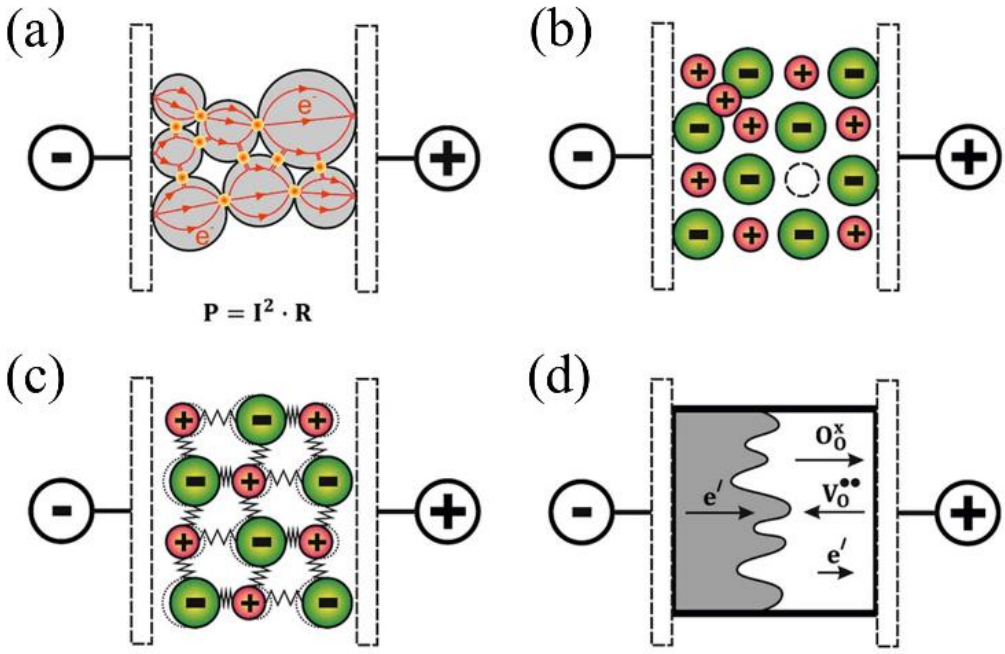

Figure 1.7. Influence of electric current and field on sintering; (a) joule heating (P = power, I = current, R = resistance); (b) formation of Frenkel defects; (c) activation of phonon modes; and (d) electrochemical blackening.

(Source: Guillon, O. et al., 2023)[77]

1.4. Motivation and goals

Traditionally ceramics are sintered at elevated temperatures e.g., above 1000 °C with long dwell times by classical sintering techniques e.g., solid state, liquid phase, and pressure-assisted sintering. Consequently, the sintering process is a crucial step in ceramic processing and uses a lot of energy. High energy costs and the emission of greenhouse gases (GHGs) are the results of conventional sintering at high temperatures.[91] Therefore, the scientific community has been on a never-ending search for sintering methods that consume less energy.[92] In recent years, different sintering strategies have been introduced to allow the densification of ceramics and glasses with lower energy requirements compared to conventional sintering, which are broadly called advanced or unconventional sintering techniques. By using such advanced techniques, it was shown

that the energy consumption of sintering processes can be greatly reduced. Comparing the energy consumption of various sintering processes, the energy consumption in the sintering of perovskite $BaTiO_3$ is about 2800 kJ/g for conventional sintering i.e., solid-state sintering. This energy consumption can be reduced to 2000 kJ/g for liquid phase sintering and 1050 kJ/g for current-assisted sintering techniques. This value can decrease further to 540 kJ/g for microwave sintering and 130 kJ/g for fast firing, to even around 30 kJ/g for the CSP.[93] It should be noted that the properties of ceramics sintered by such techniques with low energy consumption should be comparable to or superior to those of conventional sintering. Besides, to govern the resultant microstructures and properties, crucial sintering parameters encompass the heating rate, maximum temperature, dwell time, and the atmosphere. Supplementary options include the application of mechanical pressure, electric fields or currents, electromagnetic waves, as well as the incorporation of sintering additives, among others.[77] Therefore, the applications of cold sintering techniques that enable densification at low temperatures below 400 °C or other novel methods that shorten sintering times (from seconds to a few minutes) with fast heating rates to ceramic materials are becoming increasingly important by utilizing these possible parameters.

This thesis aims to utilize advanced sintering techniques currently available along the data presented. Ceramics produced using these methods are compared to their traditional counterparts in terms of process-structure-property relationships. In this context, Chapter 2 presents a general sintering overview and a comprehensive review of cold sintering techniques that gained popularity in 2016 but have been experimented with extensively since the 1970s. Subsequently, studies on cold sintering process (CSP) for various materials, including soda-lime glass, regolith, and potassium sodium niobate (KNN) materials, are presented in Chapters 3-5. Another cold sintering technique, in other words, a different low-temperature densification concept, rHLPD process, was employed for perovskite ceramics such as $BaTiO_3$ and $SrTiO_3$ in Chapters 6&7. Furthermore, in Chapters 8&9, ceramics with different compositions were produced using the fast-firing process currently widely applied in the industry, and these were compared with those produced using traditional methods. Chapters 10-12 give the investigation of joule heating-based sintering techniques, such as ultrafast high-temperature sintering and flash sintering, for the densification of KNN and Zirconia. Furthermore, the effects of the atmosphere conditions in UHS were investigated in order to answer the query of whether

the atmosphere matters in sintering. In this regard, UHS experiments were conducted in a nitrogen atmosphere instead of an argon atmosphere which is a typical atmosphere for UHS. The majority of the mentioned ceramic systems were sintered and documented for the first time using these current sintering techniques. Each technique and its respective procedure were anticipated to exhibit distinct densification and grain growth behaviors for these materials. Finally, Chapter 13 presents a comparison of current sintering techniques used in terms of applicability, equipment, materials, and so on. The pros & cons and limitations of such techniques were explained. Certain algorithms were proposed based on the sintering techniques used.

CHAPTER 2

COLD SINTERING OF CERAMICS AND GLASSES: A REVIEW

The following chapter is published in Curr. Opin. Solid State Mater. Sci. 24(1) (2020) 100807 (Reproduced from [5] with permission from Elsevier).

Abstract

Traditionally ceramic artifacts are processed at high temperatures (>1000°C) by classical sintering techniques such as solid state, liquid phase and pressure-assisted sintering. Recently, inspired from the geology, novel sintering approaches that allow the densification of ceramic components at relatively low temperatures ≤ 400° C have been proposed. While initial efforts for such low temperature densification concept were developed in the mid-70s, the topic has become increasingly prominent in the last decade. Currently, these low temperature methods can be classified into four main groups: (i) hydrothermal reaction sintering (HRS), (ii) hydrothermal hot pressing (HHP), (iii) pressure-assisted densification techniques: room-temperature densification (RTD), cold sintering (CS), warm press (WP), and finally no-pressure assisted method called (iv) reactive hydrothermal liquid phase densification (rHLPD). Above named techniques are commonly assisted by an aqueous solution used as either reactant or transient liquid phase to assist densification. Starting from the background in traditional sintering processes, this review aims to explore in depth the existing literature about low temperature densification approaches along with their advantages & disadvantages, and probable application areas.

2.1. Sintering overview

The term *sintering* basically defines a process of bonding, densification and/or recrystallization of powder compacts, i.e. a treatment in which a green-body is converted to a stronger monolith [1-4]. While ceramic artifacts found in archaeological sites indicate sintering practice even in the upper Paleolithic era, i.e. specifically Gravettian around 26,000 years ago [5], the first steps towards establishing sintering theory and practice were only developed starting from early 1900s [2, 6]. One of the first scientific works was published by Ferguson J. B. in 1918 [7, 8]. In the late 1940s, the main qualitative analysis on sintering were postulated by Rhines [9] for solid state and Lenel [10] for liquid phase sintering. Then, the quantitative models for sintering were built by Frenkel [11] in 1945 and Kuczynski [12] in 1949. Lenel [10], Kingery and Berg [13] and later on Coble, contributed to the sintering theory for ceramic materials, published series of remarkable works [3, 14-17].

For more details on sintering, the interested reader is referred the published works of German R.M. [3, 6, 18], and a recent review by Bordia et al. [8]. Here, only a brief overview will be mentioned. There must be a net reduction in the free energy between the two particles to be sintered on a local scale towards thermodynamic minimum for sintering to take place [2, 19]. At early stages of sintering the driving force to minimize the free energy is related to the annihilation of surface curvatures. Mass flow is a function of chemical potential gradient of the surface, and this is proportional to the surface curvature [20]. Later on, the dominant driving force turns to be the interfacial energy reduction by the replacement of higher energy interfaces with the lower energy ones via pore reduction and grain growth. The densification driving forces can be enhanced with the externally applied pressure which results in the amplified stress levels on the initial small particle contacts. Over time the rate decreases, and in the late stages of sintering diffusional events which are related to the processing temperature, controls the densification as in the case for methods such as hot pressing (HP) or hot isostatic pressing (HIP) [21]. A much stronger driving force can be obtained, in principle, from a chemical reaction during sintering which can provide significant free energy reduction. However, because the microstructural evolution is difficult to control, it is barely ever considered to achieve densification [2, 17].

Conventional sintering is generally categorized in three basic forms: (i) solid-state, (ii) liquid phase, and (iii) viscous sintering. Typically, when a green body is densified at temperatures not causing the liquid formation, the process is called solid state sintering (SSS). The particles start to join each other accompanied by the reduction in the porosity because of the atomic diffusion [22]. Mass transport in SSS occurs through surface (non-densifying) and bulk (densifying) transport. The former one produces neck growth by mass flow from surface sources, i.e. transport originating and terminating at the surface by evaporation-condensation, surface diffusion and volume (lattice) diffusion, resulting in no densification or shrinkage. To attain densification, internal mass sources must be transferred to the neck, i.e. diffusion from interior to pore by grain boundary diffusion, volume and plastic flow which predominantly observed in metals [2, 3, 17, 18]. While non-densifying mechanisms do not directly contribute to densification process. These mechanisms reduce the surface curvature and consequently lower the rate [2]. In another words; for kinetic considerations both mechanisms should be considered when sintering in solid state is practiced.

In liquid phase sintering (LPS) the solid mixture carries typically few volume percent of liquid (depending on the system but generally below 15 vol.%[21]) at the sintering temperature. Densification in LPS can occur both by liquid flow akin to viscous flow and mass transport similar to the ones observed for SSS [8]. In the classical LPS theory the chemical reaction between the solid and the liquid phase is assumed to play a little role. The process is considered to follow three successive stages: (i) rearrangement, (ii) solution-precipitation, (iii) elimination of porosity [18, 23-25]. The initial stage of LPS is liquid redistribution and particle rearrangement to reach ideal packing due to capillary gradients. In the following solution-precipitation stage, solids dissolve at the higher chemical potential sites, and precipitate on the sites with lower chemical potential [26]. The densification of the skeletal network surrounded by liquid phase controls the final stage. It should be noted that several important parameters such as the wettability, liquid volume, viscosity and solubility of solid and liquid, etc. influences LPS [24].

Compared to that in LPS, when sufficiently large liquid volume (25-30 vol%) is used the process is called as *viscous flow (vitrification for clay based materials) sintering* as seen in the traditional clay based ceramic manufacturing where above 50 vol% of liquid is practiced commonly (e.g. porcelains). Such densification process is believed to occur through pore filling by viscous flow [22, 27]. In transient liquid phase sintering, a liquid

phase forms in the body at an early stage of sintering but it disappears in the course of sintering progresses, leaving no glassy phase on the grain boundaries, contrary to the other LPS techniques in which the liquid phase may persist over the course of firing. While the control on the microstructure is challenging, the process results in components having higher suitability for high temperature applications than those produced by other LPS processes [17, 19].

Densification of amorphous powder compacts occurs by material flow over the entire volume, i.e. viscous (flow) sintering. Different than SSS and LPS, for viscous sintering the geometric variables such as particle and pore size & shape are not important while the relative density of the green-body is of great importance [8, 22]. Besides, as known the sintering of glass may be impeded by crystallization. However by enhancing the heating rate, it is still possible to sinter the glass to full density before the onset of crystallization[28]. While crystallization depends on nucleation and growth, glass sintering is merely related to viscous flows. Because for nucleation not only rheological properties but also the amount of undercooling is critical, a faster heating rate gives an advantage to sintering process.[28, 29]

In addition to the pressureless sintering, there are pressure-assisted sintering techniques (HP, HIP, sinter/hot and gas forging, etc., commonly all are non-economical and sample size is limited). In such techniques, both externally applied (uniaxial, hydrostatic or triaxial hybrid) pressure and surface curvature may contribute for densification. During the initial stage, external pressure is amplified at the particle contacts. At these points effective pressure is much higher than that of the applied one, and causes a stress level higher than the yield strength of the material, i.e. plastic flow and grain re-arrangements (particle centers get closer) are active. When particle coordination increases, the stress at the local contact points falls below yielding. For most materials, at low temperatures the yield strength is high and for this reason elevated (in the range of GPa) consolidation pressures is needed to attain full density. This is beneficial to avoid grain growth and obtain fine grained highly dense microstructures but there are equipment limitations to reach such pressures. As a remedy, heating (thermal softening) is applied to decrease required pressure levels since diffusion is enhanced at elevated temperatures [17, 21, 30].

The pressure during heating imposes complex stress states on the particles. When stress and diffusion (atomic motion) is combined, creep (a time-dependent deformation)

may occur at stress levels below yielding, and in pressure-assisted sintering this is the most dominant densification mechanism. Atomic transport can proceed by (i) Coble creep [31-33], i.e. grain boundary diffusion, (note that in geology if liquid/solution trapped at the grain boundaries assist densification, the mechanism is called pressure-solution creep via dissolution-precipitation process [30, 34-36]), and (ii) Nabarro-Herring creep [37] i.e. volume diffusion controlled creep [38].

Traditional sintering practices have limits to control the microstructure effectively. For example, it is difficult to produce nano-structured materials because of the grain growth in the final stage of sintering [8]. Some of the contemporary techniques address this problem: sintering under the effect of electrical current and pressure, i.e. spark plasma sintering (SPS) [39-41], sintering by microwave [42-44], sintering by electrical joule heating, i.e. flash sintering allowing very rapid densification (< 60 s) [45], and selective laser sintering [46].

2.2. Low temperature densification methods

Several sintering examples can be found in nature; ice sinters akin to pressure-assisted sintering and transforms into a glacier [47-49]. Another one is *lithification* in which loose particles become sedimentary rock. Lithification is a chemical process that enables densification by reducing porosity via compression (pressure) and cementation [50]. Thermal sintering processes also be seen but generally at low shear stresses, see **Fig. 2.1**. Instead, in natural shock sintering initial temperatures may be low but pressure levels are high, i.e. cold plastic flow processes. Industrially, reaching to few gigapascals of pressure is not an easy task, while in nature much higher pressures occur. Implications on kinetics are important as well, since in industrial manufacturing the processes are required to be finalized as fast as possible which may take significantly longer in nature (hundreds of years [50].

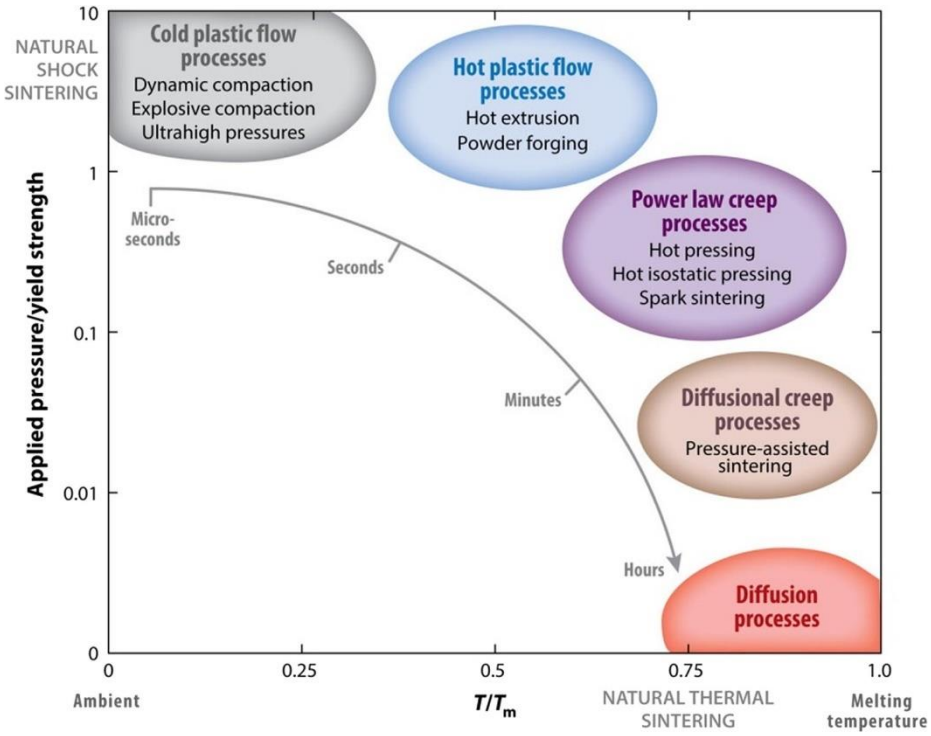

Figure 2.1. Pressure-assisted sintering techniques portrayed on applied pressure/yield strength versus temperature (T) to melting temperature (T_m) (Reprinted from [21, 50], Copyright (2014) & (2016), with permission from Elsevier and Annual Reviews).

Inspired from the above mentioned natural processes, scientists have put efforts to produce dense and strong ceramic and glass compositions at low temperatures <~ 400°C, recently referred to as *cold sintering*. All these techniques rely on the externally applied pressure and sometimes as in the case for Hydrothermal Reaction Sintering (HRS) or Hydrothermal Hot Pressing (HHP) specially designed apparatus are needed. Sintering without the application of high temperature necessitates an externally applied pressure to intensify the driving force for densification (**Fig. 2.1**). Another typical feature is the assistance of liquid phase (commonly water) with or without the application of mild heating. In **Figs. 2.2(a&b)** the number of publications and patents recorded from 1970 is given, highlighting the contemporary growing interest. This review aims to explore such existing literature on all currently published low temperature densification works along with their advantages and disadvantages.

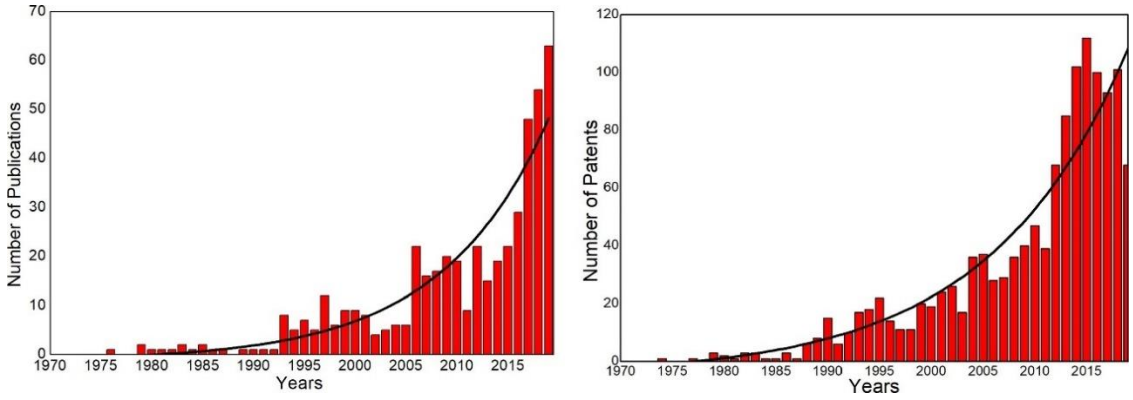

Figure 2.2. (a) Number of publications resulting from a *web of science* search with the keywords: "cold sintering", "low temperature sintering", "low temperature densification", "low temperature solidification", "hydrothermal densification", "hydrothermal sintering", "hydrothermal reaction sintering", "hydrothermal solidification", all data is merged into same plot in order to show the contemporary trend of such topic. (b) Number of published patents found from Questel database by searching the abstracts using following queries: ((low 1w temperature 1w densif+) + ((low 1w temperature 1w sint+) + ((low 1w temperature 1w solidif+) + (((hydrothermal or (hydro 1w thermal)) 1w densif+) + (((hydrothermal or (hydro 1w thermal)) 1w sinter+) + (((hydrothermal or (hydro 1w thermal)) 1w solidif+) + ((cold 1w sinter+) for each query "(glass or ceramic)" was added and all results were merged to plot. "1w"means given two keywords should be in close proximity. Both data was extracted from 1970, and the line represents an exponential growth function fit.

Initial studies related with sintering at low temperatures were conducted by Roy et al. [51, 52] on cement mortar. The authors sintered the green compacts both by hot pressing around 150^{o}C with pressures in between 172-344 MPa, and without heating under a pressure of ~700 MPa. The formed components demonstrated to have high relative densities with very few observable porosities and compressive strength values reaching around 510 MPa. Concurrently, novel instruments for hydrothermal reaction sintering, hydrothermal hot pressing were developed and practiced by Japanese researchers for the production of oxide ceramics in between 70-80s [53]. In late 70s, pure

metals, alloys and few ceramic compositions like NaCl, MgO, TiC, etc. were sintered at room temperature (RT) under high (e.g. 4 GPa) pressures [54, 55].

2.2.1. Hydrothermal reaction sintering

Hydrothermal reaction sintering (HRS) is one of the most efficient methods used to obtain very high relative density (e.g. > 99%) ceramic materials. As given in **Eq. 2.1**, reaction between highly pure metal (Me) powder or chips and water at a specific temperature (500-1000°C) and pressure (100 MPa) levels results in the formation of sintered metal oxide (MeO) and hydrogen (H_2) gas [53]. The resultant H_2 gas while leaving the system, induces the reaction to proceed further and more efficient compression for the component [62]. Although the temperatures specified in the process sounds like high, it is important to note that the formed oxides are commonly sintered at considerably higher temperatures than those stated. For example, traditionally hafnium oxide (HfO_2) is sintered at temperatures around 1800°C, instead similar relative densities can be achieved by HRS at temperatures in between 900-1000°C. HRS, therefore, is a relatively mild temperature sintering method [63], and is characterized by three distinct stages: (i) hydrothermal (by supercritical water) oxidation of the metal, (ii) diffusion of the H_2 gas from the capsule, and (iii) sintering of the oxide powder consolidate [64].

$$Me + H_2O \rightarrow MeO + H_2 \qquad (2.1)$$

The innovative work of Hirano and Somiya [62] showed how to obtain pure chromium oxide (Cr_2O_3) tablets by using chromium (Cr) powder (see **Fig. 2.3(a)**). The authors also formed stoichiometric magnetite single crystal without any other secondary phase formation [65]. During the monolithic Cr_2O_3 production; chromium powder and water were mixed and placed into the platinum capsule. The air was sealed with electric arc, and the capsule was placed in a test tube type pressure vessel (**Fig. 2.3(b)**). A pressure of 98 MPa was applied at 1000°C, and it was observed that 99.2% relative density was reached after 3 h. For comparison, conventional sintering of Cr_2O_3 with MgO sintering aid (up to 0.1% by mass) at 1600°C / 1h resulted in the formation of magnesium chromite-

spinel phase at the grain boundaries which prevented the grain growth, and densities of over 99% were obtained [66].

HfO_2 production was achieved with hafnium (Hf) metal chips at a temperature range of 800-1200°C under 100 MPa for 3 h process. No sintering was observed at 800°C whereas components with relative densities of 92% and 98% were obtained at 900°C and 1000°C, respectively. X-ray density of HfO_2 was only reached by 1200°C treatment [64]. The formation of monolithic ZrO_2 ceramics with no flaws is difficult to obtain by traditional sintering due to crack formation during monoclinic-tetragonal phase transition, besides temperatures above 1600°C are required. HRS was used as a remedy to sinter ZrO_2 at temperatures below the phase transition causing no cracking. Samples with a relative density of 99% were formed by HRS as a result of the reaction between metallic Zr and supercritical water at 1000°C / 3h under 98 MPa pressure. H_2O/Zr initial ratio was found to be critical for densification and above certain level no well sintered bodies were obtained [67-69]. Apart from the ceramic compositions given above, the technique was also conducted to obtain others such as iron oxides (FeO, Fe_3O_4) and lanthanum chromite ($LaCrO_3$) [53].

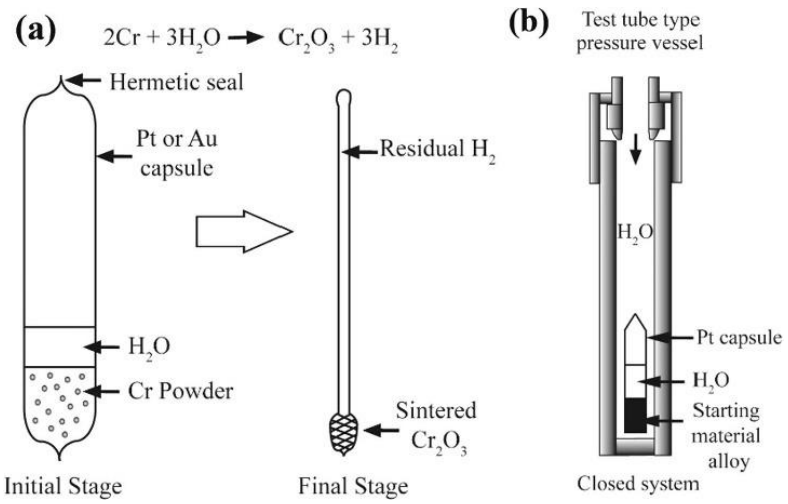

Figure 2.3. (a) HRS stages of Cr_2O_3, (b) apparatus used for hydrothermal reaction sintering [53] (Reprinted by permission from Springer: Hydrothermal Reactions for Materials Science and Engineering by S. Sōmiya Copyright 1989).

2.2.2. Hydrothermal hot pressing

Hydrothermal hot pressing (HHP) is used to sinter inorganic powders under hydrothermal conditions but at much lower temperatures (< 500°C) compared to HRS [70, 71]. HHP was described as a process of artificial lithification [72], since the processing temperatures are as low as seen in geology, it can also be called as a geo-mimetic process.

There are two basic prerequisites for HHP to proceed successfully: compaction of the sample under hydrothermal conditions, and a path (space) for water removal. Compression accelerates the packing of the initial powder, meanwhile avoiding the development of shrinkage cracks. Compaction is dependent on the speed at which water is removed from the starting powder mixture. If there is no path for the water retreat, it remains in the pores and prevents densification [70]. The final relative density in the HHP depends on processing temperature, pressure, time and amount of water used [70]. **Figure 2.4(a)** provides the schematic drawing of the HHP equipment, while **Fig. 2.4(b)** shows the autoclave details [53, 73].

One of the first applications of HHP was conducted on a mixture of α-quartz and amorphous silica. After addition of NaOH including aqueous solutions, the blend was pressed under 180 MPa pressure. The sample then placed in autoclave which was heated in between 120-350ºC under 27 MPa pressure for 30 min [72]. In other studies; $CaCO_3$ [74], and subsequently TiO_2 was formed. In the process; TiO_2 (800 nm average particle size) was mixed with water, placed in autoclave, compressed by the push rod to 200 MPa pressure while heated to 350°C for 30 min. The relative density of sintered TiO_2 pellet was found to be 71 % [75].

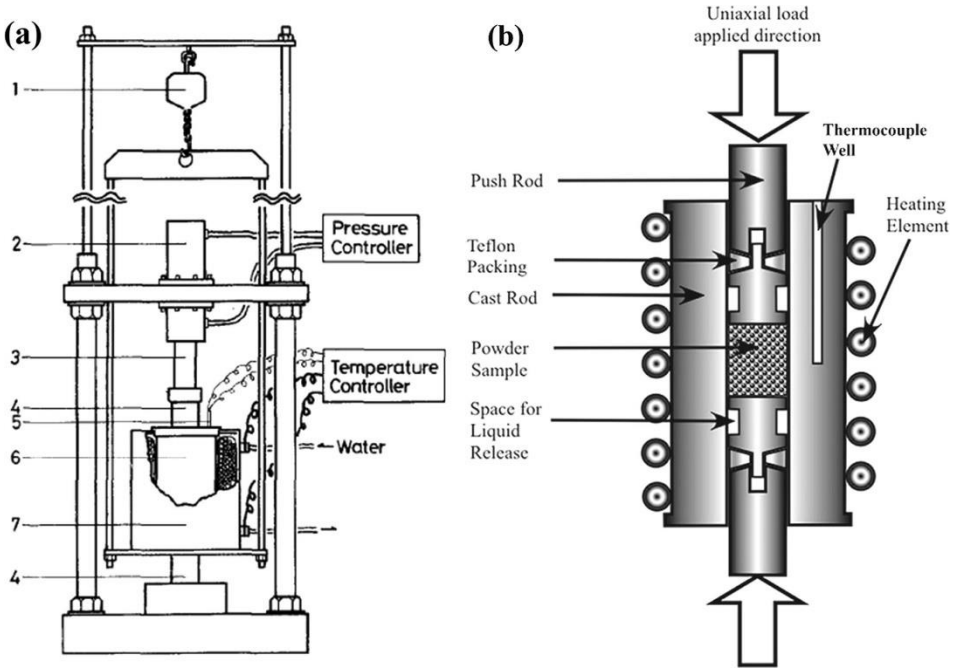

Figure 2.4. (a) HHP equipment details 1:crane for adjusting the furnace position, 2:pump, 3:ram, 4:autoclave push rod, 5:thermocouple, 6:autoclave, 7:induction furnace [53, 72], (b) hydrothermal hot pressing autoclave (Reprinted by permission from Springer: Hydrothermal Reactions for Materials Science and Engineering by S. Sōmiya Copyright 1989) (Reprinted from [73], Copyright (2015), with permission from Elsevier).

In a more recent work, silica (50 nm in size) synthesized by Stöber process was mixed with NaOH aqueous solutions to improve silica dissolution-precipitation process. Initially the blend was pressed by 190 MPa, followed by cold isostatic pressing at 500 MPa / 5 min. The relative densities of the green bodies were in between 50-55%. These tablets were subjected to "hydrothermal sintering" using a modified HHP equipment operated at RT with 127 MPa pressure, then at 150°C, and finally at 300°C under 350 MPa pressure for 90 min. Monolithic amorphous silica samples having 86% relative density was obtained by using the lowest NaOH concentration while α-quartz having 98% relative density was reached when concentrated NaOH solution was used [76]. The same research group studied also the effect of water. Three different types of silica: naturally hydrated, partially dehydrated, and deliberately added water powders were all subjected to HHP procedure. After the formation of green bodies, densification was followed under

95 MPa pressure at RT, followed by the application of 190 MPa pressure at 300°C for 90 min. The relative densities of natural hydrated, partially hydrated, and added water were found to be around 67%, 63-67%, and 75%, respectively. The study suggested that the addition of water enhances the densification [77]. Apart from those few detailed ones, there are numerous compositions obtained by using HHP as given in **Table 2.1.**

Table 2.1. List of materials produced by hydrothermal hot pressing, together with processing conditions and some of the observed properties.

Materials	Processing conditions	Properties	Relative density (%)	Ref.
Al_2O_3	110 °C 40 MPa 2 h	SSA = 450 m^2/g	~33*	[78]
$AlPO_4$	150 °C 40 MPa 2 h	SSA = 40-107 m^2/g	~35-54*	[79]
$Ca_5(PO_4)_3(OH)$-$(Ti_{0.40}Zr_{0.10}Cu_{0.36}Pd_{0.14})_{99}Ca_1$	150 °C 40 MPa 2 h	N.A.	N.A.	[80, 81]
AlO(OH)	180 °C 80 MPa 3 h	N.A.	N.A.	[82]
Calcium aluminate / phosphate cement	300 °C 40 MPa 1 h	σ ~ 5-27.5 MPa	N.A.	[83]
$Ca_3Co_4O_9$	200-300 °C 50-200 MPa 1-5 h	ρ ~ 90-210 μΩ.m **λ** ~ 1.1-1.5 W/m/K	75-90	[84, 85]
$CaCO_3$	50-260 °C 5-68 MPa 0.17-10 h	σ_c ~ 5-160 MPa σ ~ 2-8 MPa H_v = 0.3-10 GPa	~56-92*	[56, 74, 86-89]
$CaCO_3$-$MgCO_3$	300 °C 25 MPa 10 min	σ_c = 37.1-44.3 MPa	N.A.	[90]
$CaCO_3$-$SrCO_3$	200-300 °C 25 MPa	N.A.	~85*	[91]
Ca_2O_4Si	200 °C 10-20 MPa 17-30 min	σ ~ 3-10 MPa σ_{bs} = 11 MPa	~43-69*	[92, 93]
$Ce(PO_3)_4$	150-200 °C 40-80 MPa 2 h	N.A.	~72-84	[94, 95]
$Cu_3(PO_4)_2$ & $Cu_2P_4O_{12}$	150 °C 40 MPa 2 h	SSA = 0.5-3 m^2/g	~53-82	[96]
Geopolymers	200 °C 8.5 MPa 45 min	σ_c ~ 55.3-103.3 MPa	N.A.	[97]

(cont. on next page)

Table 2.1 (cont.)

Glass	100-350 °C 15-60 MPa 5min-8h	H_v = 1-3 GPa σ_c = 150-460 MPa σ ~ 4-65 MPa λ ~ 0.1-0.2 W/m°C	N.A.	[73, 98-110]
$Ca_{10}(PO_4)_6(OH)_2$	100-300 °C 10-150 MPa 0-48 h	H_v = 0.4-2.9 GPa σ ~ 1-22 MPa σ_c = 15-150 MPa	~30-98	[111-124]
$Ca_{10}(PO_4)_6(OH)_2$ -Chitosan	150 °C 40 MPa 2 h	σ ~ 12-20 MPa	~50	[114, 125]
$Ca_{10}(PO_4)_6(OH)_2$ -Glass	325 °C 47 MPa 30 min	σ_c = 206 MPa	65	[126]
$Ca_{10}(PO_4)_6(OH)_2$ -$Ca_3(PO_4)_2$	250 °C 150 MPa 1-3 h	σ_c = 2.5 MPa	30-40	[127, 128]
$Ca_{10}(PO_4)_6(OH)_2$ -AZ31; Mg-3Al-lZn	150 °C 40 MPa 3 h	N.A.	N.A.	[129, 130]
$Ca_{10}(PO_4)_6(OH)_2$ -Ti alloy	50-150 °C 20-80 MPa 2-24 h	N.A.	N.A.	[131-137]
$Ca_{10}(PO_4)_6(OH)_2$ - $Ti_{40}Zr_{10}Cu_{36}Pd_{14}$	150 °C 40 MPa 2 h	N.A.	N.A.	[138, 139]
$La(PO_3)_3$	50-150 °C 5-30 MPa 1 h	N.A.	N.A.	[140, 141]
$La_{1-x}Sr_xMnO_3$-SiO_2	300 °C 350 MPa 90 min	$\rho = 960 - 7.8x10^7$ Ωcm	~80	[142, 143]
$Na_xCo_2O_4$	200-350 °C 100-200 MPa 1 h	ρ = 20-45 μΩ.m	~94-99	[144]
$Ca_8(HPO_4)_2(PO_4)_45H_2O$	110 °C 40 MPa 2 h	σ_c = 33 MPa	N.A.	[145]
Phosphate bonded Al_2O_3	250 °C 40 MPa 1 h	σ = 3-24 MPa	N.A.	[146]
SiO_2	100-350 °C 20-350 MPa 0-12 h	SSA = 467-1339 m^2/g σ_c = 5-230 MPa H_v ~ 0.7-2.1 GPa	~23-98*	[70, 76, 77, 147-157]
$SrCO_3$	200-300 °C 25 MPa	σ_c ~ 80-190 MPa	~93	[91]
$Sn_{1.24}Ti_{1.94}O_{3.66}(OH)_{1.50}F_{1.42}$	210-300 °C 60-120 MPa 0-4 h	N.A.	~86-99	[158]
TiO_2	100-350 °C 15-200 MPa 0.17-6 h	SSA = 50-300 m^2/g H_v = 0.2-7.8 GPa σ_c = 5-60 MPa	~42-98*	[70, 75, 159-164]
$Ca_6Si_6O_{17}(OH)_2$-Chitosan	150 °C 20 MPa 10-30 min	σ ~ 5-12 MPa	N.A.	[165]
Y-Zeolite	110-200 °C 40 MPa 1-12 h	SSA = 540-890 m^2/g H_v = 0.2-3 GPa	~57-99*	[166-168]

(cont. on next page)

Table 2.1 (cont.)

Zeolite-Al	130 °C 40 MPa 1 h	N.A.	N.A.	[169]
Zeolite-Kaolin clay	110-220 °C 40.53 MPa 0.5 h	σ_c = 10-24.7 MPa SSA = 70-118 m^2/g	N.A.	[170]
ZrO_2	350 °C 70 MPa	N.A.	N.A.	[171]
Materials to cure environmental problems	-	-	-	[172-188]

N.A.: Not available, **SSA:** Specific surface area, **σ:** Tensile strength, **σ_{bs}:** Bending strength, **σ_c:** Compressive strength, **λ:** Thermal conductivity, **ρ:** Electrical resistivity, **H_v:** Vickers hardness, ***Calculated**

After the application of HHP, a new technique called *double layered capsule hydrothermal hot-pressing* (DC-HHP) was developed particularly to prepare coatings like hydroxyapatite on metals. In this method, a cylindrical capsule that has double layer structure is used and subjected to isostatic pressing, see **Fig. 2.5** for device schematics. Between inner and outer capsule, alumina powder is placed to maintain the space for water retreat. Hydroxyapatite-coated magnesium,[129] and titanium,[133, 134, 189] were produced by using DC-HHP.

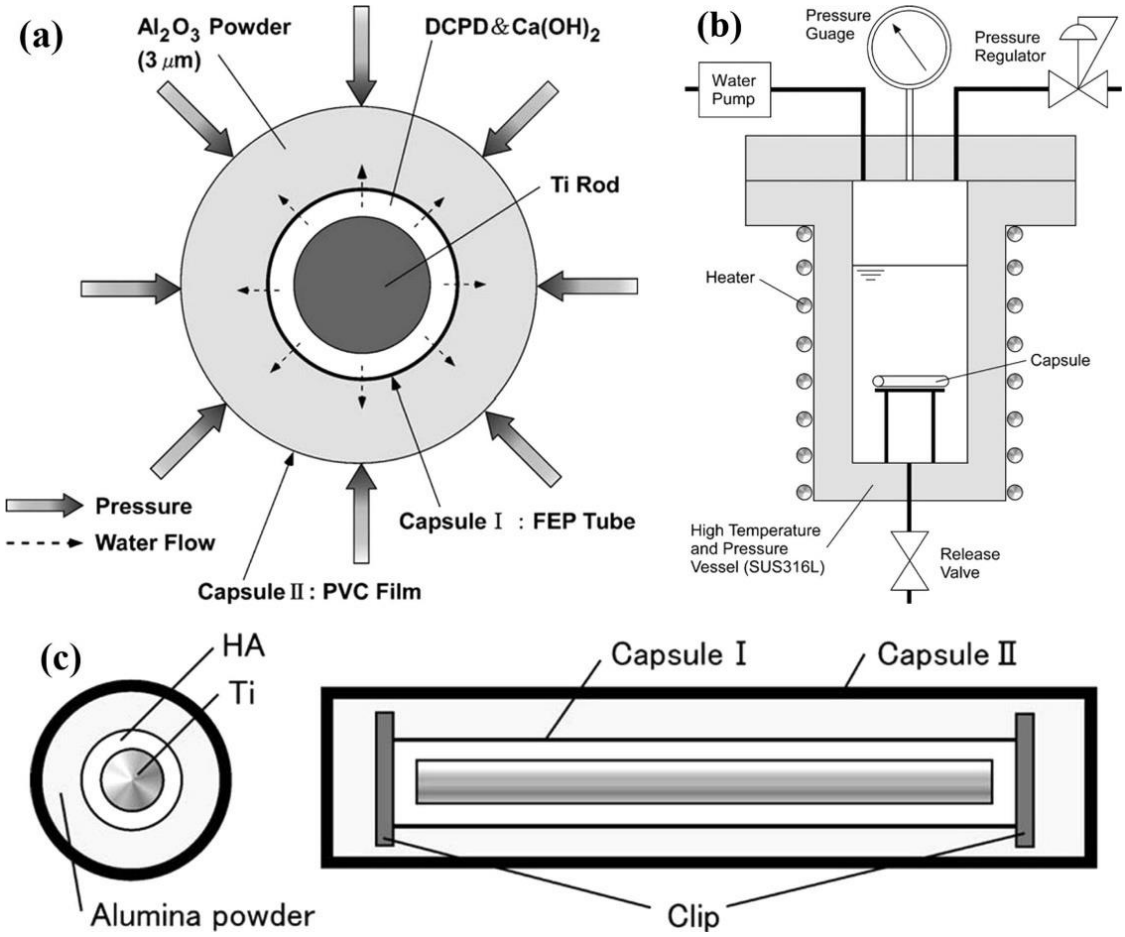

Figure 2.5. Schematic representation of double layered capsule hydrothermal hot-pressing (DC-HHP) system: (a) top view of the DC-HHP, (b) cross-sectional view of the autoclave with reaction capsule, (c) cross-section of the capsule (Reprinted from [133], Copyright (2006), with permission from Elsevier).

2.2.3. Room-temperature densification

It should be noted here that the terminology describing below is currently not standardized and can be confusing; consequently, we merged all the studies conducted at RT to densify ceramic and glass artifacts in room-temperature densification (RTD) section.

In late 90s, a research group from Brazil worked on compaction of nanosized ceramics powders under very high pressures (4.5-5 GPa) at RT. Both γ-Al_2O_3 powder (in water) and silica-gel (15 nm particle size) were consolidated at nearly hydrostatic

conditions which yielded in the formation of transparent SiO_2 samples having 86%, and translucent alumina components having 92% relative density. It was one of the first studies that obtained densified γ-Al_2O_3, and the measured Vickers microhardness (50 g) values were around 4.0 GPa for the silica, and 5.7 GPa for the γ-Al_2O_3. For silica components, the densification was related with the bridging silanol groups promoting the dehydration (up to 60%), and the consolidation mechanism was named as “cold sintering" [190-192]. During the last decade, the published studies using cold sintering terminology (see later) have become the object of steadily growing interest. However, the "cold sintering" term in those contemporary works defines a variant process (with much milder pressure and higher temperature conditions) from the ones given obtained by RT processes.

In 2014, researchers from Oulu University demonstrated the possibility to produce monolithic lithium molybdate (Li_2MoO_4) ceramics at RT. The authors called the method as room-temperature densification (RTD) which was simply based on the compression (under 130 MPa pressure) of the Li_2MoO_4 powder (sieved below 180 μm) together with small amount of water. The pellets were then processed in different ways: (i) conventionally sintered at 540°C (control sample), (ii) application of RTD and dried at 120°C, and (iii) application of RTD and dried at RT. While the densification mechanisms were not discussed in detail, it was shown that Li_2MoO_4 solubility in water caused the formation of dense components even at RT. In **Figs. 2.6(a&b)** SEM images taken from Li_2MoO_4 tablets produced by both conventional sintering and RTD are given, and as seen the microstructures resemble each other [58, 193]. The same group studied the formation of Li_2MoO_4 - MnZn ferrite [194] and Li_2MoO_4 - TiO_2 [195] ceramic composites, besides processing, applications such as ultra-wideband (UWB) or circular polarized GPS antennas were explored [196, 197].

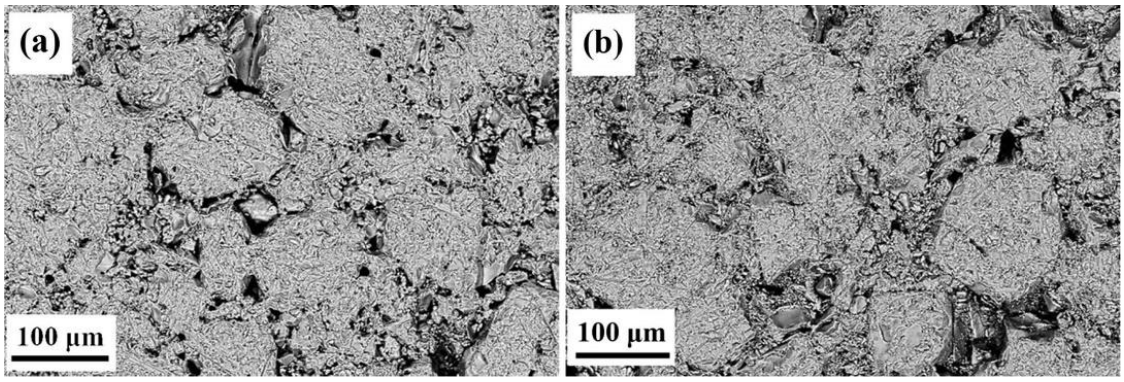

Figure 2.6. Backscattered electron images of Li_2MoO_4 sample (a) conventionally sintered at 540°C, and (b) sintered and dried at RT. (Reproduced from [58], with permission from John Wiley and Sons, Copyright 2014).

Recently, Bouville and Studart [35] synthesized nanosized $CaCO_3$; vaterite with average size of 37 nm and agglomerated as 600 nm forms. The synthesized nano-vaterite together with water was subjected to sintering under pressures up to 800 MPa at RT. Relative density of 87% was obtained by 500 MPa pressure at RT, and the samples demonstrated 30 GPa elastic modulus, 50 MPa flexural, and 225 MPa compressive strength. It has been shown that RT densified nano-vaterite component exhibited higher mechanical properties than that of several state-of-the-art construction materials such as stone or concrete. In a recent variant work by Jiang et al., used an isostatic pressure to densify the silica components instead of the uniaxial pressure at RT, and named the process as *cold hydrostatic sintering* [198]. In **Table 2.2** ceramic compositions currently produced by RTD, processing conditions and the obtained properties are given.

Table 2.2. Materials produced by room-temperature densification method, the processing conditions, some of the extracted properties and application areas.

Materials	Application	Processing conditions	Properties	Relative density (%)	Ref.
Al_2O_3	General	1- 5.6 GPa	H_v = 5.7 GPa	~90	[190]
$CaCO_3$	General	500 MPa 34 min	σ_c = 225 MPa E = 30 GPa	~87	[35]
Li_2MoO_4	Dielectric	30-150 MPa	ε_r = 4.6-5.2	~84-93	[58]
Li_2MoO_4-TiO_2 / $BaTiO_3$ / MnZn Ferrite	Dielectric	150 MPa	ε_r = 6.9-21.7	86-90	[193-195]
Li_2MoO_4-$Ba_{0.55}Sr_{0.45}TiO_3$ / PZT	Electrical	250 MPa	ε_r ~ 200 d_{33} = 84 pC/N g_{33} = 33 mVm/N	~90	[199, 200]
NaCl	Dielectric	5-300 MPa 0-24 h	σ_c = 10-15 MPa ε_r ~ 5.6	~90-99	[201, 202]
SiO_2	General	1- 7.7 GPa	H_v = 4-4.2 GPa	~86	[190-192]
SiO_2	General	300 MPa 5-60 min	H_v ~ 1.4 GPa	~77	[198]

ε_r: Relative permittivity, **σ_c:** Compressive strength, **E:** Elastic modulus, **H_v:** Vickers hardness, **d_{33}:** Piezoelectric coefficient, **g_{33}:** Voltage constant.

2.2.4. Cold sintering

Cold sintering (CS) allows densification under mid/high pressures (below 1 GPa) and low temperatures (< 350°C) with the aid of a deliberately added temporary fluid (solvent/liquid) [203, 204]. In the process, the initial raw material mixture is continuously compressed by using a simple uniaxial press. Heating is carried out by a resistance jacket wrapped around the mold/die system, see **Figs. 2.7(a-c)** for the CS equipment used [205].

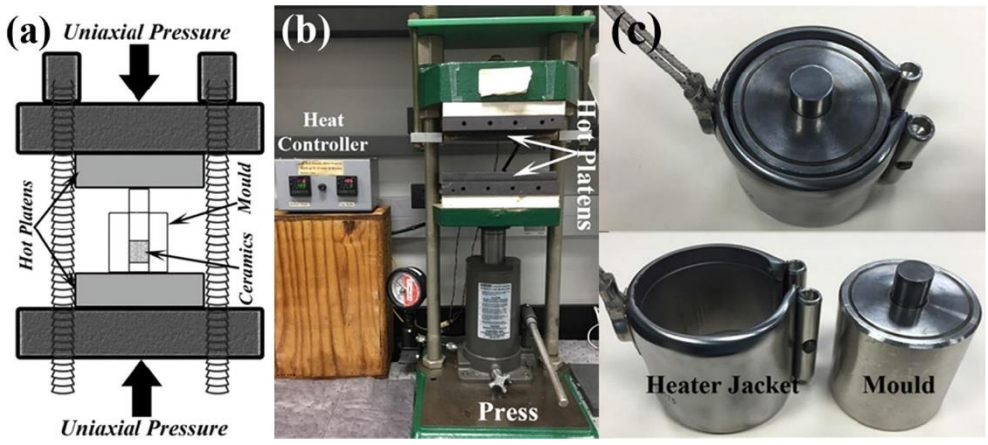

Figure 2.7. Equipment used for cold sintering process: (a) simple press drawing, (b) the actual used CS instrument, and (c) the mold and heater jacket used for CS (Reproduced from [60], with permission from John Wiley and Sons, Copyright 2016).

The CS process, as defined by Maria et al. [201], consists of two stages in which different densification mechanisms probably proceeding, see **Fig. 2.8.** First, compaction is applied to a mixture of ceramic powder (generally nano-sized since high surface-to-volume ratio delivers a strong driving force) with liquid (mostly water) under a uniaxial force similar to that of conventional pressing. In this step the liquid phase serves as a lubrication medium increasing the particle sliding, while discharging continuously from the die tolerance. Besides, probably the applied pressure increases the solubility of the particles having sharp edges, and overall causing a better compaction compared to that of dry consolidation. Such issue has already been documented by Shotton and Rees to consolidate NaCl at RT under varying humidity conditions [206].

Second, the system is heated to higher temperatures while compressing under moderate pressure levels (e.g. 500 MPa). The solubility of the powder is further increased and together with the evaporation of a liquid phase, the formation of supersaturated liquid is ensured. At this stage the applied pressure, as in the case for pressure-assisted conventional sintering, promotes densification. It is proposed that the latter stage is dominated by dissolution-precipitation events assisted by pressure and temperature[201].

It should be noted that the formation of a supersaturated liquid is essential for densification and it can also be accomplished by dissolving the starting particles in acidic

or basic solutions or just by preloading the liquid phase with the corresponding chemical groups, i.e. the addition of a water-soluble salts instead of modifying the acidity. Accordingly, ZnO (basic nature) could be cold sintered to high levels (relative density over 90%) simply by using a liquid consisting of acetic acid solution (in water) [205], a liquid/solution consisting of dissolved zinc salts such as zinc acetate or dimethyl sulfoxide [207], similar to the case for Y_2O_3 which has very low solubility [201].

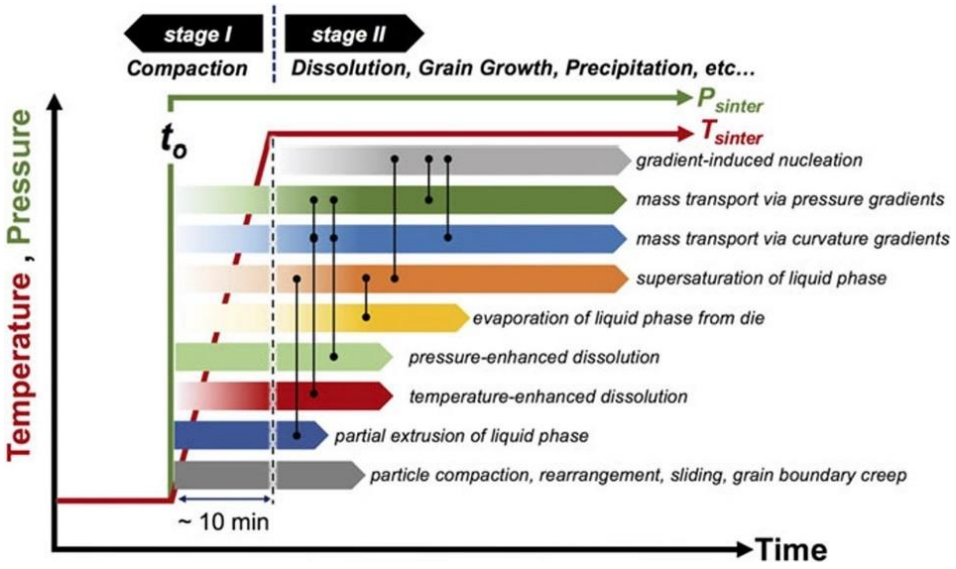

Figure 2.8. Schematic representation of cold sintering process (Reproduced from [201], with permission from Cambridge University Press, Copyright 2017).

Table 2.3 shows the list of the ceramic components produced by CS process together with the data extracted for properties. Although CS technique is broadly used nowadays, and wide variety of chemistries from the family of oxides, carbonates, phosphates, bromides, chlorides, and fluorides have already been produced, most of these published works in the scientific literature so far, have been primarily directed to the production of electro-ceramics. The details for the production of such components can be found elsewhere [60, 203, 208], and here only few essential compositions will be discussed.

At present, some compositions cannot be produced directly by CS such as carbides. Besides, some oxides such as ZrO_2 with high relative density have not been

achieved by CS although several attempts were conducted. An additional heat treatment process (around 1100°C) was needed to obtain high relative densities ~95%. Despite that such that temperatures are still lower than the conventional sintering temperatures, suggesting the benefits of the process [209-212].

A recent study compared the electrical properties of the CS made ZnO ceramics with that of solid-state sintered ceramics (green pellet was formed under 180 MPa by using 240 nm average particle size and sintering at 1400°C in air). The results demonstrated that the samples produced by CS at 300°C exhibited the same electrical conductivity characteristics as those produced by conventional sintering. Such data is important considering the production cost and greenness of CS for industrial applications (varistors, sensors, etc.) [205].

Different ferroelectric materials (KH_2PO_4, $Pb(Zr,Ti)O_3$, $NaNO_2$, $SrTiO_3$ and $BaTiO_3$) were produced at temperatures below 300°C [60, 213-215]. For the production of $BaTiO_3$, the $Ba(OH)_2/TiO_2$ (µm sized TiO_2 powder) suspension was prepared, mixed with a certain amount of $BaTiO_3$ powder, followed by compaction. The samples subjected to CS at 180°C/ 3h resulted in high densification (94.4%). However, $BaTiO_3$ samples produced by CS had cubic crystal structure and/or amorphous grain boundaries, making the piezoelectric properties inadequate. Accordingly, an additional annealing process (T=900°C / 3 h) to transform the crystal structure into the tetragonal one was conducted and the piezoelectric properties were improved, as shown in **Figs. 2.9(a&b)** [203, 208].

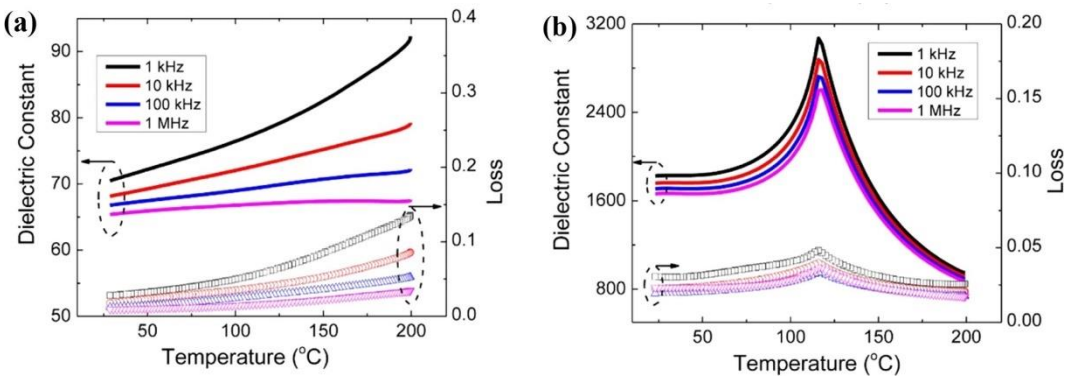

Figure 2.9. Dielectric properties of $BaTiO_3$ obtained from different conditions; (a) the sample made by using CS at 180°C, (b) the same sample after annealing at 900°C (Reprinted with permission from [203, 208]. Copyright (2016) American Chemical Society).

In a slightly different study, the authors demonstrated the ability to print and cold sinter Li_2MoO_4 capacitor structures on both Nickel foil and PET film at low temperatures which would be complicated due to Nickel oxidation above 300°C by conventional techniques. The study showed the possibility to sinter such composite systems and obtain additional process functionality (see later for co-sintering) [216]. Similar studies have been performed for $Li_{1.5}Al_{0.5}Ge_{1.5}(PO_4)_3$ [217] and $Ca_3Co_4O_9$ [218]. $LiFePO_4$ ceramics used as a cathode material for rechargeable batteries were produced by CS as well. LiOH aqueous solution was used for the process and relative densities above 89% were obtained at sintering temperatures around 240°C [219, 220]. A recent review described the possible implementation of CS for solid-state lithium batteries, and highlighted the great potential of the process for battery and solid electrolyte production [221].

Table 2.3. Materials produced by cold sintering method, the processing conditions, some of the extracted properties and application areas.

Materials	**Application**	**Processing conditions**	**Properties**	**Relative density (%)**	**Ref.**
AgI	Electrical	N.A.	N.A.	N.A.	[201]
$AgVO_3$	Optical	N.A.	N.A.	N.A.	[201]
α-Al_2O_3	-	N.A.	N.A.	N.A.	[201]
Al_2O_3-NaCl	Dielectric	120 °C 200 MPa 50 min	$\varepsilon_r \sim 6.5$, $\tan\delta=0.007$ @ 1 MHz $\varepsilon_r \sim 6.0$, $\tan\delta=0.002$ @ 5 GHz	96	[222]
Al_2SiO_5-NaCl	Dielectric	120 °C 200 MPa 50 min	$\varepsilon_r \sim 5.4$, $\tan\delta=0.005$ @ 1 MHz $\varepsilon_r \sim 4.7$, $\tan\delta=0.002$ @ 1 MHz	N.A.	[223]
$BaMoO_4$	Optical	N.A.	N.A.	N.A.	[201]
$BaTiO_3$	Ferroelectric	180 °C 430 MPa 1-180 min	$\varepsilon_r = 2332$, $\tan\delta=0.01$ @ 10^{-3} MHz after HT @ 900 °C	~80-97*	[60, 203, 208, 213]
Bi_2O_3	Electrical	N.A.	N.A.	N.A.	[201]

(cont. on next page)

Table 2.3 (cont.)

Bi_2Te_3	Thermoelectric	N.A.	N.A.	N.A.	[201]
$BiVO_4$	Photocatalyst	N.A.	N.A.	N.A.	[201]
$(Bi_{0.95}Li_{0.05})(V_{0.9}Mo_{0.1})O_4$-$Na_2Mo_2O_7$	Dielectric	150 °C 200 MPa 30 min	ε_r = 40-48, tanδ=0.0012	95-96	[224]
$Ca_3Co_4O_9$	Thermoelectric	135-350 °C 350 MPa 60 min	λ = 41 S/cm	~85-90	[218]
$Ca_5(PO_4)_3(OH)$	Medical	N.A.	N.A.	N.A.	[201]
$Ca_5(PO_4)_3(OH)$	Environmental	200 °C 500 MPa 10 min	H_v = 2.2-2.6 GPa σ_c ~ 175 MPa	~95-97	[225-227]
CeO_2	General	180°C 500 MPa 24 h	Ea = 1.13 eV	~70	[228]
CsBr	Optical	N.A.	N.A.	N.A.	[201]
CsH_2PO_4	Energy	120-200°C 300 MPa 1 h	Ea = 0.38-0.4 eV $\lambda = 2.3x10^{-4}$ S/cm at 200 °C	93-98	[229]
$CsSO_4$	Catalyst	N.A.	N.A.	N.A.	[201]
Cs_2WO_4	Insulator	N.A.	N.A.	N.A.	[201]
CuCl	General	N.A.	N.A.	N.A.	[201]
$Gd_2(MoO_4)_3$	Ferroelectric	N.A.	N.A.	N.A.	[201]
$InGaZnO_4$	Electrical	25-180 °C 100-350 MPa 10 min	N.A.	~92-99 After HT=1200 °C	[230]
KH_2PO_4	Ferroelectric	120 °C 350 MPa 30 min	N.A.	>98	[60]
$K_2Mo_2O_7$	Dielectric	120 °C 350 MPa 15-20 min	ε_r = 9.8, tanδ=0.00083	~94	[204, 231]
$K_{0.5}Na_{0.5}NbO_3$	Piezoelectric	120 °C 350 MPa 30 min	d_{33} = 131 pC/N after HT @ 1115 °C	~65	[232]
KPO_3	General	N.A.	N.A.	N.A.	[201]
$LiAl_{0.5}Ge_{1,5}(PO_4)_3$	Energy storage	120 °C 400 MPa 20 min	$\lambda = 5.4 \times 10^{-5}$ S/cm @ 25°C after HT @ 650 °C	79	[217]

(cont. on next page)

Table 2.3 (cont.)

$Li_{1.5}Al_{0.5}Ge_{1.5}(PO_4)_3$ / $Li_{1+x+y}Al_xTi_{2-x}Si_yP_{3-y}O_{12}$- LiTFSI	Energy storage	130 ºC 380-620 MPa 2 h	$\lambda = 2.3x10^{-4}$ S/cm at RT	~90	[233]
$(LiBi)_{0.5}MoO_4$	Dielectric	RT-120 ºC 250-350 MPa 20 min	ε_r = 33.7-37.1	~88-89	[231]
$Li_{0,5x}Bi_{1-0,5x}Mo_xV_{1-x}O_4$	Dielectric	N.A.	N.A.	N.A.	[201]
(1-x)$(LiBi)_{0.5}MoO_4$-xPTFE	Dielectric	RT-120 ºC 250-350 MPa 20 min	ε_r ~ 10-40	>85	[231]
Li_2CO_3	General	N.A.	N.A.	N.A.	[201]
$LiCoPO_4$	Energy storage	N.A.	N.A.	N.A.	[201]
$LiFePO_4$ -CNF	Energy storage	180 ºC 240 MPa 10 min	VC = 373 mAh/cm^3 @ 0.1 C (discharge rate)	~70	[220]
$LiFePO_4$ - PVDF-C	Energy storage	240 ºC 30-750 MPa 30 min	VC ~ 340 mAh/cm^3 @ 0.03-0.1 C	~89	[219]
$Li_2Mg_3TiO_6$	Dielectric	180 ºC 300 MPa 1 h	ε_r = 15.51-15.68 after HT @ 800-950 ºC	~90	[234]
Li_2MoO_4	Dielectric	120 ºC 37-74 MPa 15-20 min	ε_r = 5.6	~96	[231]
Li_2MoO_4-PTFE	Dielectric	120 ºC 37-74 MPa 15-20 min	ε_r = 5.8-2.9	>90	[231]
Li_2MoO_4-$BaFe_{12}O_{19}$	Dielectric	120 ºC 55-70 MPa 10-40 min	ε_r = 5.6-5.8	94-97	[235]
$LiVO_3$	Energy storage	N.A.	N.A.	N.A.	[201]
Li_2WO_4	Catalyst	N.A.	N.A.	N.A.	[201]
MgO	General	N.A.	N.A.	N.A.	[201]
$Mg_2P_2O_7$	Biological	N.A.	N.A.	N.A.	[201]
MnO	General	100-300 ºC 530 MPa 30-60 min	N.A.	94	[207]

(cont. on next page)

Table 2.3 (cont.)

MoO_3	Dielectric	120-150 °C 100-150 MPa 10-30 min	ε_r = 9.91 after HT @ 700 °C	77	[201, 236]
MoS_2-Graphite	Energy storage	140 °C 520 MPa 1 h	SC = 950 mAh/g at 0.1 A/g	88	[237]
$Na_{0.5}Bi_{0.5}MoO_4$-Li_2MoO_4	Dielectric	150 °C 200 MPa 30 min	ε_r ~ 17.4, tanδ=0.0008	~93-96	[238]
$Na_{0.5}Bi_{0.5}TiO_3$	Piezoelectric	180 °C 200-550 MPa 15-75 min	ε_r = 681, tanδ=0.08 at RT d_{33} = 52.5 pC/N after HT @ 900 °C	74	[239]
NaCl	General	25-120 °C 300 MPa 10 min	ε_r ~ 5.9	~93-99	[240]
$Na_xCO_2O_4$	Thermoelectric	N.A.	N.A.	N.A.	[201]
$Na_{3.256}Mg_{0.128}Zr_{1.872}Si_2PO_{12}$	Energy storage	120-180 °C 300-780 MPa 10-120 min	λ ~1.4 x 10^{-3} S/cm λ_i=0.88 mS/cm after HT @ 1100 °C	~83	[241]
$Na_{3.4}Sc_{0.4}Zr_{1.6}Si_2PO_{12}$	-	250 °C 300 MPa 10 min	λ = 10^{-6}-10^{-3} S/cm after HT @ 200-1100 °C	~82	[242]
$Na_2Mo_2O_7$	Dielectric	120 °C 250-350 MPa 15-20 min	ε_r = 13.4	~94	[231]
$NaNbO_3$-PVDF	Energy storage	180 °C 550 MPa 10 min	E_b = 1345 kV/cm	~97	[243]
$NaNO_2$	Ferroelectric	N.A.	N.A.	98	[60]
$NaNO_3$-$Ca(OH)_2$	Energy storage	120 °C 500 MPa 10 min	σ_c ~ 20-120 MPa E_{es} = 59.48 %	N.A.	[244]
Na_2WO_4	Catalyst	N.A.	N.A.	N.A.	[201]
Na_2ZrO_3	Electrical	N.A.	N.A.	N.A.	[201]
PbTe	Thermoelectric	N.A.	N.A.	N.A.	[201]
$Pb(Zr,Ti)O_3$	Ferroelectric	300 °C 500 MPa 150 min	d_{33} = 4 pC/N @ CSP d_{33} = 197 pC/N @ 900 °C for 3 h	89	[214]

(cont. on next page)

Table 2.3 (cont.)

SnO	Electrical	70-265 °C 350 MPa 45 min	λ = 0.01-0.02 S/cm	~85	[245]
$SrTiO_3$	Ferroelectric	180 °C 350-550 MPa 60 min	N.A.	~96-97 after HT= 950 °C	[215]
TiO_2	General	150 °C 250-500 MPa 30 min	SSA = 117 m^2/g	68	[246]
V_2O_3	Electrical	N.A.	N.A.	N.A.	[201]
V_2O_5	Electrical	120 °C 350 MPa 20 min	$\lambda = 4.8 \times 10^{-4}$ S/cm E_a ~ 0.3 eV	92	[201, 247]
V_2O_5-CNF	Electrical	120 °C 350 MPa 20 min	$\lambda = 10\text{-}10^2$ S/cm VC = 800 mAh/cm^3 @ ~0.2 C-Rate	~89	[247]
V_2O_5-PEDOT-PSS	Electrical	120-140 °C 300-350 MPa 20-45 min	$\lambda = 10^{-3}\text{-}10^{-2}$S/cm E_a ~ 0.2 eV ρ = 6.34 Ωm	~90	[248, 249]
WO_3	Electrical	N.A.	N.A.	N.A.	[201]
$ZnMoO_4$	Electrical	N.A.	N.A.	N.A.	[201]
ZnO	Thermoelectric	25-305 °C 0-530 MPa 5-300 min	λ = 12 S/cm σ_0 ~ 64.4 MPa m = 8.2	~65-99	[205, 207, 218, 250-253]
ZnO- $Ti_3C_2T_x$	Electrical	300 °C 250 MPa 60 min	Hv ~ 2-5 GPa E ~ 60-110 GPa λ = 16 S/cm	92-98	[254]
ZnO-PTFE	Electrical	285 °C 300 MPa 60 min	α = 3-7 E_b = 3225 V/mm E_a ~ 0.8 eV	>90	[255]
ZnTe	Electrical	N.A.	N.A.	N.A.	[201]
ZrF_4	Optical	N.A.	N.A.	N.A.	[201]
ZrO_2	General	180 °C 350 MPa 30-180 min	Hv = 0.5 GPa @ CSP Hv = 13.6 GPa after HT @ 1200 °C	~56-96	[209-211]

N.A.: Not available, **HT:** Heat treatment, **ε_r:** Relative permittivity, **σ_c:** Compressive strength, **E:** Elastic modulus, **λ:** DC conductivity, **λ_i:** Ionic conductivity, **d_{33}:** Piezoelectric coefficient, **E_a:** Activation energy, **E_b:** Electrical breakdown field, **VC:** Volumetric capacity, **Hv:** Hardness, **α:** Nonlineer coefficient, **SC:** Specific capacity, **ρ:** Resistivity, **Ees:** Energy storage efficiency, **m:** Weibull modulus, **σ_0:** Characteristic strength, *Calculated.

2.2.5. Warm press

Similar to CS, a uniaxial press is used for the warm press (WP) technique. The main difference, simply, lies in the application of the heat. While in CS a jacket surrounding the die heats the system, in WP both top and bottom platens of the pressing device (< 300 MPa) have electrical resistance (temperature reaching around 300°C) resembling conventional hot press, see **Fig. 2.10** for the used equipment [258].

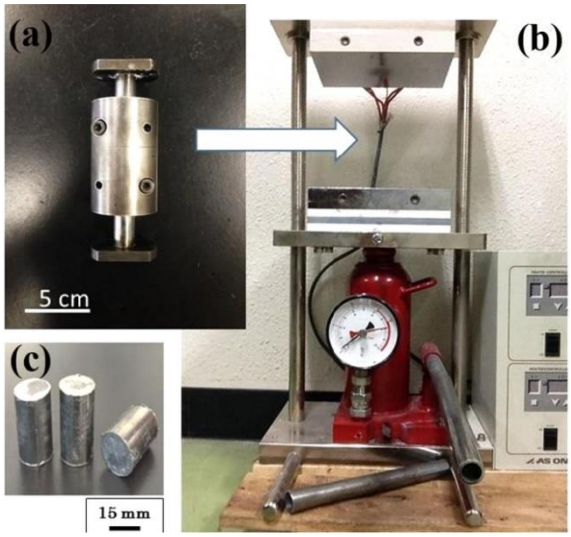

Figure 2.10. Warm press equipment; (a) die, (b) press device, and (c) hardened bodies. (Reproduced from [259])

A mixture of fly ash, NaOH solution and sodium water glass was heated to 130°C / 2 h under 200 MPa pressure. The formed components had 71% relative density and high compressive strength values reaching 149 MPa [59, 259]. It is known that dense calcium hydroxide body (slaked lime plaster) is hard to obtain by conventional sintering approaches. Calcium hydroxide was compressed uniaxially under 60-240 MPa while heated in between 100-250°C. Under such processing conditions dehydration of lime (or the moisture in the air) assisted the sintering, leading dissolution-precipitation reaction in slaked lime pseudo-sintering, similar to what is observed in CS studies. The sample under 240 MPa pressure at 150°C for 90 min sintering, gave a relative density of 81% and compressive strength of 57 MPa [258]. In **Table 2.4** ceramic compositions currently produced by WP, processing conditions and the obtained properties are given.

Table 2.4. Materials produced by warm press, the processing conditions, some of the extracted properties and application areas.

Materials	Application	Processing conditions	Properties	Relative density (%)	Ref.
$CaCO_3$	General	150 °C 240MPa 10-180 min	σ_c ~ 40 MPa	~87	[260]
$Ca(OH)_2$	General	100-250 °C 60-240MPa 10-180 min	σ_c ~ 20-57 MPa	59-81	[258]
Geopolymer	General	130-200 °C 200 MPa 10-60 min	σ_c ~ 20-150 MPa	N.A.	[59, 259]
Geopolymer-SiC	General	130°C 240 MPa 30 min	σ_c ~ 10-75 MPa	~72-80	[261]

N.A.: Not available, **σ_c:** Compressive strength.

$CaCO_3$ powder alone or mixed with 10 wt% water was compressed under a pressure of 240 MPa at 150 to 280°C. Samples with a relative density of 87%, and compressive strength of 40 MPa was obtained after 180 min of WP at 150°C, see **Figs. 11(a-c)** for the microstructural evolution [260]. In another study, geopolymer-SiC components were produced by using geo-polymer as a binder. At the end of 30 min at 130°C under a pressure of 240 MPa, depending on the initial precursor type, relative densities reaching to 90% (having around 170 MPa compressive strength) was able to be achieved [261].

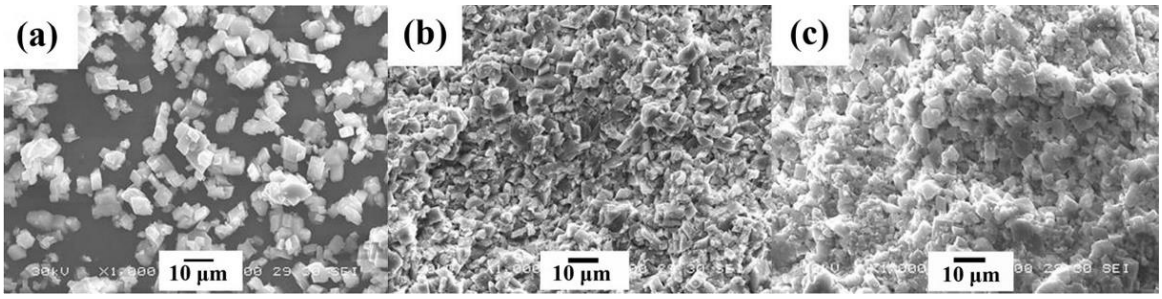

Figure 2.11. SEM images obtained from; (a) $CaCO_3$ raw powder, and fracture surfaces obtained from the samples produced by warm press conducted at (b) 150 °C, and (c) at 280°C (Reprinted from [260], Copyright (2017), with permission from Elsevier).

2.2.6. Reactive hydrothermal liquid phase densification

Compared to above mentioned techniques, reactive hydrothermal liquid phase densification (rHLPD) process is a different low temperature densification concept [61]. The technique is based on the hydrothermal reaction, infiltration, reactive crystallization and liquid phase sintering principles. **Figure 2.12** gives the **s**chematic representation of the process. In the study to produce $BaTiO_3$ monoliths, green TiO_2 bodies were prepared and infiltrated with $Ba(OH)_2/H_2O$ solution. Subsequently, the system was subjected to a hydrothermal reaction at temperatures in between 90-240° C up to 72 h. $BaTiO_3/TiO_2$ (residual titania was found to be below < 5 %) ceramics with relative densities around 90% was obtained.

In rHLPD, there is no application of pressure which assists densification, so the center of the particles does not get closer by the effect of externally applied pressure. There is actually a need for hydrothermal crystallization reaction with products having higher molar volume (compared to green body), such the one given in **Reaction 2.2**. In the case of the reaction (2) resulting in 100% yield, the TiO_2 molar volume (20.2 cm^3/mol) expands 91.6% while transforming into Barium titanate (molar volume of 38.7 cm^3). Such volume change (expansion) fills the pore spaces and results in densification. With this technology, various systems including $SrTiO_3[TiO_2]$, $Ca(PO_4)F_2[CaF_2]$, $Sr(PO_4)(OH)_2[SrTiO_3[TiO_2]]$, $CaC_2O_4/Ca(OH)_2$, $CaCO_3$ -$SiO_2[-CaSiO_3]$ and other similar composite systems can be produced [262].

$$Ba(OH)_{2\,(sol)} + TiO_{2\,(s)} = BaTiO_{3\,(s)} + H_2O_{\,(l)} \qquad (2.2)$$

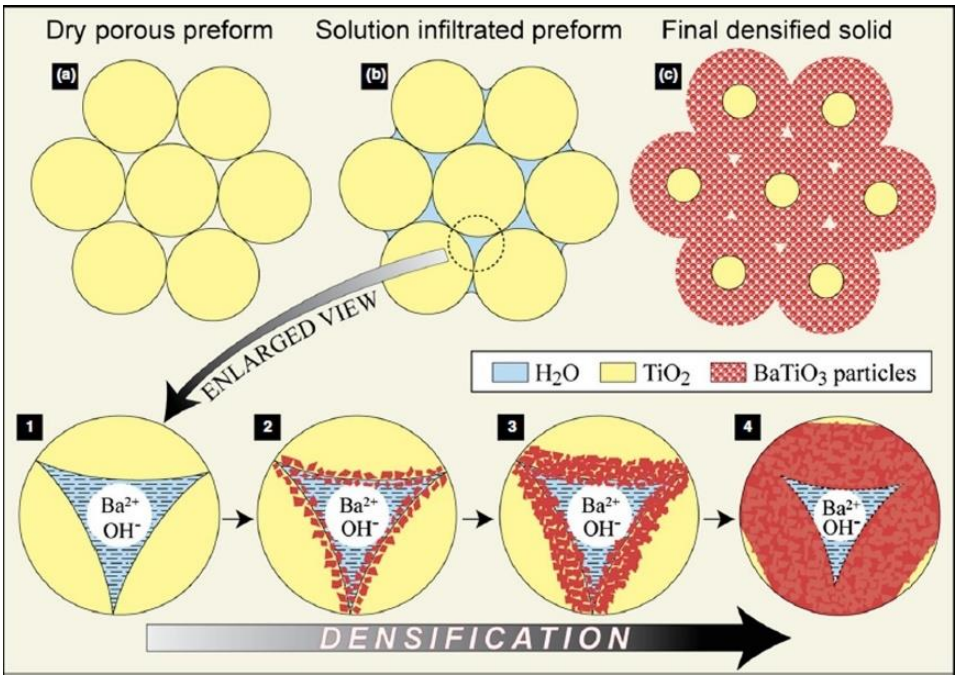

Figure 2.12. Schematic representation of the reactive hydrothermal liquid phase densification process (Reproduced from [61], with permission from John Wiley and Sons, Copyright 2016).

2.3. Comparison of the low temperature densification methods

For the techniques discusses above, the processing conditions (applied pressure and temperature) were analyzed and plotted in **Fig. 2.13**. In the top-right inset of the figure, a magnified area of P < 1000 MPa & T < 400°C is shown, and as one could see the major part of the studies were actually conducted in this zone, outlining the boundary conditions for low temperature densification methods.

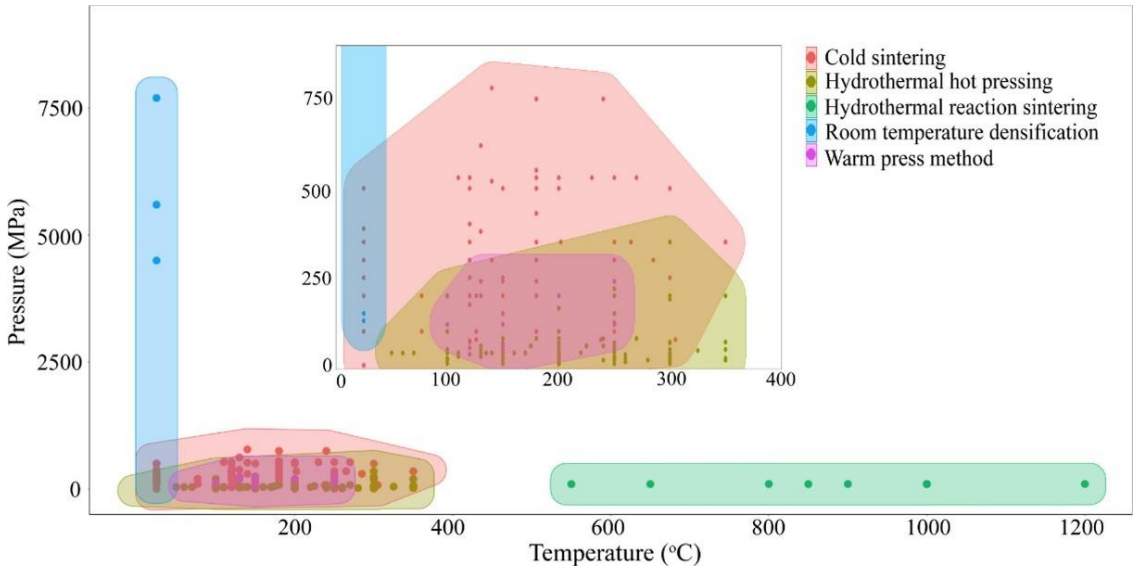

Figure 2.13. Applied pressure (P=MPa) versus temperature (T=°C) chart which was made by using RStudio software's Ggforce module with the data collected from the published papers. In the top-right inset, magnified area of T < 400°C is given.

Although HRS is one of the earliest techniques, it utilizes a metal powder or chips that are oxidized under hydrothermal conditions by supercritical water in a capsule under mild pressures (100 MPa) and mid/high temperatures (1000°C). The process consumes less energy compared to conventional sintering of the same composition, and it enables to sinter materials having high vapor pressure, phase transformation and/or high decomposition rate at sintering temperatures. The driving force of HRS is primarily an exothermic chemical reaction between metal particles and water as well as applied external pressure which increases contact area relative to the cross-sectional area of the metal particles. The liquid phase used for the production of the bulk material is used as a reactant for the oxidation of metal instead of only a mass transport media [53]. As a result of HRS the obtained sintered bodies have fine grained uniform microstructure, high purity and density. On the other hand, in some cases metal-hydride or oxide film formation may retard the sintering, besides it necessitates a specific instrument which clearly casts limitation on the sample size [69]. Moreover, there are uncertainties arising from lack of suffice information related with the purity, size and shape of raw materials, the ratio of metal to water, and other processing conditions (temperature, pressure, time, etc.) [263].

It is also important to note that chemical reactions occurring in HRS are exothermic processes: e.g. oxidation of metal, and thus the actual process temperatures could be much higher than those of the ones measured.

Broadly speaking, HHP is a more practical method to densify ceramics compared to HRS since the application parameters ($T < 350°C$, $P < 25$ MPa, $t < 2$ h) are milder. A suspension of powder is uniaxially consolidated in a heated pressing apparatus while the powder re-crystallizes hydrothermally. Normally, the products have relative densities (< 80%) [115], however, if the applied pressure is increased, e.g. (> 80 MPa), highly dense (98.3 %) materials can be obtained [158]. For HHP, water is used as a transport media for species obtained by dissolving the raw powder. Successive re-crystallization in pore surfaces proceeds concurrent consolidation under the applied pressure. In this way, HHP is similar to pressure assisted techniques since they all require externally applied pressure and heat [201]. However similar to HRS, it necessitates a specialized equipment to ensure hydrothermal reaction conditions, limiting the sample size as well [61]. It should be noted that not only the monolithic ceramics, glasses and ceramic-metal composites were produced but also organic materials were processed by HHP [264-267]. Besides, the efforts to address environmental problems such as to recycling toxic and hazardous wastes or immobilization of heavy metals and low/high-level radioactive materials [268, 269]. While for HHP and HRS a special reaction chamber is needed, for other low temperature densification methods, ordinary presses with heating elements can be used.

As name implies, RTD was conducted only at RT, this imposed higher pressure levels than CS and WP when the selected composition has low solubility. In fact, for all RTD, CS and WP processes at least a moderate solubility of the raw powder or high pressure levels to consolidate the green-body is needed.

In CS resistance jacket surrounding the reaction chamber was used for heating, and compared to WP, similar temperature ranges but higher pressure levels (< 1 GPa) were followed [201].

There are very limited published works in which a throughout comparison of CS and Hydrothermal sintering/HHP is given,[270] and thus further studies are certainly required. Instrumental differences should be stated first since as known the device used for CS is basically as an `open reactor` while HHP apparatus can be thought as a closed system to ensure the hydrothermal reaction conditions which affect densification rate and crystal growth. While both processes give similar densification trends and relative density

values, suggesting analogous mechanical-chemical contributions, in the study to compare Hydrothermal sintering and CS of ZnO monoliths, the authors showed that these two processes differ in their chemical activities [270]. In fact under the same processing parameters (temperature, pressure, etc.), the outcome from those two processes might be different. Furthermore, highly congruent dissolution was found to be crucial for the high rate solution-precipitation process. Incongruent or limited dissolution was detrimental to obtain high density at low temperatures,[215] and therefore such components should be additionally heat treated at elevated temperatures or similar strategy to rHLPD might be followed.

WP has great similarity with HHP and CS in terms of procedure [260]. Usually, it is operated with the help of a solution (solution-precipitation assisting medium) at temperatures < 300°C under a constant uniaxial pressure (e.g. < 240 MPa) to densify the products. The heat is conducted axially through pressing plates similar to the direction of the applied pressure which is different for CS and HHP. Therefore, homogeneous heat distribution across the sample should be carefully regulated especially for thick components. While sample size is still a relevant concern, all these processes can be effectively used to produce porous ceramic and glass artifacts [246], or various composites (polymer/metal/ceramic) [256] extending the utilization of the techniques in wide range of application areas and industries.

The last method rHLPD is a reactive process in which the starting solid and liquid reacts to form a new, higher volume crystalline product. rHLPD enables densification in a hydrothermal reactor as a result of reaction and crystallization events, i.e. no pressure is applied during the process instead in all others there is an application of pressure throughout densification. By separating consolidation from the hydrothermal reaction step, a wide range of conventional forming technology can be used, allowing for great variety of shapes and sizes as well as being more amenable to mass production. Because no pressure is applied and densification occurs by reactive crystallization, the process does not induce shrinkage, so that large objects can be densified without probable distortion or cracking. The limitation of rHLPD system is based on the fact that there must be a net molar volume increase for densification to occur. Besides, unless the starting green body is made from a very fine or porous powder, it is hard to avoid composite formation even with extended sintering periods, indicating a limited application prospect when phase pure systems are considered.

It is worth mentioning that currently there are very few studies performed to produce a monolith having similar chemical composition by different low temperature densification approaches, and compare the observed properties, the economic and environmental impacts (e.g. carbon footprint) apart from a very recent works on comparison of CS with traditional techniques[271], and on theoretical analysis of the active mechanisms during cold sintering conducted both by isostatic or uniaxial pressure.[272, 273]. A very recent study reported the properties of zinc oxide (ZnO) produced both by hydrothermal sintering and the cold sintering.[270] $CaCO_3$ artifacts were produced via pressure assisted techniques by two different groups. Yamasaki et al. [56] used micron sized aragonite powder for HHP (< 300°C & ~65 MPa pressure) and demonstrated that the resulted tablets had 60 MPa compressive strength. When chitosan was added to initial aragonite powder, the strength was improved to ~160MPa at around 90% relative density [86]. Following these works, RTD was applied to consolidate nanosized vaterite under pressures below 800 MPa. Samples with 87% relative density and compressive strength of 225 MPa were obtained. Although there are dissimilarities in the obtained properties, it is not easy to speculate on these results due to the discrepancies in the reported characterization data.

2.4. Concluding remarks

Currently available low temperature densification (LTD) methods were classified into four main groups: (i) hydrothermal reaction sintering (HRS), (ii) hydrothermal hot pressing (HHP), (iii) pressure-assisted densification techniques: room-temperature densification (RTD), cold sintering (CS), warm press (WP), and finally (iv) reactive hydrothermal liquid phase densification (rHLPD). The densification mechanisms of these methods still have not been completely analyzed yet. Aforementioned techniques are commonly assisted by an aqueous solution used as either reactant or transient liquid phase to assist densification. Another most notable similarity in HHP, RTD, CS, WP and rHLPD is that they all involve series of solution-precipitation events, throughout densification. All these methods take place at relatively lower temperatures and higher pressures compared to those for conventional sintering (excluding pressure assisted ones).

It should be recalled that currently there are very limited studies performed to compare the properties of a same-single component (preferably having similar relative density, grain size, etc.) produced by using all currently known low temperature densification approaches, yet. When the compositions given in the tables are analyzed, it can be seen that, in general, oxides (mostly to be used as electro-ceramics) were produced under such low temperature and mild/high pressure levels, and therefore further studies are still necessary to explore novel methods and/or compositions such as carbides. Furthermore, the implementation of these low temperature densification processes as industrial manufacturing technologies poses challenges to ceramic industry using conventional sintering since new instruments are needed to be installed.

References

[1] R.F. Walker, Mechanism of material transport during sintering, J. Am. Ceram. Soc. 38 (1955) 187-197. https://doi.org/10.1111/j.1151-2916.1955.tb14928.x.

[2] M.N. Rahaman, Sintering of Ceramics, CRC press, 2007.

[3] R.M. German, Sintering Theory and Practice, Wiley, 1996.

[4] M.N. Rahaman, Sintering theory and fundamentals, in: P. Samal, J. Newkirk (Eds.) Powder Metall., ASM International, 2015.

[5] P.B. Vandiver, O. Soffer, B. Klima, J. Svoboda, The origins of ceramic technology at Dolní Věstonice, Czechoslovakia, Science 246 (1989) 1002-1008. https://doi.org/10.1126/science.246.4933.1002.

[6] R. German, History of sintering: empirical phase, Powder Metall. 56 (2013) 117-123. https://doi.org/10.1179/1743290112Y.0000000025.

[7] J.B. Ferguson, Note on the sintering of magnesia, J. Am. Ceram. Soc. 1 (1918) 439-440. https://doi.org/10.1111/j.1151-2916.1918.tb18608.x.

[8] R.K. Bordia, S.J.L. Kang, E.A. Olevsky, Current understanding and future research directions at the onset of the next century of sintering science and technology, J. Am. Ceram. Soc. 100 (2017) 2314-2352. https://doi.org/10.1111/jace.14919.

[9] F. Rhines, Seminar on the theory of sintering, Trans. AIME 166 (1946) 474.

[10] F. Lenel, Sintering in the presence of a liquid phase, Trans. AIME 175 (1948) 878-905.

[11] J. Frenkel, Viscous flow of crystalline bodies under the action of surface tension, J. phys. 9 (1945) 385.

[12] G.C. Kuczynski, Self-Diffusion in sintering of metallic particles, Met. Trans. 1 (1949) 169-178. https://doi.org/10.1007/978-94-009-0741-6_33.

[13] W.D. Kingery, M. Berg, Study of the initial stages of sintering solids by viscous flow, evaporation-condensation, and self-diffusion, J. Appl. Phys. 26 (1955) 1205-1212. https://doi.org/10.1063/1.1721874.

[14] R. Coble, Initial sintering of alumina and hematite, J. Am. Ceram. Soc. 41 (1958) 55-62. https://doi.org/10.1111/j.1151-2916.1958.tb13519.x.

[15] R.L. Coble, Sintering crystalline solids. I. Intermediate and final state diffusion models, J. Appl. Phys. 32 (1961) 787-792. https://doi.org/10.1063/1.1736107.

[16] R.L. Coble, Sintering crystalline solids. II. Experimental test of diffusion models in powder compacts, J. Appl. Phys. 32 (1961) 793-799. https://doi.org/10.1063/1.1736108.

[17] M.N. Rahaman, Ceramic Processing and Sintering, CRC press, 2003.

[18] R.M. German, P. Suri, S.J. Park, Liquid phase sintering, J. Mater. Sci. 44 (2009) 1-39. https://doi.org/10.1007/s10853-008-3008-0.

[19] S.-J.L. Kang, Sintering: Densification, Grain Growth and Microstructure, Elsevier, Amsterdam, 2004.

[20] W. Zhang, I. Gladwell, Performance of mol for surface motion driven by a laplacian of curvature, Springer Berlin Heidelberg, Berlin, Heidelberg, 2000, pp. 419-429.

[21] R. German, Sintering: From Empirical Observations to Scientific Principles, Butterworth-Heinemann, 2014.

[22] S. Somiya, Handbook of Advanced Ceramics: Materials, Applications, Processing, and Properties, Academic press, 2013.

[23] S. Hampshire, Silicon nitride ceramics–review of structure, processing and properties, J. Achiev. Mater. Manuf. Eng. 24 (2007) 43-50.

[24] W. Kingery, Densification during sintering in the presence of a liquid phase. I. Theory, J. Appl. Phys. 30 (1959) 301-306. https://doi.org/10.1063/1.1735155

[25] W. Kingery, M. Narasimhan, Densification during sintering in the presence of a liquid phase. II. Experimental, J. Appl. Phys. 30 (1959) 307-310. https://doi.org/10.1063/1.1735156.

[26] W.A. Kaysser, G. Petzow, Liquid phase sintering of ceramics, in: R.F. Davis, H. Palmour, R.L. Porter (Eds.) Emergent Process Methods for High-Technology Ceramics, Springer US, Boston, MA, 1984, pp. 225-231.

[27] W.D. Kingery, H.K. Bowen, D.R. Uhlmann, Introduction to Ceramics, Wiley, , New York, 1976.

[28] P.C. Panda, W.M. Mobley, R. Raj, Effect of the heating rate on the relative rates of sintering and crystallization in glass, J. Am. Ceram. Soc. 72 (1989) 2361-2364. https://doi.org/10.1111/j.1151-2916.1989.tb06090.x.

[29] M. Biesuz, V.M. Sglavo, Flash sintering of ceramics, J. Eur. Ceram. Soc. 39 (2019) 115-143. https://doi.org/10.1016/j.jeurceramsoc.2018.08.048.

[30] B. Dzepina, D. Balint, D. Dini, A phase field model of pressure-assisted sintering, J. Eur. Ceram. Soc. 39 (2019) 173-182. https://doi.org/10.1016/j.jeurceramsoc.2018.09.014.

[31] R. Coble, Mechanisms of densification during hot pressing, in: G.C. Kuczynski, N.A. Hooton, C.F. Gibbon (Eds.) Sintering and Related Phenomena, Gordon and Breach, New York, 1967, pp. 329-350.

[32] R.L. Coble, Diffusion models for hot pressing with surface energy and pressure effects as driving forces, J. Appl. Phys. 41 (1970) 4798-4807. https://doi.org/10.1063/1.1658543.

[33] R. Coble, A model for boundary diffusion controlled creep in polycrystalline materials, J. Appl. Phys. 34 (1963) 1679-1682. https://doi.org/10.1063/1.1702656.

[34] G. Pharr, M. Ashby, On creep enhanced by a liquid phase, Acta Metall. 31 (1983) 129-138. https://doi.org/10.1016/0001-6160(83)90072-X.

[35] F. Bouville, A.R. Studart, Geologically-inspired strong bulk ceramics made with water at room temperature, Nat. Commun. 8 (2017) 14655. https://doi.org/10.1038/ncomms14655.

[36] J.-P. Gratier, D.K. Dysthe, F. Renard, The role of pressure solution creep in the ductility of the Earth's upper crust, Advances in Geophysics, Elsevier, 2013, pp. 47-179.

[37] C. Herring, Diffusional viscosity of a polycrystalline solid, J. Appl. Phys. 21 (1950) 437-445. https://doi.org/10.1063/1.1699681.

[38] D.S. Wilkinson, M. Ashby, Pressure sintering by power law creep, Acta Metall. 23 (1975) 1277-1285. https://doi.org/10.1016/0001-6160(75)90136-4.

[39] Z. Munir, U. Anselmi-Tamburini, M. Ohyanagi, The effect of electric field and pressure on the synthesis and consolidation of materials: a review of the spark plasma sintering method, J. Mater. Sci. 41 (2006) 763-777. https://doi.org/10.1007/s10853-006-6555-2.

[40] J. Garay, Current-activated, pressure-assisted densification of materials, Annu. Rev. Mater. Res. 40 (2010) 445-468. https://doi.org/10.1146/annurev-matsci-070909-104433.

[41] E.A. Olevsky, E.V. Aleksandrova, A.M. Ilyina, D.V. Dudina, A.N. Novoselov, K.Y. Pelve, E.G. Grigoryev, Outside mainstream electronic databases: review of studies conducted in the USSR and post-soviet countries on electric current-assisted consolidation of powder materials, Materials 6 (2013) 4375-4440. https://doi.org/10.3390/ma6104375.

[42] W.H. Sutton, Microwave processing of ceramics-an overview, Mater. Res. Soc. Symp. Proc. 269 (1992). https://doi.org/10.1557/PROC-269-3.

[43] J.D. Katz, Microwave sintering of ceramics, Annu. Rev. Mater. Sci. 22 (1992) 153-170. https://doi.org/10.1146/annurev.ms.22.080192.001101.

[44] M. Oghbaei, O. Mirzaee, Microwave versus conventional sintering: a review of fundamentals, advantages and applications, J. Alloys Compd. 494 (2010) 175-189. https://doi.org/10.1016/j.jallcom.2010.01.068.

[45] M. Yu, S. Grasso, R. Mckinnon, T. Saunders, M.J. Reece, Review of flash sintering: materials, mechanisms and modelling, Adv. Appl. Ceram. 116 (2017) 24-60. https://doi.org/10.1080/17436753.2016.1251051.

[46] P. Bertrand, F. Bayle, C. Combe, P. Gœuriot, I. Smurov, Ceramic components manufacturing by selective laser sintering, Appl. Surf. Sci. 254 (2007) 989-992. https://doi.org/10.1016/j.apsusc.2007.08.085.

[47] D. Wilkinson, A pressure-sintering model for the densification of polar firn and glacier ice, J. Glaciol. 34 (1988) 40-45. https://doi.org/10.1017/S0022143000009047.

[48] J.R. Blackford, Sintering and microstructure of ice: a review, J. Phys. D. 40 (2007) R355-R385. https://doi.org/10.1088/0022-3727/40/21/R02.

[49] W. Kingery, Regelation, surface diffusion, and ice sintering, J. Appl. Phys. 31 (1960) 833-838. https://doi.org/10.1063/1.1735704.

[50] J.G. Spray, Lithification mechanisms for planetary regoliths: The glue that binds, Annu. Rev. Earth Pl. Sc. 44 (2016) 139-174. https://doi.org/10.1146/annurev-earth-060115-012203.

[51] D.M. Roy, G. Gouda, A. Bobrowsky, Very high strength cement pastes prepared by hot pressing and other high pressure techniques, Cem. Concr. Res. 2 (1972) 349-366. https://doi.org/10.1016/0008-8846(72)90075-0.

[52] D.M. Roy, G. Gouda, High strength generation in cement pastes, Cem. Concr. Res. 3 (1973) 807-820. https://doi.org/10.1016/0008-8846(73)90013-6.

[53] S. Sõmiya, Hydrothermal reactions for materials science and engineering: An overview of research in Japan, Springer Science & Business Media, 2012.

[54] E. Gutmanas, A. Rabinkin, M. Roitberg, Cold sintering under high pressure, Scr. Mater. 13 (1979) 11-15. https://doi.org/10.1016/0036-9748(79)90380-6.

[55] E. Gutmanas, High-pressure compaction and cold sintering of stainless steel powders, Powder Metall. Int. 12 (1980) 178-183.

[56] N. Yamasaki, T. Weiping, Hydrothermal hot-pressing of calcium carbonate with sea water, J. Mater. Sci. Lett. 12 (1993) 516-519. https://doi.org/10.1007/BF00452814.

[57] P. De Silva, L. Bucea, V. Sirivivatnanon, D.R. Moorehead, Carbonate binders by "cold sintering" of calcium carbonate, J. Mater. Sci. 42 (2007) 6792-6797. https://doi.org/10.1007/s10853-006-1428-2.

[58] H. Kähäri, M. Teirikangas, J. Juuti, H. Jantunen, Dielectric properties of lithium molybdate ceramic fabricated at room temperature, J. Am. Ceram. Soc. 97 (2014) 3378-3379. https://doi.org/10.1111/jace.13277.

[59] H. Takeda, S. Hashimoto, H. Matsui, S. Honda, Y. Iwamoto, Rapid fabrication of highly dense geopolymers using a warm press method and their ability to absorb neutron irradiation, Constr. Build. Mater. 50 (2014) 82-86. https://doi.org/10.1016/j.conbuildmat.2013.09.014.

[60] H. Guo, A. Baker, J. Guo, C.A. Randall, Cold sintering process: a novel technique for low-temperature ceramic processing of ferroelectrics, J. Am. Ceram. Soc. 99 (2016) 3489-3507. https://doi.org/10.1111/jace.14554.

[61] C. Vakifahmetoglu, J.F. Anger, V. Atakan, S. Quinn, S. Gupta, Q. Li, L. Tang, R.E. Riman, Reactive hydrothermal liquid-phase densification (rHLPD) of ceramics–a study of the $BaTiO_3$ [TiO_2] composite system, J. Am. Ceram. Soc. 99 (2016) 3893-3901. https://doi.org/10.1111/jace.14468.

[62] S.I. Hirano, S. Somiya, Hydrothermal reaction sintering of pure Cr_2O_3, J. Am. Ceram. Soc. 59 (1976) 534-534. https://doi.org/10.1111/j.1151-2916.1976.tb09432.x.

[63] C. Curtis, L. Doney, J. Johnson, Some properties of hafnium oxide, hafnium silicate, calcium hafnate, and hafnium carbide, J. Am. Ceram. Soc. 37 (1954) 458-465. https://doi.org/10.1111/j.1151-2916.1954.tb13977.x.

[64] H. Toraya, M. Yoshimura, S. Somiya, Hydrothermal reaction-sintering of monoclinic HfO_2, J. Am. Ceram. Soc. 65 (1982) c159-c160. https://doi.org/10.1111/j.1151-2916.1982.tb10527.x.

[65] S.-i. Hirano, S. Somiya, Hydrothermal crystal growth of magnetite in the presence of hydrogen, J. Cryst. Growth 35 (1976) 273-278. https://doi.org/10.1016/0022-0248(76)90184-6.

[66] P. Ownby, G.E. Jungquist, Final sintering of Cr_2O_3, J. Am. Ceram. Soc. 55 (1972) 433-436. https://doi.org/10.1111/j.1151-2916.1972.tb11334.x.

[67] M. Yoshimura, S. Sōmiya, Fabrication of dense, nonstabilized ZrO_2 ceramics by hydrothermal reaction sintering, Hydrothermal Reactions for Materials Science and Engineering, Springer, 1989, pp. 15-15.

[68] M. Yoshimura, S. Sōmiya, Hydrothermal reaction sintering of monoclinic zirconia, Hydrothermal Reactions for Materials Science and Engineering, Springer, 1989, pp. 16-23.

[69] S. Sōmiya, Reactions for hydrothermal reaction sintering, Sintering Key Papers, Springer, 1990, pp. 679-685.

[70] K. Yanagisawa, Q. Feng, N. Yamasaki, Preparation of ceramics by hydrothermal hot-pressing, High Press. Res. 20 (2001) 343-349. https://doi.org/10.1080/08957950108206182.

[71] G. Goglio, A. Ndayishimiye, A. Largeteau, C. Elissalde, View point on hydrothermal sintering: main features, today's recent advances and tomorrow's promises, Scripta Mater. 158 (2019) 146-152. https://doi.org/10.1016/j.scriptamat.2018.08.038.

[72] N. Yamasaki, K. Yanagisawa, M. Nishioka, S. Kanahara, A hydrothermal hot-pressing method: apparatus and application, J. Mater. Sci. Lett. 5 (1986) 355-356. http://doi.org/10.1007/978-94-009-0743-0_70.

[73] Z. Matamoros-Veloza, J. Rendón-Angeles, K. Yanagisawa, E. Mejia-Martínez, J. Parga, Low temperature preparation of porous materials from TV panel glass

compacted via hydrothermal hot pressing, Ceram. Int. 41 (2015) 12700-12709. https://doi.org/10.1016/j.ceramint.2015.06.102.

[74] N. Yamasaki, W. Tang, J. Ke, Low-temperature sintering of calcium carbonate by a hydrothermal hot-pressing technique, J. Mater. Sci. Lett. 11 (1992) 934-936. http://doi.org/10.1007/bf00729099.

[75] K. Yanagisawa, M. Sasaki, M. Nishioka, K. Ioku, N. Yamasaki, Preparation of sintered compacts of anatase by hydrothermal hot-pressing, J. Mater. Sci. Lett. 13 (1994) 765-766. http://doi.org/10.1007/bf00461398.

[76] A. Ndayishimiye, A. Largeteau, M. Prakasam, S. Pechev, M.-A. Dourges, G. Goglio, Low temperature hydrothermal sintering process for the quasi-complete densification of nanometric α-quartz, Scripta Mater. 145 (2018) 118-121. https://doi.org/10.1016/j.scriptamat.2017.10.023.

[77] A. Ndayishimiye, A. Largeteau, S. Mornet, M. Duttine, M.-A. Dourges, D. Denux, M. Verdier, M. Gouné, T.H. de Beauvoir, C. Elissalde, Hydrothermal sintering for densification of silica. Evidence for the role of water, J. Eur. Ceram. Soc. 38 (2018) 1860-1870. https://doi.org/10.1016/j.jeurceramsoc.2017.10.011.

[78] A. Nakahira, H. Nishimoto, Y. Hamada, Y. Yamasaki, Synthesis and characterization of dense mesoporous alumina, Key Eng. Mater., Trans Tech Publ, 2014, pp. 252-257.

[79] H. Onoda, R. Sakai, A. Nakahira, I. Tanaka, Synthesis of porous aluminum phosphate bulks by hydrothermal hot pressing process and their analytical characterizations, Inorg. Mater. 45 (2009) 1048-1052. http://doi.org/10.1134/s0020168509090180.

[80] T. Onoki, X. Wang, S. Zhu, Y. Hoshikawa, N. Sugiyama, M. Akao, E. Yasuda, M. Yoshimura, A. Inoue, Bioactivity of titanium-based bulk metallic glass surfaces via hydrothermal hot-pressing treatment, J. Ceram. Soc. Jpn. 116 (2008) 115-117. https://doi.org/10.2109/jcersj2.116.115.

[81] T. Onoki, X.M. Wang, S.L. Zhu, Y. Hoshikawa, N. Sugiyama, M. Akao, E. Yasuda, M. Yoshimura, A. Inoue, Apatite forming ability of bulk metallic glass surface via hydrothermal treatment, Key Eng. Mater., Trans Tech Publ, 2008, pp. 249-252.

[82] M. Li, H.-y. Sun, X.-l. Liu, H.-y. Xu, Y. Ren, D.-l. Cui, X. Tao, Preparation of porous boehmite nanosolid and its composite fluorescent materials by a novel hydrothermal

hot-press method, Mater. Lett. 60 (2006) 2738-2742. https://doi.org/10.1016/j.matlet.2006.01.081.

[83] K. Sato, T. Hashida, H. Takahashi, N. Yamasaki, Development of high strength calcium aluminate-phosphate cement by hydrothermal hot-pressing, J. Mater. Sci. Lett. 16 (1997) 1464-1468. http://doi.org/10.1023/a:1018546318785.

[84] S. Katsuyama, M. Ito, Synthesis of $Ca_3Co_4O_9$ ceramics by citric acid complex and hydrothermal hot-pressing processes and its thermoelectric properties, Thermoelectrics, 2006. ICT'06. 25th International Conference on, IEEE, 2006, pp. 543-547.

[85] S. Katsuyama, Y. Takiguchi, M. Ito, Synthesis of $Ca_3Co_4O_9$ ceramics by polymerized complex and hydrothermal hot-pressing processes and the investigation of its thermoelectric properties, J. Mater. Sci. 43 (2008) 3553-3559. http://doi.org/10.1007/s10853-008-2561-x.

[86] N. Yamasaki, T. Weiping, H. Lei, K. Hosoi, Solidification of aragonite-type $CaCO_3$ powder containing chitosan with acetic acid by hydrothermal hot pressing, J. Mater. Sci. Lett. 14 (1995) 1751-1753. http://doi.org/10.1007/bf00270997.

[87] K. Hosoi, T. Hashida, H. Takahashi, N. Yamasaki, T. Korenaga, Low temperature solidification of calcium carbonate through vaterite-calcite wet transformation, J. Mater. Sci. Lett. 15 (1996) 812-814. http://doi.org/10.1007/bf00274614.

[88] K. Hosoi, T. Hashida, H. Takahashi, N. Yamasaki, T. Korenaga, Solidification behaviour of calcium carbonate via aragonite-calcite wet transformation with hydrothermal hot pressing, J. Mater. Sci. Lett. 16 (1997) 382-385. http://doi.org/10.1023/a:1018506714049.

[89] N. Yamasaki, L. Fei, S. Shimomto, Q. Chen, Fabrication of colored $CaCO_3$ compacts by hydrothermal hot-pressing method, Mater. Res. Innovations 2 (1998) 45-48. https://doi.org/10.1007/s100190050060.

[90] N. Yamasaki, T. Weiping, K. Jiajun, K. Hosoi, Low-temperature sintering of calcium and magnesium carbonate by the hydrothermal hot-pressing technique, J. Mater. Sci. Lett. 14 (1995) 1268-1270. http://doi.org/10.1007/bf01262263.

[91] N. Yamasaki, T. Weiping, K. Yanagisawa, Solidification of $CaCO_3$ containing $SrCO_3$ by hydrothermal hot-pressing, J. Mater. Res. 8 (1993) 1972-1976. http://doi.org/10.1557/JMR.1993.1972.

[92] C. Udawatte, K. Yanagisawa, T. Kamakura, Y. Matsumoto, N. Yamasaki, Hardening of hydrothermal hot pressed calcium silicate compacts with rice husk as fiber reinforcement, Mater. Res. Innovations 3 (2000) 297-301. http://doi.org/10.1007/s100190000048.

[93] T. Kamakura, Y. Matsumoto, T. Kuroki, N. Yamasaki, M. Uragami, G. Bignall, Development of continuous hydrothermal hot-pressing apparatus, High Press. Res. 20 (2001) 421-428. https://doi.org/10.1080/08957950108206190.

[94] H. Onoda, Y. Inagaki, A. Kuwabara, N. Kitamura, K. Amezawa, A. Nakahira, I. Tanaka, Synthesis and electrical conductivity of tetra-valent cerium polyphosphate bulks, Phosphorus Res. Bull. 23 (2009) 20-24. http://doi.org/10.3363/prb.23.20.

[95] H. Onoda, Y. Inagaki, A. Kuwabara, N. Kitamura, K. Amezawa, A. Nakahira, I. Tanaka, Synthesis and electrical conductivity of bulk tetra-valent cerium pyrophosphate, J. Ceram. Process Res. 11 (2010) 344-347.

[96] H. Onoda, K.-i. Okumoto, A. Nakahira, I. Tanaka, Mechanochemical effects on the synthesis of copper orthophosphate and cyclo-tetraphosphate bulks by the hydrothermal hot pressing method, Materials 2 (2009) 1-9. http://doi.org/10.3390/ma2010001.

[97] H. Song, L. Wei, Y. Ji, L. Cao, F. Cheng, Heavy metal fixing and heat resistance abilities of coal fly ash-waste glass based geopolymers by hydrothermal hot pressing, Adv. Powder Technol. 29 (2018) 1487-1492. https://doi.org/10.1016/j.apt.2018.03.013.

[98] K. Hosoi, S. Kawai, K. Yanagisawa, N. Yamasaki, Densification process for spherical glass powders with the same particle size by hydrothermal hot pressing, J. Mater. Sci. 26 (1991) 6448-6452. http://doi.org/10.1007/bf00551895.

[99] T. Yoshikawa, S. Sato, T. Tanaka, Fabrication of low temperature foaming glass materials using hydrothermal treatment, ISIJ Int. 48 (2008) 130-133. http://doi.org/10.2355/isijinternational.48.130.

[100] K. Ioku, T. Kai, M. Nishioka, K. Yanagisawa, N. Yamasaki, Bioactive glass-ceramics prepared by hydrothermal hot-pressing, J. Chem. Soc. Japan 1991 (1991) 1408-1412. http://doi.org/10.1246/nikkashi.1991.1408

[101] N. Yamasaki, T. Kai, M. Nishioka, K. Yanagisawa, K. Ioku, Preparation of biologically active glass ceramics with rod-shaped crystals dispersion by

hydrothermal hot-pressing, J. Mater. Sci. Lett. 11 (1992) 233-234. http://doi.org/10.1007/bf00741430.

[102] M. Nishioka, K. Yanagisawa, N. Yamasaki, Solidification of glass powder by a hydrothermal hot-pressing technique, Hydrothermal Reactions for Materials Science and Engineering, Springer, 1989, pp. 417-422.

[103] K. Yanagisawa, M. Nishioka, N. Yamasaki, Densification process of borosilicate glass powders under hydrothermal hot-pressing conditions, J. Mater. Sci. 24 (1989) 4052-4056. http://doi.org/10.1007/bf01168973

[104] Z.M. Veloza, K. Yanagizawa, N. Yamasaki, Recycling waste glasses by means of the hydrothermal hot pressing method, J. Mater. Sci. Lett. 18 (1999) 1811-1813. http://doi.org/10.1023/a:1006622616850.

[105] Z.M. Veloza, K. Yanagisawa, N. Yamasaki, Hydrothermal hot pressing for recycling of waste glass, High Press. Res. 20 (2001) 351-359. https://doi.org/10.1080/08957950108206183.

[106] N. Yamasaki, A. Shirakawa, N. Hirano, T. Hashida, Examination of solidified waste glass powder after hydrothermal hot pressing, J. Mater. Sci. Lett. 21 (2002) 711-713. https://doi.org/10.1023/A:1015785021932.

[107] Z. Matamoros-Veloza, K. Yanangisawa, J. Rendon-Angeles, S. Oishi, M. Cisneros-Guerrero, Preparation of porous glass-ceramics under different hydrothermal hot pressing conditions, Solid State Ion. 172 (2004) 597-600. https://doi.org/10.1016/j.ssi.2004.04.034.

[108] Z. Matamoros-Veloza, J. Rendón-Angeles, K. Yanagisawa, M. Cisneros-Guerrero, M. Cisneros-Guerrero, L. Aguirre, Preparation of foamed glasses from CRT TV glass by means of hydrothermal hot-pressing technique, J. Eur. Ceram. Soc. 28 (2008) 739-745. https://doi.org/10.1016/j.jeurceramsoc.2007.09.014.

[109] T. Yoshikawa, S. Sato, T. Tanaka, Fabrication of low temperature foaming glass materials using hydrothermal treatment, Mater. Sci. Forum 561-565 (2007) 1673-1675. https://doi.org/10.4028/www.scientific.net/MSF.561-565.1673

[110] Z. Matamoros-Veloza, K. Yanagisawa, J. Rendon-Angeles, S. Oishi, The effect of hydrothermal hot-pressing parameters on the fabrication of porous ceramics using waste glass, J. Phys.: Condens. Matter 16 (2004) S1361. https://doi.org/10.1088/0953-8984/16/14/049.

[111] N. Yamasaki, T. Kai, M. Nishioka, K. Yanagisawa, K. Ioku, Porous hydroxyapatite ceramics prepared by hydrothermal hot-pressing, J. Mater. Sci. Lett. 9 (1990) 1150-1151. https://doi.org/10.1007/BF00721872.

[112] K. Ioku, K. Yamamoto, K. Yanagisawa, N. Yamasaki, Low temperature sintering of hydroxyapatite by hydrothermal hot-pressing, Phosphorus Res. Bull. 4 (1994) 65-70. https://doi.org/10.3363/prb1992.4.0_65.

[113] K. Hosoi, T. Hashida, H. Takahashi, N. Yamasaki, T. Korenaga, New processing technique for hydroxyapatite ceramics by the hydrothermal hot-pressing method, J. Am. Ceram. Soc. 79 (1996) 2771-2774. https://doi.org/10.1111/j.1151-2916.1996.tb09048.x.

[114] K. Hosoi, T. Korenaga, T. Hashida, H. Takahashi, N. Yamasaki, New synthesis technique for making hydroxyapatite ceramics using hydrothermal hot-pressing, Rev. High Pres. Sci. Tech. 7 (1998) 1405-1407. https://doi.org/10.4131/jshpreview.7.1405.

[115] K. Yanagisawa, T. Fujino, K. Zhu, K. Ioku, A. Onda, K. Kajiyoshi, C.-W. Chen, R.E. Riman, Development of low temperature sintering of hydroxyapatite ceramics using hydrothermal hot-pressing method, Phosphorus Res. Bull. 17 (2004) 231-234. https://doi.org/10.3363/prb1992.17.0_231.

[116] A. Nakahira, T. Murakami, T. Onoki, T. Hashida, K. Hosoi, Fabrication of porous hydroxyapatite using hydrothermal hot pressing and post-sintering, J. Am. Ceram. Soc. 88 (2005) 1334-1336. https://doi.org/10.1111/j.1551-2916.2005.00238.x.

[117] J.G. Li, T. Hashida, In situ formation of hydroxyapatite-whisker ceramics by hydrothermal hot-pressing method, J. Am. Ceram. Soc. 89 (2006) 3544-3546. https://doi.org/10.1111/j.1551-2916.2006.01149.x.

[118] H. Song, S.R. Kim, H.J. Kim, J.H. Hwang, W.T. Kwon, Y. Kim, Preparation and Characterization of Porous Hydroxyapatite Block Using a HHP Method, Key Eng. Mater., Trans Tech Publ, 2006, pp. 1067-1070.

[119] K. Yanagisawa, K. Zhu, T. Fujino, A. Onda, K. Kajiyoshi, K. Ioku, Preparation of hydroxyapatite ceramics by hydrothermal hot-pressing technique, Key Eng. Mater., Trans Tech Publ, 2006, pp. 57-60.

[120] J. Li, T. Hashida, Preparation of hydroxyapatite ceramics by hydrothermal hot-pressing method at 300 C, J. Mater. Sci. 42 (2007) 5013-5019. https://doi.org/10.1007/s10853-006-0613-7.

[121] K. Yanagisawa, J.-H. Kim, C. Sakata, A. Onda, E. Sasabe, T. Yamamoto, Z. Matamoros-Veloza, J.C. Rendón-Angeles, Hydrothermal sintering under mild temperature conditions: preparation of calcium-deficient hydroxyapatite compacts, Z. Naturforsch., B: Chem. Sci. 65 (2010) 1038-1044. https://doi.org/10.1515/znb-2010-0810.

[122] J.-H. Kim, K. Yanagisawa, A. Onda, E. Sasabe, T. Yamamoto, Densification behavior of hydroxyapatite green pellets prepared by different methods, J. Ceram. Soc. Jpn. 123 (2015) 1097-1101. https://doi.org/10.2109/jcersj2.123.1097.

[123] K. Montoya-Cisneros, J. Rendón-Angeles, Z. Matamoros-Veloza, A. Matamoros-Veloza, K. Yanagisawa, Low-temperature densification of Mg-doped hydroxyapatite fine powders under hydrothermal hot processing conditions, Ceram. Int. 43 (2017) 11907-11919. https://doi.org/10.1016/j.ceramint.2017.06.039.

[124] E. Erydani Mejia-Martinez, Z. Matamoros-Veloza, K. Yanagisawa, J. Carlos Rendon-Angeles, B. Moreno-Perez, Influence of temperature on hydrothermal hot-pressing of magnesium hydroxyapatite powder, Bol. Soc. Esp. Ceram. V. 57 (2018) 45-54. https://doi.org/10.1016/j.bsecv.2017.06.003.

[125] T. Onoki, A. Nakahira, T. Tago, Y. Hasegawa, T. Kuno, Novel low temperature processing techniques for apatite ceramics and chitosan polymer composite bulk materials and its mechanical properties, Appl. Surf. Sci. 262 (2012) 263-266. https://doi.org/10.1016/j.apsusc.2012.09.031.

[126] N. Yamasaki, K. Yanagisawa, N. Kakiuchi, Production of hydroxyapatite-glass compacts by hydrothermal hot-pressing technique, J. Mater. Res. 5 (1990) 647-653. https://doi.org/10.1557/JMR.1990.0647.

[127] Y. Kim, S.R. Kim, H. Song, H. Yoon, Preparation of porous hydroxyapatite/TCP composite block using a hydrothermal hot pressing method, Mater. Sci. Forum, Trans Tech Publ, 2005, pp. 117-120.

[128] H. Song, S.R. Kim, J.H. Hwang, Y. Kim, Preparation of porous hydroxyapatite/tricalcium phosphate composite block using a HHP method, Key Eng. Mater., Trans Tech Publ, 2006, pp. 1071-1074.

[129] T. Onoki, S.-y. Yamamoto, Hydroxyapatite ceramics coating on magnesium alloy via a double layered capsule hydrothermal hot-pressing, J. Ceram. Soc. Jpn. 118 (2010) 749-752. https://doi.org/10.2109/jcersj2.118.749.

[130] T. Onoki, S.y. Yamamoto, H. Onodera, A. Nakahira, New technique for bonding hydroxyapatite ceramics and magnesium alloy by hydrothermal hot-pressing method, Mater. Sci. Eng., C 31 (2011) 499-502. https://doi.org/10.1016/j.msec.2010.09.002.

[131] T. Onoki, K. Hosoi, T. Hashida, Joining hydroxyapatite ceramics and titanium alloys by hydrothermal method, Key Eng. Mater., Trans Tech Publ, 2003, pp. 571-574.

[132] T. Onoki, K. Hosoi, T. Hashida, New technique for bonding hydroxyapatite ceramics and titanium by the hydrothermal hot-pressing method, Scripta Mater. 52 (2005) 767-770. https://doi.org/10.1016/j.scriptamat.2004.12.011.

[133] T. Onoki, T. Hashida, New method for hydroxyapatite coating of titanium by the hydrothermal hot isostatic pressing technique, Surf. Coat. Technol. 200 (2006) 6801-6807. https://doi.org/10.1016/j.surfcoat.2005.10.016.

[134] T. Onoki, T. Hashida, Novel method for hydroxyapatite coating by hydrothermal hot-pressing via double layered capsule, Key Eng. Mater., Trans Tech Publ, 2006, pp. 647-650.

[135] T. Onoki, K. Hosoi, T. Hashida, Effects of water location in starting materials on bonding behavior of hydroxyapatite and titanium via hydrothermal hot-pressing, AIP Conference Proceedings, AIP, 2006, pp. 112-115.

[136] M.a. Tanaka, T. Onoki, K. Hosoi, T. Hashida, Effects of pressure and reaction time on bonding of hydroxyapatite ceramics and titanium by hydrothermal hot-pressing, AIP Conference Proceedings, AIP, 2006, pp. 82-84.

[137] T. Onoki, K. Hosoi, T. Hashida, Y. Tanabe, T. Watanabe, E. Yasuda, M. Yoshimura, Effects of titanium surface modifications on bonding behavior of hydroxyapatite ceramics and titanium by hydrothermal hot-pressing, Mater. Sci. Eng., C 28 (2008) 207-212. https://doi.org/10.1016/j.msec.2006.12.002.

[138] T. Onoki, T. Higashi, X. Wang, S. Zhu, N. Sugiyama, Y. Hoshikawa, M. Akao, N. Matsushita, A. Nakahira, E. Yasuda, Interface structure between Ti-based bulk metallic glasses and hydroxyapatite ceramics jointed by hydrothermal techniques, Mater. Trans. 50 (2009) 1308-1312. https://doi.org/10.2320/matertrans.ME200815.

[139] T. Onoki, X. Wang, S. Zhu, N. Sugiyama, Y. Hoshikawa, M. Akao, N. Matsushita, A. Nakahira, E. Yasuda, M. Yoshimura, Effects of growing integrated layer [GIL] formation on bonding behavior between hydroxyapatite ceramics and Ti-based bulk

metallic glasses via hydrothermal hot-pressing, Mater. Sci. Eng., B 161 (2009) 27-30. https://doi.org/10.1016/j.mseb.2008.11.011.

[140] H. Onoda, A. Yoshida, Synthesis and properties of bulk lanthanum phosphates obtained by hydrothermal hot pressing, J. Ceram. Process Res. 13 (2012) 622-626.

[141] H. Onoda, T. Yamasaki, Synthesis of bulk lanthanum polyphosphate and other rare earth phosphates through hydrothermal hot-pressing, J. Adv. Ceram.. 2 (2013) 301-307. https://doi.org/10.1007/s40145-013-0074-9.

[142] A. Ndayishimiye, S. Buffière, M.-A. Dourges, A. Largeteau, M. Prakasam, S. Mornet, O. Kaman, J. Zdeněk, J. Hejtmánek, G. Goglio, Design of 0–3 type nanocomposites using hydrothermal sintering, Scripta Mater. 148 (2018) 15-19. https://doi.org/10.1016/j.scriptamat.2018.01.013.

[143] O. Kaman, Z. Jirák, J. Hejtmánek, A. Ndayishimiye, M. Prakasam, G. Goglio, Tunneling magnetoresistance of hydrothermally sintered $La_{1-x}Sr_xMnO_3$-silica nanocomposites, J. Magn. Magn. Mater. 479 (2019) 135-143. https://doi.org/10.1016/j.jmmm.2019.01.114.

[144] S. Katsuyama, A. Kishida, M. Ito, Synthesis of $Na_xCo_2O_4$ by the hydrothermal hot-pressing and its thermoelectric properties, J. Alloys Compd. 414 (2006) 215-220. https://doi.org/10.1016/j.jallcom.2005.05.050.

[145] S. Ishihara, T. Matsumoto, T. Onoki, T. Sohmura, A. Nakahira, New concept bioceramics composed of octacalcium phosphate (OCP) and dicarboxylic acid-intercalated OCP via hydrothermal hot-pressing, Mater. Sci. Eng., C 29 (2009) 1885-1888. https://doi.org/10.1016/j.msec.2009.02.023.

[146] K. Satoh, T. Hashida, H. Takahashi, N. Yamasaki, Solidification method for phosphate bonded alumina cement by hydrothermal hot-pressing, J. Ceram. Soc. Jpn. 105 (1997) 424-427. https://doi.org/10.2109/jcersj.105.424.

[147] K. Yanagisawa, M. Nishioka, K. Ioku, N. Yamasaki, Neck formation of spherical silica particles by hydrothermal hot pressing, J. Mater. Sci. Lett. 10 (1991) 7-8. https://doi.org/10.1007/bf00724415.

[148] K. Yanagisawa, M. Nishioka, K. Ioku, N. Yamasaki, Low temperature sintering of spherical silica powder by hydrothermal hot-pressing, J. Ceram. Soc. Jpn. 99 (1991) 59-62. https://doi.org/10.2109/jcersj.99.59.

[149] K. Yanagisawa, M. Nishioka, K. Ioku, N. Yamasaki, Densification of silica gels by hydrothermal hot-pressing, J. Mater. Sci. Lett. 12 (1993) 1073-1075. https://doi.org/10.1007/BF00420525.

[150] K. Yanagisawa, K. Ioku, N. Yamasaki, Pore size control of porous silica ceramics by hydrothermal hot-pressing, J. Ceram. Soc. Jpn. 102 (1994) 966-971. https://doi.org/10.2109/jcersj.102.966.

[151] H. Nagata, M. Takimura, Y. Yamasaki, A. Nakahira, Syntheses and characterization of bulky mesoporous silica MCM-41 by hydrothermal hot-pressing method, Mater. Trans. 47 (2006) 2103-2105. https://doi.org/10.2320/matertrans.47.2103.

[152] M. Takimura, H. Nagata, Y. Yamasaki, T. Suzuki, Y. Ikuhara, A. Nakahira, Synthesis and characterization of bulky FSM with interconnected mesopore-networks using an HHP method, J. Ceram. Soc. Jpn. 114 (2006) 554-557. https://doi.org/10.2109/jcersj.114.554.

[153] A. Nakahira, M. Takimura, Y. Yamasaki, Synthesis of bulky mesoporous silica (FSM) by hydrothermal hot-pressing method, J. Non-Cryst. Solids 353 (2007) 4203-4207. https://doi.org/10.1016/j.jnoncrysol.2007.07.017.

[154] M. Takimura, H. Nagata, Y. Yamasaki, A. Nakahira, Synthesis of dense mesoporous silica with high surface area by hydrothermal hot-pressing (HHP) method, Solid State Phenomena, Trans Tech Publ, 2007, pp. 1833-1836.

[155] A. Nakahira, H. Nagata, T. Onoki, Y. Yamasaki, Evaluation of microstructures and properties of bulk mesoporous silica, Res. Chem. Intermed. 34 (2008) 347-352. https://doi.org/10.1163/156856708784040696.

[156] A. Nakahira, T. Hamada, Y. Yamauchi, Synthesis and properties of dense bulks for mesoporous silica SBA-15 by a modified hydrothermal method, Mater. Lett. 64 (2010) 2053-2055. https://doi.org/10.1016/j.matlet.2010.06.035.

[157] N. Suzuki, Y.-T. Huang, Y. Nemoto, A. Nakahira, Y. Yamauchi, Highly densified mesoporous bulk silica prepared with colloidal mesoporous silica nanoparticles toward a new low-k material, Chem. Lett. 41 (2012) 1518-1519. https://doi.org/10.1246/cl.2012.1518.

[158] Y. Xie, S. Yin, H. Yamane, T. Hashimoto, T. Sato, Low temperature sintering and color of a new compound $Sn_{1.24}Ti_{1.94}O_{3.66}(OH)_{1.50}F_{1.42}$, Solid State Sci. 11 (2009) 1703-1708. https://doi.org/10.1016/j.solidstatesciences.2009.05.025.

[159] K. Yanagisawa, K. Ioku, N. Yamasaki, Crystallization of amorphous hydrous titania under hydrothermal hot-pressing conditions, J. Ceram. Soc. Jpn. 102 (1994) 1091-1093. https://doi.org/10.2109/jcersj.102.1091.

[160] K. Yanagisawa, K. Ioku, N. Yamasaki, Post-sintering of anatase compact prepared by hydrothermal hot-pressing, J. Mater. Sci. Lett. 14 (1995) 161-163. https://doi.org/10.1007/BF00318242.

[161] K. Yanagisawa, K. Ioku, N. Yamasaki, Formation of anatase porous ceramics by hydrothermal hot-pressing of amorphous titania spheres, J. Am. Ceram. Soc. 80 (1997) 1303-1306. https://doi.org/10.1111/j.1151-2916.1997.tb02982.x.

[162] T. Kubo, A. Nakahira, Y. Yamasaki, Fabrication of mesoporous bulk composed of titanate nanotubes by hydrothermal hot-pressing technique, J. Mater. Res. 22 (2007) 1286-1291. https://doi.org/10.1557/jmr.2007.0160.

[163] T. Kubo, M. Takeuchi, M. Matsuoka, M. Anpo, A. Nakahira, Morphologic control of Pt supported titanate nanotubes and their photocatalytic property, Catal. Lett. 130 (2009) 28-36. https://doi.org/10.1007/s10562-009-9851-z.

[164] A. Nakahira, T. Kubo, Y. Yamasaki, Microstructural control of mesoporous bulk composed of TiO_2-derived titanate nanotubes, ACS Appl. Mater. Interfaces. 2 (2010) 1136-1140. https://doi.org/10.1021/am900931v.

[165] C. Udawatte, K. Yanagisawa, T. Kamakura, Y. Matsumoto, N. Yamasaki, Solidification of xonotlite fibers with chitosan by hydrothermal hot pressing, Mater. Lett. 45 (2000) 298-301. https://doi.org/10.1016/S0167-577X(00)00121-X.

[166] A. Nakahira, S. Takezoe, Y. Yamasaki, Synthesis of dense Y-zeolite bulks with large surface area using a hydrothermal hot-pressing (HHP) process, Chem. Lett. 33 (2004) 1400-1401. https://doi.org/10.1246/cl.2004.1400.

[167] S. Takezoe, K. Hosoi, M. Tajika, Y. Yamasaki, A. Nakahira, Syntheses of bulky Y-zeolite by hydrothermal hot-pressing (HHP) technique, Key Eng. Mater., Trans Tech Publ, 2006, pp. 97-100.

[168] A. Nakahira, S. Takezoe, Y. Yamasaki, Y. Sasaki, Y. Ikuhara, Synthesis and evaluation of bulky Y-Zeolites by hydrothermal hot-pressing method, J. Am. Ceram. Soc. 90 (2007) 2322-2326. https://doi.org/10.1111/j.1551-2916.2007.01721.x.

[169] T. Onoki, Zeolite Y deposition on aluminum substrate without structure directing agents (SDAs), Mater. Lett. 71 (2012) 25-27. https://doi.org/10.1016/j.matlet.2011.11.095.

[170] F.-S. Xiao, G. Pang, T. Ji, X. Meng, W. Pang, R. Xu, Catalytic cracking activity and physicochemical properties of rey zeolite mixed with kaolin clay treated by hydrothermal hot pressing method, Appl. Catal., A 133 (1995) 305-320. https://doi.org/10.1016/0926-860X(95)00176-X.

[171] H. Nishizawa, H. Tebika, N. Yamasaki, Fabrication of stabilized zirconia compressed body under hydrothermal conditions and its sintering, J. Ceram. Soc. Jpn. 92 (1984) 420.

[172] T. Yoshikawa, M. Hosokawa, T. Tanaka, MgO effect on hydrothermal solidification of blast furnace slag, ISIJ Int. 48 (2008) 557-562. https://doi.org/10.2355/isijinternational.48.557.

[173] S.-J. Tae, T. Tanaka, K. Morita, Effect of microwave irradiation on hydrothermal treatment of blast furnace slag, ISIJ Int. 49 (2009) 1259-1264. https://doi.org/10.2355/isijinternational.49.1259.

[174] Y. Nakane, K. Sato, H. Takahashi, N. Yamasaki, T. Hashida, Development of solidification technique for recycle of concrete wastes by hydrothermal hot-pressing and its mechanical property, J. Ceram. Soc. Jpn. 102 (1994) 405-407. https://doi.org/10.2109/jcersj.102.405.

[175] K. Sato, T. Hashida, H. Takahashi, N. Yamasaki, Strengthening of hydrothermal hot-pressed concrete waste by the addition of slag, J. Ceram. Soc. Jpn. 105 (1997) 262-264. https://doi.org/10.2109/jcersj.105.262.

[176] Y. Nakane, T. Hashida, H. Takahashi, N. Yamasaki, Strengthening of hydrothermal hot-pressed concrete wastes by the addition of fresh cement, J. Ceram. Soc. Jpn. 103 (1995) 511-514. https://doi.org/10.2109/jcersj.103.511.

[177] P. Sun, H.-C. Wu, Transition from brittle to ductile behavior of fly ash using PVA fibers, Cem. Concr. Compos. 30 (2008) 29-36. https://doi.org/10.1016/j.cemconcomp.2007.05.008.

[178] P. Sun, H.-C. Wu, Splitting tensile strength of fly ash activated by hydrothermal hot-pressing process, J. Mater. Civ. Eng. 21 (2009) 356-361. https://doi.org/10.1061/(ASCE)0899-1561(2009)21:8(356).

[179] F. Xue, H. Song, Y. Ji, L. Cao, F. Cheng, Hydrothermal hot-pressing solidification of coal fly ash and its ability of fixing heavy metal, J. Residuals Sci. Tech. 12 (2015). https://doi.org/10.12783/issn.1544-8053/12/3/4.

[180] M. Nishioka, S. Hirai, K. Yanagisawa, N. Yamasaki, Solidification of glass powder with simulated high-level radioactive waste during hydrothermal hot-pressing, J. Am. Ceram. Soc. 73 (1990) 317-322. https://doi.org/10.1111/j.1151-2916.1990.tb06512.x.

[181] K. Yanagisawa, M. Nishioka, N. Yamasaki, Immobilization of cesium into pollucite structure by hydrothermal hot-pressing, J. Nucl. Sci. Technol. 24 (1987) 51-60. https://doi.org/10.3327/jnst.24.51.

[182] N. Yamasaki, M. Nishioka, K. Yanagisawa, Immobilization of simulated hlw by hydrothermal hot-pressing of glass powder, J. At. Energy Soc. Jpn. 30 (1988) 815-820.

[183] N. Yamasaki, K. Yanagisawa, K. Kinoshita, T. Kashiwai, Solidification of waste containing sodium borate by hydrothermal hot-pressing, J. At. Energy Soc. Jpn. 30 (1988) 714-724. https://doi.org/10.3327/jaesj.30.714.

[184] K. Yanagisawa, M. Nishioka, N. Yamasaki, Immobilization of low-level radioactive waste containing sodium sulfate by hydro-thermal hot-pressing, J. Nucl. Sci. Technol. 26 (1989) 395-397. https://doi.org/10.1080/18811248.1989.9734322.

[185] K. Yanagisawa, N. Yamasaki, N. Kozai, S. Muraoka, Leachability of waste form containing cesium produced by hydrothermal hot-pressing, J. Nucl. Sci. Technol. 27 (1990) 1072-1074. https://doi.org/10.1080/18811248.1990.9731294.

[186] M. Nishioka, K. Yanagisawa, N. Yamasaki, Solidification of sludge ash by hydrothermal hot-pressing, J. Water Pollut. Control Fed. (1990) 926-932.

[187] K. Yanagisawa, Z. Matamoros-Veloza, J. Rendon-Angeles, J. López-Cuevas, Novel route for recycling of steelmaking slag by means of the hydrothermal hot-pressing method, J. Mater. Sci. Lett. 21 (2002) 693-695. https://doi.org/10.1023/A:1015724803277.

[188] O. Khelifi, Y. Kozuki, H. Murakami, K. Kurata, M. Nishioka, Nutrients adsorption from seawater by new porous carrier made from zeolitized fly ash and slag, Mar. Pollut. Bull. 45 (2002) 311-315. https://doi.org/10.1016/S0025-326X(02)00107-8.

[189] T. Onoki, T. Kuno, A. Nakahira, T. Hashida, Effects of titanium surface treatment on adhesive properties of hydroxyapatite ceramics coating to titanium substrates by

double layered capsule hydrothermal hot-pressing, J. Ceram. Soc. Jpn. 118 (2010) 530-534. https://doi.org/10.2109/jcersj2.118.530.

[190] M. Gallas, A. Rosa, T. Costa, J. Da Jornada, High pressure compaction of nanosize ceramic powders, J. Mater. Res. 12 (1997) 764-768. https://doi.org/10.1557/JMR.1997.0111.

[191] T. Costa, M. Gallas, E. Benvenutti, J. Da Jornada, Infrared and thermogravimetric study of high pressure consolidation in alkoxide silica gel powders, J. Non-Cryst. Solids 220 (1997) 195-201. https://doi.org/10.1016/S0022-3093(97)00236-6.

[192] J.B. Brito, T.M.H. Costa, F.S. Rodembusch, N.M. Balzaretti, Photoluminescence of silica monoliths prepared from cold sintering of nanometric aerosil precursors under high pressure, J. Lumin. 187 (2017) 154-159. https://doi.org/10.1016/j.jlumin.2017.03.013.

[193] H. Kähäri, M. Teirikangas, J. Juuti, H. Jantunen, Improvements and modifications to room-temperature fabrication method for dielectric Li_2MoO_4 ceramics, J. Am. Ceram. Soc. 98 (2015) 687-689. https://doi.org/10.1111/jace.13471.

[194] M. Väätäjä, H. Kähäri, J. Juuti, H. Jantunen, Li_2MoO_4-based composite ceramics fabricated from temperature-and atmosphere-sensitive MnZn ferrite at room temperature, J. Am. Ceram. Soc. 100 (2017) 3626-3635. https://doi.org/10.1111/jace.14914.

[195] H. Kähäri, M. Teirikangas, J. Juuti, H. Jantunen, Room-temperature fabrication of microwave dielectric Li_2MoO_4–TiO_2 composite ceramics, Ceram. Int. 42 (2016) 11442-11446. https://doi.org/10.1016/j.ceramint.2016.04.081.

[196] H. Kähäri, P. Ramachandran, J. Juuti, H. Jantunen, Room-temperature-densified Li_2MoO_4 ceramic patch antenna and the effect of humidity, Int. J. Appl. Ceram.Tec.. 14 (2017) 50-55. https://doi.org/10.1111/ijac.12615.

[197] P. Ramachandran, H. Kähäri, J. Juuti, H. Jantunen, Room temperature densified ceramics for weight optimized circular polarized gps antenna design, Microw. Opt. Techn. Let. 60 (2018) 1061-1066. https://doi.org/10.1002/mop.31105.

[198] A. Jiang, D. Ke, L. Xu, Q. Xu, J. Li, J. Wei, C. Hu, S. Grasso, Cold hydrostatic sintering: from shaping to 3D printing, J. Materiomics. (2019). https://doi.org/10.1016/j.jmat.2019.02.009.

[199] M. Nelo, J. Peräntie, T. Siponkoski, J. Juuti, H. Jantunen, Upside-down composites: electroceramics without sintering, Appl. Mater. Today. 15 (2019) 83-86. https://doi.org/10.1016/j.apmt.2018.12.021.

[200] M. Nelo, T. Siponkoski, H. Kähäri, K. Kordas, J. Juuti, H. Jantunen, Upside-down composites: fabricating piezoceramics at room temperature, J. Eur. Ceram. Soc. 39 (2019) 3301-3306. https://doi.org/10.1016/j.jeurceramsoc.2019.04.052.

[201] J.-P. Maria, X. Kang, R.D. Floyd, E.C. Dickey, H. Guo, J. Guo, A. Baker, S. Funihashi, C.A. Randall, Cold sintering: current status and prospects, J. Mater. Res. 32 (2017) 3205-3218. https://doi.org/10.1557/jmr.2017.262.

[202] W.B. Hong, L. Li, M. Cao, X.M. Chen, Plastic deformation and effects of water in room-temperature cold sintering of NaCl microwave dielectric ceramics, J. Am. Ceram. Soc. 101 (2018) 4038-4043. https://doi.org/10.1111/jace.15572.

[203] H. Guo, J. Guo, A. Baker, C.A. Randall, Hydrothermal-assisted cold sintering process: a new guidance for low-temperature ceramic sintering, ACS Appl. Mater. Interfaces. 8 (2016) 20909-20915. https://doi.org/10.1021/acsami.6b07481.

[204] J. Guo, H. Guo, A.L. Baker, M.T. Lanagan, E.R. Kupp, G.L. Messing, C.A. Randall, Cold sintering: a paradigm shift for processing and integration of ceramics, Angew. Chem. Int. Ed. 55 (2016) 11457-11461. https://doi.org/10.1002/anie.201605443.

[205] S. Funahashi, J. Guo, H. Guo, K. Wang, A.L. Baker, K. Shiratsuyu, C.A. Randall, Demonstration of the cold sintering process study for the densification and grain growth of ZnO ceramics, J. Am. Ceram. Soc. 100 (2017) 546-553. https://doi.org/10.1111/jace.14617.

[206] E. Shotton, J. Rees, The compaction properties of sodium chloride in the presence of moisture, J. Pharm. Pharmacol. 18 (1966) 160S-167S. https://doi.org/10.1111/j.2042-7158.1966.tb07979.x.

[207] X. Kang, R. Floyd, S. Lowum, D. Long, E. Dickey, J.-P. Maria, Cold sintering with dimethyl sulfoxide solutions for metal oxides, J. Mater. Sci. 54 (2019) 7438-7446. https://doi.org/10.1007/s10853-019-03410-1.

[208] H. Guo, A. Baker, J. Guo, C.A. Randall, Protocol for ultralow-temperature ceramic sintering: an integration of nanotechnology and the cold sintering process, ACS Nano 10 (2016) 10606-10614. https://doi.org/10.1021/acsnano.6b03800.

[209] H. Guo, J. Guo, A. Baker, C.A. Randall, Cold sintering process for ZrO_2-based ceramics: significantly enhanced densification evolution in yttria-doped ZrO_2, J. Am. Ceram. Soc. 100 (2017) 491-495. https://doi.org/10.1111/jace.14593.

[210] H. Guo, T.J. Bayer, J. Guo, A. Baker, C.A. Randall, Current progress and perspectives of applying cold sintering process to ZrO_2-based ceramics, Scripta Mater. 136 (2017) 141-148. https://doi.org/10.1016/j.scriptamat.2017.02.004.

[211] H. Guo, T.J. Bayer, J. Guo, A. Baker, C.A. Randall, Cold sintering process for 8 mol% Y_2O_3-stabilized ZrO_2 ceramics, J. Eur. Ceram. Soc. 37 (2017) 2303-2308. https://doi.org/10.1016/j.jeurceramsoc.2017.01.011.

[212] D.S.B. Heidary, M. Lanagan, C.A. Randall, Contrasting energy efficiency in various ceramic sintering processes, J. Eur. Ceram. Soc. 38 (2018) 1018-1029. https://doi.org/10.1016/j.jeurceramsoc.2017.10.015.

[213] J.-P. Ma, X.-M. Chen, W.-Q. Ouyang, J. Wang, H. Li, J.-L. Fang, Microstructure, dielectric, and energy storage properties of $BaTiO_3$ ceramics prepared via cold sintering, Ceram. Int. 44 (2018) 4436-4441. https://doi.org/10.1016/j.ceramint.2017.12.044.

[214] D. Wang, H. Guo, C.S. Morandi, C.A. Randall, S. Trolier-McKinstry, Cold sintering and electrical characterization of lead zirconate titanate piezoelectric ceramics, APL Materials 6 (2018) 016101. https://doi.org/10.1063/1.5004420.

[215] R. Boston, J. Guo, S. Funahashi, A. Baker, I. Reaney, C. Randall, Reactive intermediate phase cold sintering in strontium titanate, RSC Adv. 8 (2018) 20372-20378. https://doi.org/10.1039/C8RA03072C.

[216] A. Baker, H. Guo, J. Guo, C. Randall, Utilizing the cold sintering process for flexible–printable electroceramic device fabrication, J. Am. Ceram. Soc. 99 (2016) 3202-3204. https://doi.org/10.1111/jace.14467.

[217] S.S. Berbano, J. Guo, H. Guo, M.T. Lanagan, C.A. Randall, Cold sintering process of $Li_{1.5}Al_{0.5}Ge_{1.5}(PO_4)_3$ solid electrolyte, J. Am. Ceram. Soc. 100 (2017) 2123-2135. https://doi.org/10.1111/jace.14727.

[218] S. Funahashi, H. Guo, J. Guo, A.L. Baker, K. Wang, K. Shiratsuyu, C.A. Randall, Cold sintering and co-firing of a multilayer device with thermoelectric materials, J. Am. Ceram. Soc. 100 (2017) 3488-3496. https://doi.org/10.1111/jace.14852.

[219] J.-H. Seo, J. Guo, H. Guo, K. Verlinde, D.S.B. Heidary, R. Rajagopalan, C.A. Randall, Cold sintering of a Li-ion cathode: $LiFePO_4$-composite with high

volumetric capacity, Ceram. Int. 43 (2017) 15370-15374. https://doi.org/10.1016/j.ceramint.2017.08.077.

[220] J.-H. Seo, K. Verlinde, J. Guo, D.S.B. Heidary, R. Rajagopalan, T.E. Mallouk, C.A. Randall, Cold sintering approach to fabrication of high rate performance binderless $LiFePO_4$ cathode with high volumetric capacity, Scripta Mater. 146 (2018) 267-271. https://doi.org/10.1016/j.scriptamat.2017.12.005.

[221] Y. Liu, Q. Sun, D. Wang, K. Adair, J. Liang, X. Sun, Development of the cold sintering process and its application in solid-state lithium batteries, J. Power Sources 393 (2018) 193-203. https://doi.org/10.1016/j.jpowsour.2018.05.015.

[222] I. Induja, M. Sebastian, Microwave dielectric properties of cold sintered Al_2O_3-NaCl composite, Mater. Lett. 211 (2018) 55-57. https://doi.org/10.1016/j.matlet.2017.09.083.

[223] I. Induja, M. Sebastian, Microwave dielectric properties of mineral sillimanite obtained by conventional and cold sintering process, J. Eur. Ceram. Soc. 37 (2017) 2143-2147. https://doi.org/10.1016/j.jeurceramsoc.2017.01.007.

[224] D. Wang, S. Zhang, D. Zhou, K. Song, A. Feteira, Y. Vardaxoglou, W. Whittow, D. Cadman, I.M. Reaney, Temperature stable cold sintered $(Bi_{0.95}Li_{0.05})(V_{0.9}Mo_{0.1})O_4$-$Na_2Mo_2O_7$ microwave dielectric composites, Materials 12 (2019) 1370. https://doi.org/10.3390/ma12091370.

[225] S. Venkatesan, M. ul Hassan, H.J. Ryu, Adsorption and immobilization of radioactive ionic-corrosion-products using magnetic hydroxyapatite and cold-sintering for nuclear waste management applications, J. Nucl. Mater. 514 (2019) 40-49. https://doi.org/10.1016/j.jnucmat.2018.11.026.

[226] M. ul Hassan, S. Iqbal, J.-I. Yun, H.J. Ryu, Immobilization of radioactive corrosion products by cold sintering of pure hydroxyapatite, J. Hazard. Mater. 374 (2019) 228-237. https://doi.org/10.1016/j.jhazmat.2019.04.038.

[227] M. ul Hassan, H.J. Ryu, Cold sintering and durability of iodate-substituted calcium hydroxyapatite (IO-HAp) for the immobilization of radioiodine, J. Nucl. Mater. 514 (2019) 84-89. https://doi.org/10.1016/j.jnucmat.2018.11.024.

[228] T. Charoonsuk, U. Sukkha, T. Kolodiazhnyi, N. Vittayakorn, Enhancing the densification of ceria ceramic at low temperature via the cold sintering assisted two-step sintering process, Ceram. Int. 44 (2018) S54-S57. https://doi.org/10.1016/j.ceramint.2018.08.253.

[229] H. Nakaya, M. Iwasaki, T.H. de Beauvoir, C.A. Randall, Applying cold sintering process to a proton electrolyte material: CsH_2PO_4, J. Eur. Ceram. Soc. 39 (2019) 396-401. https://doi.org/10.1016/j.jeurceramsoc.2018.09.001.

[230] J.-A. Liu, C.-H. Li, J.-J. Shan, J.-M. Wu, R.-F. Gui, Y.-S. Shi, Preparation of high-density $InGaZnO_4$ target by the assistance of cold sintering, Mater. Sci. Semicond. Process. 84 (2018) 17-23. https://doi.org/10.1016/j.mssp.2018.04.030.

[231] J. Guo, A.L. Baker, H. Guo, M. Lanagan, C.A. Randall, Cold sintering process: a new era for ceramic packaging and microwave device development, J. Am. Ceram. Soc. 100 (2017) 669-677. https://doi.org/10.1111/jace.14603.

[232] J. Ma, H. Li, H. Wang, C. Lin, X. Wu, T. Lin, X. Zheng, X. Yu, Composition, microstructure and electrical properties of $K_{0.5}Na_{0.5}NbO_3$ ceramics fabricated by cold sintering assisted sintering, J. Eur. Ceram. Soc. 39 (2019) 986-993. https://doi.org/10.1016/j.jeurceramsoc.2018.11.044.

[233] W. Lee, C.K. Lyon, J.H. Seo, R. Lopez-Hallman, Y. Leng, C.Y. Wang, M.A. Hickner, C.A. Randall, E.D. Gomez, Ceramic–salt composite electrolytes from cold sintering, Adv. Funct. Mater. 29 (2019) 1807872. https://doi.org/10.1002/adfm.201807872.

[234] Y. Liu, P. Liu, C. Hu, Low-temperature preparation and microwave dielectric properties of cold sintered $Li_2Mg_3TiO_6$ nanocrystalline ceramics, Ceram. Int. 44 (2018) 21047-21052. https://doi.org/10.1016/j.ceramint.2018.08.141.

[235] S.S. Faouri, A. Mostaed, J.S. Dean, D. Wang, D.C. Sinclair, S. Zhang, W.G. Whittow, Y. Vardaxoglou, I.M. Reaney, High quality factor cold sintered Li_2MoO_4-$BaFe_{12}O_{19}$ composites for microwave applications, Acta Mater. 166 (2019) 202-207. https://doi.org/10.1016/j.actamat.2018.12.057.

[236] D. Zhou, L.-X. Pang, D.-W. Wang, I.M. Reaney, Novel water-assisting low firing MoO_3 microwave dielectric ceramics, J. Eur. Ceram. Soc. 39 (2019) 2374-2378. https://doi.org/10.1016/j.jeurceramsoc.2019.01.052.

[237] S. Nayir, D.R. Waryoba, R. Rajagopalan, C. Arslan, C.A. Randall, Cold sintering of a covalently bonded MoS_2/graphite composite as a high capacity Li–Ion electrode, ChemNanoMat 4 (2018) 1088-1094. https://doi.org/10.1002/cnma.201800342.

[238] D. Wang, D. Zhou, S. Zhang, Y. Vardaxoglou, W.G. Whittow, D. Cadman, I.M. Reaney, Cold-sintered temperature stable $Na_{0.5}Bi_{0.5}MoO_4$–Li_2MoO_4 microwave

composite ceramics, Acs. Sustain. Chem. Eng. 6 (2018) 2438-2444. https://doi.org/10.1021/acssuschemeng.7b03889.

[239] H. Huang, J. Tang, J. Liu, Preparation of $Na_{0.5}Bi_{0.5}TiO_3$ ceramics by hydrothermal-assisted cold sintering, Ceram. Int. 45 (2019) 6753-6758. https://doi.org/10.1016/j.ceramint.2018.12.166.

[240] L. Li, W.B. Hong, S. Yang, H. Yan, X.M. Chen, Effects of water content during cold sintering process of NaCl ceramics, J. Alloys Compd. 787 (2019) 352-357. https://doi.org/10.1016/j.jallcom.2019.02.112.

[241] H. Leng, J. Huang, J. Nie, J. Luo, Cold sintering and ionic conductivities of $Na_{3.256}Mg_{0.128}Zr_{1.872}Si_2PO_{12}$ solid electrolytes, J. Power Sources 391 (2018) 170-179. https://doi.org/10.1016/j.jpowsour.2018.04.067.

[242] J.G.P. da Silva, M. Bram, A.M. Laptev, J. Gonzalez-Julian, Q. Ma, F. Tietz, O. Guillon, Sintering of a sodium-based NASICON electrolyte: a comparative study between cold, field assisted and conventional sintering methods, J. Eur. Ceram. Soc. 39 (2019) 2697-2702. https://doi.org/10.1016/j.jeurceramsoc.2019.03.023.

[243] D.S. Gyan, A. Dwivedi, Structural and electrical characterization of $NaNbO_3$-PVDF nanocomposites fabricated using cold sintering synthesis route, J. Appl. Phys. 125 (2019) 024103. https://doi.org/10.1063/1.5046458.

[244] Q. Yu, Z. Jiang, L. Cong, T. Lu, B. Suleiman, G. Leng, Z. Wu, Y. Ding, Y. Li, A novel low-temperature fabrication approach of composite phase change materials for high temperature thermal energy storage, Appl. Energy. 237 (2019) 367-377. https://doi.org/10.1016/j.apenergy.2018.12.072.

[245] S.H. Bang, T.H. De Beauvoir, C.A. Randall, Densification of thermodynamically unstable tin monoxide using cold sintering process, J. Eur. Ceram. Soc. 39 (2019) 1230-1236. https://doi.org/10.1016/j.jeurceramsoc.2018.11.026.

[246] V. Medri, F. Servadei, R. Bendoni, A.N. Murri, A. Vaccari, E. Landi, Nano-to-macroporous TiO_2 (anatase) by cold sintering process, J. Eur. Ceram. Soc. 39 (2019) 2453-2462. https://doi.org/10.1016/j.jeurceramsoc.2019.02.047.

[247] D.S.B. Heidary, J. Guo, J.-H. Seo, H. Guo, R. Rajagopalan, C.A. Randall, Microstructures and electrical properties of V_2O_5 and carbon-nanofiber composites fabricated by cold sintering process, Jpn. J. Appl. Phys. 57 (2018) 025702. https://doi.org/10.7567/JJAP.57.025702.

[248] J. Guo, H. Guo, D.S.B. Heidary, S. Funahashi, C.A. Randall, Semiconducting properties of cold sintered V_2O_5 ceramics and co-sintered V_2O_5-PEDOT:PSS composites, J. Eur. Ceram. Soc. 37 (2017) 1529-1534. https://doi.org/10.1016/j.jeurceramsoc.2016.11.021.

[249] Y. Zhao, S.S. Berbano, L. Gao, K. Wang, J. Guo, K. Tsuji, J. Wang, C.A. Randall, Cold-sintered V_2O_5-PEDOT: PSS nanocomposites for negative temperature coefficient materials, J. Eur. Ceram. Soc. 39 (2019) 1257-1262. https://doi.org/10.1016/j.jeurceramsoc.2018.10.018.

[250] J. Gonzalez-Julian, K. Neuhaus, M. Bernemann, J.P. da Silva, A. Laptev, M. Bram, O. Guillon, Unveiling the mechanisms of cold sintering of ZnO at 250° C by varying applied stress and characterizing grain boundaries by kelvin probe force microscopy, Acta Mater. 144 (2018) 116-128. https://doi.org/10.1016/j.actamat.2017.10.055.

[251] X. Kang, R. Floyd, S. Lowum, M. Cabral, E. Dickey, J.P. Maria, Mechanism studies of hydrothermal cold sintering of zinc oxide at near room temperature, J. Am. Ceram. Soc. 102 (2019) 4459-4469. https://doi.org/10.1111/jace.16340.

[252] Y. Jing, N. Luo, S. Wu, K. Han, X. Wang, L. Miao, Y. Wei, Remarkably improved electrical conductivity of ZnO ceramics by cold sintering and post-heat-treatment, Ceram. Int. 44 (2018) 20570-20574. https://doi.org/10.1016/j.ceramint.2018.07.192.

[253] S. Lowum, R. Floyd, R. Bermejo, J.-P. Maria, Mechanical strength of cold-sintered zinc oxide under biaxial bending, J. Mater. Sci. 54 (2019) 4518-4522. https://doi.org/10.1007/s10853-018-3173-8.

[254] J. Guo, B. Legum, B. Anasori, K. Wang, P. Lelyukh, Y. Gogotsi, C.A. Randall, Cold sintered ceramic nanocomposites of 2D MXene and zinc oxide, Adv. Mater. 30 (2018) 1801846. https://doi.org/10.1002/adma.201801846.

[255] X. Zhao, J. Guo, K. Wang, T. Herisson De Beauvoir, B. Li, C.A. Randall, Introducing a ZnO–PTFE (polymer) nanocomposite varistor via the cold sintering process, Adv. Eng. Mater. (2018) 1700902. https://doi.org/10.1002/adem.201700902.

[256] J. Guo, X. Zhao, T. Herisson De Beauvoir, J.H. Seo, S.S. Berbano, A.L. Baker, C. Azina, C.A. Randall, Recent progress in applications of the cold sintering process

for ceramic–polymer composites, Adv. Funct. Mater. (2018) 1801724. https://doi.org/10.1002/adfm.201801724.

[257] W.T. Chen, A.E. Gurdal, S. Tuncdemir, J. Guo, H. Guo, C.A. Randall, Considering the possibility of bonding utilizing cold sintering for ceramic adhesives, J. Am. Ceram. Soc. 100 (2017) 5421-5432. https://doi.org/10.1111/jace.15098.

[258] S. Hashimoto, W. Shimoda, H. Takeda, Y. Daiko, S. Honda, Y. Iwamoto, Fabrication of slaked lime compacts (plasters) with high compressive strength using a warm press method, Constr. Build. Mater. 110 (2016) 65-69. https://doi.org/10.1016/j.conbuildmat.2016.02.009.

[259] S. Hashimoto, K. Kubota, K. Ando, Y. Diko, S. Honda, Y. Iwamoto, Effect of grinding treatment of fly ash on compressive strength of hardened geopolymers using warm press method, MATEC Web of Conferences, EDP Sciences, 2017, pp. 01120.

[260] S. Hashimoto, S. Kusawake, Y. Daiko, S. Honda, Y. Iwamoto, Fabrication of pure phase calcium carbonate hardened bodies as a means of creating novel geomimetic ceramics, Constr. Build. Mater. 135 (2017) 405-410. https://doi.org/10.1016/j.conbuildmat.2016.12.211.

[261] S. Hashimoto, K. Kubota, K. Ando, M. Tsutani, Y. Diko, S. Honda, Y. Iwamoto, Fabrication of SiC hardened bodies with geopolymer binders using a warm press method, AIP Conference Proceedings, AIP Publishing, 2017, pp. 020011.

[262] R.E. Riman, V. Atakan, Method of hydrothermal liquid phase sintering of ceramic materials and products derived therefrom"; US Patent #8,313,802 B2, November 20, 2012; US Patent No. US 8,709,960 B2, April 29, 2014.

[263] K. Byrappa, M. Yoshimura, 10 - Hydrothermal Processing of Materials, in: K. Byrappa, M. Yoshimura (Eds.) Handbook of Hydrothermal Technology, William Andrew Publishing, Norwich, NY, 2001, pp. 754-II.

[264] M. Kaneko, Solidification of ion-exchange resins by hydrothermal hot-pressing, J. Mater. Sci. Lett. 12 (1993) 591-593. https://doi.org/10.1007/BF00278334.

[265] A. Irie, J. Ohno, T. Hayakawa, H. Kido, T. Fukushima, Transparent film formation of DNA/cationic polymer complexes by hydrothermal hot pressing: observation of cell culture on films and biodegradation of films in vivo, J. Hard Tissue Biol. 22 (2013) 105-114. https://doi.org/10.2485/jhtb.22.105.

[266] Y. Inoue, M. Kawaguchi, I. Masui, H. Horibe, T. Rikimaru, M. Kuroki, Y. Katsumata, N. Mori, T. Hayakawa, T. Fukushima, Biological and chemical assessment of DNA/chitosan complex film, J. Hard Tissue Biol. 23 (2014) 399-406. https://doi.org/10.2485/jhtb.23.399.

[267] Z. Di, F. Yang, Y. Cao, F. Cheng, K. Zhang, Properties of binderless coal slime briquette via hydrothermal hot pressing dewatering, Energ. Source Part A 39 (2017) 1222-1227. https://doi.org/10.1080/15567036.2017.1318190.

[268] N. Yamasaki, Development of recycling technologies, and functional material formation by hydrothermal processes, J. Ceram. Soc. Jpn. 111 (2003) 709-715. https://doi.org/10.2109/jcersj.111.709.

[269] N. Yamasaki, Y. Yamasaki, K. Tohji, N. Tsuchiya, T. Hashida, K. Ioku, Hydrothermal dynamics on environmental problems using the aspect of earth science, J. Mater. Sci. 41 (2006) 1599-1604. https://doi.org/10.1007/s10853-006-4654-8.

[270] A. Ndayishimiye, M.Y. Sengul, S.H. Bang, K. Tsuji, K. Takashima, T.H. de Beauvoir, D. Denux, J.-M. Thibaud, A.C.T. van Duin, C. Elissalde, G. Goglio, C.A. Randall, Comparing Hydrothermal Sintering and Cold Sintering Process: Mechanisms, Microstructure, Kinetics and Chemistry, J. Eur. Ceram. Soc. (2019). https://doi.org/10.1016/j.jeurceramsoc.2019.11.049.

[271] T. Ibn-Mohammed, C.A. Randall, K. Mustapha, J. Guo, J. Walker, S. Berbano, S. Koh, D. Wang, D. Sinclair, I. Reaney, Decarbonising ceramic manufacturing: a techno-economic analysis of energy efficient sintering technologies in the functional materials sector, J. Eur. Ceram. Soc. 39 (2019) 5213-5235. https://doi.org/10.1016/j.jeurceramsoc.2019.08.011.

[272] M. Biesuz, G. Taveri, A.I. Duff, E. Olevsky, D. Zhu, C. Hu, S. Grasso, A theoretical analysis of cold sintering, Adv. Appl. Ceram. (2019) 1-15. 10.1080/17436753.2019.1692173.

[273] S. Grasso, M. Biesuz, L. Zoli, G. Taveri, A.I. Duff, D. Ke, A. Jiang, M.J. Reece, A review of cold sintering processes, Adv. Appl. Ceram. (2020) 1-29. https://doi.org/10.1080/17436753.2019.1706825.

CHAPTER 3

COLD SINTERING OF SODA-LIME GLASS

The following chapter is published in Scr. Mater. 192, 111-114. (Reproduced from [24] with permission from Elsevier).

Abstract

Ordinary recycled soda lime glass powder was densified via cold sintering process with the aid of concentrated NaOH solution. Increase in processing time, temperature and concentration of the NaOH solution resulted in the formation of monolithic glass artifacts with higher relative densities. The sample densified the most (95.2%) was obtained when the sintering was performed at 250°C with a 20 mins dwell time using 15 M NaOH solution.

In recent years, sintering strategies such as cold sintering process (CSP), hydrothermal hot pressing (HHP), and reactive hydrothermal liquid-phase densification (rHLPD) that enable the densification of ceramics at low temperatures, roughly speaking below 500 °C, broadly called as cold sintering techniques, have been proposed [1-3]. While there are several studies related with the processing of ceramic components, the works related with the densification of glass artifacts at low temperatures are only limited by the HHP technique [1, 4] or to silica [5-8]. For example high level radioactive waste were immobilized in the glass bodies via HHP, and the formed artifacts demonstrated low radioactive element leachability [9]. Nevertheless, for HHP a specially designed apparatus is needed while CSP can be conducted by using ordinary presses, and as far as the authors aware, there has been no report on the CSP of the glasses. Accordingly, in this

work, the densification of recycled soda lime glass powder via CSP was investigated for the first time.

Soda lime recycled glass with a density of 2.51 g/cm^3 was initially ground and sieved to a particle size smaller than 25 μm and used without further processing for consolidation. The main chemical composition of the powder by weight was SiO_2 (71.59 %), Al_2O_3 (1.23 %), CaO (8.73 %), MgO (4.17 %), Na_2O (13.63 %), and the others (0.65 %). NaOH solutions having different concentration (5-15 M) were prepared as aqueous stock solution to aid cold sintering. In the process, 0.4 g glass powder was mixed with 20 wt% (relative to glass) NaOH solution, put into a cylindrical die and pressed under a pressure of 250 MPa. During pressing, the mold was heated from room temperature (RT) with a heating rate of 10°C/min up to processing temperature (from 125°C to 250°C) and held at the peak temperature for varying times ranging from 1 min to 1 h, followed by drying at 80°C for 24 h to remove the residual moisture.

The bulk densities were calculated via Archimedes' method using ethanol as the infiltrating medium from three different representative specimens for each glass, and the mean relative density values were given with standard deviations. The data for all samples were verified with ones obtained from geometric density measurements, and less than 2.6% difference, due probably to the experimental measurement error, were observed. X-ray diffraction (XRD) measurements were done using a Philips X'Pert Pro (Eindhoven, The Netherlands) with CuK_α

radiation. Fourier Transform Infrared (FTIR) spectra (PerkinElmer, Inc. Spectrum 100, UATR Two, Waltham, MA, USA) was recorded from 400 to 4000 cm^{-1} with 20 scans in transmission mode. Samples were ground, dried and mixed with potassium bromide (KBr) in 1:100 ratio by weight, and then pressed into a pellet form for FTIR test. The fracture morphologies were analyzed by using a scanning electron microscope (SEM, FEI, Quanta 250 FEG, Hillsboro, Oregon, USA) with a 5 nm Au coating.

The FTIR spectra of the recycled powder and the cold sintered samples are given in **Fig. 3.1(a)**. The spectra of the non-treated recycled glass (as is) shows two major bands; broad one in between ~ 850 - 1310 cm^{-1} peaking at 1050 cm^{-1}, and another one is centered at around 475 cm^{-1} attributed to Si-O-Si vibration and bending, respectively [10, 11]. In addition, a band at ~3500 cm^{-1} indicating the presence of hydroxyl groups [12], i.e. Si-OH (note that concentrated NaOH solution was used to aid densification during cold sintering) develops in the cold sintered bodies. The sharp peak located at 1385 cm^{-1} was

also observed in the spectra. Although there are works in which the bands in between 1270 - 1390 cm^{-1} were associated with non-bridging oxygens (NBOs) [13], further studies are required to be certain here.

It is important to note that for the monolithic samples prepared via cold sintering, the bands associated with Si-O-Si shifted to lower wavenumbers (especially the one around 475 cm^{-1} moving to ~ 410 cm^{-1}). Certainly, further studies are required to establish the exact mechanism causing such result, yet we still can speculate. The shift might be correlated with depolymerization caused by the sodium ions originating from NaOH solution[14]. It was shown for soda lime glasses that the Si-O-Si band around 1050 cm^{-1} was very sensitive to structural changes and increasing the non-bridging oxygen (NBO) content could result in the IR shift. Such a matter seems to be the case here that with the increase in processing pressure, temperature and especially the NaOH concentration, the amount of NBO was enhanced (assuming no other contributions, and all Na+ is exchanged into the glass structure, then the NBO fraction is calculated to increase from 0.241 with no additive to 0.246 at 5M and 0.254 at 15M for the cold sintered specimens, calculations done based on the starting glass composition and change in the NaOH density within 5-15 M [3]), and thus the formation of a probable gel aided sintering. A similar slight shift of the broad band to higher 2θ angles can be seen from the differences in between the XRD patterns (**Fig. 3.1(b)**) of the raw powder and cold sintered glass bodies. There are no measurable crystalline phases, suggesting that the samples maintained their amorphous state after CSP at all processing conditions studied.

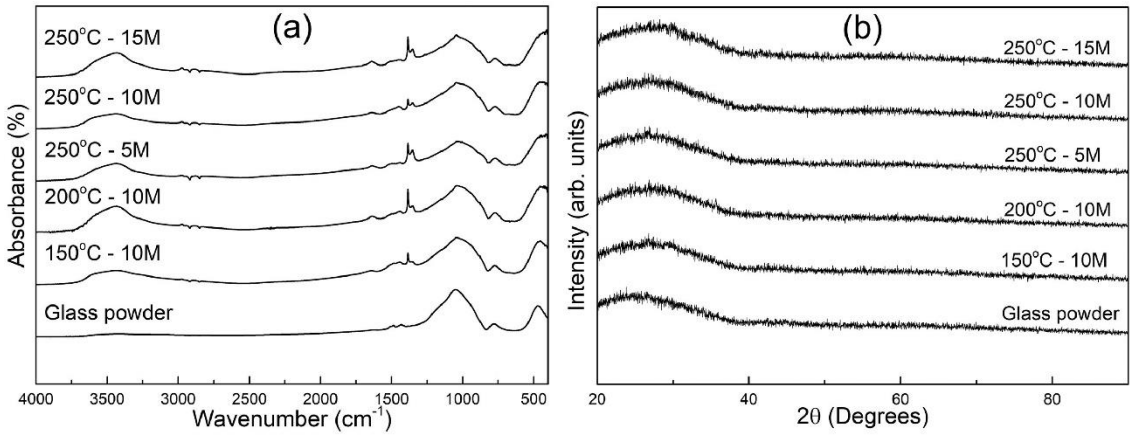

Figure 3.1. Normalized; (a) FTIR absorption spectra; and (b) X-ray diffraction patterns of the used raw glass powder and cold sintered glass monoliths prepared at 250 MPa for 20 mins with varying NaOH concentrations and sintering temperatures.

Figure 3.2 shows the microstructures obtained from the fracture surfaces of cold-sintered glass monoliths (including as is recycled glass powder) produced at different cold sintering temperatures. Loose glass particles (< 25 μm) shown in **Fig. 3.2(a)** were transformed into coherent bodies with very low amount of porosity at higher processing temperatures (> 200°C), i.e. well sintered, relatively dense components were formed (**Figs. 3.2(b-d)**). In addition, variations in the morphological features of the fracture surfaces suggest that when the cold sintering temperature was increased, enhanced particle bonding was established in the consolidated samples.

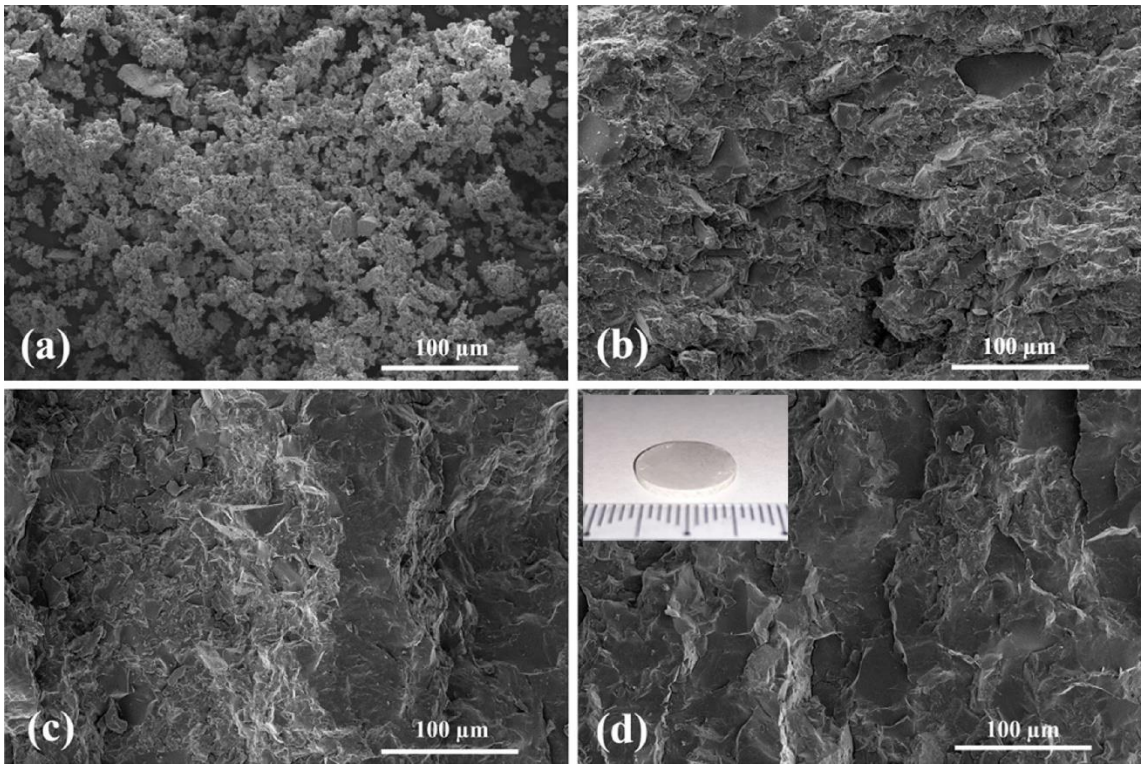

Figure 3.2. SEM images of the; (a) used recycled glass powder, and cold sintered glasses produced by using 10 M aqueous NaOH solution with a dwell time of 20 min at; (b) 150°C, (c) 200°C; (d) 250°C, and the top-left inset shows the tablet obtained at this temperature via CSP.

The densities of cold-sintered glass monoliths produced under different processing conditions are given in **Table 3.1**. As can be seen the relative density of cold sintered glass components was enhanced with increasing processing temperature. While the sample prepared at 125°C demonstrated the lowest value reaching to 89.6%, relative density of 94.7% with no observable delamination or warpage was obtained from the process conducted at 250°C (10 M, 20 mins).

The monolithic samples (see the inset in **Fig. 3.2(d)**) were not transparent (note that as-received transparent glass parts became opaque after ball-milling) akin to spark plasma sintering (SPS) studies on soda lime glass in which it was reported that transparent body was achieved only when the sample had a relative density ≥ 99% [15]. It is known that smaller particle size (especially high surface area nano scale) is usually needed to obtain highly dense monolithic bodies by CSP. That is to say; finer (especially submicron

size) glass powder and higher application temperatures/pressures that could not be conducted due to instrumental limitations might be appropriate to obtain a transparent final product.

Table 3.1. Process conditions and observed relative density values (mean average ± standard deviation) of cold-sintered glasses.

Process Conditions	Relative Density, ρ (%)
150˚C, 10 M, t=20 min	91.8 ± 0.5
200˚C, 10 M, t=20 min	92.8 ± 1.7
250˚C, 5 M, t=20 min	92.4 ± 0.8
250˚C, 10 M, t=20 min	94.3 ± 0.6
250˚C, 15 M, t=20 min	95.2 ± 0.4

Murray's equation (**Eq. 3.1**, where ρ is relative density, σ is pressure (Pa), η is viscosity (Pa.s), and t is time (s)) has been used to analyze the effect of pressure during sintering for pressure-assisted sintering techniques[16] such as hot pressing [17, 18] and HHP [9, 19, 20]. The slope of the *ln(1-ρ) vs t* is followed to estimate the viscosity for a given temperature.

$$\ln(1-\rho) = -\left(\frac{3\sigma}{4\eta}\right)t + c \tag{3.1}$$

The linear relationship found in **Fig. 3.3(a)** provides the viscosity of glass compact during densification (up to 20 mins) which was around $5.7\text{x}10^{11}$ Pa.s at 250°C, and slightly higher values were found for the lower processing temperatures. The calculated values are similar to those found for densification of borosilicate glass via HHP[19], and somewhat higher than that of Kuzcynzki's data for the viscous flow of glass sintering with a similar chemical composition [21].

The relative density of glass compacts cold-sintered for only 1 min dwell at 250 °C (10 M) was 91.2%. As the holding time increased from 1 min to 20 mins then to 1 h, the relative density was enhanced first to 94.7% and then slightly more to 94.8%. That is

to say, a rapid densification was observed at the beginning of the process, similar to borosilicate glass monoliths produced by HHP [19, 22]. Comparable densification effect was observed with the increase in the NaOH concentration of the aqueous solution. Going from 5 M to 15 M, the relative density was improved from 92.4% to 95.2% (at 250°C for 20 min). Nishioka et.al.[19] reported that the activation energy required for densification of borosilicate glass powder by HHP decreases with increasing normality of the NaOH in the liquid phase. High concentration of NaOH is considered to improve dissolution and thereby assist the densification process. Furthermore, it was shown that increasing the processing temperature decreased the activation energy for densification as well[9].

Murray`s model was followed without considering the network depolymerization for densification of the glass powders in the first 20 mins of the process to provide an approximate model, and as seen from **Fig. 3.3(b)** linear dependence ($R^2 = 0.9871$) of the calculated viscosities to temperature was found with corresponding 16 kJ/mol of activation energy. However, the calculated value may not be strictly related to the activation of the viscous flow but more to a complex state in which for instance different degrees of network depolymerization occurs. This is probably why; it is lower than that of the ones observed for the densification of glass via HHP performed under milder conditions (e.g. generally < 5 M) suggesting the strong contribution of elevated NaOH amount on the activation energy reduction.

Accordingly, it is highly possible to assume that the selected processing conditions (pressure, temperature and especially such highly caustic conditions causing alkaline metal catalysis) enhanced the dissolution of the particle contacts resulting in the formation of a gel which under stress aided a porosity reduction via viscous flow, akin HHP studies on glass[19] However, additional theoretical and experimental work is certainly necessary to fully understand the exact densification mechanism. As it is known, the equipment used for cold sintering is basically considered as a partially open system whereas HHP apparatus is a closed chamber to maintain the hydrothermal conditions affecting the densification rate. Still, both processes give similar densification trends and offer analogous mechano-chemical contributions [1, 23].

Comparable systems may be found in geology linked densification works [24], and somehow different than what has been postulated for the cold sintering of ceramic powders in which the chemical reaction during sintering is barely considered to assist densification. Generally, an initial packing to produce a green pellet is followed by cold

sintering (pack then sinter) process, instead here similar to cementitious materials (e.g. via geopolymerization), glass particles were actively reacted with aqueous solution while packing (i.e. pack while sinter).

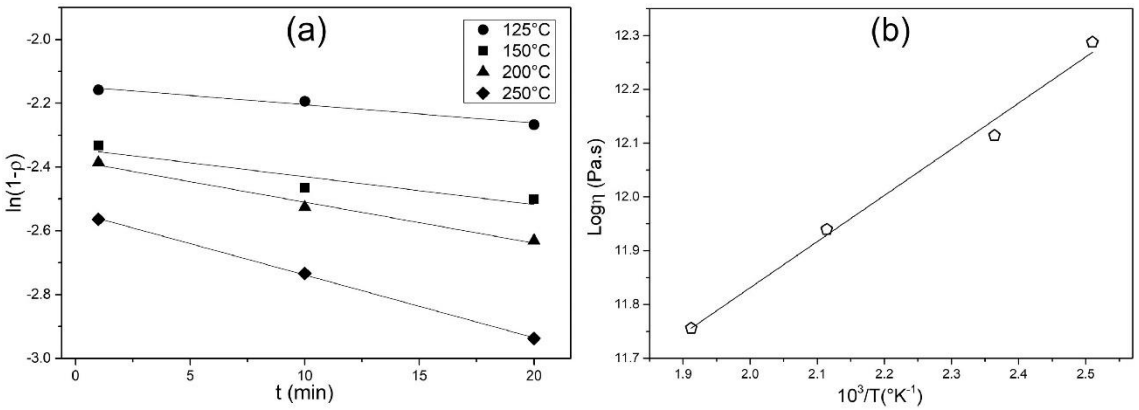

Figure 3.3. (a) The relation between ln(1-ρ) vs t (min) from 125˚C to 250˚C for 10M/250 MPa according to Murray's rate analysis, each data point represents the mean average value from three different measurements; (b) Viscosity values extracted from the Murray`s model.

It should be underlined that although it has not been frequently mentioned[25], the dies used for pressing in the CSP (generally made from working steel), wears after repeated use especially under such caustic conditions. Alternatively, it may still be possible to obtain monolithic dense glass bodies only by using distilled water but at a slightly higher sintering temperatures[19]. The proposed one-pot method can be used to produce various types of dense glass components and may address environmental problems such as immobilization of radioactive materials, heavy metals, recycling toxic and hazardous wastes.

As a summary, one-pot reactive cold sintering process that does not demand initial raw material packing was investigated, and for the first time, an ordinary recycled soda lime glass powder was densified by using NaOH aqueous phase resulting in high relative densities reaching above 90%. The increase of liquid phase concentration (from 5 M to 15 M), processing time and temperature (from 125 to 250 °C) caused an increase in the

final relative densities. The highest relative density (95.2 %) was obtained from the sample treated at 250 °C with a dwell time of 20 min using 15 M NaOH solution.

References

[1] C. Vakifahmetoglu, L. Karacasulu, Curr. Opin. Solid State Mater. Sci. 24(1) (2020) 100807.

[2] C. Vakifahmetoglu, J.F. Anger, V. Atakan, S. Quinn, S. Gupta, Q. Li, L. Tang, R.E. Riman, J. Am.Ceram. Soc. 99(12) (2016) 3893-3901.

[3] L. Karacasulu, M. Tokkan, M. Bortolotti, G. Ischia, U. Adem, C. Vakifahmetoglu, Ceram. Int. 46(10) (2020) 16670-16676.

[4] S. Grasso, M. Biesuz, L. Zoli, G. Taveri, A.I. Duff, D. Ke, A. Jiang, M.J. Reece, Adv. Appl. Ceram.119(3) (2020) 115-143.

[5] D. Ke, A. Jiang, M. Biesuz, M. Bortolotti, G. Taveri, X. Wang, M. Xu, J. Li, Y. Feng, C. Hu, S. Grasso, J.Eur. Ceram. Soc. 39(16) (2019) 5358-5363.

[6] A. Ndayishimiye, A. Largeteau, M. Prakasam, S. Pechev, M.-A. Dourges, G. Goglio, Scripta Mater.145 (2018) 118-121.

[7] G. Taveri, S. Grasso, F. Gucci, J. Toušek, I. Dlouhy, Adv. Funct. Mater. 28(48) (2018) 1805794.

[8] A. Ndayishimiye, A. Largeteau, S. Mornet, M. Duttine, M.-A. Dourges, D. Denux, M. Verdier, M.Gouné, T. Hérisson de Beauvoir, C. Elissalde, G. Goglio, J. Eur. Ceram. Soc. 38(4) (2018) 1860-1870.

[9] M. Nishioka, S. Hirai, K. Yanagisawa, N. Yamasaki, J. Am. Ceram. Soc. 73(2) (1990) 317-322.

[10] Y.-K. Lee, Y.L. Peng, M. Tomozawa, J. Non. Cryst. Solids 222 (1997) 125-130.

[11] J. Osswald, K. Fehr, J. Mater. Sci. 41(5) (2006) 1335-1339.

[12] A. Bandyopadhyai, R. Jabra, J. Phalippou, J. Mater. Sci. Lett. 8(12) (1989) 1464-1467.

[13] R. Kaur, S. Singh, O.P. Pandey, Physica B: Condens. Matter. 407(24) (2012) 4765-4769.

[14] M. Szumera, Spectrochim. Acta A: Mol. Biomol. Spectrosc. 130 (2014) 1-6.

[15] L. Ramond, G. Bernard-Granger, A. Addad, C. Guizard, J. Am. Ceram. Soc. 94(9) (2011) 2926-2932.

[16] P. Murray, E. Rodgers, A. Williams,Trans. Brit. Ceram. Soc., 53 (1954), 474-510.

[17] V. Günay, Ceram. Int. 23(4) (1997) 291-296.

[18] M. Decottignies, J. Phalippou, J. Zarzycki, J. Mater. Sci. 13(12) (1978) 2605-2618.

[19] M. Nishioka, K. Yanagisawa, N. Yamasaki, in: S. Sōmiya (Ed.), Hydrothermal Reactions for Materials Science and Engineering: An Overview of Research in Japan, Springer Netherlands, Dordrecht, (1989), 417-422.

[20] K. Yanagisawa, M. Nishioka, N. Yamasaki, J. Mater. Sci. 24(11) (1989) 4052-4056.

[21] G. Kuczynski, J. Appl. Phys. 20(12) (1949) 1160-1163.

[22] N. Yamasaki, A. Shirakawa, N. Hirano, T. Hashida, J. Mater. Sci. Lett. 21(9) (2002) 711-713.

[23] A. Ndayishimiye, M.Y. Sengul, S.H. Bang, K. Tsuji, K. Takashima, T. Hérisson de Beauvoir, D. Denux, J.-M. Thibaud, A.C.T. van Duin, C. Elissalde, G. Goglio, C.A. Randall, J. Eur. Ceram. Soc. 40(4) (2020) 1312-1324.

[24] E. Gundersen, F. Renard, D.K. Dysthe, K. Bjørlykke, B. Jamtveit, J. Geophys. Res. Solid Earth 107(B11) (2002) ECV 19-1-ECV 19-19.

[25] M. Biesuz, G. Taveri, A.I. Duff, E. Olevsky, D. Zhu, C. Hu, S. Grasso, Adv. Appl. Ceram. 119(2)(2020) 75-89.

CHAPTER 4

COLD SINTERING AS A PROMISING ISRU TECHNIQUE: A CASE STUDY OF MARS REGOLITH SIMULANT

The following chapter is published in Icarus. 389 (2023) 115270 (Reproduced from [94] with permission from Elsevier).

Abstract

Mars regolith simulant (MGS-1) was densified for the first time via a cold sintering process (CSP) as a novel in-situ resource utilization (ISRU) concept. The technique comprises the utilization of NaOH solution as a liquid media during the densification of simulant powder with < 100 μm particle size. In as short as 30 min, with the increase in the NaOH concentration (from 3 M to 10 M) and processing temperature (from 150°C to 250°C), the relative densities of the regolith compacts and the mechanical properties were enhanced. The artifacts produced with Mars regolith simulant powder at 250°C using 10 M NaOH solution yielded a relative density of around 88% and compressive strength reaching ~ 45 MPa.

4.1. Introduction

Increasing human space exploration capabilities require appropriate use of the available resources for a sustainable life outside our planet. Therefore, materials found in space deserve particular attention (Alexiadis et al., 2017; Cesaretti et al., 2014). In this sense, the in-situ resource utilization (ISRU) concept aims for on-site collection and

storage, processing, and use of indigenous materials encountered during space exploration (human or robotic) so that related risks, mass, and costs can be reduced (Sacksteder and Sanders, 2007).

One important ISRU research field is the study of different bonding concepts to directly process the local surface minerals covering planetary bodies called regolith into solid structures in situ. Starting in the Apollo Era, a wide array of works on the different approaches to bond regolith has been produced, which have been discussed in various reviews focusing on regolith bonding for the Moon and Mars in conjunction (Happel, 1993; Lim et al., 2017; Naser, 2019). Some of these works include dry consolidation (Chow et al., 2017; Meek et al., 1987; Simonds, 1973), melting (Blacic, 1985; Dalton and Hohmann, 1972; Zocca et al., 2020), geopolymerization (Alexiadis et al., 2017; Montes et al., 2015), self-propagating high-temperature synthesis (Corrias et al., 2012), slip casting (Karl et al., 2018), additive manufacturing, including solar sintering (Fateri et al., 2019; Meurisse et al., 2018), material extrusion (robocasting) and layer-wise slurry deposition (LSD) (Karl et al., 2020a, 2020b) as well as vat polymerization (VP) technique called lithography-based ceramic manufacturing (LCM) (Altun et al., 2021) were proposed using various regolith simulants.

In a recent review focusing on Martian regolith, the authors proposed categorizing different consolidation techniques, such as sintering, melting, freezing, etc., and discussed the merits of the individual approach in detail for ISRU on Mars (Karl et al., 2022). This classification was used in an overview of the currently available mechanical property data for regolith consolidation concepts using Martian regolith simulants (reproduced in **Fig. 4.1**), evaluating how much of the final structure would be made from directly accessible proven surface minerals on the Mars surface. It is of note that **Fig. 4.1** does not cover the relative density of the compacts and does not consider the required energy or the complexity of implementing applications; these characteristics are expected to be firmly in favor of the cold sintering process (CSP).

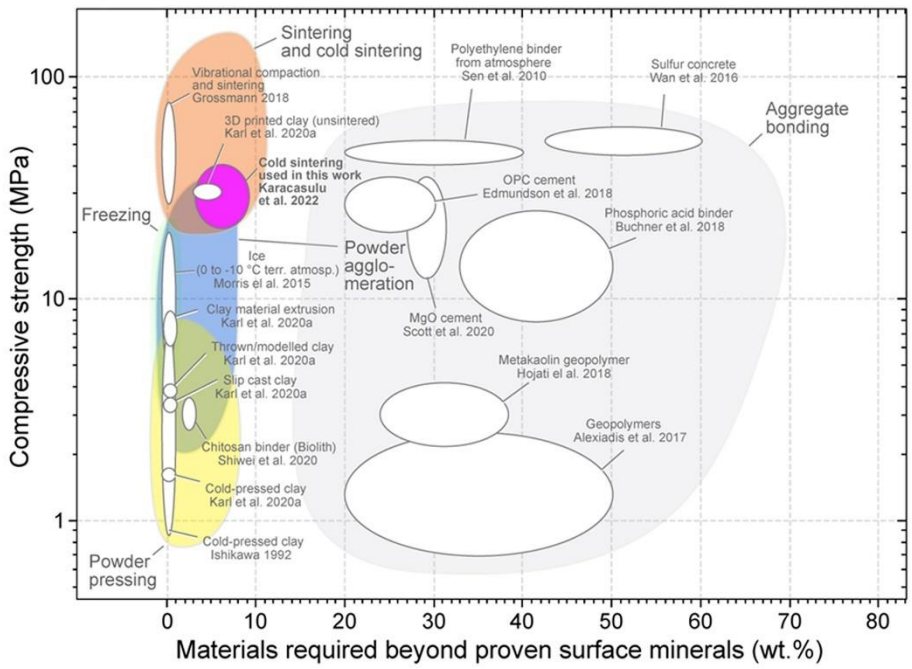

Figure 4.1. Review of compressive strength over materials required additionally on the surface of Mars (besides directly accessible proven surface minerals on Mars) of all studies using Martian regolith simulants. Image reworked with open access permission (CC-BY). For the detailed bibliographic citations of the referenced articles, see also (Karl et al., 2022).

An essential consideration for all ISRU regolith consolidation concepts is the power needed for processing. Some of the processes mentioned above are highly energy-intensive, and novel ISRU approaches with lower power consumption are required. Comparing different consolidation techniques to manufacture components, it is possible to state that the cold sintering process (CSP) may be credited with one requiring the least amount of energy. An example is Barium Titanate, for which the energy consumption decreased from 2800 kJ/g for conventional consolidation techniques (solid-state sintering requiring furnace heating) to below 50 kJ/g for CSP (Sohrabi Baba Heidary et al., 2018). Despite that, it is to be noted that CSP has not been reported for any ISRU research work so far.

CSP can be defined as a technique to produce strong and dense inorganic solids (i.e., ceramics, glasses) at low temperatures <~ 250°C, without the application of high temperatures so as not to require a specific high temperate furnace, and commonly

assisted by an externally applied pressure even via an ordinary press (Galotta and Sglavo, 2021; Sohrabi Baba Heidary et al., 2018; Vakifahmetoglu and Karacasulu, 2020). Parts made by CSP resemble those obtained via reactive hydrothermal liquid-phase densification, liquid phase sintering, and hot pressing due to a solvent/liquid phase with the application of heat and/or pressure (Galotta et al., 2021; Karacasulu et al., 2020; Vakifahmetoglu and Karacasulu, 2020).

Because of its relatively low energy demands compared to traditional high-temperature consolidation techniques, simplicity, and minimum equipment requirements, CSP could be an ideal candidate for ISRU in remote locations for obtaining construction materials such as stone-like blocks, bricks, facades, etc. Accordingly, the main goal of the present study was to demonstrate proof of concept to obtain Mars regolith (MGS-1) simulant monoliths at low temperatures (≤ 250°C) and under relatively low pressures via CSP for the first time. During the study, the effect of sodium hydroxide concentration and processing temperature was deliberately altered to obtain monoliths with high relative density and compressive strength that is comparable to or higher than those prepared by other ISRU consolidation techniques and general-purpose concrete.

4.2. Materials and methods

Martian regolith simulant (MGS-1) was developed as one of the standard simulant materials by Cannon et al. (Cannon et al., 2019). It is based on Mars Science Laboratory (MSL) rover Curiosity's XRD results at Rocknest aeolian bedform. It was representative of global basaltic soil at the Gale crater on Mars (Bish et al., 2013), supplied by Exolith Lab (CLASS/UCF, Orlando, USA). The main chemical composition of the Martian regolith simulant by weight was SiO_2 (44.36 %), Al_2O_3 (12.71 %), FeO (11.90%), MnO (0.1%), MgO (13.84%), CaO (7.36 %), Na_2O (1.65 %), K_2O (0.46%), TiO_2 (0.39%), P_2O_5 (0.11%), Cr_2O_3 (0.13%), and the LOI (5.53 %) (Karl et al., 2020a).

As-delivered MGS-1 powder from a batch received in 2019 was ground in a vibratory disc mill TS250 (Siebtechnik GmbH, Germany) using a chrome steel milling vessel. The 8 min milling was performed in four 2 min process intervals with 2 min cooling intervals to avoid changes in particle characteristics owing to the heat, followed by sieving below 250 μm.

True density was obtained using five repetitions using a helium gas expansion multivolume pycnometer 1305 (Micromeritics Instrument Corp., USA) of dried powders (105°C for 72 h under vacuum). Particle size distributions (PSD) were measured by dispersing powder particles in DI-water using a wet cell of an LS 13 320 (Beckman Coulter, USA) laser diffraction particle size analyzer.

Aqueous 3 and 10 M NaOH (1310-73-2, 98-100.5%, Sigma Aldrich, USA) solutions were used to aid during CSP. To obtain a monolithic body, 1.2 g milled MGS-1 regolith powder was mixed with 0.4 g NaOH solution (separately prepared to be either 3 M (using ~3.4wt% NaOH in the dry mixture) or 10 M (~9.1wt% NaOH in the dry mixture)) using a pestle and mortar for 5 min. The prepared paste was immediately transferred into a cylindrical die (Ø = 12.7 mm) and pressed uniaxially using a hydraulic press initially under a pressure of 50 MPa and held for 15 min., then under a pressure of 400 MPa. During the second pressing step under a pressure of 400 MPa, the mold was heated using a heating jacket wrapped around the die up to processing temperature (from 150 °C to 250 °C) with a heating rate of 10 °C/min for 30 min. Finally, the cold-sintered samples were dried at 80 °C in the convection oven (Memmert, UN55, France).

The bulk densities of the specimens were calculated via Archimedes' principle using ethanol as the buoyant medium by using three different representative examples for each sample. Powder-X-ray diffraction patterns were collected in a reflection mode with the X'Pert PRO (Panalytical, the Netherlands) operated at 40 kV and 30 mA using $Cu_{K\alpha}$ at 1.5406 Å. The morphology of the used MGS-1 simulant powder, fracture, and polished surfaces of cold sintered specimens (sputter-coated using gold) were analyzed by Scanning Electron Microscopy (SEM, FEI Quanta 250 FEG, USA). The cold crushing strength (CCS) properties were determined using a TA.XT Plus Texture Analyzer (Stable Micro System Ltd., Godalming, Surrey, UK). Each data set was obtained from cut, and polished cubic-shaped samples (~ 2.5 x 2.5 x 2.5 mm^3) prepared from cold sintered disc specimens using IsoMet™ low-speed precision cutter (Buehler, Lake Bluff, IL, USA) and the strength was calculated from the first collapse point. Dissolution tests were conducted on the blend prepared using the same amount of milled MGS-1 powder and NaOH solution used for CSP (3 M and 10 M) upon ultrasonication in polypropylene falcon tubes for 1 min. The solutions were left to stand at room temperature (RT) for 1 h, close to the total interaction time in CSP. Dissolved species were extracted into the DI-water in a 50 ml solution. The suspensions were sonicated for 10 min, then centrifuged at

6000 rpm for 15 min to obtain the supernatant. The cation concentration was analyzed by an inductively coupled plasma-optical emission spectrometer (ICP-OES, Agilent 5110 Dual View, Australia).

4.3. Results and Discussion

Figure 4.2(a&b) demonstrates the characteristics of MGS-1 regolith simulants used for CSP. In **Fig. 4.2(a),** the micrograph shows the broad particle size range, and the top-right inset info demonstrates the compositional constituents of the MGS-1 regolith simulants (Karl et al., 2020a). The as-delivered and milled MGS-1 powder particle size data demonstrates a multimodal distribution, as given in **Fig. 4.2(b)**. Dry milling reduced the average particle size, as clearly seen in the median particle size values (d_{50}). The true density of the used MGS-1 powder was found as 3.041 g/cm^3 by using a helium pycnometer.

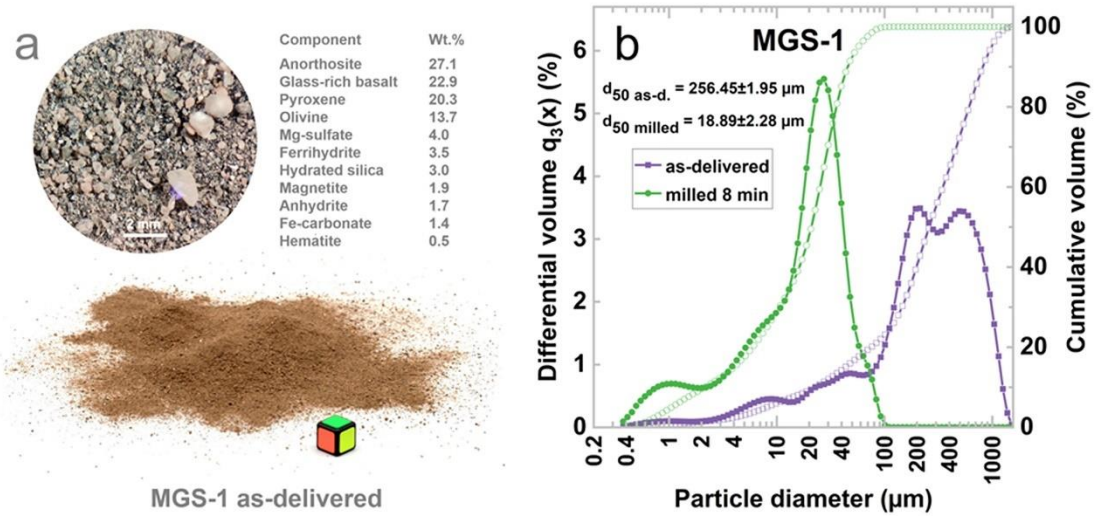

Figure 4.2. Characteristics of MGS-1 regolith simulant, (a) micrograph and composition of the as-delivered MGS-1, (b) particle size distribution of as-received and milled MGS-1 powders.

The processing diagram shown in **Fig. 4.3(a)** reveals that the total cold sintering process takes only around 1 h to be completed. The digital photo images of the pellets obtained using CSP at 250 °C are also given in the figure. While samples produced using 3 M were light brown, when the strength of the solution was increased, darker tablets were formed. In **Fig. 4.3(b)**, relative densities of MGS-1 regolith compacts were given after cold sintering (under different NaOH concentrations and processing temperatures). The densification of compacts was enhanced by increasing the processing temperature and NaOH concentration, and the effect of the latter was more substantial. The highest relative density of cold sintered regolith compacts prepared with 10 M solution at 250°C yielded around 88%. It is worth mentioning that when DI-water was used alone, instead of NaOH solution as a liquid medium, a relative density reaching only around 80% was obtained under the same CSP conditions (250°C & 400 MPa), but the mechanical integrity of the samples was not as before.

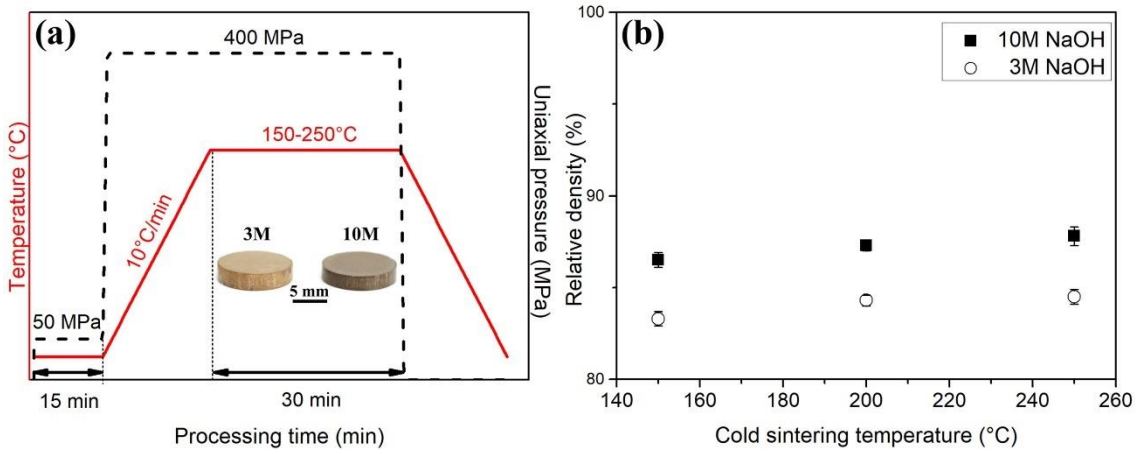

Figure 4.3. (a) Processing diagram showing time, temperature, and pressure alterations during CSP of MGS-1 regolith simulant. The inset under the temperature curve demonstrates the digital photo images of the pellets obtained using CSP at 250 °C, (b) the observed relative densities of MGS-1 regolith compacts after cold sintering (under different NaOH concentrations and processing temperatures) were given together with standard deviation values.

Figure 4.4 shows the X-ray diffraction data obtained from the entire set of samples, including the used MGS-1 regolith simulant powder. Crystalline phases associated with the members of the plagioclase family, the pyroxene group, hematite, siderite (Fe-carbonate), olivine, and forsterite were able to be assigned, parallel to the detailed synchrotron XRD studies of the same MGS-1 simulant powder (Karl et al., 2020a). All samples formed via CSP exhibited a similarly high number of diffractions, corresponding to the pattern obtained from the initial raw material having different crystalline constituents (see **Fig. 4.2(a)**). Within the detection limits of XRD, this implies that the selected processing conditions did not induce pronounced alterations during the densification of MGS-1 powder in cold sintering (Galotta et al., 2021). It can be seen from the normalized XRD plots that the average intensity of the most intense peaks was higher with increasing sintering temperature, probably because crystallization was favored under such reaction conditions. In contrast, the peak intensity decreased with NaOH concentration increase, perhaps due to enhanced dissolution events, similar to other cold sintering studies using NaOH solution (Grady et al., 2020; Lowum et al., 2020).

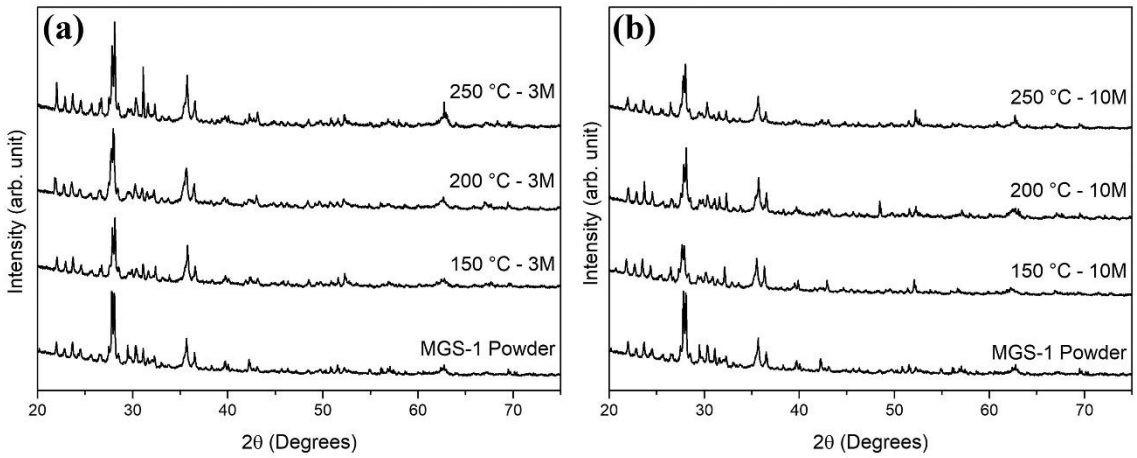

Figure 4.4. X-ray diffraction patterns of MGS-1 powder and cold sintered MGS-1 regolith compacts; (a) produced samples using 3 M NaOH, (b) produced samples using 10 M NaOH.

Figure 4.5(a-f) shows the micrographs obtained from the fracture surfaces of MGS-1 pellets processed at different cold sintering temperatures and NaOH

concentrations. Samples made by using low solution concentration and sintering temperature (3 M and 150°C) were found to have large fracture sites (cavities), see **Fig. 4.5(a)**; the increase of both process parameters resulted in a denser microstructure consisting of web-like forms between small-sized particulates (see the inset in **Fig. 4.5(d)**). Analogous to previous works, the increased processing temperature enhanced the particle bonding in the monolithic structures, as shown in **Fig. 4.5(c&f)**. In other words, MGS-1 simulant powder was transformed into well-consolidated monolithic bodies having low total porosity via CSP, corroborating the relative density data given in **Fig. 4.3(b).**

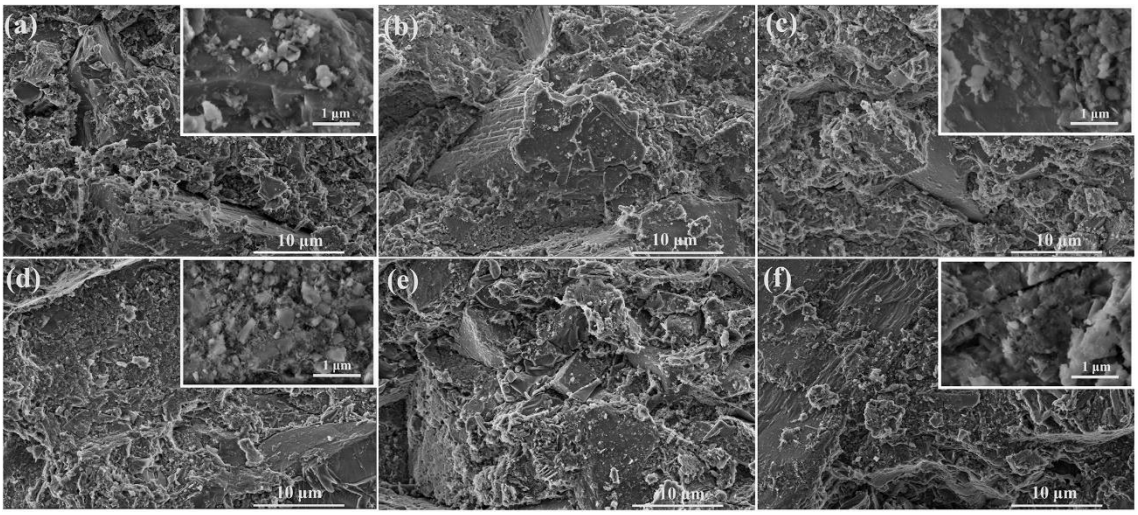

Figure 4.5. SEM images of cold-sintered MGS-1 regolith compacts produced at 400 MPa for 30 min under 3 M and at: (a) 150°C, (b) 200°C, (c) 250°C, and under 10 M and at: (d) 150°C, (e) 200°C, (f) 250°C (the top right insets taken from the higher magnifications).

In addition to fracture surface analysis via SEM, backscattered images obtained from the epoxy-embedded, polished samples are given in **Fig. 4.6(a-f)**. The obtained cold-sintered specimens were constituted by different-sized grains. For all samples, relatively dense morphology, including remarkably coarse grains approaching even 100 µm size [e.g., Si (grey), Fe (white)], were seen. While the improvement of densification (from the relatively fragile tablet to a monolith with high mechanical integrity, see later) with

increasing temperature was observed in the samples produced with 3 M, consolidation was apparently further enhanced when a 10 M solution was used.

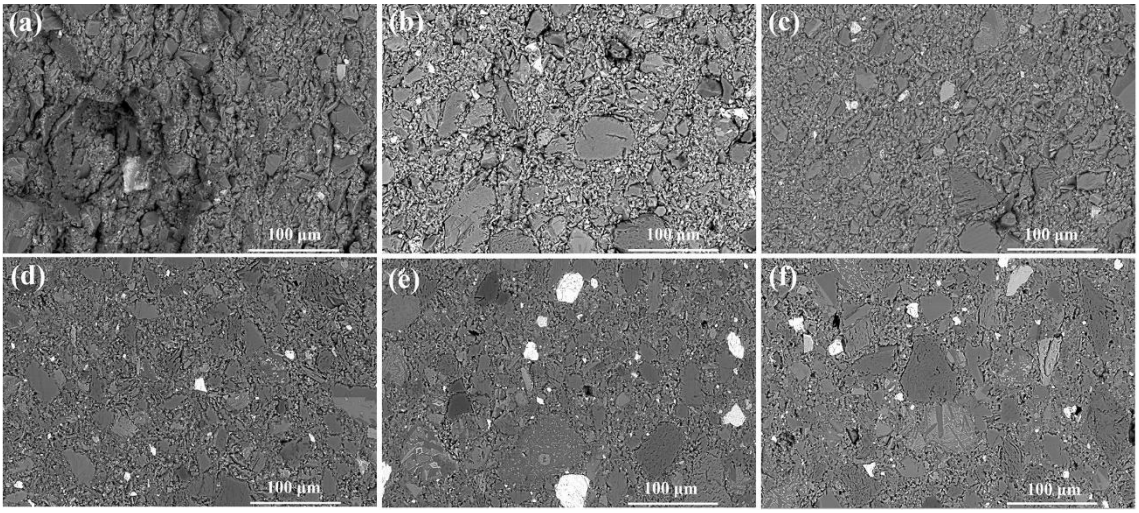

Figure 4.6. Backscatter images obtained from the epoxy mounted and polished cold sintered MGS-1 tablet surfaces produced at 400 MPa in 30 min, (a) 150°C-3 M, (b) 200°C-3 M, (c) 250°C-3 M, (d) 150°C-10 M, (e) 200°C-10 M, (f) 250°C-10 M.

Elemental mapping obtained from the MGS-1 pellet, which was cold sintered at 250°C with 10 M NaOH solution, is given in **Fig. 4.7**. Silicon, aluminum, iron, magnesium, calcium, oxygen, and sulfur (associated with magnesium sulfate) were seen on the mapping, resembling the chemical composition of the MGS-1 simulant. In addition, sodium can be observed in the entire microstructure due probably to sodium hydroxide, as with other specimens produced under different cold sintering temperatures and solution concentrations (data not shown for brevity). The large grains (marked by the white arrows in the image) probably belong to the olivine group, which was already noted by the XRD analysis.

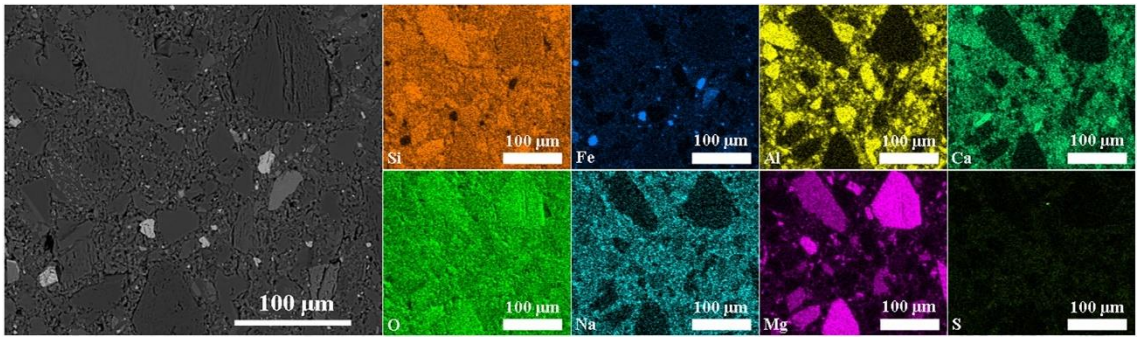

Figure 4.7. Elemental mapping of polished MGS-1 pellets cold sintered with 10 M NaOH solution at 250°C.

Since CSP was conducted in a closed chamber (a metal die), it is difficult to determine the dissolution products rigorously under different solution strengths. For this reason, dissolution tests were separately conducted to mimic, to a certain extent, the conditions present in situ, at least to get a perspective on elements that dissolve more and possibly assist densification. The results, based on the interaction between the powder and liquid phase in the CSP using ICP-OES, are given in **Table 4.1**. Elements such as Cr, Mn, and P, found in the main chemical composition of MGS-1 powder, were not detected in the extracted solution, probably due to the limited ability of the dissolution in an alkali medium. Instead, Al, Ca, Fe, Si, and Ti were observed, and they were higher in the samples prepared with 10 M NaOH solution than those made by using 3 M. Differently, Mg decreased with the increase in the NaOH concentration due probably to its higher solubility in acidic solutions (Sangwal, 1980).

The elements with the highest solubility were Ca, Si, and Al. Si was the most soluble in both NaOH levels, and it was determined that the solubility of Si increased by more than 30% as the solution concentration increased, presumably contributing to the densification via CSP. It is important to note that, for dissolution tests, the powder mixture with NaOH solution was always kept in polypropylene falcon tubes before analysis, i.e., there was no possibility of container-related contamination. Instead, the paste was prepared in a mortar for cold sintering practice, and even if it was transferred into the die promptly for cold sintering, there might still be some Si leaching.

Na ions in the liquid phase may aid depolymerization of the silica, forming Si-based complexes (e.g., SiO_4 and Si_2O_7 dimers), resulting in the formation of invert glass,

followed by higher ordering during CSP (Karacasulu et al., 2021; Kohara et al., 2004; Tognonvi et al., 2012). It is important to note that this data only estimates the elements that can be dissolved in a high alkaline environment at RT when simulant regolith was used, but it cannot accurately represent the actual cold sintering conditions because, for example, there is no pressure as in the case for CSP. Further theoretical and experimental work is required to establish the proper mechanism causing the regolith simulant densification observed here. However, it is possible to postulate that the selected processing conditions (highly caustic environment, temperature, and pressure) caused partial particle dissolution, assisting the formation of denser bodies under stress (Galotta et al., 2021).

Table 4.1. Dissolution data (mmol/L) The concentration of dissolved species (all in mg/L and mol/L) obtained from ICP-OES for the MGS-1 samples prepared with 3 M and 10 M NaOH solution.

Element	**3 M**		**10 M**	
	mmol/L	% dissolved	mmol/L	% dissolved
Al	0.055	0.092	0.226	0.378
Ca	0.110	0.350	0.190	0.604
Fe	0.003	0.007	0.008	0.021
Mg	0.009	0.011	0.007	0.008
Si	0.665	0.376	0.881	0.497
Ti	< 0.001	0.018	< 0.001	0.036

*Cr, Mn, and P were not detected.

Mechanical properties of the cold sintered components are the least investigated features, presumably because of the difficulties inherent in test sample preparation (Karacasulu et al., 2020; Liu et al., 2022, 2020; Vakifahmetoglu et al., 2016). The compressive (cold crushing) strength data of the selected cold sintered specimens are given in **Fig. 4.8**. It is important to note that all cold sintered samples demonstrated similar data only with an elastic deformation up to the fracture point, i.e., Hookean. The utilization of the NaOH solution enhanced the mechanical integrity of the samples that can ultimately be prepared for the cold crushing strength tests. As seen, while the strength

values of cold sintered MGS-1 regolith compacts were greater with increased relative density, the improvement was mainly benefited from the elevated NaOH solution concentration, indicating stronger bonding. Besides, all values had relatively high standard deviation, possibly because of the combination of factors including non-standard, moderately small sample size, errors during sample preparation (dimensional, surface finish), etc. The cold crushing strength of the monoliths obtained by using 3 M NaOH solution at 150°C was enhanced from ~21 MPa to 43 MPa when the solution strength and processing temperature were increased to 10 M and 250°C, respectively. These values are higher than those obtained from slip cast, high-temperature sintered regolith components, and general-purpose concrete (Karl et al., 2020a).

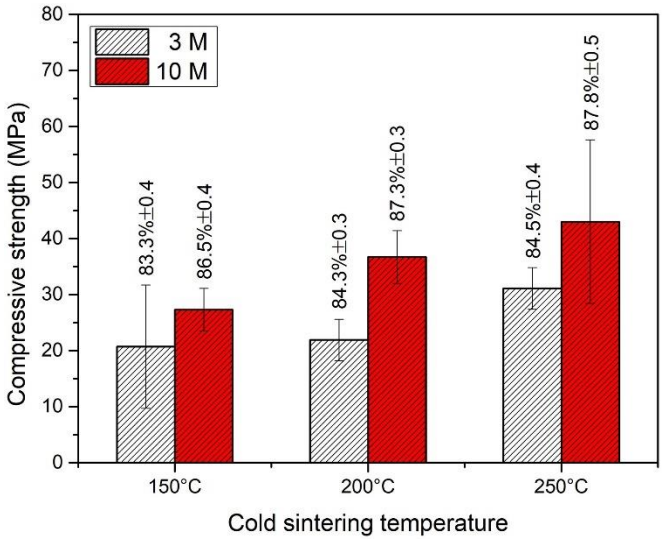

Figure 4.8. Cold crushing strength of cold sintered MGS-1 regolith compacts produced at different processing temperatures using NaOH solutions having 3 and 10 M. The numbers above the standard deviation lines represent the relative density of each sample set.

In some of the studies (see **Fig.1**) dealing with regolith simulants, monolithic components were formed without a heat treatment procedure, e.g., via extrusion-based robocasting, yielding a green body compressive strength of 7.6 MPa, higher than that of those made via traditional methods such as dry pressing, slip casting, and hand building, generally having a green body strength below 5 MPa (Karl et al., 2020a). When samples

with similar compositions were produced via geopolymerization (using up to 8 M NaOH), only a compressive strength of about 2.5 MPa was obtained, a much lower value than ordinary concrete (Alexiadis et al., 2017). Instead, high strength values were observed from the samples produced using smectite clay containing MGS-1C/8 regolith (5 wt.% clay) via layer-wise slurry deposition (LSD), resulting in strength of 30.8 MPa (no heat treatment) (Karl et al., 2020a).

Regolith composites were also produced, and comparable data to the current work were demonstrated. For instance, polyethylene (PE) was initially synthesized using a simulated Martian atmosphere, followed by the formation of Mars regolith compacts containing 20 wt.% PE. The composites were produced at 140°C, at which PE was molten and infiltrated the voids in the simulant powder by applying 240 MPa pressure, resulting in parts with compressive strength of about 40 MPa (Sen et al., 2010). In another study, sulfur concrete was produced by mixing 50 wt% sulfur with a different mars soil simulant (JSC Mars-1A) at about 120 °C, and a compressive strength above 50 MPa was measured (Wan et al., 2016).

For all ISRU concepts, an essential consideration is which materials are readily available on the planet or could, in theory, be produced from accessible extraterrestrial raw materials with minimal effort. Accordingly, the primary component to utilize CSP would be the regolith, ubiquitous on the planet's surface (e.g., Mars). Even if it does not constitute a condition *sine qua non* for CSP, the other factor is a liquid/solvent to aid sintering. The components were cold sintered in this work using up to 9.1 wt.% NaOH. For Mars ISRU scenarios via CSP, while water should not be an issue in preparing such a caustic solution, the hydroxide component has not been pointed yet. However, the essential chemicals to produce NaOH are readily available, such as Halite (Sodium Chlorite, NaCl), detected on Mars (Thomas et al., 2019). One possible synthesis method for NaOH may be the Chlor-alkali process (widely used on Earth), forming chlorine, hydrogen, and sodium hydroxide via electrolytic hydrolysis (Shiwei et al., 2020).

In the current work, the cold sintering was applied to the particles with a course (d_{50} ~ 10 μm) and wide range (100 nm to 100 μm) distribution. The particle size and distribution are important for particle packing and density enhancement in cold sintering (Zahabi et al., 2021). Besides, as already shown, when the high specific surface area, reactive particles (e.g., nanoscale), or particles with a bimodal size distribution are used instead of monomodal coarse particles, cold sintering generally results in enhanced

densification (Guo et al., 2016; Nur et al., 2021; Serrano et al., 2020). Still, for the first time, even with such coarse-sized particles, cold sintering was followed to obtain Martian regolith compacts exhibiting satisfactory compressive strength, reaching 43 MPa. It should be noted that the effect of Martian gravity on CSP should be examined. Besides, in future work, cold sintering of regolith simulant under different processing conditions (e.g., in Martian atmosphere model mix with high CO_2) will be investigated. Many basic chemicals found in Martian brines or salt deposits could also be utilized for regolith consolidation in combination with CSP.

4.4. Conclusions

Martian regolith simulant (MGS-1) powder was densified via a cold sintering process (CSP) as a novel ISRU approach. The powder was densified at different temperatures, always below 250°C, using NaOH solutions at different strengths as a liquid media. The increase of liquid phase concentration (from 3 M to 10 M) and processing temperature (from 150°C to 250°C), the relative densities of the compacts, and the cold crushing strength values was enhanced in a relatively short time of 30 min. The highest strength, 43 MPa, was obtained from the monolithic body with a relative density reaching 88% produced at 250°C using 10 M NaOH solution. CSP is an important addition to the regolith consolidation studies and may be considered for ISRU building materials on Mars and other extraterrestrial surfaces.

References

Alexiadis, A., Alberini, F., Meyer, M.E., 2017. Geopolymers from lunar and Martian soil simulants. Adv. Space Res. 59, 490–495. https://doi.org/10.1016/j.asr.2016.10.003

Altun, A.A., Ertl, F., Marechal, M., Makaya, A., Sgambati, A., Schwentenwein, M., 2021. Additive manufacturing of lunar regolith structures. Open Ceramics 5, 100058. https://doi.org/10.1016/j.oceram.2021.100058

Bish, D.L., et al., 2013. X-ray Diffraction Results from Mars Science Laboratory: Mineralogy of Rocknest at Gale Crater. Science (1979) 341. https://doi.org/10.1126/science.1238932

Blacic, J.D., 1985. Mechanical properties of lunar materials under anhydrous, hard vacuum conditions: Applications of lunar glass structural components, in: Lunar Bases and Space Activities of the 21st Century. p. 487.

Cannon, K.M., Britt, D.T., Smith, T.M., Fritsche, R.F., Batcheldor, D., 2019. Mars global simulant MGS-1: A Rocknest-based open standard for basaltic martian regolith simulants. Icarus 317, 470–478. https://doi.org/10.1016/j.icarus.2018.08.019

Cesaretti, G., Dini, E., de Kestelier, X., Colla, V., Pambaguian, L., 2014. Building components for an outpost on the Lunar soil by means of a novel 3D printing technology. Acta Astronaut. 93, 430–450. https://doi.org/10.1016/j.actaastro.2013.07.034

Chow, B.J., Chen, T., Zhong, Y., Qiao, Y., 2017. Direct Formation of Structural Components Using a Martian Soil Simulant. Sci. Rep. 7, 1151. https://doi.org/10.1038/s41598-017-01157-w

Corrias, G., Licheri, R., Orrù, R., Cao, G., 2012. Self-propagating high-temperature reactions for the fabrication of Lunar and Martian physical assets. Acta Astronaut. 70, 69–76. https://doi.org/10.1016/j.actaastro.2011.07.022

Dalton, C., Hohmann, E., 1972. Conceptual design of a lunar colony. NASA/ASEE Systems Design Institute.

Fateri, M., Meurisse, A., Sperl, M., Urbina, D., Madakashira, H.K., Govindaraj, S., Gancet, J., Imhof, B., Hoheneder, W., Waclavicek, R., 2019. Solar sintering for lunar additive manufacturing. J. Aerosp. Eng. 32, 04019101.

Galotta, A., Giust, E., Bortolotti, M., Sorarù, G.D., Sglavo, V.M., Biesuz, M., 2021. Cold sintering of diatomaceous earth. J. Am. Ceram. Soc. 104, 4329–4340. https://doi.org/10.1111/jace.17863

Galotta, A., Sglavo, V.M., 2021. The cold sintering process: A review on processing features, densification mechanisms and perspectives. J. Eur. Ceram. Soc. 41, 1–17. https://doi.org/10.1016/j.jeurceramsoc.2021.09.024

Grady, Z.M., Tsuji, K., Ndayishimiye, A., Hwan-Seo, J., Randall, C.A., 2020. Densification of a Solid-State NASICON Sodium-Ion Electrolyte Below 400 °C by

Cold Sintering With a Fused Hydroxide Solvent. ACS Appl. Energy Mater. 3, 4356–4366. https://doi.org/10.1021/acsaem.0c00047

Guo, H., Baker, A., Guo, J., Randall, C.A., 2016. Protocol for Ultralow-Temperature Ceramic Sintering: An Integration of Nanotechnology and the Cold Sintering Process. ACS Nano 10, 10606–10614. https://doi.org/10.1021/acsnano.6b03800

Happel, J.A., 1993. Indigenous Materials for Lunar Construction. Appl. Mech. Rev. 46, 313–325. https://doi.org/10.1115/1.3120360

Karacasulu, L., Ogur, E., Piskin, C., Vakifahmetoglu, C., 2021. Cold sintering of soda-lime glass. Scr. Mater. 192, 111–114. https://doi.org/10.1016/j.scriptamat.2020.10.015

Karacasulu, L., Tokkan, M., Bortolotti, M., Ischia, G., Adem, U., Vakifahmetoglu, C., 2020. Electrical characteristics of low temperature densified barium titanate. Ceram. Int. 46, 16670–16676. https://doi.org/10.1016/j.ceramint.2020.03.240

Karl, D., Cannon, K.M., Gurlo, A., 2022. Review of space resources processing for Mars missions: Martian simulants, regolith bonding concepts and additive manufacturing. Open Ceramics 9, 100216. https://doi.org/10.1016/j.oceram.2021.100216

Karl, D., Duminy, T., Lima, P., Kamutzki, F., Gili, A., Zocca, A., Günster, J., Gurlo, A., 2020a. Clay in situ resource utilization with Mars global simulant slurries for additive manufacturing and traditional shaping of unfired green bodies. Acta Astronaut. 174, 241–253. https://doi.org/10.1016/j.actaastro.2020.04.064

Karl, D., Kamutzki, F., Lima, P., Gili, A., Duminy, T., Zocca, A., Günster, J., Gurlo, A., 2020b. Sintering of ceramics for clay in situ resource utilization on Mars. Open Ceramics 3, 100008. https://doi.org/10.1016/j.oceram.2020.100008

Karl, D., Kamutzki, F., Zocca, A., Goerke, O., Guenster, J., Gurlo, A., 2018. Towards the colonization of Mars by in-situ resource utilization: Slip cast ceramics from Martian soil simulant. PLOS ONE 13, e0204025. https://doi.org/10.1371/journal.pone.0204025

Kohara, S., Suzuya, K., Takeuchi, K., Loong, C.-K., Grimsditch, M., Weber, J.K.R., Tangeman, J.A., Key, T.S., 2004. Glass Formation at the Limit of Insufficient Network Formers. Science (1979) 303, 1649–1652. https://doi.org/10.1126/science.1095047

Lim, S., Prabhu, V.L., Anand, M., Taylor, L.A., 2017. Extra-terrestrial construction processes – Advancements, opportunities and challenges. Adv. Space Res. 60, 1413–1429. https://doi.org/10.1016/j.asr.2017.06.038

Liu, B., Lin, F.L., Hu, C.C., Song, K.X., Zhang, J.H., Lu, C., Huang, Y.H., 2022. Novel transparent LiF ceramics enabled by cold sintering at 150 °C. Scr. Mater. 220, 114917. https://doi.org/10.1016/j.scriptamat.2022.114917

Liu, M., Jin, Q., Shen, P., 2020. Cold sintering of NaNO3/MgO heat-storage composite. Ceram. Int. 46, 28955–28960. https://doi.org/10.1016/j.ceramint.2020.08.066

Lowum, S., Floyd, R., Maria, J.-P., 2020. Hydroflux-assisted densification: applying flux crystal growth techniques to cold sintering. J. Mater. Sci. 55, 12747–12760. https://doi.org/10.1007/s10853-020-04926-7

Meek, T.T., Vaniman, D.T., Blake, R.D., Godbole, M.J., 1987. Sintering of lunar soil simulants using 2.45 GHz microwave radiation, in: Lunar and Planetary Science Conference.

Meurisse, A., Makaya, A., Willsch, C., Sperl, M., 2018. Solar 3D printing of lunar regolith. Acta Astronaut. 152, 800–810. https://doi.org/10.1016/j.actaastro.2018.06.063

Montes, C., Broussard, K., Gongre, M., Simicevic, N., Mejia, J., Tham, J., Allouche, E., Davis, G., 2015. Evaluation of lunar regolith geopolymer binder as a radioactive shielding material for space exploration applications. Adv. Space Res. 56, 1212–1221. https://doi.org/10.1016/j.asr.2015.05.044

Naser, M.Z., 2019. Extraterrestrial construction materials. Prog. Mater. Sci. 105, 100577. https://doi.org/10.1016/j.pmatsci.2019.100577

Nur, K., Mishra, T.P., Silva, J.G.P. da, Gonzalez-Julian, J., Bram, M., Guillon, O., 2021. Influence of powder characteristics on cold sintering of nano-sized ZnO with density above 99 %. J. Eur. Ceram. Soc. 41, 2648–2662. https://doi.org/10.1016/j.jeurceramsoc.2020.11.007

Sacksteder, K., Sanders, G., 2007. In-Situ Resource Utilization for Lunar and Mars Exploration, in: 45th AIAA Aerospace Sciences Meeting and Exhibit. American Institute of Aeronautics and Astronautics, Reston, Virigina. https://doi.org/10.2514/6.2007-345

Sangwal, K., 1980. Mechanism of dissolution of MgO crystals in acids. J. Mater. Sci. 15, 237–246. https://doi.org/10.1007/BF00552450

Sen, S., Carranza, S., Pillay, S., 2010. Multifunctional Martian habitat composite material synthesized from in situ resources. Adv. Space Res. 46, 582–592. https://doi.org/10.1016/j.asr.2010.04.009

Serrano, A., Caballero-Calero, O., García, M.Á., Lazić, S., Carmona, N., Castro, G.R., Martín-González, M., Fernández, J.F., 2020. Cold sintering process of ZnO ceramics: Effect of the nanoparticle/microparticle ratio. J. Eur. Ceram. Soc. 40, 5535–5542. https://doi.org/10.1016/j.jeurceramsoc.2020.05.059

Shiwei, N., Dritsas, S., Fernandez, J.G., 2020. Martian biolith: A bioinspired regolith composite for closed-loop extraterrestrial manufacturing. PLoS One. 15, e0238606. https://doi.org/10.1371/journal.pone.0238606

Simonds, C.H., 1973. Sintering and hot pressing of Fra Mauro composition glass and the lithification of lunar breccias. Am. J. Sci. 273.

Sohrabi Baba Heidary, D., Lanagan, M., Randall, C.A., 2018. Contrasting energy efficiency in various ceramic sintering processes. J. Eur. Ceram. Soc. 38, 1018–1029. https://doi.org/10.1016/j.jeurceramsoc.2017.10.015

Thomas, N.H., Ehlmann, B.L., Meslin, P. -Y., Rapin, W., Anderson, D.E., Rivera-Hernández, F., Forni, O., Schröder, S., Cousin, A., Mangold, N., Gellert, R., Gasnault, O., Wiens, R.C., 2019. Mars Science Laboratory Observations of Chloride Salts in Gale Crater, Mars. Geophys. Res. Lett. 46, 10754–10763. https://doi.org/10.1029/2019GL082764

Tognonvi, M.T., Soro, J., Gelet, J.-L., Rossignol, S., 2012. Physico-chemistry of silica / Na silicate interactions during consolidation. Part 2: Effect of pH. J. Non-Cryst. Solids. 358, 492–501. https://doi.org/10.1016/j.jnoncrysol.2011.11.005

Vakifahmetoglu, C., Anger, J.F., Atakan, V., Quinn, S., Gupta, S., Li, Q., Tang, L., Riman, R.E., 2016. Reactive Hydrothermal Liquid-Phase Densification (rHLPD) of Ceramics - A Study of the $BaTiO_3$ [TiO_2] Composite System. J. Am. Ceram. Soc. 99, 3893–3901. https://doi.org/10.1111/jace.14468

Vakifahmetoglu, C., Karacasulu, L., 2020. Cold sintering of ceramics and glasses: A review. Curr. Opin. Solid State Mater. Sci. 24, 100807. https://doi.org/https://doi.org/10.1016/j.cossms.2020.100807

Wan, L., Wendner, R., Cusatis, G., 2016. A novel material for in situ construction on Mars: experiments and numerical simulations. Constr. Build. Mater. 120, 222–231. https://doi.org/10.1016/j.conbuildmat.2016.05.046

Zahabi, M., Said, A., Memari, A., 2021. Cold Sintering of Calcium Carbonate for Construction Material Applications. ACS Omega 6, 2576–2588. https://doi.org/10.1021/acsomega.0c04617

Zocca, A., Fateri, M., Al-Sabbagh, D., Günster, J., 2020. Investigation of the sintering and melting of JSC-2A lunar regolith simulant. Ceram. Int. 46, 14097–14104. https://doi.org/10.1016/j.ceramint.2020.02.212

CHAPTER 5

COLD SINTERING ASSISTED TWO-STEP SINTERING OF POTASSIUM SODIUM NIOBATE (KNN) CERAMICS

The following chapter is published in Mater. Sci. Eng. B. 297 (2023) 116709 (Reproduced from [95] with permission from Elsevier).

Abstract

Potassium sodium niobate (KNN) ceramics were densified using a multiple-stage sintering process in which initially applied cold sintering process (CSP) was followed by the solid-state sintering between 1100-1120°C. Comparative assessments demonstrated that multi-step sintered samples yielded better properties than conventionally sintering ones. The highest relative density (94.7%) and the best electrical properties were obtained from the sample subjected to cold sintering at 120°C / 1h using 5 wt% deionized water subsequently heat-treated at 1120°C / 2h, resulting in a monolithic KNN ceramic having a piezoelectric coefficient of 120 pC/N.

5.1. Introduction

The cold sintering process (CSP) enables the densification of inorganic solids under mild pressures (below 1 GPa) and relatively low temperatures (< 350°C) [6,22,23,109]. The technique resembles liquid phase sintering and hot pressing due to a transient solvent, temperature, and pressure [6,22,23,27].

$K_{0.5}Na_{0.5}NbO_3$ (KNN) has attracted recent attention as a lead-free piezoelectric. Besides presenting a high Curie temperature ($T_c \cong 418°C$), it has a reasonably largepiezoelectric coefficient (d_{33} = 80 pC/N). These properties are susceptible to composition, requiring the conservation of the desired stoichiometry during densification [110,111]. High relative densities (> 90%) are difficult to be obtained by solid-state sintering due to the volatilization of used oxides [112]. Besides, solid-state sintering temperatures (~1120°C) approach the KNN melting point (1140°C), which may cause structural defects and stoichiometry shifts [113].

The problems mentioned above were mainly the reasons that have motivated the recent attention to the low-temperature densification of KNN [98,114–121]. In these works, the relative density reaching around 70% was obtained when single-step cold sintering was conducted. Highly caustic, reactive solutions were also used to get denser components, but poor electrical properties were subsequently observed [98,120].

Unlike single-step CSP, multiple-stage processes were also followed, aiming to produce highly dense KNN monoliths. For example, in a recent one, the samples were cold-sintered at 120°C under a pressure of 350 MPa for 45 min using H_2O. Then the samples were cold sintered again under different pressures (350-550 MPa) at the same temperature for 30 min, followed by heat treatment at 800°C, resulting in a relative density of 75% [121]. In pursuing denser monolithic components having controlled stoichiometry and appropriate piezoelectric properties, this study focused on synthesizing KNN powder and its sintering via cold sintering-assisted solid-state sintering.

5.2. Experimental procedure

The precursor Nb_2O_5 (CAS#:12034-59-2, 99.9%, Sigma–Aldrich, USA), Na_2CO_3 (CAS#:497-18-8, ≥99%, Sigma Aldrich, USA), and K_2CO_3 (CAS#:584-08-7, ≥99.5%, Sigma Aldrich, USA) were weighed according to the stoichiometric ratio and mixed using a planetary ball mill in ethanol at 250 rpm for 24 h. After the slurry was dried, it was calcinated at 850°C for 5 h. Finally, the obtained powder was ball-milled to reduce particle size. Particle size distribution was analyzed in ethanol by a Malvern dynamic light scattering (DLS) Nano-ZS instrument (Worcestershire, UK).

0.8 g milled powder was mixed with different liquid phases (5-20 wt.%, DI-water, KOH+NaOH / Nb_2O_5 suspension, acetic acid, NaOH-KOH solutions having different concentrations or eutectic molten NaOH-KOH) to aid consolidation. The obtained mixture was introduced into a cylindrical die (D = 12.7 mm), and pressed uniaxially under a pressure of 350 MPa while it was heated using a heating jacket wrapped around to processing temperature up to 250°C with a heating rate of 10 ˚C/min for varying times 1h to 18h. Finally, the cold-sintered samples were dried at 90°C for 24h.

Generally, PVA solutions were used to act as a binder for the target powder to be heat treated [122]. Here, for conventional sintering, 5 wt% PVA binder solution (87-89%, Sigma Aldrich) was mixed with KNN powder in DI-water using a ball mill at 250 rpm for 24 h. Then, the slurry was dried, passed through a 325 mesh sieve (<45 μm micron particle size), and was pressed at 100 MPa in the same diameter die of 12.7 mm and sintered for 2 h at different temperatures (1100-1120°C).

The bulk densities of the specimens were measured both by the geometric method and Archimedes' principle using ethanol as a buoyancy medium from three different representative samples. Crystallographic phases were identified using an X-ray diffractometer (XRD, Panalytical X'Pert PRO, The Netherlands) with a Copper anode X-Ray source (CuKα = 1.5406 Å at 40kV, 30 mA). The morphology of the milled powder and the fracture surfaces of the specimens were analyzed by scanning electron microscopy (SEM, FEI Quanta 250 FEG, USA). All samples were polished and reduced to 1 mm thickness for electrical characterization. The polished pellets were coated with silver paste on both surfaces and then cured at 200°C for 20 min. The dielectric properties of the samples were evaluated using an E4980AL Precision LCR meter (Keysight Technologies, Santa Clara, CA, USA) between room temperature (RT) and 250°C. Ferroelectric hysteresis loop measurements were done using TF analyzer (aixACCT TF Analyzer 1000, Aachen, Germany) at RT. To determine the piezoelectric coefficient d_{33}, a d_{33} meter (Sinocera Piezoelectronics, YE2730A, China) was used. Poling of the samples was carried out at 100°C for 30 min under 30 kV/cm of an electric field.

5.3. Results and discussion

As known, particle size and distribution are essential parameters for particle packing and density enhancement [108]. Typically densification enhances when the high specific surface area, reactive particles (nanoscale, generally below 100 nm), or particles with a narrow distribution, e.g., 40-100 nm, are used instead of coarse particles in CSP [18,123–125]. The morphology of the powders obtained after grinding and the particle size distributions analyzed by the DLS method are given in **Fig. 5.1**. The powder used in all sintering processes had an average particle size of 260 nm with a broad distribution from 100 to 600 nm.

In the initial cold sintering studies, different amount of DI-water was used as the liquid phase, see **Fig. 1(c)**. Liquid slipped away from the mold during pressing above a certain amount (15 wt.%), causing a similar relative density to those prepared using a lower amount. Not a significant change in densification (relative density from 70-77%) was detected from the samples obtained at different temperatures (120-240°C) and under the uniaxial pressures (350-500MPa). Accordingly, to improve energy efficiency, the lowest temperature of 120°C was selected as the cold sintering temperature for further experimenting. In **Fig. 5.1(d)**, SEM images obtained from the fractured surface of the sample subjected to CSP at 120°C under 350 MPa for 1 h with 5%wt DI water use are given. The samples are porous (parallel with relative density data), and some agglomerated sections can be seen due to possible dissolution and precipitation processes.

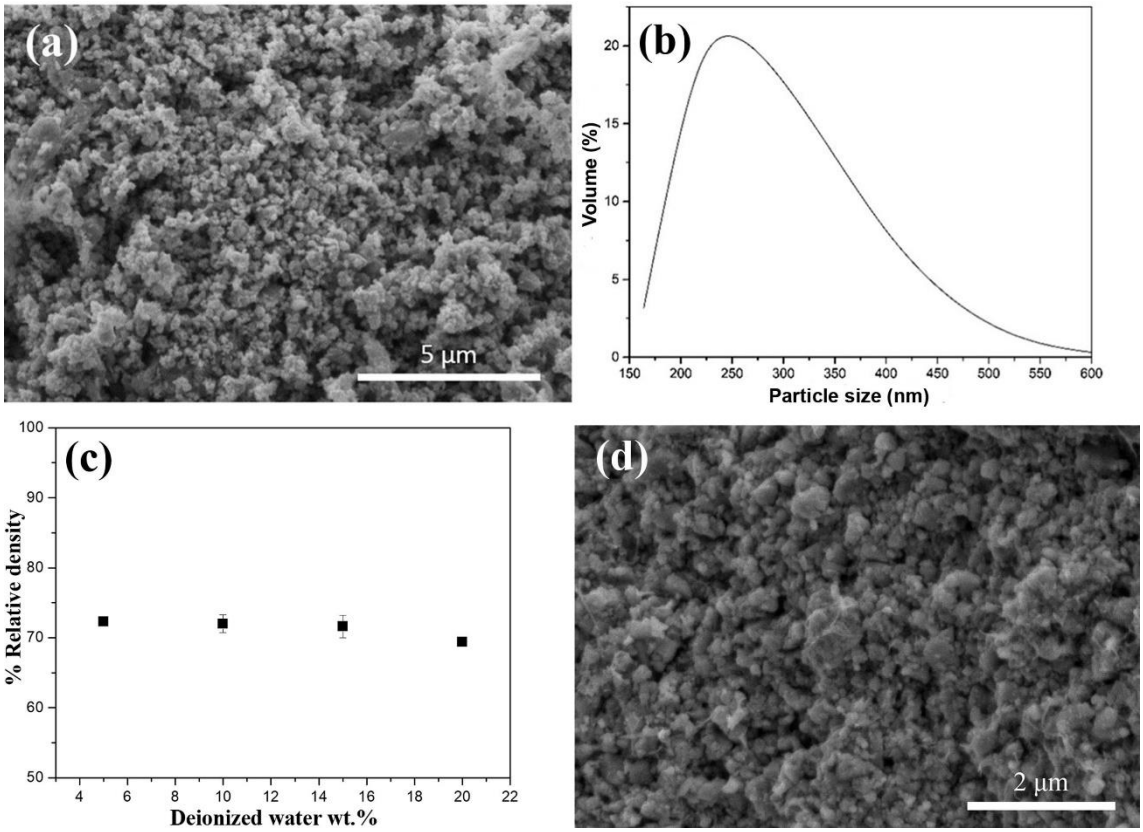

Figure 5.1. a) SEM image, and (b) Particle size distribution of synthesized and milled KNN powder using DLS analysis; (c) Relative density values of the cold sintered samples obtained at 120°C under 350 MPa for 1 h, related to the amount of used DI water; and (d) SEM image of the cold sintered sample at 120°C under 350 MPa for 1 h with 5%wt DI water use.

In an aqueous medium, KNN dissolves incongruently; the A site cations dissolve more readily at lower pH levels, whereas the B site cations dissolve more at higher pH levels. At pH 7, the potassium concentration was found to be higher than that of sodium [126]. Thus, potassium in the particle can dissolve into the aqueous part, and potassium-rich (i.e., $K_4Nb_6O_{17}$) phases can be formed at the grain boundaries. In contrast, Nb and Na-rich phases can be seen within the grains. [114,126]. It was shown that when such phases evolve, the electrical properties of the final KNN decay [114].

Nevertheless, to enhance densification, different amounts of DI-Water with diverse pH levels, such as KOH+NaOH / Nb_2O_5 suspension, acetic acid, and NaOH-KOH solutions having different concentrations, have been applied as a liquid phase. High

relative density values reaching around 90% were demonstrated when an aqueous solution of NaOH and KOH mixtures was used to assist CSPs [118]. However, our results differed from those, and relative densities were consistently below 80% for CSPs.

Since the relative densities of the samples were low via CSP, additional heat treatments between 1100-1120°C were applied, akin to conditions of the conventional sintering process and the other CSP & subsequent post-annealing studies works [127–129]. As given in **Table 5.1**, cold-sintered samples had a higher relative density than conventional ones for all heat treatment temperatures. Apart from the differences in the microstructural development (see later), CSP favors the subsequent sintering.

Table 5.1. Relative densities of cold-sintered & heat-treated samples and conventional sintered samples at different heat treatment temperatures with a dwell time of 2h.

	Processing conditions	**RD(%) before heat treatment**	**RD(%) after sintering at 1100°C**	**RD(%) after sintering at 1120°C**
Cold Sintering Process CSP	120°C-350 MPa-5 wt% DI-Water	72.3±0.6	92.9±0.8	94.7±2.1
	120°C-350 MPa-10 wt% DI-Water	72.0±1.3	92.7±0.5	94.4±2.1
Solid State Sintering SSS	100 MPa for powder compaction	60.0±1.2	89.1±2.1	93.5±0.9

***RD:** Relative Density

Figure 5.2 shows XRD patterns of all KNN samples. All the produced samples, including the synthesized powder, only includes peaks associated with the ICDD data of $K_{0.5}Na_{0.5}NbO_3$ (ICDD # 96-230-0500), exhibiting an orthorhombic structure. Besides, as heat treatment temperature increased, the observed peaks became sharper and narrower, leading to enhanced crystallinity, especially when compared to solid-state synthesized powder.

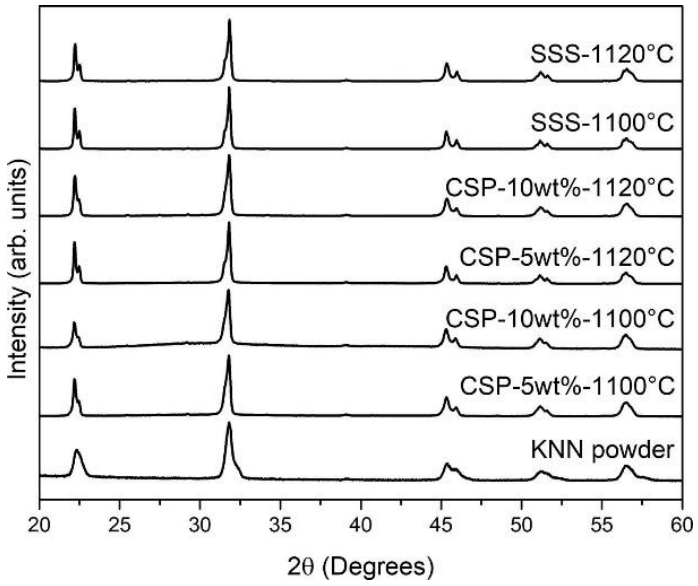

Figure 5.2. X-ray diffraction (XRD) patterns of synthesized KNN powder via the solid-state route (KNN powder), cold sintered & heat-treated samples (CSP): 5%wt. at 1100°C; 10%wt. at 1100°C; 5%wt. at 1120°C; 10%wt. at 1120°C; and conventional sintered samples (SSS): 1100°C; 1120°C.

SEM images obtained from the fracture surfaces of the samples processed cold sintering-assisted solid-state sintering and separately solid-state sintered are given in **Fig. 5.3(a-f)**. While highly dense microstructures were formed in both processing strategies, conventionally sintered samples experienced grain growth in segregated areas (see **Fig. 5.3(e&f).** In contrast, initially, cold sintered samples had homogenously distributed smaller cubic crystals implying a significant potential of the CSP on the initial nucleation kinetics and morphological control.

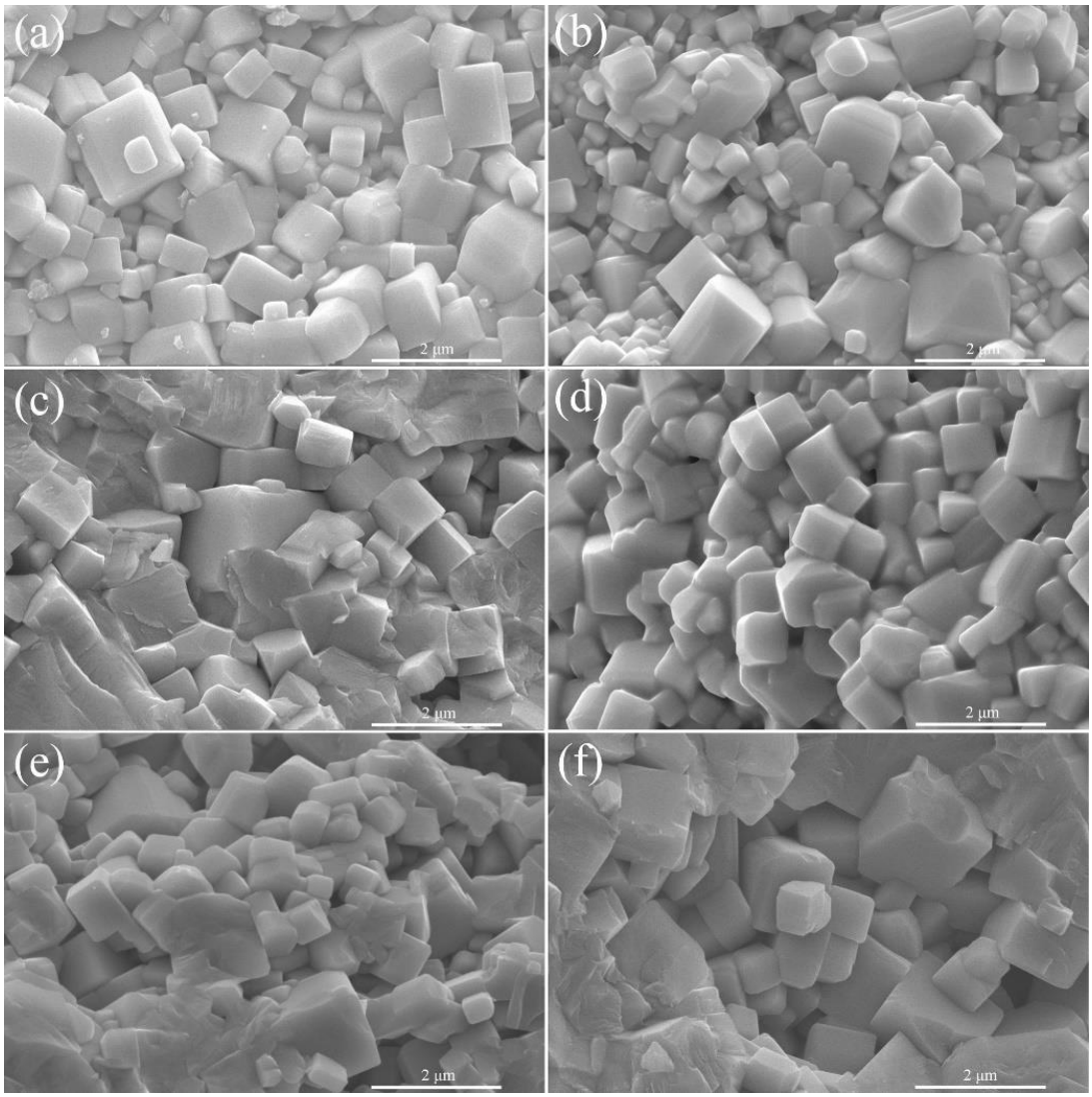

Figure 5.3. Fracture surface morphologies of cold sintering assisted heat-treated samples; (a) 5 wt% DI-Water at 1100°C, (b) 10% wt. at 1100°C, (c) 5% wt. at 1120°C, (d) 10% wt. at 1120°C; of conventional sintered samples: (e)1100°C; (f) 1120°C.

Temperature-dependent dielectric properties are given in **Fig. 5.4**. All samples have a dielectric constant above 400 at RT at different frequencies (1-10-100 kHz). Orthorhombic-tetragonal phase transformation occurred at about 190°C (**Table 5.2**) [130]. Dielectric losses were increased with decreasing frequency, and all samples have comparable dielectric properties similar to other works [119].

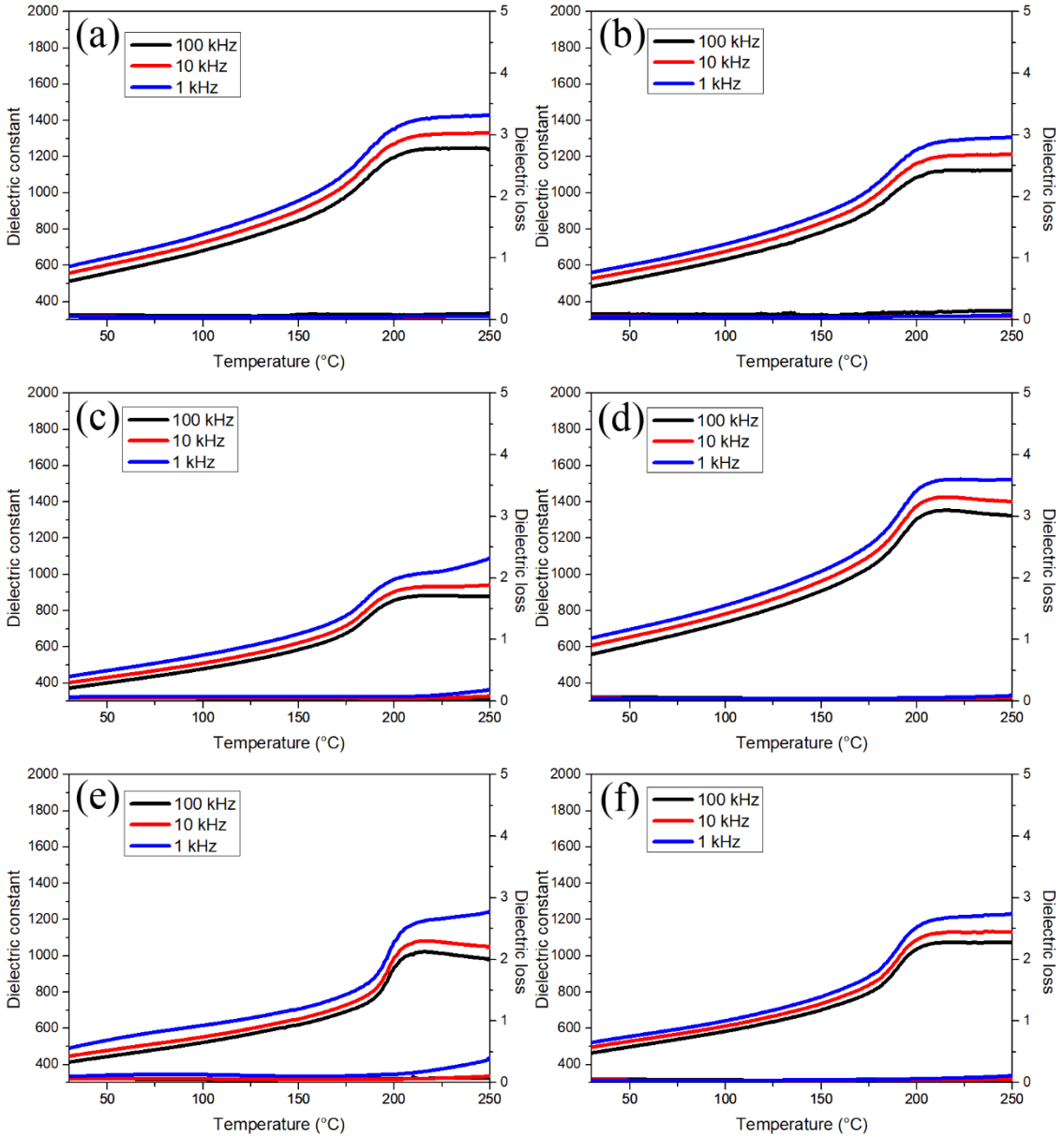

Figure 5.4. Temperature-dependent dielectric constant and losses of cold sintered & heat-treated samples: (a) 5%wt. at 1100°C; (b) 10%wt. at 1100°C; (c) 5%wt. at 1120°C; (d) 10%wt. at 1120°C; of conventional sintered samples: (e)1100°C; (f) 1120°C.

Figure 5.5 shows the hysteresis loops at RT and a frequency of 1 Hz under 3 kV. All samples showed ferroelectric properties having a single loop. Cold-sintering assisted 1120 °C solid-state sintered samples had the highest remanent and saturation polarization. Compared to all specimens produced by cold sintering assisted solid state sintering,

conventionally sintered samples demonstrated low remanent and saturation polarizations, akin to other work [114]. The polarization increase may be attributed to enhanced densification [131]. Note also that the pore volume and permeability significantly influence the evaporation of K and Na during heat treatments. This means that one of the main factors in suppressing the strong volatilization of the alkalis for the same temperature might be the higher packing density before the additional heat treatment and higher sintering density of samples by cold sintering-assisted solid-state sintering [114]. Furthermore, all samples demonstrated butterfly-shaped strain loops that reach negative values, exhibiting normal ferroelectric behavior.

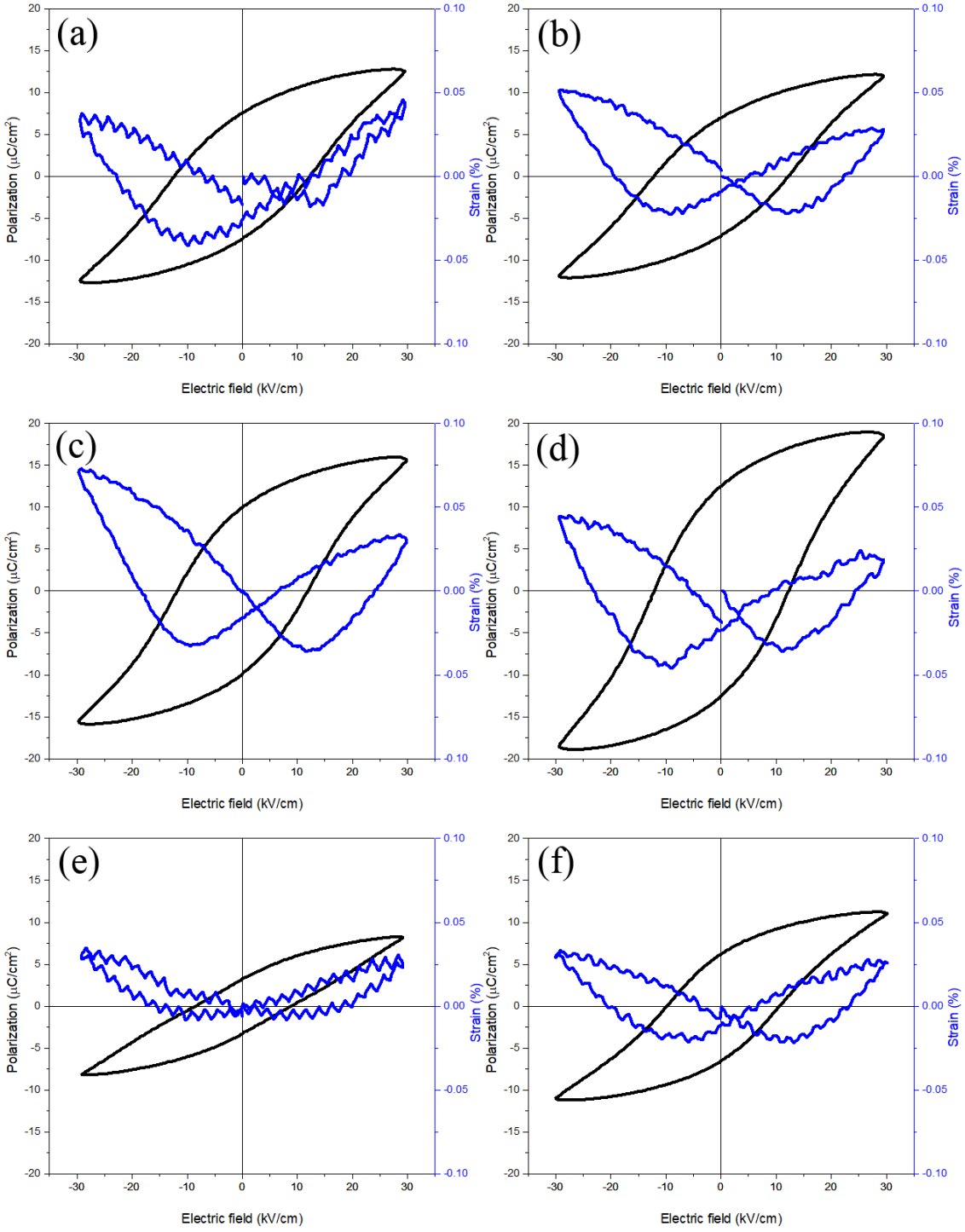

Figure 5.5. Hysteresis loops and strain curves of cold sintering assisted heat-treated samples under 3 kV at 1 Hz and RT: (a) 5%wt. at 1100°C; (b) 10%wt. at 1100°C; (c) 5%wt. at 1120°C; (d) 10%wt. at 1120°C; of conventional sintered samples: (e)1100°C; (f) 1120°C.

The piezoelectric coefficients (d_{33}) are given in **Table 5.2**. The piezoelectric d_{33} coefficients of densified KNN ceramics obtained by conventional sintering usually vary between 80 and 110 pC/N [130], reaching 160 pC/N with a relative density of ~ 99% via hot pressing [132]. It should be underlined that the poling conditions (e.g., temperature & time) and/or aging processes can be optimized to enhance the piezoelectric d_{33} coefficients [31,133]. The piezoelectric coefficient of the sample produced by conventional sintering at 1120°C was 86 pC/N, while initially cold sintered and additionally 1120°C heat treated samples gave 120 pC/N, exceeding typical d_{33} values of conventionally sintered products. When all the electrical characterization results were analyzed, it is possible to state that the electrical properties (saturation and remanent polarization, strain, and d_{33} values) of cold-sintered assisted solid-state sintered samples were better than those of the conventional sintered samples. As mentioned, CSP may provide lower alkalı volatilization, causing more stable sintering conditions compared to traditional sintered products [114].

Table 5.2. Orthorombic-Tetragonal transition temperature (T_{O-T}), Remanent polarization (P_r), coercive field (E_c), maximum polarization (P_m), and piezoelectric coefficients (d_{33}) of the samples.

	Process Conditions	**T_{O-T} (°C)**	**P_r (μC/cm²)**	**E_c (kV/cm)**	**P_m (μC/cm²)**	**d_{33} (pC/N)**
CSP 120°C-350 MPa	5 wt% DI-Water +1100°C	186	7.54	12.27	12.54	117
	10 wt% DI-Water +1100°C	186	6.98	12.25	11.96	113
	5 wt% DI-Water +1120°C	186	9.95	11.88	15.69	120
	10 wt% DI-Water +1120°C	192	12.51	12.26	18.58	110
SSS	1100°C	197	3.20	8.86	8.22	71
	1120°C	189	6.21	10.62	11.09	86

5.4. Conclusions

Potassium sodium niobate (KNN) ceramics were densified by the cold sintering process (CSP) using different liquid phases to aid sintering. While low relative densities were obtained by CSP, successive heat treatments between 1100-1120°C were applied for the initially cold-sintered samples. It was found that the relative densities and the electrical properties of cold-sintered heat-treated samples were better than conventional sintered samples. The highest relative density (~95%) was obtained from the KNN sample subjected to initial CSP at 120°C with a dwell time of 1h using 5% wt DI-water subsequently heat-treated at 1120°C for 2h, yielding a piezoelectric coefficient of 120 pC/N. For the KNN system, CSP should be considered a primary or intermediate step to enhance initial densification, decrease the final sintering temperature and increase overall densification upon applying subsequent sintering at higher temperatures. Multi-step sintering proposed here can be a key alternative to systems that require high-cost equipment such as Spark plasma sintering (SPS), Hot Isostatic Pressing (HIP), etc.

References

[1] C. Vakifahmetoglu, L. Karacasulu, Cold sintering of ceramics and glasses: A review, Curr. Opin. Solid State Mater. Sci. 24 (2020) 100807. https://doi.org/10.1016/j.cossms.2020.100807.

[2] A. Galotta, V.M. Sglavo, The cold sintering process: A review on processing features, densification mechanisms and perspectives, J. Eur. Ceram. Soc. 41 (2021) 1–17. https://doi.org/10.1016/j.jeurceramsoc.2021.09.024.

[3] S. Grasso, M. Biesuz, L. Zoli, G. Taveri, A.I. Duff, D. Ke, A. Jiang, M.J. Reece, A review of cold sintering processes, Advances in Applied Ceramics. 119 (2020) 115–143. https://doi.org/10.1080/17436753.2019.1706825.

[4] M. Biesuz, G. Taveri, A.I. Duff, E. Olevsky, D. Zhu, C. Hu, S. Grasso, A theoretical analysis of cold sintering, Advances in Applied Ceramics. 119 (2020) 75–89. https://doi.org/10.1080/17436753.2019.1692173.

[5] A. Galotta, E. Giust, M. Bortolotti, G.D. Sorarù, V.M. Sglavo, M. Biesuz, Cold sintering of diatomaceous earth, J. Am. Ceram. Soc. 104 (2021) 4329–4340. https://doi.org/10.1111/jace.17863.

[6] C. Piskin, L. Karacasulu, M. Bortolotti, C. Vakifahmetoglu, Synthesis of potassium–sodium niobate (KNN) from NbO_2, Open Ceramics. 7 (2021) 100159. https://doi.org/10.1016/j.oceram.2021.100159.

[7] C. Piskin, L. Karacasulu, G. Ischia, M. Bortolotti, C. Vakifahmetoglu, Hydrothermal synthesis of potassium–sodium niobate powders, J. Am. Ceram. Soc. 105 (2022) 3809–3819. https://doi.org/10.1111/jace.18349.

[8] B. Malič, J. Koruza, J. Hreščak, J. Bernard, K. Wang, J.G. Fisher, A. Benčan, Sintering of lead-free piezoelectric sodium potassium niobate ceramics, Materials. 8 (2015) 8117–8146.

[9] R. López, F. González, M.P. Cruz, M.E. Villafuerte-Castrejon, Piezoelectric and ferroelectric properties of $K_{0.5}Na_{0.5}NbO_3$ ceramics synthesized by spray drying method, Mater Res Bull. 46 (2011) 70–74.

[10] J. Ma, H. Li, H. Wang, C. Lin, X. Wu, T. Lin, X. Zheng, X. Yu, Composition, microstructure and electrical properties of $K_{0.5}Na_{0.5}NbO_3$ ceramics fabricated by cold sintering assisted sintering, J Eur Ceram Soc. 39 (2019) 986–993.

[11] M. Chi, W. Ma, J. Guo, J. Wu, T. Li, S. Wang, P. Zhang, Effect of NaCl on the microstructure and electrical properties of $K_{0.5}Na_{0.5}NbO_3$ ceramics prepared by cold sintering process, Journal of Materials Science: Materials in Electronics. 30 (2019) 21435–21443.

[12] B. Deng, J. Jiang, H. Li, C. Zhao, C. Lin, X. Wu, M. Gao, T. Lin, Enhanced piezoelectric property in Mn-doped $K_{0.5}Na_{0.5}NbO_3$ ceramics via cold sintering process and $KMnO_4$ solution, J. Am. Ceram. Soc. 105 (2022) 5774-5782.

[13] L. Cong, W. Huajing, M. Jianzhang, D. Baoyu, W. Xiao, L. Tengfei, Z. Xinghua, Y. Xing, Effect of dwell time on cold sintering assisted sintering based highly transparent $0.9K_{0.5}Na_{0.5}NbO_3$-$0.1LiBiO_3$ ceramics, J Alloys Compd. 826 (2020) 154249.

[14] B. Deng, Y. Ma, T. Chen, H. Wang, J. Lin, C. Lin, X. Wu, C. Zhao, T. Lin, M. Gao, Elevating electrical properties of (K, Na)NbO_3 ceramics via cold sintering process and post-annealing, J. Am. Ceram. Soc. 105 (2022) 461–468.

[15] J. Lan, X. Chen, L. Liu, H. Lian, Y. He, Y. Song, L. Zhu, P. Liu, Low-temperature synthesis of $K_{0.5}Na_{0.5}NbO_3$ ceramics in a wide temperature window via cold-sintering assisted sintering method and enhanced electrical properties, J. Eur. Ceram. Soc. 43 (2023) 73–81.

[16] S. Lowum, R. Floyd, J.-P. Maria, Hydroflux-assisted densification: applying flux crystal growth techniques to cold sintering, J. Mater. Sci. 55 (2020) 12747–12760. https://doi.org/10.1007/s10853-020-04926-7.

[17] K. Tsuji, Z. Fan, S.H. Bang, S. Dursun, S. Trolier-McKinstry, C.A. Randall, Cold sintering of the ceramic potassium sodium niobate, $(K_{0.5}Na_{0.5})NbO_3$, and influences on piezoelectric properties, J. Eur. Ceram. Soc. 42 (2022) 105–111. https://doi.org/10.1016/j.jeurceramsoc.2021.10.002.

[18] J. Jiang, S. Chen, C. Zhao, C. Lin, X. Wu, M. Gao, T. Lin, C. Fang, Composition segregation and grain growth in $(K_{0.5}Na_{0.5})NbO_3$ piezoceramics prepared by two-step cold sintering process, J. Am. Ceram. Soc. 106 (2023) 913-922.

[19] C. Vakifahmetoglu, Zeolite decorated highly porous acicular calcium silicate ceramics, Ceram Int. 40 (2014) 11925–11932. https://doi.org/10.1016/j.ceramint.2014.04.028.

[20] M. Zahabi, A. Said, A. Memari, Cold Sintering of Calcium Carbonate for Construction Material Applications, ACS Omega. 6 (2021) 2576–2588. https://doi.org/10.1021/acsomega.0c04617.

[21] A. Serrano, O. Caballero-Calero, M.Á. García, S. Lazić, N. Carmona, G.R. Castro, M. Martín-González, J.F. Fernández, Cold sintering process of ZnO ceramics: Effect of the nanoparticle/microparticle ratio, J. Eur. Ceram. Soc. 40 (2020) 5535–5542. https://doi.org/10.1016/j.jeurceramsoc.2020.05.059.

[22] K. Nur, T.P. Mishra, J.G.P. da Silva, J. Gonzalez-Julian, M. Bram, O. Guillon, Influence of powder characteristics on cold sintering of nano-sized ZnO with density above 99 %, J. Eur. Ceram. Soc. 41 (2021) 2648–2662. https://doi.org/10.1016/j.jeurceramsoc.2020.11.007.

[23] H. Guo, A. Baker, J. Guo, C.A. Randall, Protocol for ultralow-temperature ceramic sintering: an integration of nanotechnology and the cold sintering process, ACS Nano. 10 (2016) 10606–10614.

[24] L. Karacasulu, D. Karl, A. Gurlo, C. Vakifahmetoglu, Cold sintering as a promising ISRU technique: A case study of Mars regolith simulant, Icarus. 389 (2023) 115270.

[25] O. Ozmen, C. Ozsoy-Keskinbora, E. Suvaci, Chemical stability of $KNbO_3$, $NaNbO_3$, and $K_{0.5}Na_{0.5}NbO_3$ in aqueous medium, J. Am. Ceram. Soc. 101 (2018) 1074–1086.

[26] B. Liu, L. Li, K.X. Song, M.M. Mao, Z. Lu, G. Wang, L. Li, D. Wang, D. Zhou, A. Feteira, I.M. Reaney, Enhancement of densification and microwave dielectric properties in LiF ceramics via a cold sintering and post-annealing process, J. Eur. Ceram. Soc. 41 (2021) 1726–1729. https://doi.org/10.1016/j.jeurceramsoc.2020.09.073.

[27] B. Liu, K. Sha, Y.Q. Jia, Y.H. Huang, C.C. Hu, L. Li, D.W. Wang, D. Zhou, K.X. Song, High quality factor cold sintered LiF ceramics for microstrip patch antenna applications, J. Eur. Ceram. Soc. 41 (2021) 4835–4840. https://doi.org/10.1016/j.jeurceramsoc.2021.03.052.

[28] D.H. Jin, B. Liu, K.X. Song, K.W. Xu, Y.H. Huang, C.C. Hu, Y.Y. Hu, Boosting densification and microwave dielectric properties in cold sintered BaF_2 ceramics for 5.8 GHz WLAN applications, J Alloys Compd. 886 (2021) 161141. https://doi.org/10.1016/j.jallcom.2021.161141.

[29] H. Birol, D. Damjanovic, N. Setter, Preparation and characterization of $(K_{0.5}Na_{0.5})NbO_3$ ceramics, J. Eur. Ceram. Soc. 26 (2006) 861–866.

[30] R. Zuo, J. Rödel, R. Chen, L. Li, Sintering and Electrical Properties of Lead-Free $Na_{0.5}K_{0.5}NbO_3$ Piezoelectric Ceramics, J. Am. Ceram. Soc. 89 (2006) 2010–2015. https://doi.org/10.1111/j.1551-2916.2006.00991.x.

[31] R.E. Jaeger, L. Egerton, Hot pressing of potassium-sodium niobates, Journal of the American Ceramic Society. 45 (1962) 209–213.

[32] L. Karacasulu, M. Tokkan, M. Bortolotti, G. Ischia, U. Adem, C. Vakifahmetoglu, Electrical characteristics of low temperature densified barium titanate, Ceram. Int. 46 (2020) 16670–16676. https://doi.org/10.1016/j.ceramint.2020.03.240.

[33] Z. Zhao, Y. Lv, Y. Dai, S. Zhang, Ultrahigh electro-strain in acceptor-doped KNN lead-free piezoelectric ceramics via defect engineering, Acta Mater. 200 (2020) 35–41. https://doi.org/10.1016/j.actamat.2020.08.073.

CHAPTER 6

ELECTRICAL CHARACTERISTICS OF LOW TEMPERATURE DENSIFIED BARIUM TITANATE

The following chapter is published in Ceram. Int. 46 (2020) 16670-16676 (Reproduced from [31] with permission from Elsevier).

Abstract

A low temperature densification technique, i.e. reactive hydrothermal liquid-phase densification (rHLPD) was followed to obtain highly dense $BaTiO_3$ components at temperatures ≤ 240°C. The formed ceramics were characterized concerning not only the structural features but also the electrical properties. The increase of both reaction time and temperature resulted in enhanced densification of $BaTiO_3$ components reaching about 90% of theoretical density. The presence of the tetragonal $BaTiO_3$ was demonstrated by both XRD and TEM analysis. Despite the low reaction temperatures, the samples showed promising dielectric, ferroelectric and piezoelectric functionality without additional annealing. A broad dielectric peak was observed around 135°C at the Curie temperature; saturated hysteresis loops and corresponding butterfly-shaped strain-electric field loops were obtained. $BaTiO_3$ sample subjected to hydrothermal reaction at 240°C for 72 h yielded a piezoelectric coefficient of 84 pC/N.

6.1. Introduction

Generally speaking, ceramic components are processed at high temperatures by following traditional sintering methods namely solid state, liquid phase, pressure-assisted

sintering, etc. Recently, different sintering approaches that allow the densification of ceramic artifacts at temperatures below around 400°C, i.e. low temperature densification techniques which are broadly called as cold sintering (CS), have been proposed [1]. Among others, rHLPD process is a concept of low temperature densification consisting of an infiltration, hydrothermal reaction, and reactive crystallization. Firstly, conventional shaping techniques are used to form a porous matrix. Then, the structure is infiltrated with a solution including reactive species, followed by hydrothermal reaction, similar to ordinary crystallization studies [2]. However, specifically for rHLPD during the hydrothermal process; the pores act as local micro-reactors and depending on the molar volume expansion of the aimed reaction, theoretically, 100 % dense components can be obtained. In other words; the only requirement of the process is a hydrothermal crystallization reaction with reaction products having a higher molar volume compared to that of the green body [3].

Barium titanate ($BaTiO_3$) is one of the most well-known ferroelectric materials. It is widely used in electrical applications such as multilayer capacitors due to its high dielectric constant and low dielectric losses [4, 5]. While highly dense $BaTiO_3$ components were produced by high temperature sintering via various processes such as two step sintering [6, 7], hot isostatic pressing [8, 9], spark plasma sintering [4, 10-12], and flash sintering [13, 14], relatively limited number of works were published concerning the low temperature densification of $BaTiO_3$[3, 15-20]. Guo et al.[16, 17] utilized a $BaTiO_3$ powder having bimodal particle size distribution. Water assisted powder was subjected to a CS process at 180 °C for 3 h resulting in a high densification reaching to 94.4%. However, the samples produced by CS showed limited dielectric properties, i.e. no peak appeared in the dielectric constant at the Curie temperature and dielectric constant remained quite low up to 200°C. Because of such an issue, an additional annealing process (at 900 °C for 3h) was conducted and the dielectric properties were improved. In another study, a $BaTiO_3$ powder (< 100 nm particle size) was used for CS under similar conditions, resulting in the samples with relative density above 96% yet comparable additional heat treatment at 900°C was followed to enhance the dielectric properties [18]. While in those works $BaTiO_3$ was formed by following CS, rHLPD was also followed to produce $BaTiO_3$ starting from a TiO_2 pellet and $Ba(OH)_2$ solution under hydrothermal conditions [3]. Although the process kinetics, densification and mechanical properties of the samples were analyzed, the electrical properties of such

components were never discussed. Therefore, in this study, it was aimed to investigate dielectric, ferroelectric and piezoelectric properties of the $BaTiO_3$ ceramics densified via rHLPD at temperatures below 240°C.

6.2. Experimental procedure

3 g of Titanium oxide (TiO_2, titania) (Anatase, 99.8%, Sigma Aldrich, CAS#: 1317-70-0) powder was mixed in 12 ml of deionized (DI) water with a gram of 10 wt.% polyvinyl alcohol (PVA) aqueous solution for 24 h using a planetary ball mill (Retsch PM-100, Germany) in a high density polyethylene (HDPE) jar with zirconia balls. The TiO_2 suspension was then dried, sieved, and pressed uniaxially at 30 MPa into 10 mm-disc-shaped pellets. The green samples were heated to 400°C for PVA binder burnout procedure.

Barium hydroxide ($Ba(OH)_2.8H_2O$) (>%98, Acros Organics, CAS#: 12230-71-6) was used as barium source. The pressed pellets were first subjected to pre-infiltration by wetting the sides of the green-body with a prepared solution of barium hydroxide, followed by placement of the sample into the Teflon liner containing vessel (Parr Instruments 4748 model, USA), addition of the reaction solution, hydrothermal processing at 180°C and 240°C up to 72 h, washing by DI water and drying. The obtained samples were coded as BT1 for the sample formed at 240°C for 24 h, and BT2 for the one obtained at 240°C for 72 h. Similarly the samples produced at 180°C for 24 h and 72 h were coded as BT3 and BT4, respectively.

The bulk densities were measured by Archimedes' method. The data together with the calculated theoretical density from rule of mixtures (ROM by taking the Rietveld volume fractions) value were used to find out the final relative densities. X-ray diffraction measurements were performed on a Rigaku D-Max III (Tokyo, Japan) instrument operating in Bragg-Brentano geometry and equipped with a Copper anode X-Ray source ($Cu_{k\alpha}$ = 1.5406 Å at 40 kV, 30 mA), diffracted beam graphite monochromator, 1° divergence and receiving slit and 5° diffracted beam Soller slits. Scans were performed over the 5°-135° (2Θ) range, with a 0.02° step size and 2 s counting time per step. Instrumental broadening was characterized by means of an Y_2O_3 powder (99.99%, Sigma-Aldrich, CAS# 1314-36-9) annealed at 1400°C for 24 hours. The morphological

properties and microstructure were analyzed by using a scanning electron microscope (SEM, FEI, Quanta 250 FEG, USA) and a transmission electron microscopy (TEM, ThermoFisher Talos F200S FEG, Netherlands) operating at 200 kV. Prior to SEM analysis all the samples were coated by sputter coating. TEM sample was prepared suspending a small amount of powder in ethanol, performing a 5 mins sonication treatment and putting 50 μL of solution on a TEM copper grid covered by amorphous carbon.

In order to measure the electrical properties, silver epoxy was deposited on the surface of the pellets to form electrical contacts. The silver epoxy was cured at 135 °C for 7 mins. Dielectric properties were evaluated using a Keysight E4980AL Precision LCR meter (USA) between room temperature (RT) and 250°C. Ferroelectric hysteresis loop measurements were done using an Aixacct TF Analyzer 1000 (Germany) at RT. To assess the piezoelectric coefficient d_{33}, a d_{33} meter (Sinocera Piezoelectronics, YE2730A, China) was used. Poling of the samples was carried out at 70°C for 15 mins under electric fields larger than 35 kV/cm [21], also using the Aixacct instrument.

6.3. Results & discussion

The relative density (RD) of green TiO_2 pellets prepared by dry pressing was about 0.55. After rHLPS process, the obtained final densities of $BaTiO_3$ samples are given in **Table 6.1**. As expected, the relative density of the final components was enhanced with increasing reaction time and temperature. The sample coded as BT2 which was subjected to rHLPS at 240 ºC for 72 h demonstrated the highest relative density reaching 86.8%, resembling the previous studies [3]. The XRD plots obtained from whole set of samples are given in **Fig. 6.1**, exhibiting clearly similar diffraction features between each other; reference reflection marks for tetragonal $BaTiO_3$ (ICDD PDF# 00-005-0626) are also reported on the bottom of the plot, and the occurrence of other peaks belonging to residual TiO_2 is visible.

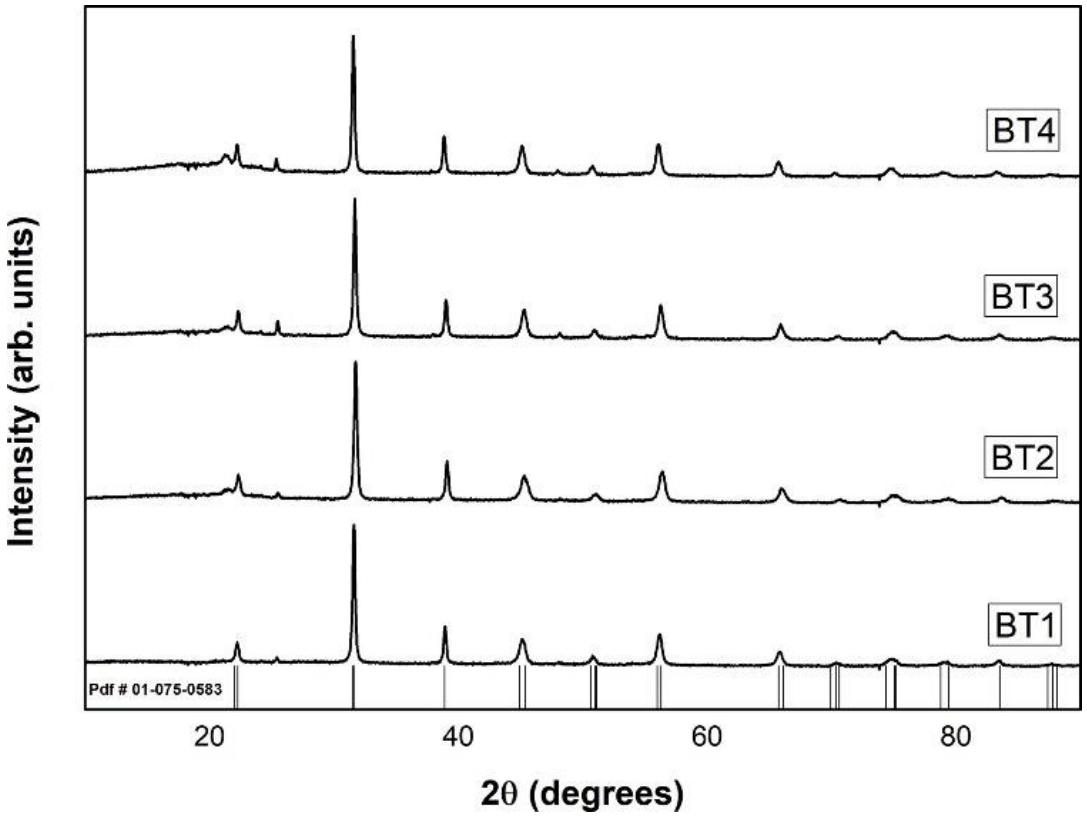

Figure 6.1. The normalized XRD patterns obtained from the whole set of samples. At the bottom of the experimental data, reference reflection marks for tetragonal $BaTiO_3$ (ICDD PDF# 00-005-0626) are given.

Quantitative powder diffraction analysis was performed by full-profile Rietveld approach as implemented in the software ReX [22], by starting from a three-phase mixture model ($BaTiO_3$[23], TiO_2 [24] and $BaCO_3$ [25]) and refining the volume fractions of all the phases as well as the lattice parameters and average volume-weighted crystallite size of $BaTiO_3$ [26]. For the refinement, both cubic and tetragonal symmetries of $BaTiO_3$ were tested; the best fit was obtained by using the tetragonal phase, whose presence was also confirmed in a conclusive manner by TEM observation (see later). Despite the absence of an evident tetragonal peak splitting in the XRD patterns, a larger peak broadening can be observed in corresponding reflections (e.g. (2 0 0)), which is indeed better accounted for by modeling the data with the tetragonal phase and independently fitting the *a* and *c* cell parameters. As an example, the refinement plot obtained from BT2 sample is shown in **Fig. 6.2** (for all sample sets, the refined quantitative values are given in **Table 6.1**.). Both the flatness of the residual error curve and the goodness of fit, R (%)

values ranging from 2.89 to 3.06, indicate an accurate modeling of the diffraction data. It could be seen that the amount of TiO_2 decreases with increasing processing time. In a similar fashion; when the reaction temperature was increased from 180ºC to 240ºC, titania amount was reduced considerably. Similar to other studies, $BaCO_3$ was also detected but was always below 1.5 vol%, this is as known to be a common problem when $BaTiO_3$ was synthesized under hydrothermal reaction conditions from $Ba(OH)_2$ and TiO_2 [3, 27-29].

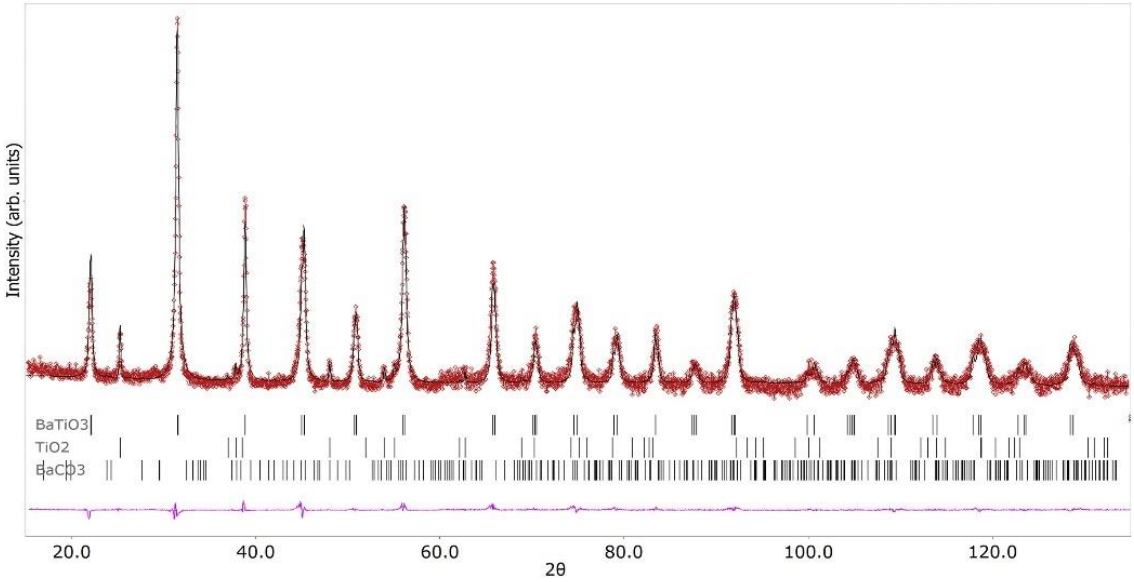

Figure 6.2. Rietveld refinement of the x-ray diffraction pattern (the straight black lines correspond to the experimental data, the red dots correspond to the calculated pattern, and below the pattern, first the peak positions for $BaTiO_3$, TiO_2 and $BaCO_3$ and then the residual fitting error plot is given), for the sample reacted for 72 h at 240°C.

The tetragonality of the $BaTiO_3$ phase was followed starting from the reference phase [3] and refining both the *a* and *c* parameters in the analysis. Reaction temperature seems to have the greatest effect on the *c/a* ratio, followed by reaction time. Accordingly, sample BT2 exhibits the highest *c/a* value (1.0058), followed by sample BT1 (1.0053); samples processed at lower temperature (180°C), i.e. BT3 and BT4 presented the lower value (1.0041) with no significant differences. The *c* lattice parameter remains relatively

stable among the different samples whereas parameter *a* decreases when both the reaction time and temperature increases, implying the enhancement in the tetragonality; similarly as indicated in the previous studies that systems subject to longer reaction times or higher temperatures resulted in higher tetragonality [30]. As a consequence, $BaTiO_3$ cell volume follows the same trend, with BT2 showing the lowest volume and BT3 being the highest, and BT1 and BT4 exhibiting intermediate values. On the other hand, average volume-weighted crystallite size did not show any clear dependence on reaction time and/or temperature, with the exception of BT2 sample showing the highest value; it has to be noted that crystallite size, being defined as the average volume of coherently scattering crystalline domains, differs in general from grain size (as observed e.g. from SEM images, see later), and the two are thus not simply comparable.

Table 6.1. The relative densities, quantitative parameters obtained from Rietveld refinements, Curie temperature (T_c), remanent polarization (P_r), coercive field (E_c) and maximum polarization (P_m) values of all samples.

Sample	BT1	BT2	BT3	BT4
T (°C)	240	240	180	180
t (h)	24	72	24	72
RD (*100)	80.1	86.8	71.3	74.3
Goodness of Fit	2.89	3.02	3.06	2.92
$BaTiO_3$ (vol %)	89.24%	95.40%	85.03%	88.31%
TiO_2 (vol %)	9.47%	3.80%	14.06%	10.46%
$BaCO_3$ (vol %)	1.29%	0.79%	0.91%	1.23%
$BaTiO_3$ crystal size (Å)	392	494	461	464
$BaTiO_3$ cell a (Å)	4.0041	4.0024	4.0088	4.0081
$BaTiO_3$ cell c (Å)	4.0255	4.0257	4.0252	4.0246
$BaTiO_3$ c/a ratio	1.0053	1.0058	1.0041	1.0041
$BaTiO_3$ cell volume ($Å^3$)	64.530	64.485	64.686	64.656
T_C (°C) at 10 kHz	140	135	142	142
P_r ($\mu C/cm^2$)	2.10	1.72	1.22	1.40
E_c (kV/cm)	8.1	5.52	8.5	6.82
P_m ($\mu C/cm^2$)	6.03	7.44	4.39	5.68

SEM image taken from the fracture surface of the un-reacted TiO_2 pellet, i.e. the starting green substrate body is shown in **Fig. 6.3(a)**. While from the fracture surface of the green body, porosity and some agglomeration can be seen, the sample subjected to hydrothermal reaction at 240°C for 72 h demonstrated to have a relatively dense structure, see **Fig. 6.3(b)**, corroborating the data given in **Table 6.1**.

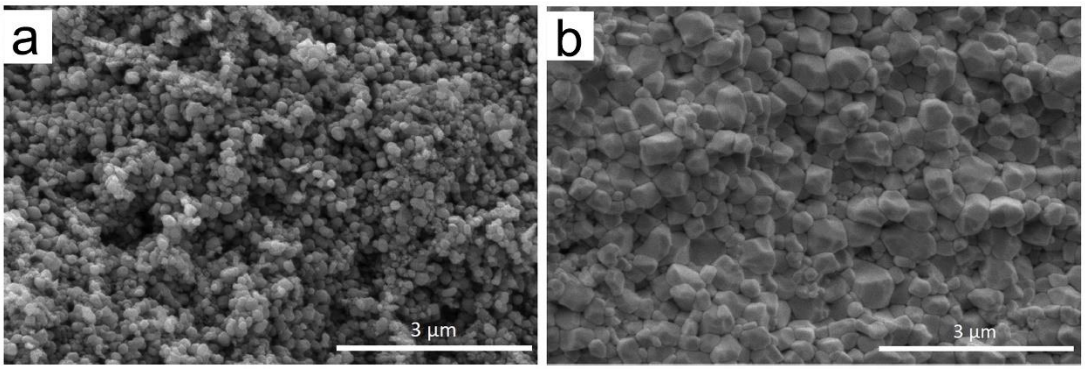

Figure 6.3. SEM images taken from the fracture surfaces of (a) green-body, (b) BT2 sample obtained by hydrothermal reaction at 240°C for 72 h.

TEM images obtained from the densest sample (BT2) are given in **Figs. 6.4(a&b)**. No core/shell structure was found in the analyzed particles. The particles have dimensions ranging from few hundred nanometers to microns. The same sample was also investigated through selected area electron diffraction (SAED); the obtained diffraction pattern was indexed by using the ProcessDiffraction software [31]. The spectrum was compared with the $BaTiO_3$ tetragonal card, see **Fig. 6.4(c)**. The presence of the tetragonal $BaTiO_3$ structure is consistent with the doubling of the peaks evident in the SAED pattern (see white arrows in **Fig. 6.4(b)**). The presence of the cubic $BaTiO_3$ structure cannot be excluded, however the relative intensities of the peak doublet suggest that the tetragonal phase is by large the principal one; however, the lack of the statistics does not allow any quantitative evaluation. Finally, there is no evidence of the presence of TiO_2 in the SAED, due probably to the sampling problem; indeed, the high level of spatial resolution of TEM may make it difficult to detect phases present in such small quantity, see **Table 6.1**.

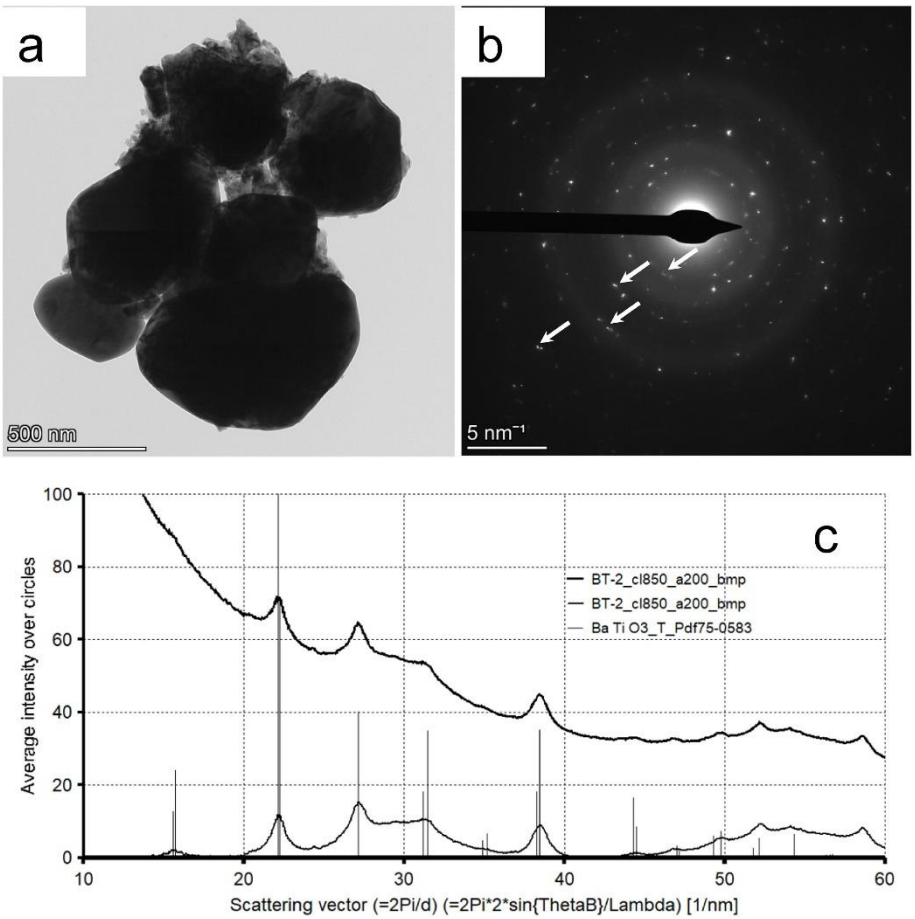

Figure 6.4. TEM analysis of BT2 sample obtained by hydrothermal reaction at 240°C for 72 h (a) image of an agglomerate, (b) SAED of the agglomerate, (c) integration of the SAED and its comparison with $BaTiO_3$ tetragonal card.

Temperature dependence of the dielectric constant and loss of all samples were measured at 10 kHz, and the data is given in **Fig. 6.5**. BT2 sample has the largest dielectric constant followed by BT1 and BT4. BT2 also showed the lowest dielectric loss. A broad peak in the dielectric constant can be observed for all samples at around 130°C, marking the ferroelectric-paraelectric phase transition. All peak temperatures are included in Table 1. Differences in the transition temperatures of the samples might have been caused by the diffuse nature of the phase transition which was likely originate from the coexisting tetragonal and cubic phases. Such a diffuse phase transition was previously reported for cold sintered $BaTiO_3$ [16]. As the tetragonality increases, the dielectric peak at the Curie becomes sharper and transition becomes less diffuse with lower Curie temperature. BT2

had the highest tetragonality and showed the sharpest phase transition and in turn the lowest phase transition temperature of 135 °C quite similar to that of conventionally sintered $BaTiO_3$. In contrast, BT3 and BT4 with the lowest tetragonality values demonstrated the broadest phase transition with the largest transition temperatures. In addition to tetragonality, the amount of residual phases also affect the dielectric properties.BT2 sample which was subjected to hydrothermal process at 240°C for 72 h, has the highest amount of $BaTiO_3$, tetragonality as well as the lowest amount of residual titania; all of which accounts for the best dielectric properties i.e. sharpest phase transition and largest dielectric peak at the transition. This is in agreement with previous study on cold-sintering of $BaTiO_3$, where the dielectric peak at the phase transition could only be obtained after the additional heat treatment at 700 °C, which did not increase the relative density much (relative density was already 93 % after cold sintering at 180 °C) but increased the tetragonality significantly [16].

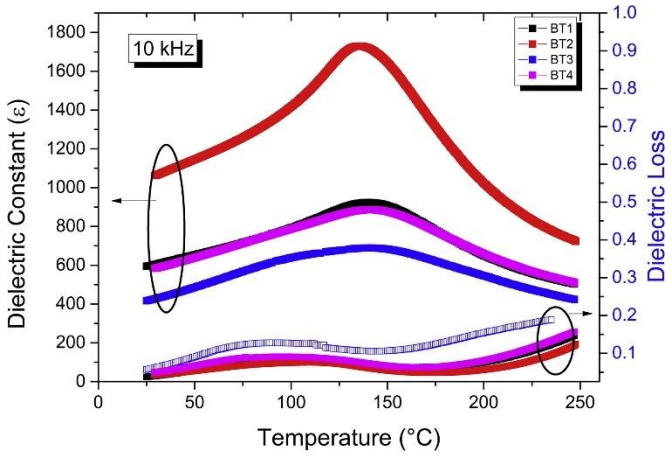

Figure 6.5. The temperature dependence of the dielectric constant, and dielectric loss at 10 kHz.

Similar dielectric behavior, i.e. broad peak at the Curie temperature and relatively low dielectric constant was very recently reported for cold sintered $BaTiO_3$ ceramics obtained at 300°C and explained mainly in terms of grain size effects [32]. Together with this recent report, the data in the current work supports that it is possible to obtain decent dielectric properties even by sintering at low processing temperatures via rHLPD.

In **Figures 6.6(a-d)**, ferroelectric hysteresis loops measured at 1 Hz and under different voltages are given. The applied electric field was increased gradually until the samples experienced dielectric breakdown. Hysteresis loops for all samples reached saturation before the dielectric breakdown took place. In **Figure 6.6(e)**, hysteresis loops for all samples measured up to 50 kV/cm are provided for comparison. BT2 had the largest saturation polarization followed by BT1, BT4 and BT3. This order was the same as for the dielectric constant and should also be related with the purity of the sample as well as its tetragonality level. The largest saturation polarization values obtained in this study on BT2 sample were lower (less than half) than that of the recently reported ones [32]. This difference might be related to few factors including the residual titania in the samples, and the dissimilarities in the processing temperatures (60 degrees lower reaction temperature was used in the current study) which resulted in different densification levels and tetragonality. Coercive field (E_c) as well as remanent (P_r) and maximum polarization (P_m) values are also given in the Table 1. BT2 having the lowest amount of residual impurities showed the smallest E_c whereas BT3 with the highest impurity content had the largest E_c. Impurity phases are known to impede domain wall motion and thus increase the coercive field [33].

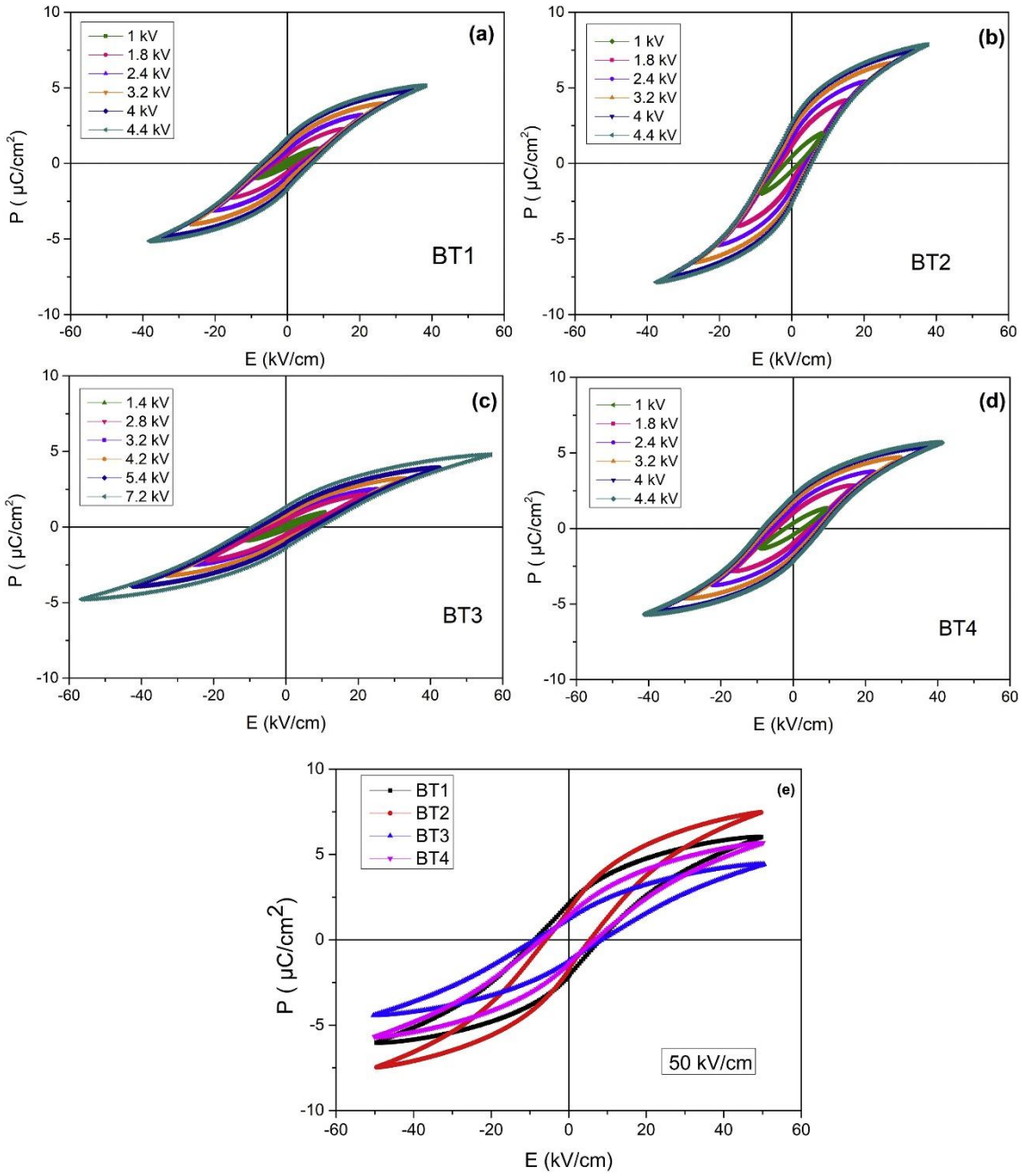

Figure 6.6. Development of ferroelectric hysteresis loops under increasing voltage (a) BT1, (b) BT2, (c) BT3, and (d) BT4, and (e) comparison of the hysteresis loops of all samples at 50 kV/cm.

To complement the ferroelectric hysteresis measurements, displacement of the samples was measured and resulting strain values are shown in **Figs. 6.7(a-d)**, together with the hysteresis loops obtained in the simultaneous measurement. For all samples, butterfly shaped strain loops are observed; slightly reaching negative values, indicating

normal ferroelectric behavior [34]. Maximum strain of 0.05 % at around 50 kV/cm was obtained again for the BT2 sample at around 50 kV/cm, consistent with its relatively large ferroelectric polarization and dielectric constant among other samples in this study.

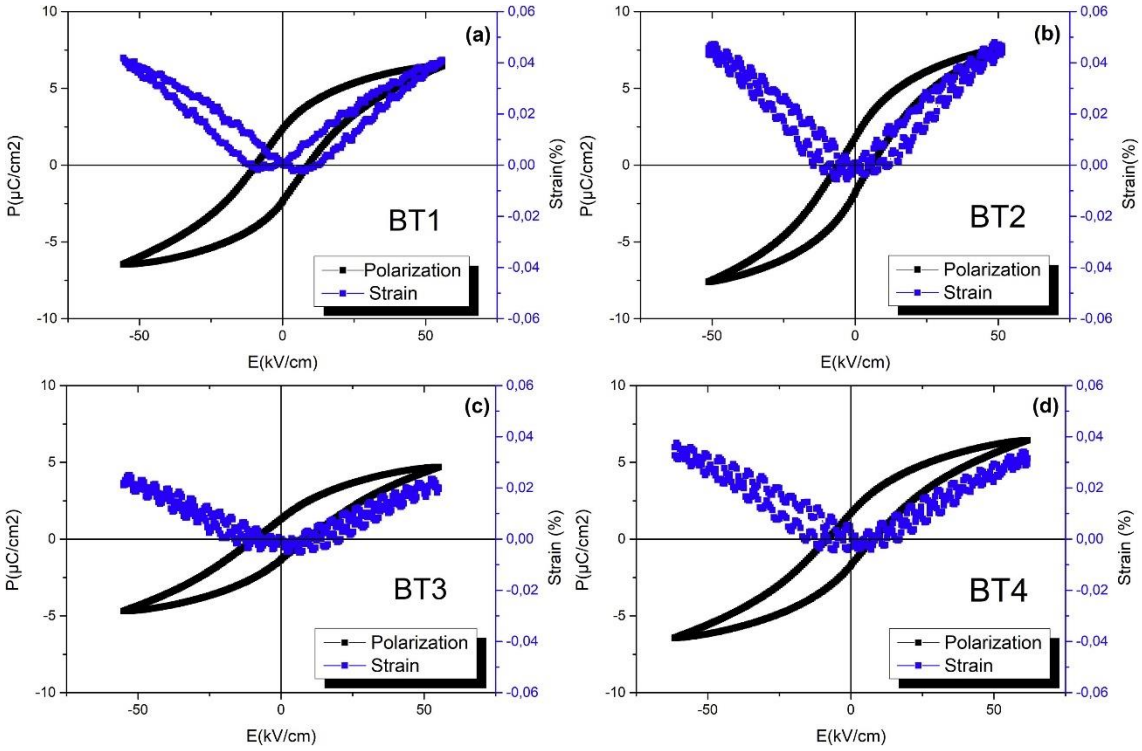

Figure 6.7. Hysteresis (P-E) and Strain loops (S-E) of **(a)** BT1, **(b)** BT2, **(c)** BT3 and, **(d)** BT4 measured at 1 kHz.

Piezoelectric d_{33} coefficients (pC/N) of the samples were found to be 50 pC/N (for BT1), 84 pC/N (for BT2), 34 pC/N (for BT3), and finally 38 pC/N (for BT4). It should be noted that the poling process conditions (temperature and time) can be optimized to enhance the d_{33} values. Nevertheless, obtained values are much lower than that of the conventionally sintered $BaTiO_3$ ceramics for which d_{33} values lie in the range of 350-500 pC/N [35]. Conventional sintering is typically done around 1350°C and the resulting samples have relative density values greater than 95% [36].

6.4. Conclusions

$BaTiO_3$ ceramics were prepared via reactive hydrothermal liquid-phase densification (rHLPD) technique. The increase of both reaction time and temperature resulted in $BaTiO_3$ components having enhanced densification reaching to 86.8%. The samples showed acceptable electrical properties without any additional annealing processes. $BaTiO_3$ sample subjected to hydrothermal reaction at 240°C for 72 h showed a saturated hysteresis loop and the corresponding butterfly shaped strain-electric field loop, together with a broad Curie temperature around 135°C. The sample with the most favorable processing conditions yielded a piezoelectric coefficient d_{33} of 84 pC/N.

References

[1] C. Vakifahmetoglu, L. Karacasulu, Cold sintering of ceramics and glasses: a review, Curr. Opin. Solid State Mater. Sci. (2020) 100807. https://doi.org/10.1016/j.cossms.2020.100807.

[2] C. Vakifahmetoglu, Zeolite decorated highly porous acicular calcium silicate ceramics, Ceram. Int. 40 (2014) 11925-11932. https://doi.org/10.1016/j.ceramint.2014.04.028.

[3] C. Vakifahmetoglu, J.F. Anger, V. Atakan, S. Quinn, S. Gupta, Q. Li, L. Tang, R.E. Riman, Reactive hydrothermal liquid-phase densification (rHLPD) of ceramics–a study of the $BaTiO_3$ [TiO_2] composite system, J. Am. Ceram. Soc. 99 (2016) 3893-3901. https://doi.org/10.1111/jace.14468.

[4] X. Deng, X. Wang, H. Wen, A. Kang, Z. Gui, L. Li, Phase transitions in nanocrystalline barium titanate ceramics prepared by spark plasma sintering, J. Am. Ceram. Soc. 89 (2006) 1059-1064. https://doi.org/10.1111/j.1551-2916.2005.00836.x.

[5] G.H. Haertling, Ferroelectric ceramics: history and technology, J. Am. Ceram. Soc. 82 (1999) 797-818. https://doi.org/10.1111/j.1151-2916.1999.tb01840.x.

[6] T. Karaki, K. Yan, M. Adachi, Barium titanate piezoelectric ceramics manufactured by two-step sintering, Jpn. J. Appl. Phys. 46 (2007) 7035. https://doi.org/10.1143/JJAP.46.7035.

[7] X.H. Wang, X.Y. Deng, H.L. Bai, H. Zhou, W.G. Qu, L.T. Li, I.W. Chen, Two-step sintering of ceramics with constant grain-size, II: $BaTiO_3$ and Ni–Cu–Zn Ferrite, J. Am. Ceram. Soc. 89 (2006) 438-443. https://doi.org/10.1111/j.1551-2916.2005.00728.x.

[8] H. Maiwa, Dielectric and electromechanical properties of $BaTiO_3$ ceramics prepared by hot isostatic pressing, Ferroelectrics 463 (2014) 15-24. https://doi.org/10.1080/00150193.2014.891419.

[9] H. Maiwa, Piezoelectric properties of $BaTiO_3$ ceramics prepared by hot isostatic pressing, J. Ceram. Soc. Jpn. 121 (2013) 655-658. http://dx.doi.org/10.2109/jcersj2.121.655.

[10] T. Takeuchi, E. Betourne, M. Tabuchi, H. Kageyama, Y. Kobayashi, A. Coats, F. Morrison, D. Sinclair, A. West, Dielectric properties of spark-plasma-sintered $BaTiO_3$, J. Mater. Sci. 34 (1999) 917-924. https://doi.org/10.1023/A:1004506905278.

[11] T. Takeuchi, M. Tabuchi, H. Kageyama, Y. Suyama, Preparation of dense $BaTiO_3$ ceramics with submicrometer grains by spark plasma sintering, J. Am. Ceram. Soc. 82 (1999) 939-943. https://doi.org/10.1111/j.1151-2916.1999.tb01857.x.

[12] H. Maiwa, Electromechanical properties of $BaTiO_3$ ceramics prepared by spark plasma sintering and other methods, Jpn. J. Appl. Phys. 48 (2009) 09KD04. https://doi.org/10.1143/JJAP.48.09KD04.

[13] J.-C. M'Peko, J.S. Francis, R. Raj, Field-assisted sintering of undoped $BaTiO_3$: microstructure evolution and dielectric permittivity, J. Eur. Ceram. Soc. 34 (2014) 3655-3660. https://doi.org/10.1016/j.jeurceramsoc.2014.04.041.

[14] R. Shi, Y. Pu, W. Wang, Y. Shi, J. Li, X. Guo, M. Yang, Flash sintering of barium titanate, Ceram. Int. 45 (2019) 7085-7089. https://doi.org/10.1016/j.ceramint.2018.12.211.

[15] H. Guo, A. Baker, J. Guo, C.A. Randall, Cold sintering process: a novel technique for low-temperature ceramic processing of ferroelectrics, J. Am. Ceram. Soc. 99 (2016) 3489-3507. https://doi.org/10.1111/jace.14554.

[16] H. Guo, J. Guo, A. Baker, C.A. Randall, Hydrothermal-assisted cold sintering process: a new guidance for low-temperature ceramic sintering, ACS Appl. Mater. Interfaces 8 (2016) 20909-20915. https://doi.org/10.1021/acsami.6b07481.

[17] H. Guo, A. Baker, J. Guo, C.A. Randall, Protocol for ultralow-temperature ceramic sintering: an integration of nanotechnology and the cold sintering process, ACS nano 10 (2016) 10606-10614. https://doi.org/10.1021/acsnano.6b03800.

[18] J.-P. Ma, X.-M. Chen, W.-Q. Ouyang, J. Wang, H. Li, J.-L. Fang, Microstructure, dielectric, and energy storage properties of $BaTiO_3$ ceramics prepared via cold sintering, Ceram. Int. 44 (2018) 4436-4441. https://doi.org/10.1016/j.ceramint.2017.12.044.

[19] M. Biesuz, G. Taveri, A.I. Duff, E. Olevsky, D. Zhu, C. Hu, S. Grasso, A theoretical analysis of cold sintering, Adv. Appl. Ceram. 119 (2020) 75-89. https://doi.org/10.1080/17436753.2019.1692173.

[20] S. Grasso, M. Biesuz, L. Zoli, G. Taveri, A.I. Duff, D. Ke, A. Jiang, M.J. Reece, A review of cold sintering processes, Adv. Appl. Ceram. (2020) 1-29. https://doi.org/10.1080/17436753.2019.1706825.

[21] J. Cheng, Y. Chen, J.-W. Wu, X.-R. Ji, S.-H. Wu, 3D printing of $BaTiO_3$ piezoelectric ceramics for a focused ultrasonic array, Sensors 19 (2019) 4078. https://doi.org/10.3390/s19194078.

[22] M. Bortolotti, L. Lutterotti, I. Lonardelli, ReX: a computer program for structural analysis using powder diffraction data, J. Appl. Crystallogr. 42 (2009) 538-539. https://doi.org/10.1107/S0021889809008309.

[23] N. Yasuda, H. Murayama, Y. Fukuyama, J. Kim, S. Kimura, K. Toriumi, Y. Tanaka, Y. Moritomo, Y. Kuroiwa, K. Kato, H. Tanaka, M. Takata, X-ray diffractometry for the structure determination of a submicrometre single powder grain, J. Synchrotron Radiat. 16 (2009) 352-357. https://doi.org/10.1107/S090904950900675X.

[24] M. Rezaee, S.M.M. Khoie, K.H. Liu, The role of brookite in mechanical activation of anatase-to-rutile transformation of nanocrystalline TiO_2: an XRD and raman spectroscopy investigation, CrystEngComm 13 (2011) 5055-5061. https://doi.org/10.1039/C1CE05185G.

[25] S.M. Antao, I. Hassan, The orthorhombic structure of $CaCO_3$, $SrCO_3$, $PbCO_3$ and $BaCO_3$: linear structural trends, The Canadian Mineralogist 47 (2009) 1245-1255. https://doi.org/10.3749/canmin.47.5.1245.

[26] P. Paufler, R. A. Young (ed.). The rietveld method. International union of crystallography. Oxford University Press 1993. 298 p. Price £ 45.00. ISBN 0–19–

855577–6, Crystal Research and Technology 30 (1995) 494-494. https://doi.org/10.1002/crat.2170300412.

[27] J.O. Eckert Jr, C.C. Hung-Houston, B.L. Gersten, M.M. Lencka, R.E. Riman, Kinetics and mechanisms of hydrothermal synthesis of barium titanate, J. Am. Ceram. Soc. 79 (1996) 2929-2939. https://doi.org/10.1111/j.1151-2916.1996.tb08728.x.

[28] A. Chien, J. Speck, F. Lange, A. Daykm, C. Levi, Low temperature/low pressure hydrothermal synthesis of barium titanate: powder and heteroepitaxial thin films, J. Mater. Res. 10 (1995) 1784-1789. https://doi.org/10.1557/JMR.1995.1784.

[29] T. Tsumura, K. Matsuoka, M. Toyoda, Formation and annealing of $BaTiO_3$ and $SrTiO_3$ nanoparticles in KOH solution, Journal of Materials Science & Technology 26 (2010) 33-38. https://doi.org/10.1016/S1005-0302(10)60005-9.

[30] T. Kubo, M. Hogiri, H. Kagata, A. Nakahira, Synthesis of nano-sized $BaTiO_3$ powders by the rotary-hydrothermal process, J. Am. Ceram. Soc. 92 (2009) S172-S176. https://doi.org/10.1111/j.1551-2916.2008.02739.x.

[31] J.L. Lábár, Consistent indexing of a (set of) single crystal SAED pattern(s) with the ProcessDiffraction program, Ultramicroscopy 103 (2005) 237-249. https://doi.org/10.1016/j.ultramic.2004.12.004.

[32] K. Tsuji, A. Ndayishimiye, S. Lowum, R. Floyd, K. Wang, M. Wetherington, J.-P. Maria, C.A. Randall, Single step densification of high permittivity $BaTiO_3$ ceramics at 300 ºC, J. Eur. Ceram. Soc. (2019). https://doi.org/10.1016/j.jeurceramsoc.2019.12.022.

[33] T.E. Luke, Impurity control of domain switching in ferroelectric bismuth titanate, J. Appl. Phys. 45 (1974) 1605-1610. https://doi.org/10.1063/1.1663463.

[34] S.-T. Zhang, A.B. Kounga, E. Aulbach, T. Granzow, W. Jo, H.-J. Kleebe, J. Rödel, Lead-free piezoceramics with giant strain in the system $Bi_{0.5}Na_{0.5}TiO_3$–$BaTiO_3$–$K_{0.5}Na_{0.5}NbO_3$. I. Structure and room temperature properties, J. Appl. Phys. 103 (2008) 034107. https://doi.org/10.1063/1.2838472.

[35] M. Acosta, N. Novak, V. Rojas, S. Patel, R. Vaish, J. Koruza, G.A. RossettiJr., J. Rödel, $BaTiO_3$-based piezoelectrics: fundamentals, current status, and perspectives, Appl. Phys. Rev. 4 (2017) 041305. https://doi.org/10.1063/1.4990046.

[36] T. Karaki, K. Yan, M. Adachi, Subgrain microstructure in high-performance $BaTiO_3$ piezoelectric ceramics, Appl. Phys. Express 1 (2008) 111402. http://dx.doi.org/10.1143/APEX.1.111402.

CHAPTER 7

FORMATION OF MONOLITHIC $SrTiO_3$-TiO_2 CERAMIC HETEROSTRUCTURES BY REACTIVE HYDROTHERMAL SINTERING

The following chapter is published in J. Eur. Ceram. Soc. 43 (2023) 6982-6988 (Reproduced from [96] with permission from Elsevier).

Abstract

In a one-pot approach, monolithic $SrTiO_3$-TiO_2 ceramic heterostructures were obtained using the reactive hydrothermal liquid phase densification (rHLPD). Structural, morphological, and photocatalytic properties of the obtained ceramics were analyzed. The relative density of the formed components reached about 80% with reaction time, temperature, and NaOH concentration variation. It was observed via Rietveld refinement that there was no XRD detectable phase other than TiO_2 and $SrTiO_3$ in the final structure. The monolithic $SrTiO_3$-TiO_2 ceramics obtained by hydrothermal reaction at 120°C for 24 h in 1M NaOH concentration showed a dielectric constant being around 500, and the dielectric loss was below 0.25 at frequencies higher than 10 kHz. The $SrTiO_3$-TiO_2 heterostructured monoliths having only 20 vol% total porosity and low specific surface area, demonstrated ~60% efficiency (in 5h) in degrading Methylene Blue photo-catalytically.

7.1. Introduction

Due to their unique properties, metal oxide perovskites with the chemical formula ABO_3 are commonly used in many areas as solar cells, supercapacitors, light-emitting diodes, and photocatalytic applications [134–138]. Strontium titanate ($SrTiO_3$), one of the perovskite-structured inorganic solids, is a paraelectric material and has been widely used in various applications [139–141]. To obtain a dense component, commercially available $SrTiO_3$ powder is usually pelletized, followed by densification at high temperatures, e.g., between 1250-1500°C, via conventional solid-state sintering [142]. However, this is a time and energy-consuming process [143].

The formation of heterostructures between $SrTiO_3$ and other photocatalytic oxides improves the system's photocatalytic properties [144]. For instance, TiO_2 is characterized by a relatively large band gap (3.2 ev) [145] and suffers the formation of bounded electron-hole pairs, which hinder photocatalytic activity[146]. The combination of titania with $SrTiO_3$, possessing a conduction band edge 200 mV below that of titania, dramatically improves the photocatalytic activity (improved transfer of electron-hole pair) of the system [147,148]. The formation of monolithic $SrTiO_3$-TiO_2 ceramic heterostructures has been investigated only on the particulates processed through complicated strategies [149].

Recent works on sintering inorganic solids have aimed to minimize energy consumption and reduce carbon footprint [6,23,25,150,151]. Among the techniques, the cold sintering process (CSP) and hydrothermal liquid phase densification (rHLPD) are the most promising. Here, the ceramic consolidation is aided at low temperatures by external pressure application and by the addition of a liquid solvent, usually a water solution. The processes have been applied to different ceramics and also to perovskite-structured oxides [19,31,152–155], including $SrTiO_3$ [156,157]. While most of the works aimed at maximizing the density of the sintered body (though not always full density could be achieved), the photocatalytic activity is enhanced in porous systems where "sintering" is simply needed to consolidate the body in a solid network. Such results can be easily achieved by the mentioned low-temperature consolidation approaches.

In this context, reactive hydrothermal liquid phase densification (rHLPD) allows the production of ceramic components in one step by combining the synthesis and sintering at low temperatures, eventually yielding direct manufacturing of

heterostructured structures [6,30,31]. While many chemical systems were proposed [29], no study focused on the formation, characterization, and application trials of $SrTiO_3$-TiO_2 ceramic heterostructures produced in one step via rHLPD.

7.2. Experimental Procedure

All experiments were performed using Strontium hydroxide octahydrate ($Sr(OH)_2.8H_2O$, 99% purity, Alfa Aesar), Titanium dioxide (TiO_2, 99.8% anatase, Merck), Sodium hydroxide (NaOH, 98-100%, Merck), Polyvinyl alcohol (PVA, M_w=31000-50000, 87-89%, Merck) and deionized (DI) water. During the production of $SrTiO_3$ by rHLPD, three different parameters were altered, temperature: 90C, 120C, 140C (°C), time: 6h, 24h, 72h, and NaOH concentration: 0 M (i.e., no NaOH) or 1M.

To obtain a porous titania matrix, 10 wt.% PVA solution and TiO_2 powder were ground in a ball mill (Retsch PM-100, Germany) with yttria-stabilized zirconia (YSZ) balls at 250 rpm for 24 h. After drying, the resulting powder was ground and sieved in a 45-mesh sieve. 0.2 g of sieved powder was pressed in a manual hydraulic press (GS25011, Specac, UK) at 40 MPa. The pellets were treated at 400°C for 5 h to remove the PVA binder. Then, a 3 M $Sr(OH)_2.8H_2O$ solution was prepared and loaded into an autoclave (Parr Instruments 4748 model, USA) for hydrothermal reaction with TiO_2 pellets at 70 vol% filling. After the reaction, the final pellets were washed with DI water and dried at 80 °C overnight.

The fracture surface morphology and elemental composition of the monolithic samples were analyzed by Scanning Electron Microscopy (SEM, FEI, Quanta 250, USA) equipped with Energy Dispersive X-Ray Analysis (EDX) detector. Before SEM analysis, the surfaces of the pellets to be examined were coated with approximately 10 nm Au. In addition, non-coated samples were used for EDS analysis.

X-ray diffraction (XRD) measurements were performed with the Philips X'Pert Pro (Holland) device, which is equipped with a Copper anode X-ray source ($Cu_{K\alpha}$ = 1.5406 Å at 40kV, 30 mA). Rietveld analysis was performed by ReX software [158], starting from the model containing the $SrTiO_3$ and TiO_2 reference crystal structures and refining phases weight fractions as well as their lattice and microstructural parameters. Nitrogen (N_2) gas sorption analyses were done by Gemini V (Micromeritics, Norcross,

GA, USA). The samples were degassed at 150°C for 12 h before examinations. Specific surface area (SSA) was determined from a BET (Brunauer–Emmett– Teller) analysis. The bulk densities of the samples were measured using Archimedes' principle with ethanol. Reaction completion (%) was calculated in two ways. The first one was based on Rietveld phase fractions from XRD data. Secondly, reaction completion values were estimated from the weight change before and after the reaction via **Eq (7.1)** where $Sr(OH)_2$ is the infiltrating species, TiO_2 is the porous solid matrix (green body), and $SrTiO_{3(s)}$ and $H_2O_{(l)}$ are the reaction products.

$$TiO_{2(s)} + Sr(OH)_2 = SrTiO_{3(s)} + H_2O_{(l)} \quad (7.1)$$

The dielectric constant measurements were obtained at room temperature in the 0.02-100 kHz range. As reported previously, the photocatalytic activity was analyzed through time-dependent photodegradation studies of a 2.5 ppm aqueous dye (Methylene Blue, MB) solution [159]. The optical properties were investigated by an ultraviolet-visible (UV–Vis) absorption double beam spectrophotometer (Cary100 Bio; Agilent Technologies Pty Ltd., Mulgrave, VIC, Australia) in a 200–500 nm wavelength range.

7.3. Results and Discussion

The porous green titania body, formed homogeneously over the entire surface, can be seen in the SEM image in **Fig. 7.1(a, and inset)**. As given in **Fig. 7.1(b)** and the detailed higher magnification image in the inset, the sample reacted at 90°C also had a porous structure. Instead, when **Fig. 7.1(c)** and **(d)** are analyzed, it can be seen that the microstructures of the samples became denser when the reaction was conducted at 120°C and 140°C, respectively.

It is already shown that a porous component can be densified via rHLPD technique without noticeable shrinkage [160]. This is because the crystalline phase of the parent porous substrate changes to another phase having a larger molar volume, i.e., volume expansion contributes to pore closure and densification. Here, in a particular example, titania has a density of (ρ_{TiO_2}) 3.9 g/cm^3, and molar volume of ($V^m_{TiO_2}$) 20.5 cm^3. Instead, $SrTiO_3$ has a density (ρ_{SrTiO_3}) of 5.1 g/cm^3, and molar volume of ($V^m_{SrTiO_3}$) 36 cm^3. If one

mole of titania is converted fully to one mole $SrTiO_3$, i.e., 100% reaction yield, a molar volume expansion of ~76% should be expected [161]. Accordingly, when the reaction proceeds via Eq.(7.1), it yields $SrTiO_3$, a higher molar volumed compound that will cause densification due to pore closure without measurable shrinkage.

The relative densities of TiO_2 green bodies used in all studies were around 52%, i.e., 48 vol% total porosity, taking the theoretical density of 3.9 g/cm^3 (anatase) [162]. The reaction completions (% mole conversion of TiO_2 to $SrTiO_3$) can be assessed from the weight changes for the samples treated at different temperatures, then the estimated values can be used to compute corresponding volume expansions to derive final relative densities ($\rho_{bulk} / \rho_{true_{via\ ROM}}$) after the reaction. As seen in **Fig. 7.1(e)**, the lowest relative density was observed from the 90°C reaction, while the highest was found as 78% for the sample reacted at 120°C for 24 h.

Hydrothermal reactions occurred sparsely in the samples produced at 90 °C, probably due to the limited solubilities of the species. The solubility enhancement determines an increase in the mass transport rates, facilitating the crystallization of $SrTiO_3$ and densification [160,162,163]. The increase in the reaction temperature caused more pronounced densification up to 120°C. While further experiments are needed to clarify such a point, the slight difference observed for 140°C treated samples can be due to the differences in the green body relative densities, experimental errors, or aggregated particles observed previously for the synthesis of $SrTiO_3$. Shen et al. [164] demonstrated that as the $SrTiO_3$ hydrothermal reaction temperature increased beyond 120°C, the $SrTiO_3$ particle size increased irregularly and formed heterogeneous microstructures.

The XRD data of the green pellet was consistent with the anatase phase (ICDD # 01-071-1166), as shown in **Fig. 7.1(f).** The characteristic peaks of the $SrTiO_3$ samples appeared at 32.0, 40.0, 46.5, 57.5, 68.0, and 77.0° and can be ascribed to the (110), (111), (200), (211), (220), and (310) planes for the cubic symmetry of $SrTiO_3$, matching well with ICDD # 01-073-0661. Apart from these crystalline phases, the XRD detected no other peaks. While it was not observed, it should be noted that $SrCO_3$ can frequently form as a byproduct when carbon dioxide or carbonate ions are present in the reaction vessel [160,162,163].

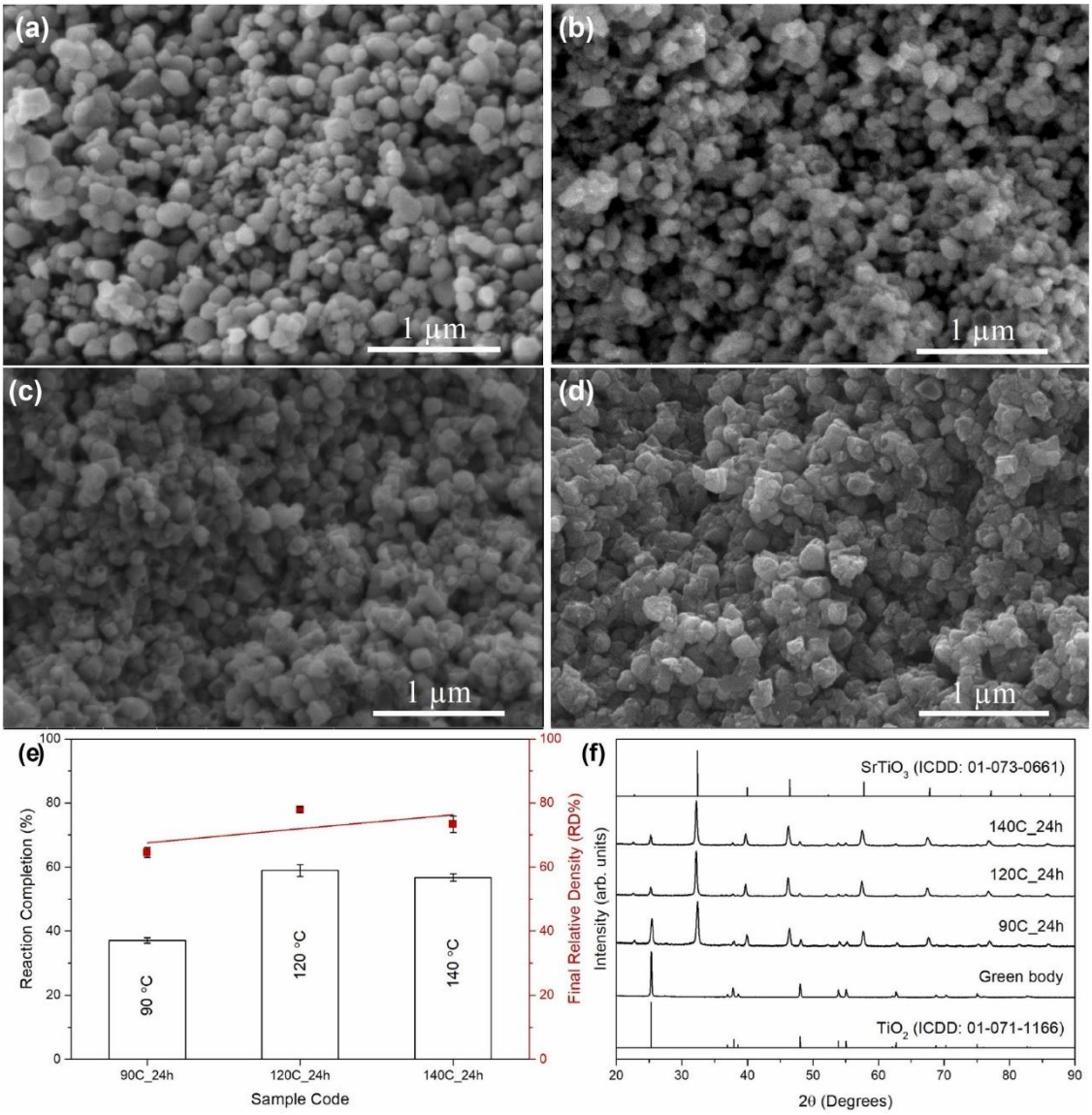

Figure 7.1. SEM images obtained from the fractured surfaces of (a) TiO_2 green body, (b-d) pellets obtained from the reactions at different temperatures in 24 h: (b) 90C_24h, (c) 120C_24h, (d) 140C_24h, (e) Reaction completion (%) vs. final relative density (RD%) data of all pellets produced at different temperatures in 24 h, (f) Normalized XRD patterns of TiO_2 green body and rHLPD sintered bodies at different reaction temperatures for 24 h, ICDD #01-071-1166 (TiO_2) and #01-073-0661 ($SrTiO_3$) were also included in the plot.

Rietveld refinement was conducted on all 24h treated samples, and a refined pattern of 120C_24h is reported in **Fig. 7.2**. For all analyzed samples, nearly full matches with relatively small residual fitting errors can be seen below the example fit. Apart from the marked $SrTiO_3$ and TiO_2 phases, no extra peak was observed for any other crystalline phase (e.g., $SrCO_3$). According to fittings conducted on selected samples, it was found that the 90C_24h had 33 mol.%, 120C_24h had 61 mol.%, and 140C_24h was found to have reaction completion of 58 mol.%. R_{wp} fitness values between 7% and 9% suggest a quite well agreement between the calculated model and the experimental data. The reaction completion calculations were followed in two ways; (i) using the initial and final weights and (ii) the relative phase fractions obtained from the Rietveld analysis, and all the data were compatible. For example, the calculated reaction completion for the 120C_24h sample was around 57 mol.% (from weight gain), close to the Rietveld fitting result of 61 mol.%. As a result, if one calculates the volume expansion related to such a mole conversion through reaction (I), a final relative density of 77%, similar to the one obtained from Archimedes' measurement of 78% can be observed.

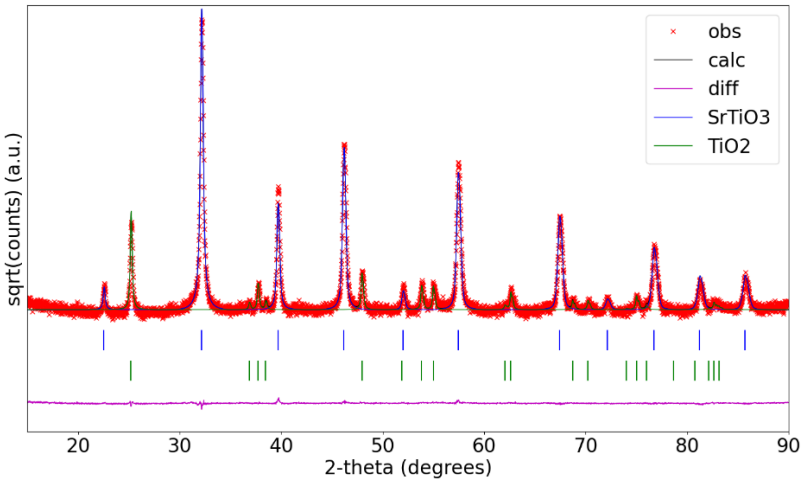

Figure 7.2. Rietveld refinement of the x-ray diffraction pattern collected on the sample reacted for 24 h at 120°C (120C_24h). The red dots correspond to the observed (obs) experimental data, whereas the continuous blue and green profiles represent the modeled signals for the $SrTiO_3$ and TiO_2 phases, respectively. Below the calculated (calc) fit, Bragg reflection positions are marked with the corresponding color code; the residual error (difference: diff) plot is reported in violet.

SEM micrograph taken from the fractured surface of the sample reacted for 72 h at 120 °C (120C_72h) is shown in **Fig. 7.3(a)**. At different temperatures, relatively dense microstructures were obtained for longer reaction times, affecting the nucleation rate [165]. The relative density values of the pellets obtained in the rHLPD experiments performed at different reaction times are shown in **Fig. 7.3(b)**. When the reaction was conducted for 72 h, comparable relative density values of around 80% were observed.

While the increase in reaction time caused enhanced $SrTiO_3$ formation, it is essential to note that the kinetics was slower than those for the other rHLPD studies [30,31]. Similar observations were reported for hydrothermal synthesis of $SrTiO_3$ using anatase to react at 200°C. A significant amount of unreacted titania was found even after 48 h of reaction [162,166–168]. XRD data obtained from the samples reacted for different periods at 120°C (see **Fig. 7.3(c)**) and 140°C (data not shown for brevity) demonstrates merely the formation of a $SrTiO_3$-TiO_2 ceramic heterostructure system.

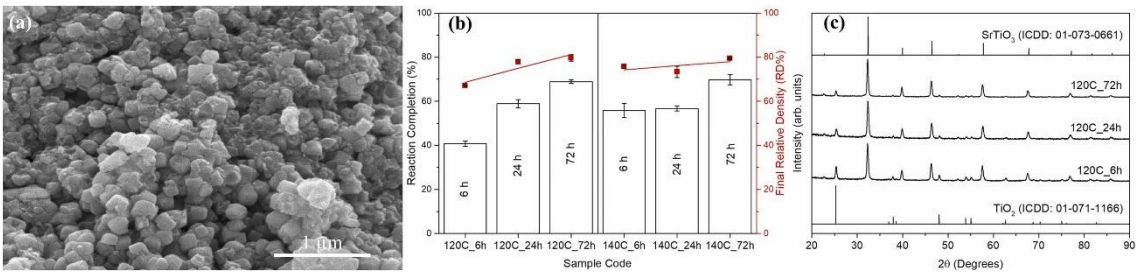

Figure 7.3. (a) SEM micrograph taken from the fractured surface of 120C_72h sample, (b) Reaction completion (%) vs. final relative density (RD%) graph of all pellets produced at different temperatures in 24 h at 120°C and 140°C, (c) XRD pattern of samples obtained at 120°C in different reaction times (6, 24, and 72 h).

SEM image taken from the fracture surface of the 120C_24h_1M sample, obtained from the reaction at 120°C for 24 h, under 1 M NaOH concentration, is given in **Fig. 7.4(a)**. A homogeneous microstructure can be seen, as in all other samples. When the EDX images obtained from the fracture surface (**Fig. 7.4(b)**) are analyzed, it is possible to see that Sr, Ti, and O are homogeneously distributed, but no Na was observed

over the entire scanned pellet surface. The examination was also conducted from the top surface to 110 μm depth (see **Fig. 7.4(c)**), and consistently, only Sr, Ti, and O were found. Accordingly, it is possible to state that the reaction proceeded virtually homogenous throughout the sample. Since the formation of $SrTiO_3$ necessitates the parent titania surface, the structure was probably composed of anatase-TiO_2-cored $SrTiO_3$, as documented in previous hydrothermal reaction studies [162].

The final relative density of the pellets obtained by rHLPD experiments performed at 1 M NaOH concentration is shown in **Fig. 7.4(d)**. Similar to other studies, the tendency of $SrTiO_3$ formation increased with NaOH, i.e., NaOH enhanced the sample relative densities and reaction conversions [169]. It was already documented that the $SrTiO_3$ synthesis is supported by increased alkalinity [160,169]. Lencka and Riman constructed a Sr-Ti-H_2O stability diagram based on theoretical calculations. The authors showed that the $SrTiO_3$ formation from TiO_2 requires an alkaline medium for enhanced dissolution of TiO_2 and subsequent precipitation of $SrTiO_3$ [160,163,170].

The XRD analysis of the samples reacted under 1 M NaOH concentrations is given in **Fig. 7.4(e)**. When the XRD patterns are examined, clear peaks of $SrTiO_3$ and TiO_2 without additional crystalline phases can be seen in all samples, corroborating that $SrTiO_3$ is the predominant reaction product in the experimental conditions [162].

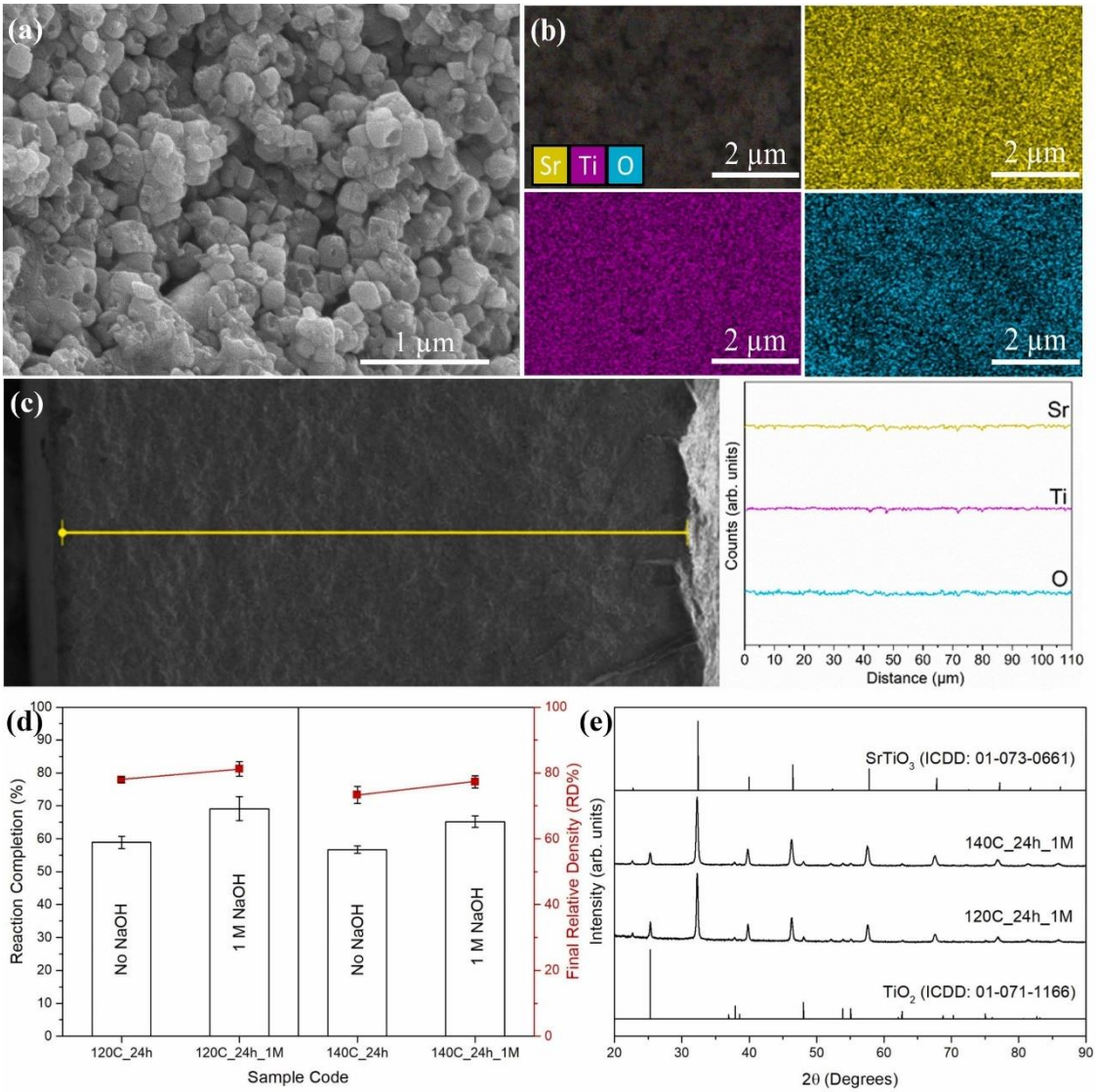

Figure 7.4. (a) SEM images of the fractured surface of the 120C_24h_1M pellet obtained at 120°C in 24 h under 1 M NaOH concentration condition, (b) EDX mapping from the center of the fracture surface of the 120C_24h_1M pellet, (c) EDX scan from the top surface to 110 µm depth, (d) Reaction completion (%) vs. final relative density (RD%) graph of all pellets produced at 120°C and 140°C in different NaOH concentrations (without NaOH and 1 M). (e) XRD pattern of samples obtained at 120°C and 140°C in 1 M NaOH concentration.

An indirect optical band gap (E_g) value of 3.25 eV, similarly observed for $SrTiO_3$-TiO_2 heterostructures [148], was found using Kubelka-Munk transformation (see **Fig. 7.5(a-inset)**) from reflectance spectra (shown in **Fig. 7.5(a)**). **Fig. 7.5(b)** demonstrates

the photocatalytic performance of the 120C_24h_1M pellet with only 20 vol% total porosity. The intensity of absorption peaks decreased with time, and the degradation efficiency of MB dye was around 60% in 5 h. The change in the concentration of MB vs. UV-Vis irradiation time can be seen in **Fig. 7.5(b-inset)**. Although the 120C_24h_1M sample had a low SSA of 5.7 m^2/g, it showed better degradation efficiency with a higher photodegradation rate constant (0.0028 min^{-1}) than other monolithic $SrTiO_3$-TiO_2 and N-doped $SrTiO_3$-TiO_2 systems with approximately five times larger surface area of 27.8 m^2/g [171,172].

The dielectric constant and dielectric loss curves obtained from the same sample (120C_24h_1M) are shown in **Fig. 7.5(c)**. The dielectric constant was around 500 at high frequencies (above 10 kHz), and the dielectric loss decreased significantly above 10 kHz, falling below 0.25 [173]. A few recent works proposed ferroelectricity-based photocatalysts with enhanced photocatalytic performance due probably to the polarization-dependent band bending of $BaTiO_3$ [174]. While $SrTiO_3$ is paraelectric and the correlation of dielectric properties with the photocatalytic performance of TiO_2-$SrTiO_3$ heterostructured monoliths is beyond the scope of the present work, further investigations are of interest.

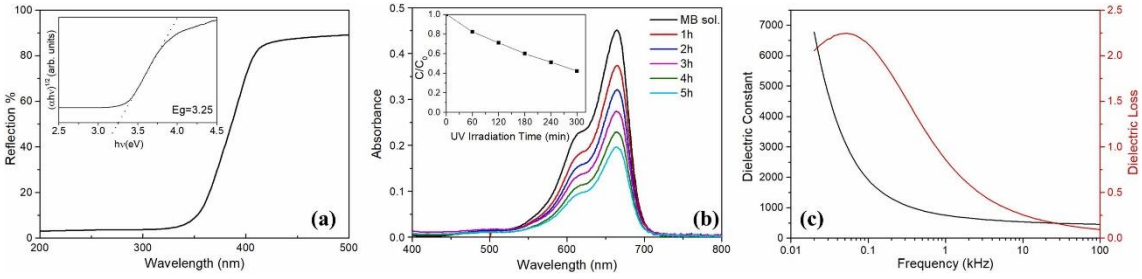

Figure 7.5. (a) Reflectance spectra of 120C_24h_1M (obtained at 120°C in 24 h under 1 M NaOH concentration) pellet (the top-left inset represents Kubelka–Munk plot of reflectance spectra to calculate the band gap energy), (b) UV-Vis absorption spectra showing the photocatalytic degradation of Methylene Blue dye using 120C_24h_1M pellet under UV-Vis irradiation (the top-left inset represents concentration change of Methylene Blue vs. UV-Vis irradiation time), and (c) Frequency-dependent dielectric constant and dielectric loss of the same sample obtained at room temperature.

7.4. Conclusions

$SrTiO_3$-TiO_2 monolithic ceramic heterostructures were produced using a novel cold sintering technique called rHLPD. The effect of different temperatures, time, and NaOH concentrations was investigated. Only $SrTiO_3$ and TiO_2 phases were observed within the XRD method limits, with no extra peaks resolvable for any other crystalline structure. The optimum reaction parameters were set at 120°C for 24 h with 1M NaOH, yielding ~80% dense components having reaction completion of 69 mol.%. The dielectric constant measurements demonstrated that at high frequencies above 10 kHz, the dielectric constant was around 500, and the dielectric loss value was below 0.25. The monolithic $SrTiO_3$-TiO_2 ceramic pellets with 20 vol% total porosity were used to degrade Methylene Blue dye photo-catalytically, and ~60% efficiency was observed in 5 h.

References

[1] P. Liu, N. Han, W. Wang, R. Ran, W. Zhou, Z. Shao, High-Quality Ruddlesden–Popper Perovskite Film Formation for High-Performance Perovskite Solar Cells, Adv. Mater. 33 (2021) 2002582. https://doi.org/10.1002/adma.202002582.

[2] H.-Y. Kim, J. Shin, I.-C. Jang, Y.-W. Ju, Hydrothermal synthesis of three-dimensional perovskite $NiMnO_3$ oxide and application in supercapacitor electrode, Energies (Basel). 13 (2019) 36. https://doi.org/10.3390/en13010036.

[3] A. Fakharuddin, M.K. Gangishetty, M. Abdi-Jalebi, S.-H. Chin, Abd.R. bin Mohd Yusoff, D.N. Congreve, W. Tress, F. Deschler, M. Vasilopoulou, H.J. Bolink, Perovskite light-emitting diodes, Nat. Electron. 5 (2022) 203–216. https://doi.org/10.1038/s41928-022-00745-7.

[4] S. Tasleem, M. Tahir, Recent progress in structural development and band engineering of perovskites materials for photocatalytic solar hydrogen production: A review, Int. J. Hydrog. Energy. 45 (2020) 19078–19111. https://doi.org/10.1016/j.ijhydene.2020.05.090.

[5] K. Wei, Y. Faraj, G. Yao, R. Xie, B. Lai, Strategies for improving perovskite photocatalysts reactivity for organic pollutants degradation: A review on recent

progress, Chem. Eng. J. 414 (2021) 128783. https://doi.org/10.1016/j.cej.2021.128783.

[6] J. Sun, T. Gao, X. Song, Y. Zhao, Y. Lin, H. Wang, D. Ma, Y. Chen, W. Xiang, J. Wang, Y. Zhang, Z. Liu, Direct Growth of High-Quality Graphene on High-κ Dielectric $SrTiO_3$ Substrates, J. Am. Chem. Soc. 136 (2014) 6574–6577. https://doi.org/10.1021/ja5022602.

[7] H. Zhan, Z.-G. Chen, J. Zhuang, X. Yang, Q. Wu, X. Jiang, C. Liang, M. Wu, J. Zou, Correlation between Multiple Growth Stages and Photocatalysis of $SrTiO_3$ Nanocrystals, J. Phys. Chem. C. 119 (2015) 3530–3537. https://doi.org/10.1021/jp512448p.

[8] S.A. Hayward, E.K.H. Salje, Cubic-tetragonal phase transition in $SrTiO_3$ revisited: Landau theory and transition mechanism, Ph. Transit. 68 (1999) 501–522. https://doi.org/10.1080/01411599908224530.

[9] M. Bäurer, H. Kungl, M.J. Hoffmann, Influence of Sr/Ti Stoichiometry on the Densification Behavior of Strontium Titanate, J. Am. Ceram. Soc. 92 (2009) 601–606. https://doi.org/10.1111/j.1551-2916.2008.02920.x.

[10] W. Bian, X. Lu, Y. Li, C. Min, H. Zhu, Z. Fu, Q. Zhang, Influence of Nd doping on microwave dielectric properties of $SrTiO_3$ ceramics, J. Mater. Sci. Mater. Electron. 29 (2018) 2743–2747. https://doi.org/10.1007/s10854-017-8201-y.

[11] Y. Zhao, Y. Guo, J. Li, P. Li, Efficient hydrogen evolution with ZnO/$SrTiO_3$ S-scheme heterojunction photocatalyst sensitized by Eosin Y, Int. J. Hydrog. Energy. 46 (2021) 18922–18935. https://doi.org/10.1016/j.ijhydene.2021.03.051.

[12] R. V Nair, V.S. Gummaluri, M.V. Matham, V. C, A review on optical bandgap engineering in TiO_2 nanostructures via doping and intrinsic vacancy modulation towards visible light applications, J. Phys. D. Appl. Phys. 55 (2022) 313003. https://doi.org/10.1088/1361-6463/ac6135.

[13] X. Wang, R.A. Caruso, Enhancing photocatalytic activity of titania materials by using porous structures and the addition of gold nanoparticles, J. Mater. Chem. 21 (2011) 20–28. https://doi.org/10.1039/C0JM02620D.

[14] T. Cao, Y. Li, C. Wang, C. Shao, Y. Liu, A Facile in Situ Hydrothermal Method to $SrTiO_3$/TiO_2 Nanofiber Heterostructures with High Photocatalytic Activity, Langmuir. 27 (2011) 2946–2952. https://doi.org/10.1021/la104195v.

[15] J. Zhang, J.H. Bang, C. Tang, P. V Kamat, Tailored TiO_2−$SrTiO_3$ Heterostructure Nanotube Arrays for Improved Photoelectrochemical Performance, ACS Nano. 4 (2010) 387–395. https://doi.org/10.1021/nn901087c.

[16] E.-C. Su, B.-S. Huang, J.-T. Lee, M.-Y. Wey, Excellent dispersion and charge separation of $SrTiO_3$-TiO_2 nanotube derived from a two-step hydrothermal process for facilitating hydrogen evolution under sunlight irradiation, Solar Energy. 159 (2018) 751–759. https://doi.org/10.1016/j.solener.2017.11.048.

[17] C. Vakifahmetoglu, L. Karacasulu, Cold sintering of ceramics and glasses: A review, Curr. Opin. Solid State Mater. Sci. 24 (2020) 100807. https://doi.org/10.1016/j.cossms.2020.100807.

[18] M. Biesuz, S. Grasso, V.M. Sglavo, What's new in ceramics sintering? A short report on the latest trends and future prospects, Curr. Opin. Solid State Mater. Sci. 24 (2020) 100868. https://doi.org/10.1016/j.cossms.2020.100868.

[19] A. Galotta, V.M. Sglavo, The cold sintering process: A review on processing features, densification mechanisms and perspectives, J. Eur. Ceram. Soc. 41 (2021) 1–17. https://doi.org/10.1016/j.jeurceramsoc.2021.09.024.

[20] J. Guo, R. Floyd, S. Lowum, J.-P. Maria, T. Herisson de Beauvoir, J.-H. Seo, C.A. Randall, Cold Sintering: Progress, Challenges, and Future Opportunities, Annu. Rev. Mater. Res. 49 (2019) 275–295. https://doi.org/10.1146/annurev-matsci-070218-010041.

[21] H. Guo, A. Baker, J. Guo, C.A. Randall, Cold Sintering Process: A Novel Technique for Low-Temperature Ceramic Processing of Ferroelectrics, J. Am. Ceram. Soc. 99 (2016) 3489–3507. https://doi.org/10.1111/jace.14554.

[22] H. Guo, J. Guo, A. Baker, C.A. Randall, Hydrothermal-assisted cold sintering process: a new guidance for low-temperature ceramic sintering, ACS Appl. Mater. Interfaces. 8 (2016) 20909–20915. https://doi.org/10.1021/acsami.6b07481.

[23] L. Karacasulu, M. Tokkan, M. Bortolotti, G. Ischia, U. Adem, C. Vakifahmetoglu, Electrical characteristics of low temperature densified barium titanate, Ceram. Int. 46 (2020) 16670–16676. https://doi.org/10.1016/j.ceramint.2020.03.240.

[24] J.-P. Ma, X.-M. Chen, W.-Q. Ouyang, J. Wang, H. Li, J.-L. Fang, Microstructure, dielectric, and energy storage properties of $BaTiO_3$ ceramics prepared via cold sintering, Ceram. Int. 44 (2018) 4436–4441. https://doi.org/10.1016/j.ceramint.2017.12.044.

[25] H.-Z. Shen, N. Guo, P. Shen, Synthesis and densification of $BaZrO_3$ ceramics by reactive cold sintering of $Ba(OH)_2{\cdot}8H_2O$-$Zr(OH)_4$ powders, J. Eur. Ceram. Soc. 43 (2023) 392–400. https://doi.org/10.1016/j.jeurceramsoc.2022.10.016.

[26] P. Castellani, C. Nicollet, E. Quarez, O. Joubert, A. Le Gal La Salle, Synthesis of Yttrium Doped Barium Zirconate/Cerate Electrolyte Materials and Densification Using Conventional and Cold-Sintering Processes, ECS Trans. 109 (2022) 13. https://doi.org/10.1149/10913.0013ecst.

[27] V.L. Vilesh, N. Santha, G. Subodh, Influence of Li_2MoO_4 and polytetrafluoroethylene addition on the cold sintering process and dielectric properties of $BaBiLiTeO_6$ ceramics, Ceram. Int. 47 (2021) 30756–30763. https://doi.org/10.1016/j.ceramint.2021.07.255.

[28] R. Boston, J. Guo, S. Funahashi, A.L. Baker, I.M. Reaney, C.A. Randall, Reactive intermediate phase cold sintering in strontium titanate, RSC Adv. 8 (2018) 20372–20378. https://doi.org/10.1039/C8RA03072C.

[29] N. Guo, H.-Z. Shen, P. Shen, One-step synthesis and densification of $BaTiO_3$ by reactive cold sintering, Scr Mater. 213 (2022) 114628. https://doi.org/10.1016/j.scriptamat.2022.114628.

[30] C. Vakifahmetoglu, J.F. Anger, V. Atakan, S. Quinn, S. Gupta, Q. Li, L. Tang, R.E. Riman, Reactive Hydrothermal Liquid-Phase Densification (rHLPD) of Ceramics - A Study of the $BaTiO_3$ [TiO_2] Composite System, J. Am. Ceram. Soc. 99 (2016) 3893–3901. https://doi.org/10.1111/jace.14468.

[31] R.E. Riman, V. Atakan, Method of hydrothermal liquid phase sintering of ceramic materials and products derived therefrom, US Patent 8,313,802, (2012).

[32] M. Bortolotti, L. Lutterotti, I. Lonardelli, ReX: a computer program for structural analysis using powder diffraction data, J Appl Crystallogr. 42 (2009) 538–539. https://doi.org/10.1107/S0021889809008309.

[33] O. Icin, C. Vakifahmetoglu, Dye removal by polymer derived ceramic nanobeads, Ceram. Int. 47 (2021) 27050–27057. https://doi.org/10.1016/j.ceramint.2021.06.118.

[34] M.M. Lencka, R.E. Riman, Hydrothermal synthesis of perovskite materials: Thermodynamic modeling and experimental verification, Ferroelectrics. 151 (1994) 159–164. https://doi.org/10.1080/00150199408244737.

[35] A. Saboori, X. Chen, C. Badini, P. Fino, M. Pavese, Reactive spontaneous infiltration of Al-activated TiO_2 by molten aluminum, Trans. Nonferrous Met. Soc. China. 29 (2019) 657–666. https://doi.org/10.1016/S1003-6326(19)64976-9.

[36] V. Kalyani, B.S. Vasile, A. Ianculescu, A. Testino, A. Carino, M.T. Buscaglia, V. Buscaglia, P. Nanni, Hydrothermal Synthesis of $SrTiO_3$: Role of Interfaces, Cryst. Growth Des. 15 (2015) 5712–5725. https://doi.org/10.1021/acs.cgd.5b00770.

[37] G. Canu, V. Buscaglia, Hydrothermal synthesis of strontium titanate: thermodynamic considerations, morphology control and crystallisation mechanisms, CrystEngComm. 19 (2017) 3867–3891. https://doi.org/10.1039/C7CE00834A.

[38] H. Shen, Y. Lu, Y. Wang, Z. Pan, G. Cao, X. Yan, G. Fang, Low temperature hydrothermal synthesis of $SrTiO_3$ nanoparticles without alkali and their effective photocatalytic activity, J. Adv. Ceram. 5 (2016) 298–307. https://doi.org/10.1007/s40145-016-0203-3.

[39] Y. Zhang, L. Zhong, D. Duan, A single-step direct hydrothermal synthesis of $SrTiO_3$ nanoparticles from crystalline P25 TiO_2 powders, J. Mater. Sci. 51 (2016) 1142–1152. https://doi.org/10.1007/s10853-015-9445-7.

[40] V. Kalyani, B.S. Vasile, A. Ianculescu, M.T. Buscaglia, V. Buscaglia, P. Nanni, Hydrothermal Synthesis of $SrTiO_3$ Mesocrystals: Single Crystal to Mesocrystal Transformation Induced by Topochemical Reactions, Cryst Growth Des. 12 (2012) 4450–4456. https://doi.org/10.1021/cg300614f.

[41] L. Fang, E. Hu, X. Hu, Z. Jiang, M.A.K.Y. Shah, J. Wang, F. Wang, Development of a Core–Shell Heterojunction TiO_2/$SrTiO_3$ Electrolyte with Improved Ionic Conductivity, ChemPhysChem. 23 (2022) e202200314. https://doi.org/10.1002/cphc.202200314.

[42] J. Ng, S. Xu, X. Zhang, H.Y. Yang, D.D. Sun, Hybridized Nanowires and Cubes: A Novel Architecture of a Heterojunctioned TiO_2/$SrTiO_3$ Thin Film for Efficient Water Splitting, Adv Funct Mater. 20 (2010) 4287–4294. https://doi.org/10.1002/adfm.201000931.

[43] S.-T. Huang, W.W. Lee, J.-L. Chang, W.-S. Huang, S.-Y. Chou, C.-C. Chen, Hydrothermal synthesis of $SrTiO_3$ nanocubes: Characterization, photocatalytic activities, and degradation pathway, J Taiwan Inst Chem Eng. 45 (2014) 1927–1936. https://doi.org/10.1016/j.jtice.2014.02.003.

[44] M.M. Lencka, R.E. Riman, Thermodynamics of the Hydrothermal Synthesis of Calcium Titanate with Reference to Other Alkaline-Earth Titanates, Chem. Mater. 7 (1995) 18–25. https://doi.org/10.1021/cm00049a006.

[45] O. Ruzimuradov, S. Nurmanov, M. Hojamberdiev, R.M. Prasad, A. Gurlo, J. Broetz, K. Nakanishi, R. Riedel, Preparation and characterization of macroporous TiO_2–$SrTiO_3$ heterostructured monolithic photocatalyst, Mater. Lett. 116 (2014) 353–355. https://doi.org/10.1016/j.matlet.2013.11.065.

[46] O. Ruzimuradov, K. Sharipov, A. Yarbekov, K. Saidov, M. Hojamberdiev, R.M. Prasad, G. Cherkashinin, R. Riedel, A facile preparation of dual-phase nitrogen-doped TiO_2–$SrTiO_3$ macroporous monolithic photocatalyst for organic dye photodegradation under visible light, J. Eur. Ceram. Soc. 35 (2015) 1815–1821. https://doi.org/10.1016/j.jeurceramsoc.2014.12.023.

[47] Z. Wang, M. Cao, Z. Yao, Q. Zhang, Z. Song, W. Hu, Q. Xu, H. Hao, H. Liu, Z. Yu, Giant permittivity and low dielectric loss of $SrTiO_3$ ceramics sintered in nitrogen atmosphere, J. Eur. Ceram. Soc. 34 (2014) 1755–1760. https://doi.org/10.1016/j.jeurceramsoc.2014.01.015.

[48] G. Panthi, M. Park, Approaches for enhancing the photocatalytic activities of barium titanate: A review, J. Energy Chem. 73 (2022) 160–188. https://doi.org/10.1016/j.jechem.2022.06.023.

CHAPTER 8

FAST-FIRING OF POTASSIUM SODIUM NIOBATE

The following chapter is written in the format of a manuscript submitted to Open Ceramics.

Abstract

Potassium sodium niobate (KNN) is one of the most promising Pb-free piezo ceramics. In present work, KNN was produced by fast-firing with different cooling strategies, i.e., fast and slow cooling. Dielectric, ferroelectric, and piezoelectric properties of fast-fired pellets were determined and compared with those of conventional-sintered products. Although the samples produced by fast-firing had higher density than those obtained by conventional sintering, fast-cooled samples following fast firing show relatively low electrical properties. When fast-firing was combined with slow cooling, the electrical properties, especially piezoelectric d_{33} values, were improved. The material subjected to fast-firing at 1120°C using slow cooling gave the highest relative density (about 95%) with fine grains microstructure and a d_{33} of 112 pC/N whereas that produced by conventional sintering resulted in d_{33} of 80 pC/N with a relative density of 88% for the same dwell time (30 min).

8.1. Introduction

Firing has been used to densify ceramics for thousands of years. Traditionally, it consists of high-temperature treatment of a powder compact using heating rates ranging from a fraction to a few degrees Celsius per minute. For over half a century,

unconventional sintering techniques have been proposed to enhance densification and/or suppress grain growth of ceramics [1].

Fast-firing (FF), introduced at the beginning of the '80s, is a very straightforward non-conventional sintering process. It enables densification by utilizing much higher heating rate (10^2-10^3 °C/min) with shorter dwell time [1,2]. In the fast-firing process, large heating rate has a vital role in enhancing densification and grain growth control, similar to other unconventional sintering techniques like spark-plasma, microwave and flash sintering [1]. For the same relative density, fast-fired samples are typically characterized by finer grain size, and reduced pore/grain boundary separation compared to those obtained by conventional sintering [1,3].

Fast-firing (FF) involves the direct introduction of the green sample into the hot zone of a furnace so that the ceramic quickly reaches the high-temperature regime. This allows the material to pass through the temperature region where grain coarsening is activated without densification in a few seconds/minutes. This phenomenon is associated with the different activation energies for the two processes, where densification (involving bulk/grain boundary diffusion) is typically characterized by higher activation energy than coarsening and, as such, requires a higher temperature for being activated [2,4,5]. Due to its "simplicity", FF resulted as a popular sintering technique with several industrial applications and has been used to sinter both traditional and advanced ceramics [6]. Fast firing was used for the densification of several systems, including traditional ceramics such as tiles and sanitaryware [7–9], technical ceramics such as alumina[10–13], barium titanate [14–17], ferrites [18], indium tin oxide [19], lanthanum gallate [20], lead magnesium niobate [21,22], lead zirconia titanate [23–26], zirconia [3,13,17,27–29], Sm_2O_3-doped CeO_2 [30], and even composites [31].

Potassium sodium niobate, $K_{0.5}Na_{0.5}NbO_3$ (KNN), has attracted tremendous attention in recent years as lead-free and environmental-friendly piezoelectric material. Besides showing a relatively high Curie temperature ($T_c \cong 418$ °C), KNN is characterized by a large piezoelectric coefficient (d_{33} = 80 pC/N) when produced by conventional sintering [32,33]. In addition to that, reducing the particle size of the starting materials of pure KNN was observed to yield distinguishable results in d_{33} piezoelectric coefficients, increasing up to 107 pC/N through conventional technique [34]. The electrical properties of KNN are highly sensitive to the composition and this requires the maintenance of the desired stoichiometry during sintering [35–37]. Nevertheless, during conventional

sintering with long dwell times, high density cannot be reached due to the volatilization of alkali elements and the formation of secondary phase [38,39]. In addition, as a result of solid-state sintering (SSS) temperature (around 1120°C) which approaches KNN melting point (1140°C), lattice defects are generated and the stoichiometry might shift [40].

In the present study, fast-firing of KNN using powders produced by the solid-state synthesis was investigated for the first time. Dielectric, ferroelectric, and piezoelectric properties of the materials produced by FF were determined and compared with the conventional solid-state sintering process.

8.2. Experimental procedures

Nb_2O_5 (CAS#:12034-59-2, 99.9%, Sigma–Aldrich, USA), Na_2CO_3 (CAS#:497-18-8, ≥99%, Sigma Aldrich, USA) and K_2CO_3 (CAS#:584-08-7, ≥99.5%, Sigma Aldrich, USA) precursors were weighed in accordance with the stoichiometric ratio and mixed in ethanol for 24 h using a planetary ball mill at 250 rpm (Retsch PM-100, Germany). After drying the slurry, calcination was carried out at 850°C for 5 h in air, followed by ball-milling with zirconia spheres for 24 h.

The obtained powder was mixed with 10 wt% distilled water and uniaxially pressed under a pressure of 100 MPa within a steel die 8 mm in diameter. The green bodies with thickness of about 1.4 mm were dried overnight at 150°C. The specimens were subjected to fast-firing using a tubular furnace (Nabertherm P330, Lilienthal, Germany) kept at various temperatures ranging from 1090°C to 1130°C. The samples were inserted quickly into the tube furnace at the selected temperature and kept there for 30 min. The fast-fired samples were extracted from the furnace in two ways. Some of them were quickly (~1 min) taken out from the furnace and cooled in air (cooling rate ~18°C/s) - fast cooling (FC). Others were extracted in ~5 min (cooling rate ~4°C/s) - slow cooling (SC). Some green samples were also conventionally sintered at the selected temperature for 30 min using 3°C/min heating and cooling rate.

The bulk density of the specimens was determined using water via the Archimedes' principle. Crystalline phases were identified using an X-ray diffractometer (XRD, Italstructures IPD3000 diffractometer, Italy) with Cu anode X-Ray source. XRD

analysis were carried out in between 10° and 130° (2θ) range with 0.02° step size for a total of 1800s acquisition time. The morphology of the fracture surfaces was analyzed using scanning electron microscopy (SEM, FEI Quanta 250 FEG, USA). To measure the electrical properties, polished pellets produced by fast firing and conventional sintering were coated with silver paste on both surfaces and then cured at 200ºC for 20 min. The dielectric permittivity and loss variation with temperature was examined using an E4980AL LCR meter (Keysight Technologies, Santa Clara, CA, USA) at 100 kHz, from room temperature to 250°C because the sample holder (aixACCT, TFA 423-7) used for the dielectric measurement can endure up to 250 °C. The heating rate during measurement was 5 °C/min which was controlled by the temperature controller (aixACCT). The measurement was controlled with a Labview program. TF analyzer (aixACCT TF Analyzer 1000, Aachen, Germany), in conjunction with high voltage amplifier (TREK 610E, TREK, Medina, NY, USA) and laser-interferometer (SIOS Meßtechnik GmbH, Germany), was employed to generate P-E and S-E loops. The voltage applied during the P-E and S-E measurements was in the form of a triangular wave and was applied at 50 Hz. The frequency of 50 Hz was chosen because it was the maximum applicable frequency to suppress the leakage contribution to the hysteresis loops. To determine the piezoelectric coefficient (d_{33}), samples were poled under 40 kV/cm DC field at 25°C for 10 min in a silicone oil bath and then analyzed using a Berlincourt type d_{33} meter (Sinocera Piezoelectronics, YE2730A, China). The poling procedure was carried out by using TF analyzer and high voltage amplifier which are same instruments mentioned above. The force applied via d33 meter has an amplitude of 0.25 N with 110 Hz frequency and the accuracy of the measurements in the range of 10-200 pC/N is ±5%.

8.3. Results and discussion

The X-ray diffraction patterns of fast-fired and conventional sintered specimens are shown in **Fig. 8.1** and compared to that of KNN powder synthesized by solid-state reaction. For all samples, no phase transformations or secondary phases are observed. All peaks are associated with the ICDD data of $K_{0.5}Na_{0.5}NbO_3$ (ICDD # 96-230-0500), presenting an orthorhombic structure. The KNN powder possesses single broader peaks with shoulders at larger angles, as it is generally observed for temperatures below 850°C

[41]. XRD peaks become narrower and sharper as the sintering temperature increases, pointing out the larger crystallinity of the system when compared to the as-synthesized powder.

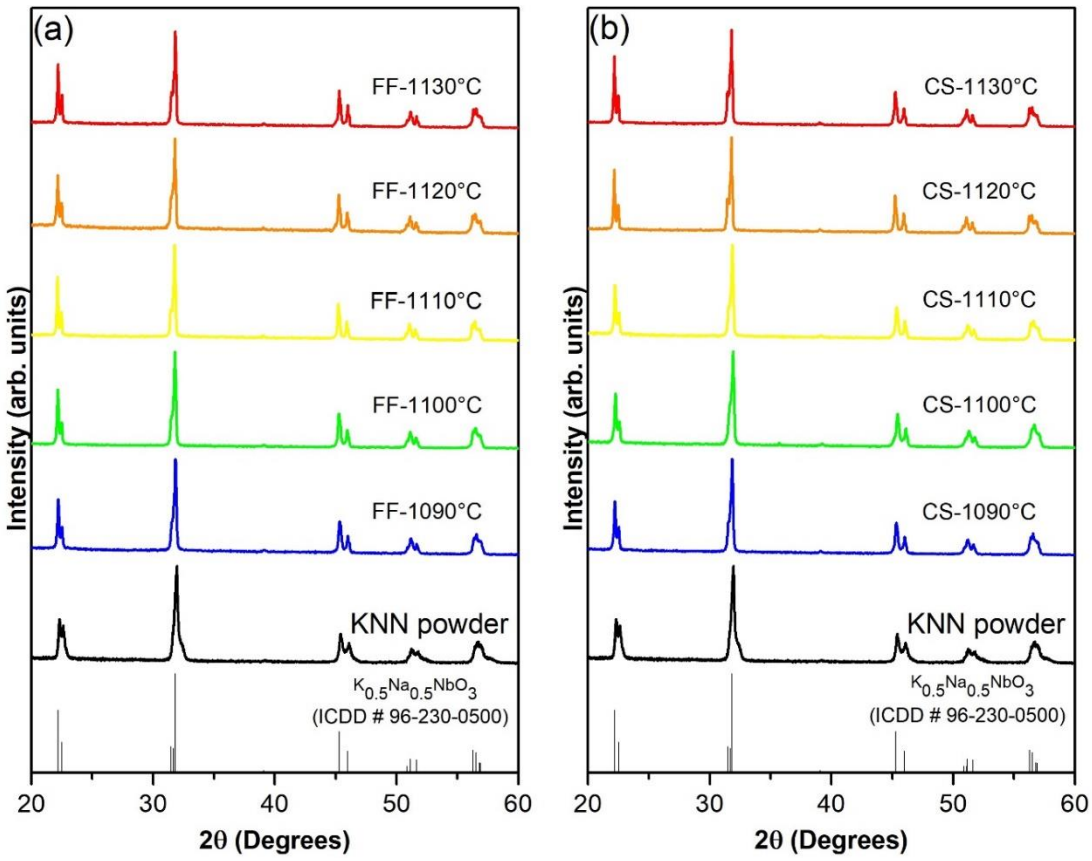

Figure 8.1. X-ray diffraction patterns of KNN samples produced at different temperatures (1090-1130°C) via (a) Fast-firing (FF) and (b) Conventional sintering (CS); the patter recorded on the KNN powder synthesized via the solid-state reaction (KNN powder) is shown for comparison.

The relative bulk density of FF samples is given in **Fig. 8.2**. While the sample sintered at 1090°C show the lowest densification (87.3%), a relative density of 93-94% was obtained from specimens sintered at 1120-1130°C, in proximity of the KNN melting point (1140°C) [40]. Conventionally sintered samples treated at the same temperatures achieved the lower densities than fast-fired ones. The sample sintered at 1130°C reaches a relative density of 91.7%, the relative density clearly increasing with temperature.

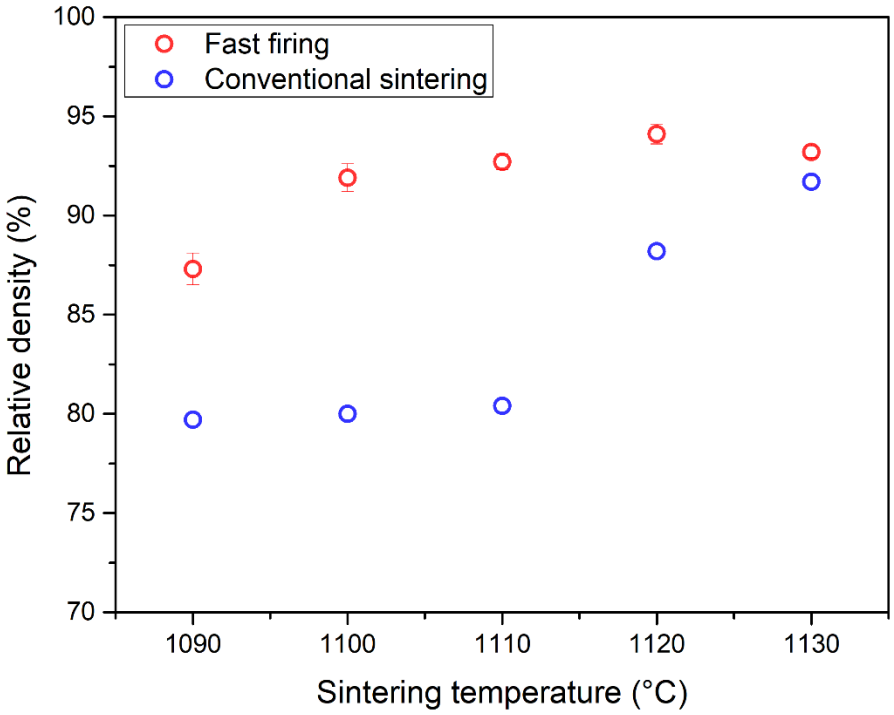

Figure 8.2. Relative density of fast-fired and conventional sintered samples as a function of temperature.

Figure 8.3 shows the fracture surface microstructure of fast-fired and conventionally sintered samples. The fracture surface of sample FFed at 1090°C shows relatively small grains. The microstructure development with increasing temperature points out grain growth and, sometimes, abnormal grain growth, similarly to conventional sintering process. Conversely, conventionally sintered samples show relatively low densification with cubic grains at 1090 and 1100°C while grain growth begins at 1110°C. At 1120°C, dense microstructure appears with bimodal grain size consisting of fine cube-shaped grains and large grains exceeding 10 µm. While intergranular fracture predominated around the smaller grains, transgranular fracture is visible in the large grains, similarly to previous study [42]. Indeed, this unique, abnormal grain growth phenomenon was observed in coarse KNN grains with specific core-shell structures. The core region consists of nano-sized grains, while the shell region has larger-sized similar self-assembled grains [43]. The extraordinary grain growth can be probably prevented by the FF because the activation energy for densification is higher than that for grain growth.

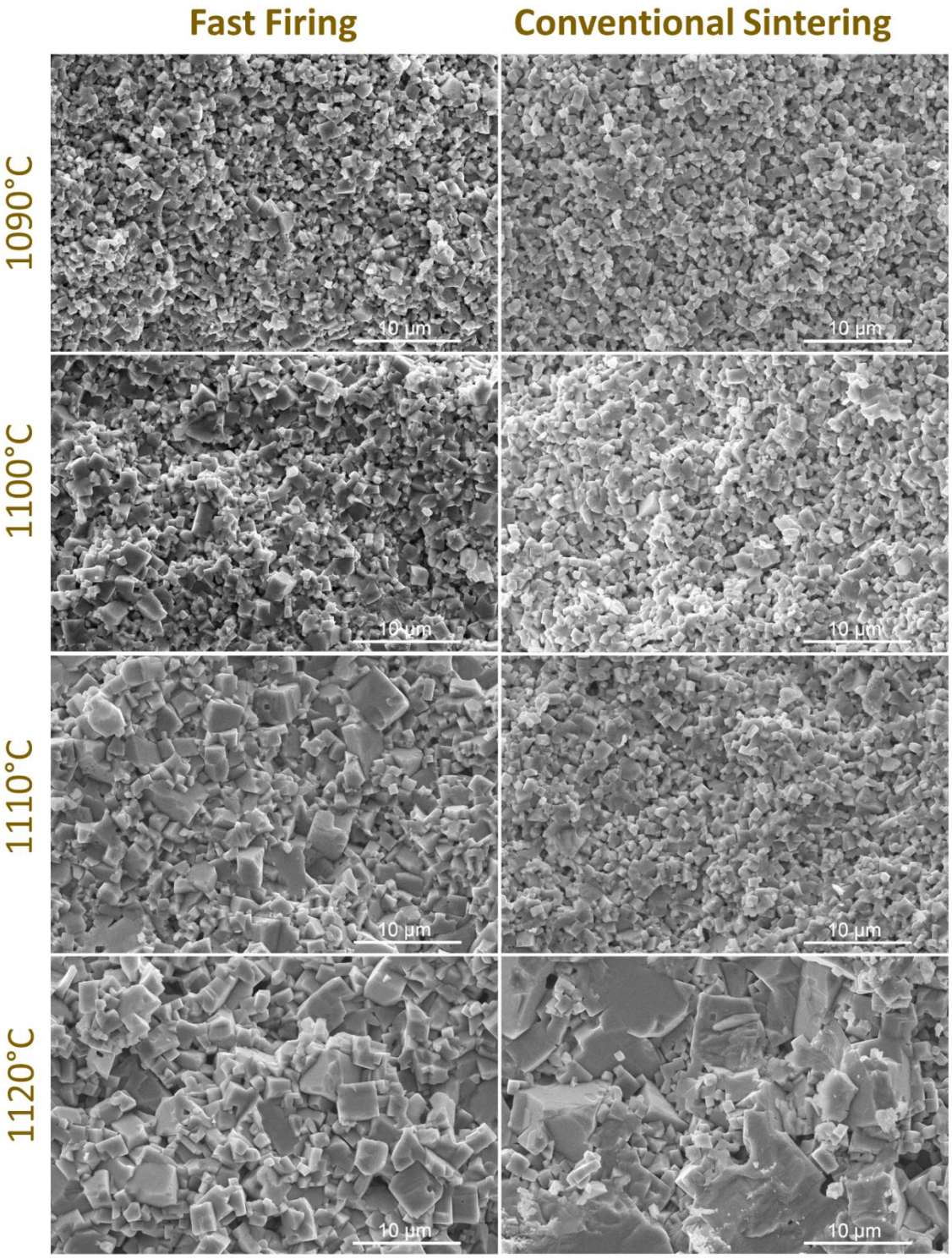

Figure 8.3. Fracture surface morphologies of conventional sintered and fast-fired samples at 1090°C, 1100°C, 1110°C and 1120°C.

Figure 8.4 shows the temperature dependence of dielectric permittivity and dielectric loss (tan δ) at 100 kHz of KNN ceramics sintered at different temperatures by FF and CS methods. In general, the dielectric permittivity decreases when increasing the FF temperature. The O-T phase transition anomaly can be seen around 210°C for all the samples (**Fig. 8.4**) [44]. On the other hand, the loss peaks of FF samples that appear at low temperatures (loss peaks are not visible for samples sintered at 1110°C and 1120°C) do not correspond to any phase transition. Still, they may show a relaxation behavior possibly resulting from the space-charge polarization effect or Schottky diode effect [45].

The dielectric permittivity and loss of samples produced by FF at 1090 and 1100°C show similar behavior (**Fig. 8.4(a)**), while the sample fast fired at 1110°C has a lower dielectric permittivity and relatively low dielectric loss. A further decrease of the dielectric permittivity can be observed in the samples sintered at 1120 and 1130°C. Higher dielectric loss values at low temperatures of the sample sintered at 1130°C may indicate higher ion mobility or conductivity contribution and enhanced imperfections in the material [46,47]. To reduce the defects, controlled (slow) cooling was used for the FF samples. By using this approach, it was observed that the dielectric permittivities increase, but significant change was not observed in the loss behavior (dashed curves in **Fig. 8.4(a)**). Besides, the loss peaks at low temperature were not observed in the samples produced by conventional sintering (**Fig. 8.4(b)**) characterized by lower loss values compared to fast fired materials. The behavious appear similar for all samples, the dielectric permittivity increasing with sintering temperature up to 1100°C and then decreasing. At 1130°C, which is close to the melting temperature of KNN, the dielectric properties of CS samples start to deterioate. Furthermore, samples conventionally sintered at 1110 and 1120°C have the highest dielectric permittivity. It is important to note that the effects of sintering temperature and dwell time on electrical properties might be intricately influenced by grain size, compositional variation due to volatilization, ceramic density and abnormal grain growth [43,48].

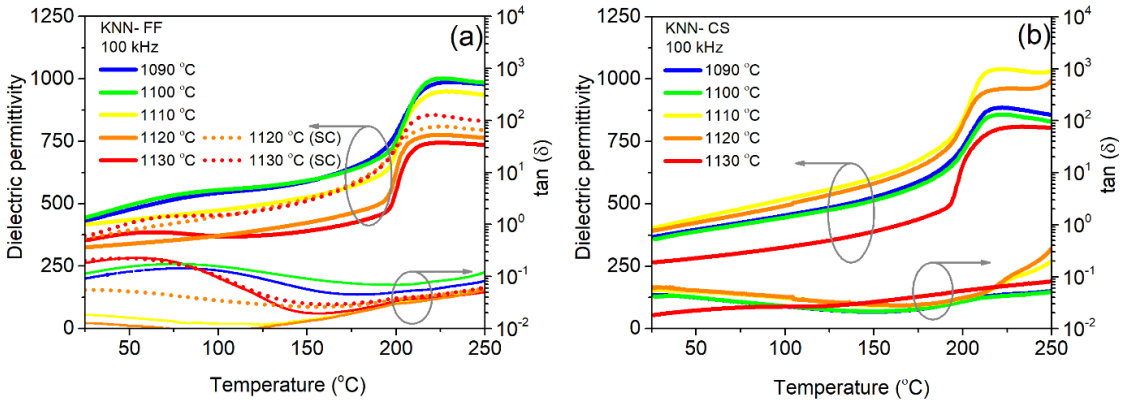

Figure 8.4. Temperature dependence of the dielectric permittivity and dielectric loss (tan δ) of KNN ceramics produced by (a) fast firing and fast firing with slow cooling (SC) and (b) conventional sintering.

Figure 8.5 shows the polarization-electric field hysteresis loops and strain-electric field curves. FF samples were measured at 50 Hz frequency to eliminate the conductivity contribution, as shown in **Fig. 8.5(a)**. However, specimens produced at 1110 and 1120°C still exhibited high conductivity contribution and an artificial polarization value [44,45]. For such reason, their hysteresis loops are given only as insets on the graph. All loops, apart from those two, are pinched with low remanent polarization. Pinching of the loops was reported for KNN samples that were sintered with cold sintering, and it was ascribed to the pinning of domain walls by either point defects or fine grains [49]. It can also be seen from the dashed loop obtained at 1130°C that the polarization values increased, and the lossy behavior decreased with slow cooling compared to fast cooling. In addition, the samples produced by fast firing-SC have higher strain values than those obtained by standard fast firing. Polarization hysteresis loops of conventional sintered samples have a similar dielectric behavior trend (**Fig. 8.4(b)**). In addition, the trend in strain values of the CS samples is compatible with the dielectric and polarization properties, and the highest strain values belong to the samples sintered at 1110 and 1120°C.

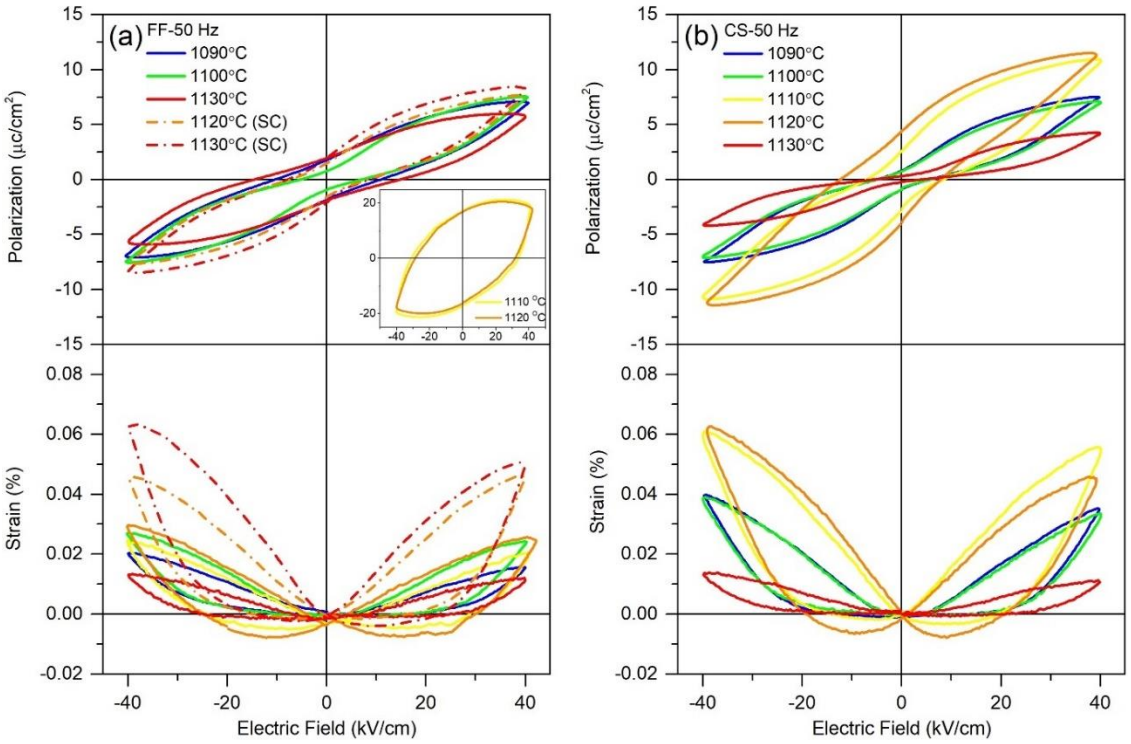

Figure 2.1. Polarization-electric field hysteresis loops and strain-electric field curves of KNN sintered by (a) fast firing and fast firing with slow cooling (SC) and (b) conventional sintering at different temperatures.

Figure 8.6 shows the sintering temperature-dependent piezoelectric coefficients, d_{33} and d_{33}*. As can be seen, lower d_{33} values are obtained by standard fast-firing. The higher d_{33} values were obtained when fast-firing with slow cooling was carried out, thus reducing the defects and, hereof, the conductivity contribution. If the cooling rate is high and the defect removal rate is slow, high defect concentrations can be present at room temperature, this influencing the ferroelectric and piezoelectric properties [50]. Reduced defect concentration can facilitate domain wall motion and increase extrinsic contribution to piezoelectricity. In addition, smaller grain size of the FFed samples might also be increasing d_{33} coefficient, as domain wall concentration is expected to increase with decreasing grain size. It is worth noting that d_{33} coefficients of typical highly dense KNN ceramics produced by conventional sintering usually range between 80 and 110 pC/N (e.g., 80 pC/N at 1120°C found in this study) [51], reaching 160 pC/N with a relative density of around 99% by hot pressing [33]. The d_{33} value of the sample subjected to FF at 1120°C is 49 pC/N, while material fast fired at 1120°C with slow cooling yields 112

pC/N, exceeding typical d_{33} values of conventional ones. The d_{33} value of samples conventionally sintered at 1130°C, which approaches the melting temperature of KNN, is found to be relatively low, similar to the obtained dielectric properties. It should be noted that the measured samples produced by both techniques usually exhibited transgranular fracture, indicating the grain boundaries with weaker path for crack propagation. The coefficient of d_{33} might be enhanced with the introduction of crack formation during poling [52]. Therefore, d_{33}* values were also calculated by utilizing strain measurements. d_{33}^* values, as shown in **Fig. 8.6(b),** which are derived from the expression d_{33}^* = (max strain) / (applied electric field), are consistent with the d_{33} values [53]. The d_{33}^* values of conventional sintered KNN were found to be 86-112 pm/V when sintered under an air atmosphere and 119 pm/V when sintered under a low O_2 atmosphere in the previous work [54]. These values are comparable with this work, especially for conventional sintered and fast-fired with slow cooling samples.

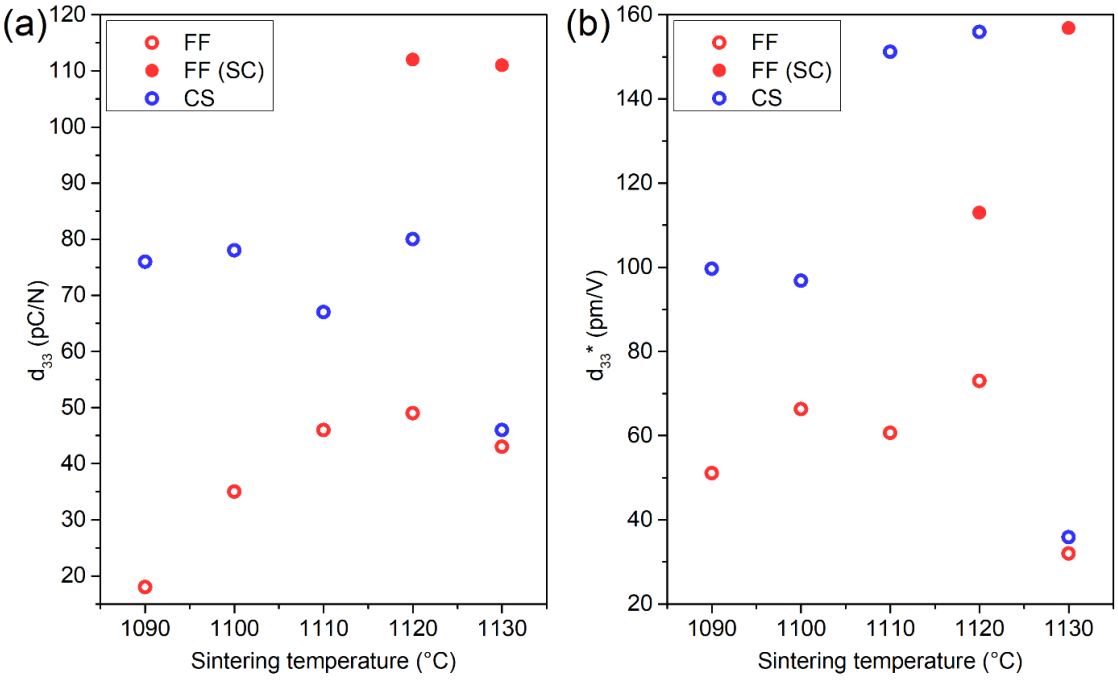

Figure 2.2. Sintering temperature-dependent piezoelectric coefficients of samples produced by fast-firing (FF), fast-firing with slow cooling (SC) and conventional sintering (CS): (a) d_{33} and (b) d_{33}*.

8.4. Conclusions

Potassium sodium niobate (KNN) ceramics were densified by fast firing at 1090-1130°C for 30 min. While higher relative densities were obtained by FF compared to conventional sintering, the fast-fired pellets demonstrated relatively low electrical properties. When FF with slow cooling was carried out, dielectric, polarization and piezoelectric properties were enhanced. While the material produced by conventional sintering had a d_{33} of 80 pC/N with a relative density of 88% (1120°C), FF at 1120°C led to higher relative density (about 95%) with a smaller grain size. If FF was followed by controlled cooling, d_{33} as high as 112 pC/N can be obtained.

References

[1] R.K. Bordia, S.-J.L. Kang, E.A. Olevsky, Current understanding and future research directions at the onset of the next century of sintering science and technology, J. Am. Ceram. Soc. 100 (2017) 2314–2352. https://doi.org/10.1111/jace.14919.

[2] M.P. Harmer, R.J. Brook, Fast firing-microstructural benefits, Trans. J. Br. Ceram. Soc. 80 (1981) 147–148.

[3] D.-H. Kim, C.H. Kim, Effect of Heating Rate on Pore Shrinkage in Yttria-doped Zirconia, J. Am. Ceram. Soc. 76 (1993) 1877–1878. https://doi.org/10.1111/j.1151-2916.1993.tb06665.x.

[4] A. Leriche, F. Cambier, S. Hampshire, Sintering of Ceramics, in: Reference Module in Materials Science and Materials Engineering, Elsevier, 2017. https://doi.org/10.1016/B978-0-12-803581-8.10288-7.

[5] S.-J.L. Kang, What we should consider for full densification when sintering, Materials. 13 (2020) 3578.

[6] D. Hotza, D.E. García, R.H.R. Castro, Obtaining highly dense YSZ nanoceramics by pressureless, unassisted sintering, International Materials Reviews. 60 (2015) 353–375. https://doi.org/10.1179/1743280415Y.0000000005.

[7] H. Moertel, Porcelain for fast firing, Ceramurgia International. 3 (1977) 65–69. https://doi.org/10.1016/0390-5519(77)90032-1.

[8] P.I. Berenshtein, Fast single firing of ceramic tiles, Glass and Ceramics. 33 (1976) 36–38. https://doi.org/10.1007/BF00702046.

[9] V. Viswabaskaran, F.D. Gnanam, Development of Fast Firing Vitreous Sanitaryware, Transactions of the Indian Ceramic Society. 59 (2000) 105–108. https://doi.org/10.1080/0371750X.2000.10799942.

[10] D.E. García, J. Seidel, R. Janssen, N. Claussen, Fast firing of alumina, J. Eur. Ceram. Soc. 15 (1995) 935–938. https://doi.org/10.1016/0955-2219(95)00071-2.

[11] D.E. García, D. Hotza, R. Janssen, Building a Sintering Front through Fast Firing, Int J Appl Ceram Technol. 8 (2011) 1486–1493. https://doi.org/10.1111/j.1744-7402.2011.02609.x.

[12] T.S. Possamai, R. Oba, V.P. Nicolau, D. Hotza, D.E. García, Numerical Simulation of the Fast Firing of Alumina in a Box Furnace, Journal of the American Ceramic Society. 95 (2012) 3750–3757. https://doi.org/10.1111/j.1551-2916.2012.05432.x.

[13] V. Prajzler, D. Salamon, K. Maca, Pressure-less rapid rate sintering of pre-sintered alumina and zirconia ceramics, Ceram Int. 44 (2018) 10840–10846. https://doi.org/10.1016/j.ceramint.2018.03.132.

[14] H. Mostaghaci, R.J. Brook, Microstructure development and dielectric properties of fast-fired BaTiO3 ceramics, J Mater Sci. 21 (1986) 3575–3580. https://doi.org/10.1007/BF00553803.

[15] W. Zhu, C.C. Wang, S.A. Akbar, R. Asiaie, Fast-sintering of hydrothermally synthesized BaTiO3 powders and their dielectric properties, J Mater Sci. 32 (1997) 4303–4307. https://doi.org/10.1023/A:1018663621241.

[16] A. Bologna Alles, R. Vanalstine, W. Schulze, Dielectric properties and aging of fast-fired barium titanate, Latin American Applied Research. 35 (2005) 29–35.

[17] V. Bijalwan, V. Prajzler, J. Erhart, J.J. Velazquez, D. Galusek, K. Maca, Rapid pressureless sintering of barium titanate–based piezoceramics and their electromechanical harvesting performance, Journal of the American Ceramic Society. 105 (2022) 6886–6897. https://doi.org/10.1111/jace.18602.

[18] A. Dias, Microstructural evolution of fast-fired nickel–zinc ferrites from hydrothermal nanopowders, Mater Res Bull. 35 (2000) 1439–1446. https://doi.org/10.1016/S0025-5408(00)00337-8.

[19] B.-C. Kim, J.-H. Lee, J.-J. Kim, H.Y. Lee, J.-S. Lee, Densification of nanocrystalline ITO powders in fast firing: effect of specimen mass and sintering

atmosphere, Mater Res Bull. 40 (2005) 395–404. https://doi.org/10.1016/j.materresbull.2004.10.006.

[20] S.L. Reis, E.N.S. Muccillo, Microstructure and electrical conductivity of fast fired Sr- and Mg-doped lanthanum gallate, Ceram Int. 42 (2016) 7270–7277. https://doi.org/10.1016/j.ceramint.2016.01.121.

[21] S.M. Landin, W.A. Schulze, Rapid Thermal Processing of Pb(Mg0.7Zn0.3)1/3Nb2/3O3 Multilayer Ceramic Capacitors, Journal of the American Ceramic Society. 73 (1990) 909–912. https://doi.org/10.1111/j.1151-2916.1990.tb05134.x.

[22] S.M. Landin, W.A. Schulze, Rapid Sintering of Stoichiometric Zinc-Modified Lead Magnesium Niobate, J. Am. Ceram. Soc. 73 (1990) 913–918. https://doi.org/10.1111/j.1151-2916.1990.tb05135.x.

[23] C.E. Baumgartner, Fast Firing and Conventional Sintering of Lead Zirconate Titanate Ceramic, J. Am. Ceram. Soc. 71 (1988) C-350-C-353. https://doi.org/10.1111/j.1151-2916.1988.tb05939.x.

[24] C.-C. Hsueh, M.L. Mecartney, W.B. Harrison, M. Renee, B. Hanson, B.G. Koepke, Microstructure and electrical properties of fast-fired lead zirconate-titanate ceramics, J Mater Sci Lett. 8 (1989) 1209–1216. https://doi.org/10.1007/BF01730072.

[25] C.R. Bowen, J. Open, J. Fitzmaurice, S. Mahon, Fast firing of electroceramics, Ferroelectrics .228 (1999) 159–166. https://doi.org/10.1080/00150199908226133.

[26] A. Seal, R. Mazumder, A. Sen, H.S. Maiti, Fast firing of lead zirconate titanate ceramics at low temperature, Mater Chem Phys. 97 (2006) 14–18. https://doi.org/10.1016/j.matchemphys.2005.05.038.

[27] S.Y. Gómez, A.L. da Silva, D. Gouvêa, R.H.R. Castro, D. Hotza, Nanocrystalline yttria-doped zirconia sintered by fast firing, Mater Lett. 166 (2016) 196–200. https://doi.org/10.1016/j.matlet.2015.12.042.

[28] V. Prajzler, S. Průša, K. Maca, Rapid pressure-less sintering of fine grained zirconia ceramics: Explanation and elimination of a core-shell structure, J Eur Ceram Soc. 39 (2019) 5309–5319. https://doi.org/10.1016/j.jeurceramsoc.2019.07.053.

[29] W. Ji, B. Parker, S. Falco, J.Y. Zhang, Z.Y. Fu, R.I. Todd, Ultra-fast firing: Effect of heating rate on sintering of 3YSZ, with and without an electric field, J Eur Ceram Soc. 37 (2017) 2547–2551. https://doi.org/10.1016/j.jeurceramsoc.2017.01.033.

[30] M. Biesuz, L. Spiridigliozzi, M. Frasnelli, G. Dell'Agli, V.M. Sglavo, Rapid densification of Samarium-doped Ceria ceramic with nanometric grain size at 900–1100°C, Mater Lett. 190 (2017) 17–19. https://doi.org/10.1016/j.matlet.2016.12.132.

[31] D.E. García, J. Wendorff, R. Janssen, N. Claussen, Fast firing of reaction-bonded aluminium oxide RBAO composites, J Mater Sci. 30 (1995) 5121–5124. https://doi.org/10.1007/BF00356058.

[32] L. Egerton, D.M. Dillon, Piezoelectric and dielectric properties of ceramics in the system potassium—sodium niobate, J. Am. Ceram. Soc. 42 (1959) 438–442.

[33] R.E. Jaeger, L. Egerton, Hot pressing of potassium-sodium niobates, J. Am. Ceram. Soc. 45 (1962) 209–213.

[34] R. Zuo, J. Rödel, R. Chen, L. Li, Sintering and Electrical Properties of Lead-Free $Na_{0.5}K_{0.5}NbO_3$ Piezoelectric Ceramics, J. Am. Ceram. Soc. 89 (2006) 2010–2015. https://doi.org/10.1111/j.1551-2916.2006.00991.x.

[35] C. Piskin, L. Karacasulu, M. Bortolotti, C. Vakifahmetoglu, Synthesis of potassium–sodium niobate (KNN) from NbO_2, Open Ceramics. 7 (2021) 100159. https://doi.org/10.1016/j.oceram.2021.100159.

[36] C. Piskin, L. Karacasulu, G. Ischia, M. Bortolotti, C. Vakifahmetoglu, Hydrothermal synthesis of potassium–sodium niobate powders, J. Am. Ceram. Soc. 105 (2022) 3809–3819. https://doi.org/10.1111/jace.18349.

[37] L. Karacasulu, C. Vakifahmetoglu, Cold sintering assisted two-step sintering of potassium sodium niobate (KNN) ceramics, Materials Science and Engineering: B. 297 (2023) 116709. https://doi.org/10.1016/j.mseb.2023.116709.

[38] B. Malič, J. Koruza, J. Hreščak, J. Bernard, K. Wang, J.G. Fisher, A. Benčan, Sintering of lead-free piezoelectric sodium potassium niobate ceramics, Materials. 8 (2015) 8117–8146.

[39] M. Bah, R. Podor, R. Retoux, F. Delorme, K. Nadaud, F. Giovannelli, I. Monot-Laffez, A. Ayral, Real-Time Capturing of Microscale Events Controlling the Sintering of Lead-Free Piezoelectric Potassium-Sodium Niobate, Small. 18 (2022) 2106825. https://doi.org/10.1002/smll.202106825.

[40] R. López, F. González, M.P. Cruz, M.E. Villafuerte-Castrejon, Piezoelectric and ferroelectric properties of $K_{0.5}Na_{0.5}NbO_3$ ceramics synthesized by spray drying method, Mater Res Bull. 46 (2011) 70–74.

[41] P. Bomlai, P. Wichianrat, S. Muensit, S.J. Milne, Effect of Calcination Conditions and Excess Alkali Carbonate on the Phase Formation and Particle Morphology of $Na_{0.5}K_{0.5}NbO_3$ Powders, J. Am. Ceram. Soc. 90 (2007) 1650–1655. https://doi.org/10.1111/j.1551-2916.2007.01629.x.

[42] D. Jenko, A. Benčan, B. Malič, J. Holc, M. Kosec, Electron microscopy studies of potassium sodium niobate ceramics, Microscopy and Microanalysis. 11 (2005) 572–580.

[43] Y. Zhen, J.-F. Li, Abnormal Grain Growth and New Core–Shell Structure in $(K,Na)NbO_3$-Based Lead-Free Piezoelectric Ceramics, J. Am. Ceram. Soc. 90 (2007) 3496–3502. https://doi.org/10.1111/j.1551-2916.2007.01977.x.

[44] Y. Su, X. Chen, Z. Yu, H. Lian, D. Zheng, J. Peng, Comparative study on microstructure and electrical properties of $(K_{0.5}Na_{0.5})NbO_3$ lead-free ceramics prepared via two different sintering methods, J Mater Sci. 52 (2017) 2934–2943. https://doi.org/10.1007/s10853-016-0587-z.

[45] K. Datta, K. Roleder, P.A. Thomas, Enhanced tetragonality in lead-free piezoelectric $(1-x)BaTiO_3–xNa_{1/2}Bi_{1/2}TiO_3$ solid solutions where x=0.05–0.40, J Appl Phys. 106 (2009) 123512. https://doi.org/10.1063/1.3268443.

[46] M.E. Lines, A.M. Glass, Principles and applications of ferroelectrics and related materials, Oxford university press, 2001.

[47] P. Kumar, M. Pattanaik, Sonia, Synthesis and characterizations of KNN ferroelectric ceramics near 50/50 MPB, Ceram Int. 39 (2013) 65–69. https://doi.org/10.1016/j.ceramint.2012.05.093.

[48] R. Serrazina, A. Tkach, L. Pereira, A.M.O.R. Senos, P.M. Vilarinho, Flash Sintered Potassium Sodium Niobate: High-Performance Piezoelectric Ceramics at Low Thermal Budget Processing, Materials. 15 (2022) 6603.

[49] K. Tsuji, Z. Fan, S.H. Bang, S. Dursun, S. Trolier-McKinstry, C.A. Randall, Cold sintering of the ceramic potassium sodium niobate, $(K_{0.5}Na_{0.5})NbO_3$, and influences on piezoelectric properties, J. Eur. Ceram. Soc. 42 (2022) 105–111. https://doi.org/10.1016/j.jeurceramsoc.2021.10.002.

[50] A.J. Moulson, J.M. Herbert, Electroceramics: materials, properties, applications, John Wiley & Sons, 2003.

[51] H. Birol, D. Damjanovic, N. Setter, Preparation and characterization of $(K_{0.5}Na_{0.5})NbO_3$ ceramics, J. Eur. Ceram. Soc. 26 (2006) 861–866.

[52] J. Mendiola, C. Alemany, L. Pardo, A. Gonzalez, Poling reversal effects on piezoelectricity of calcium modified lead titanate ceramic, Ferroelectrics. 94 (1989) 209–214. https://doi.org/10.1080/00150198908014255.

[53] Y. Zhao, Z. Xu, R. Chu, J. Hao, J. Du, G. Li, Improved piezoelectricity and high strain response of $(1 - x)(0.948K_{0.5}Na_{0.5}NbO_3 - 0.052LiSbO_3) - xBi_2O_3$ ceramics, Journal of Materials Science: Materials in Electronics. 28 (2017) 1211–1216. https://doi.org/10.1007/s10854-016-5647-2.

[54] Z. Yu, X. Chen, H. Lian, Q. Zhang, W. Wu, Microstructure and electrical properties of K0.5Na0.5NbO3 lead-free piezoelectric ceramics sintered in low pO_2 atmosphere, Journal of Materials Science: Materials in Electronics. 29 (2018) 19043–19051. https://doi.org/10.1007/s10854-018-0030-0.

CHAPTER 9

FAST-FIRING OF MARS REGOLITH SIMULANT

The following chapter is written in the format of a manuscript to be submitted. In preparation

Abstract

In the future, benefiting ISRU (In-Situ Resource Utilization) approaches holds significant importance in line with plans for space colonization. As a different ISRU concept, Mars regolith simulant (MGS-1) was sintered at different temperatures for varying dwell times by fast-firing process which is widely used in the industry. The produced specimens were also compared with slowly heated conventional sintered ones under the same conditions. As of 15 min dwell time, fast-fired specimens exhibited greater densification with higher flexural strength exceeding 25 MPa compared to those of conventional sintering process. For both processes, the bulk density values and the mechanical properties of the regolith compacts were usually enhanced with increasing dwell time. Lastly, fast-firing can be considered as a potential candidate with the development of the discussed processing strategies for the fast-firing technique in terms of rapid colonization for ISRU on Mars.

9.1. Introduction

Promising plans to colonize space require appropriate use of the available resources for a sustainable life outside our planet. In this sense, materials found in outer space deserve particular attention [1]. In-situ resource utilization (ISRU) concept is the

practice of on-site collection, processing, storing, and use of indigenous materials encountered during human or robotic space exploration. Therefore, early colonization scenarios propose the direct use of the regoliths composed of various oxide minerals [2].

In previous studies, some ISRU approaches of regolith simulants have been proposed, these including dry consolidation [3–5], melting [6–8] ,geopolymerization [1,9], self-propagating high-temperature synthesis [10], slip casting [2], additive manufacturing [11,12], and cold sintering [13] . However, further studies are still required to establish new ISRU approaches in future.

Generally, the regoliths obtained from Luna or Mars contain largely silica (~50 wt. %); this means that it may be possible to produce glass or ceramics by sintering or melting [14–18]. Therefore, different sintering approaches including conventional sintering under different atmospheric conditions [19–23], laser processing [24–27], solar sintering [28], cold sintering [13], microwave sintering [4,18,29–31], spark plasma sintering [32–34] have been proposed to densify such regoliths as ISRU process.

Fast-firing (FF), introduced at the beginning of 80s, is one of the fundamental unconventional sintering processes. It allows densification by utilizing a much faster heating rate (10^2-10^3 °C/min) with a shorter dwell time [35,36]. In fast firing process, a fast-heating rate has a crucial role to enhance densification and suppress grain growth similar to the other unconventional sintering techniques, i.e., spark-plasma sintering and flash sintering [35]. For the same density, fast-fired samples generally result in smaller grain size, finer microstructure, and reduced pore/ grain boundary separation, compared to conventional sintering process [35,37].

Fast-firing involves quick introduction of the green samples into the hot zone of a furnace so that the ceramics quickly reach high-temperature. This allows the material to pass through the temperature region where grain coarsening is activated without densification in a matter of a few seconds/minutes. This phenomenon is associated with the different activation energies for the two processes, where densification (involving bulk/grain boundary diffusion) is typically characterized by higher activation energy than coarsening and, as such, requires a higher temperature for being activated [36,38,39]. However, the said considerations are valid only for systems where densification takes place via solid state diffusion. More limited attention has been focused on the fast firing of systems characterized by liquid phase sintering or viscous flow sintering to which Mars regolith simulants belong.

Due to its rapidness and simplicity, fast-firing has gained popularity as a sintering technique with several industrial applications and has been used to sinter both traditional and advanced ceramics [40].

The main goal of this work was to demonstrate proof of concept to sinter Mars regolith (MGS-1) simulant monoliths via fast firing for the first time. The densification ability of Martian regolith by FF was investigated in comparison with conventional sintering.

9.2. Experimental procedures

Martian Regolith simulant (MGS-1) developed by Cannon et. al [41] were acquired from Mars Science Laboratory (MSL) rover Curiosity's XRD results of global basaltic soil at the Gale crater on Mars [42], supplying by Exolith Lab (CLASS/UCF, Orlando, USA). The main chemical composition of the MGS-1 simulant by weight was SiO_2 (44.36%), MgO (13.84%), Al_2O_3 (12.71%), FeO (11.90%), CaO (7.36%), LOI (5.53%), Na_2O (1.65%), K_2O (0.46%), TiO_2 (0.39%), Cr_2O_3 (0.13%), P_2O_5 (0.11%) and MnO (0.1%) [13]. Besides, mineralogical composition of MGS-1 simulant by wt.% as follows; anorthosite (27.1%), glass-rich basalt (22.9%), bronzite (20.3%), olivine (13.7%), Mg-sulfate (4%), ferrihydrite (3.5%), hydrated silica (3.5%), magnetite (1.9%), anhydrite (1.7%), Fe-carbonate (1.4%), and hematite (0.5%).

MGS-1 simulant powder was milled and sieved in a 60-mesh sieve to reduce the particle size. Thermogravimetric analysis (TGA) of the MGS-1 powder was conducted in air atmosphere up to 1200°C with a heating rate of 20°C/min using the thermobalance STA 409 (NETZSCH Geraetebau GmbH, Germany). True density was measured with 99 repetitions using a helium gas pycnometer Ultrapyc 5000 (Anton Paar GmbH, Graz, Austria), with integrated Peltier cell temperature control of the measuring chamber.

0.2 g of MGS-1 simulant was uniaxially pressed in a cylindrical-shape die with 8 mm diameter under a pressure of 200 MPa. To understand sintering characteristics of MGS-1 simulant, the dilatometry analysis was performed at a heating and cooling rate of 20°C/min with pushing forces of 150 mN using a L75 Platinum series (LINSEIS GmbH©, Germany). The green samples were sintered in two ways; i) fast firing, ii) conventional sintering. For fast firing process, the obtain pellets were inserted quickly to the hot zone

of the tube furnace (Nabertherm P330, Lilienthal, Germany) at the selected temperatures (1080-1120-1160°C) and kept there for varying times ranging from 1 min to 1 h. Fast fired samples were rapidly taken out from the furnace. The conventional sintering experiments were also carried out in the same furnace from room temperature to the same target temperature as fast-firing temperature with a heating and cooling rate of 5°C/min for the same dwell time.

Bulk densities of the samples were determined by Archimedes' method using water as buoyancy medium and a balance with sensitivity 0.1 mg. The polished surfaces were observed by SEM (JEOL Ltd.©, JSM-5500, Tokyo, Japan). Phase analysis of MGS-1 simulant powder, conventional sintered, and fast fired samples were conducted by X-ray diffractometer (XRD, Italstructures IPD3000 diffractometer, Italy) with a copper anode X-ray source (CuK_α = 1.5406 Å). Scans were carried out in between the 10°–130° (2θ) range with 0.2° per second. To determine mechanical properties, The flexural strength values of the produced specimens were calculated using the ball on three balls test [43].

9.3. Results and discussion

Fig. 9.1 shows characteristics of MGS-1 regolith simulants used for conventional sintering and fast-firing processes. TGA analysis of MGS-1 simulant powder was shown in **Fig. 9.1(a)**. TGA analysis demonstrated about ~4.7 % total weight loss until 1200°C for MGS-1 simulant which is consistent with the result (~4 %) at 1000° C by Cannon et al. Typically, the main losses in the TGA analysis are accompanied by firstly the loss of physisorbed water below around 100 °Cand then chemisorbed water until around 400 °C, and then the decomposition of carbonates and sulphates in the regolith composition (mainly Fe-carbonate and Mg-sulfate, and anhydrite). It should be noted that MGS-1 simulant contains a considerable amount of iron constituents (e.g., Fe-carbonate) susceptible to oxidation in air environment, which might slightly affect weight loss [44]. **Fig. 9.1(b)** reports shrinkage of the MGS-1 regolith compact upon heating with 20°C/min up to 1160°C. The analysis represents the relative length variation, computed as the variation measured over the initial length, as a function of temperature. We can observe that up to 1100°C the sample undergoes to thermal expansion. Above such temperature

it starts to shrink for the whole measurement range (i.e., up to 1160 °C). Note that 1160°C was chosen as maximum temperature as during a first trial at 1180°C the sample largely melted and got stuck to the dilatometer measurement system. Additionally, the true density of the used MGS-1 simulant powder was found to be 2.8885 g/cm^3 by using a gas pycnometer.

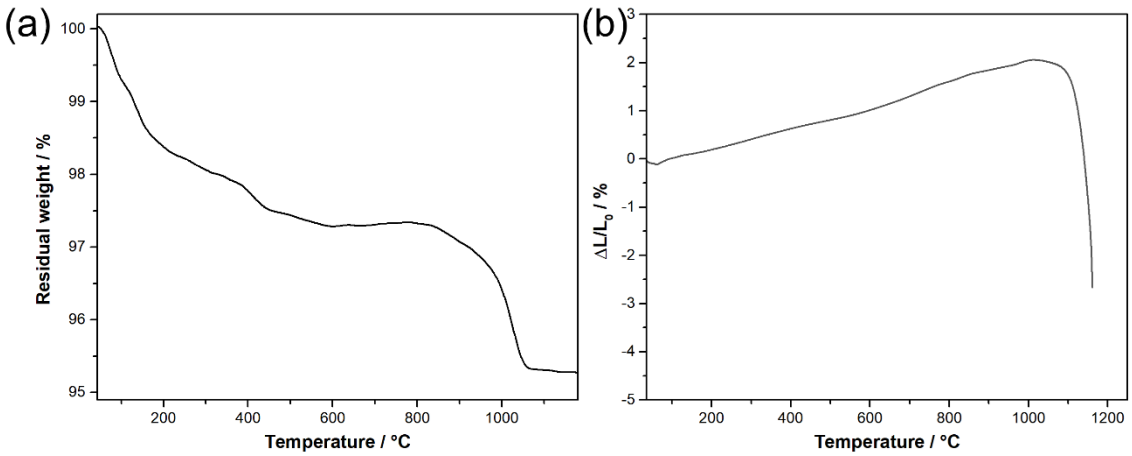

Figure 9.1. Characteristics of MGS-1 regolith simulant, (a) TGA analysis of MGS-1 simulant, and (b) dilatometer curve of green MGS-1 pellet.

First of all, the green bodies were conventionally sintered at different temperatures (1080-1160°C) for a dwell time of 60 min to investigate the sintering temperature of MGS-1 simulant. The specimens sintered at 1080 and 1120 °C had bulk densities of around 2.09 and 2.18 g/cm^3 respectively, resulting in no densification. As expected, the samples produced at 1160°C for 1h provided better densification, compared to those of lower temperatures, reaching a bulk density value of 2.39 g/cm^3. As such, the sintering evolution of MGS-1 simulant was further investigated utilizing dwell time. **Fig. 9.2** shows the bulk density values of samples fabricated at 1160 °C through fast firing and conventional sintering as a function of dwell time. While samples subjected to fast firing for 1 minute exhibited green body characteristics, those processed using conventional sintering exhibited a density of 2.24 g/cm³. Upon comparing samples produced within 5 minutes, it was observed that the conventionally sintered samples still had higher densification. Note that as conventional sintered samples approach dwell time with slow

heating rates, any substance (e.g., Mg-sulfate and Fe-carbonate) prone to decomposition undergoes regular processing, whereas, in fast-fired samples experiencing even high heating rates, they still require to undergo similar processes. In contrast, when reaching 15 minutes, it is evident that the densities of the samples produced by fast firing surpass those of conventional sintering. A slight enhancement in density was achieved at further dwell time during fast firing.

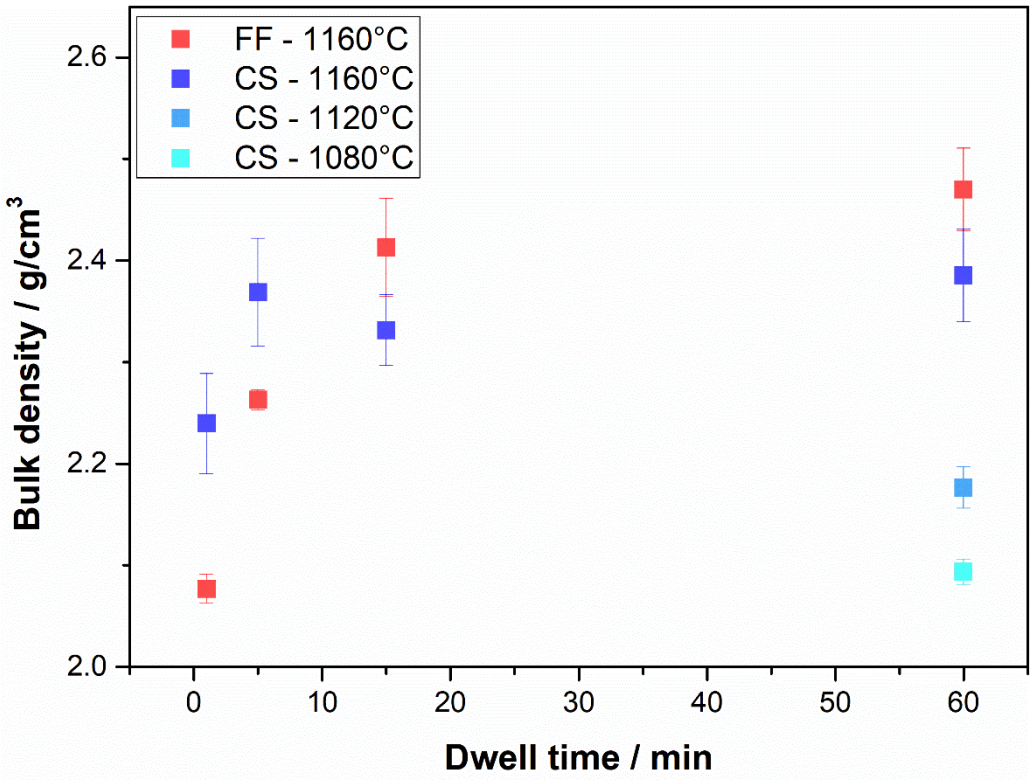

Figure 9.2. The bulk density values of MGS-1 regolith compacts produced via conventional sintering and fast-firing process.

Fig. 9.3 demonstrates SEM micrographs of fast-fired and conventional sintered samples at 1160 °C for varying dwell times ranging from 1 min to 60 min. The samples fabricated by both processes exhibited a heterogeneous microstructure, similar to common clay-based traditional ceramic components. In samples produced within 1 minute, a weak bonding characteristic lack of glassy phase was observed, particularly in samples obtained using the fast-firing method, while samples with a 5-minute dwell time

have initiated to be sintered within presence of glassy phase. As the dwell time progressed to 15 and 60 minutes, an increase in densification was seen due to the formation of the glassy phase with strong bonding structures. Besides, as expected considerable amount of Fe content (white grains) was found in all samples.

In porcelain-based traditional ceramic products, open porosity consisting of interconnected irregular channels may arise from the reduction in volume during the firing process. Similar to that, the samples especially produced by conventional sintering had such porosity types. During sintering process, the viscous flow causes the elimination of the capillaries provided by the open porosity, resulting in the development of closed porosity with spherical shape. It can be said that as the dwell time increases, open porosities turn into closed porosities in the presence of the glassy phase from the beginning of sintering, especially in fast-fired samples.

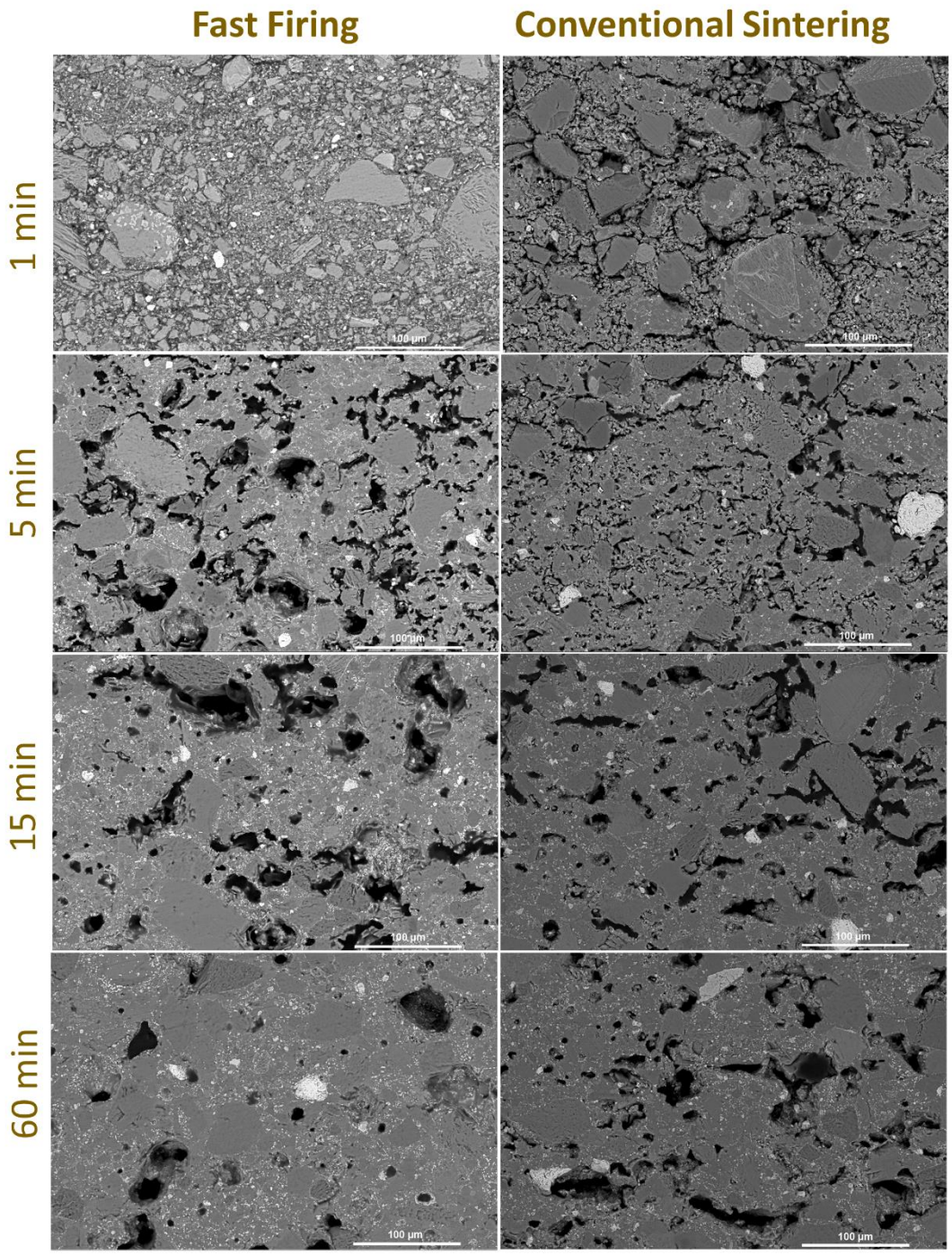

Figure 9.3. Backscattered images obtained from polished MGS-1 specimens.

Fig. 9.4(a,b) reports the x-ray diffraction patterns of the MGS-1 simulant powder, conventional sintered, and fast fired specimens. In general, the intensity of the peaks increases as the dwell time increases due probably to the favoured crystallization. All

samples formed via conventional sintering and fast firing exhibited an almost similarly high number of diffractions, corresponding to the pattern obtained from the MGS-1 simulant powder having different crystalline constituents. Besides, it is important to note that synchrotron transmission X-ray powder diffraction techniques have been previously used to detect such complicated regolith patterns [11,12,45] because whereas a traditional x-ray lacks the capacity to generate a suitable x-ray beam, a synchrotron source demonstrates significantly greater intensities and offers precise control over wavelength [45]. Therefore, further studies are required to establish detailed phase constituents here in future.

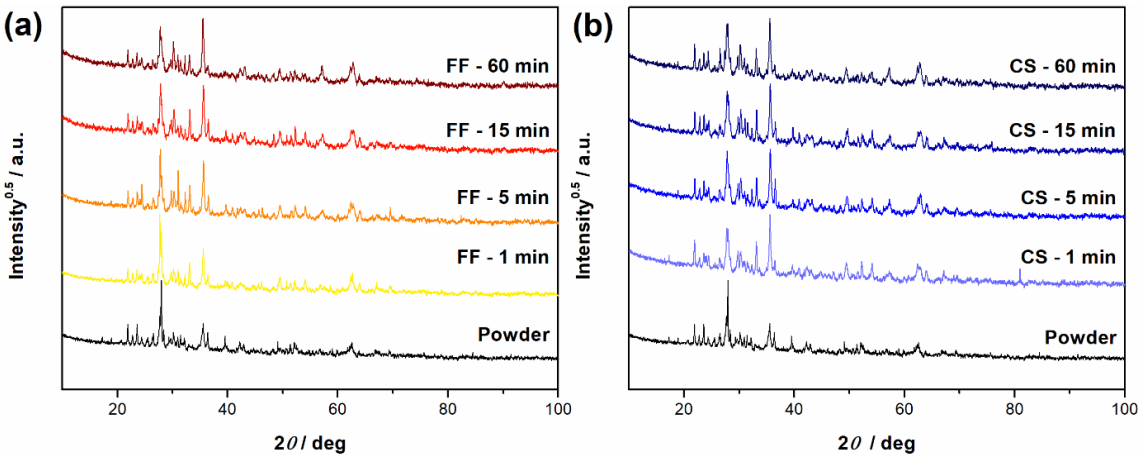

Figure 9.4. X-ray diffraction patterns of (a) fast-fired samples at 1160 °C, (b) conventional sintered samples at 1160 °C with MGS-1 powder (as is, milled).

The flexural strength data of the fast-fired and conventional sintered specimens at 1160 °C are given in **Fig. 9.5**. As seen, the flexural strength values of fast-fired compacts were greater than conventional sintered ones except for dwell time of 1 min. Fast-fired samples gave flexural strength values exceeding 25 MPa starting from the 15 min. These differences may be attributed to different porosity morphologies due to the variation of stress concentration for the decrease in mechanical strength of the produced specimens [46]. The strength obtained by both processes enhanced with increasing dwell time, such an improvement was mainly utilized from the increased densification, indicating

establishment of stronger bondings. While common non-technical ceramics such as ceramic tiles, engineering brick, facing brick, and terracotta exhibited flexural strength of up to ~ 25 MPa, even within a short duration, as much as 5 minutes, it is possible to achieve comparable flexural strength values using both processes without any additive. It should be noted that unlike the methods used, many other processing methods reported lower flexural strength with a higher weight fraction of non-ISRU materials required including shipping, synthesis, or extraction [12].

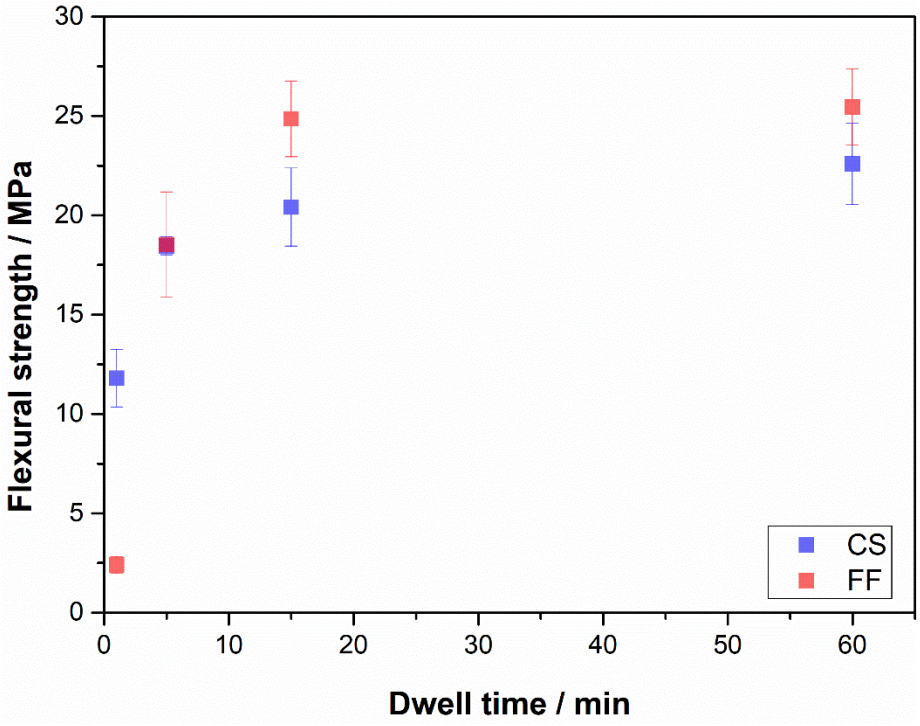

Figure 9.5. Flexural strength values of fast-fired and conventional sintered MGS-1 regolith compacts produced at 1160 °C at different dwell times.

It is worth noting that no transportation of additive material or material synthesis i.e., binder would be necessitated for the production of sintered ceramics. To evaluate the applicability of diverse ISRU material systems on Mars, it is suggested that their utilization on Earth serves as a crucial step, considering proper material systems with enough material availability, straightforward processing, and favorable properties over alternative options[12]. Besides, considering the widespread industrial utilization of fast

firing, it could emerge as a promising candidate ISRU process, compared to the other processes, thereby stepping ahead in its applicability.

Despite various In-Situ Resource Utilization (ISRU) studies being developed, many trials have been commonly conducted under Earth's atmospheric conditions [47]. It should be noted that there have been many reports on influences of sintering atmosphere on densification of the technical ceramics [39]. Some experiments have utilized different inert atmospheres [21], simulated the Martian atmosphere [12], or have been carried out under vacuum conditions [20] during sintering processes of the regoliths. In these studies, the obtained densities were higher compared to samples produced in air, causing a decrease in sintering temperature and improvement of mechanical properties [12,19,20,23]. Consequently, atmosphere-controlled fast-firing systems (e.g., under vacuum [48]), aiming to enhance densification, could potentially play a significant role in future endeavors.

9.4. Conclusions

MGS-1 simulants without any additive were sintered by fast-firing process as a different ISRU approach. The regolith compacts were densified at 1160 °C for varying dwell times ranging from 1 min to 1 h by comparing with conventional sintering method for the same conditions. As of 15 min dwell time, the specimens produced via fast-firing process had higher densification with enhanced flexural strength values (>25 MPa) compared to conventional sintering process. Fast firing could be a promising process with the development of the discussed processing strategies for the fast-firing technique in terms of rapid colonization, utilizing ISRU approaches.

References

[1] A. Alexiadis, F. Alberini, M.E. Meyer, Geopolymers from lunar and Martian soil simulants, Adv. Space Res. 59 (2017) 490–495. https://doi.org/10.1016/j.asr.2016.10.003.

[2] D. Karl, F. Kamutzki, A. Zocca, O. Goerke, J. Guenster, A. Gurlo, Towards the colonization of Mars by in-situ resource utilization: Slip cast ceramics from Martian soil simulant, PLoS One. 13 (2018) e0204025. https://doi.org/10.1371/journal.pone.0204025.

[3] C.H. Simonds, Sintering and hot pressing of Fra Mauro composition glass and the lithification of lunar breccias., Am. J. Sci. 273 (1973).

[4] T.T. Meek, D.T. Vaniman, R.D. Blake, M.J. Godbole, Sintering of lunar soil simulants using 2.45 GHz microwave radiation, in: Lunar and Planetary Science Conference, 1987.

[5] B.J. Chow, T. Chen, Y. Zhong, Y. Qiao, Direct Formation of Structural Components Using a Martian Soil Simulant, Sci. Rep. 7 (2017) 1151. https://doi.org/10.1038/s41598-017-01157-w.

[6] C. Dalton, E. Hohmann, Conceptual design of a lunar colony, NASA/ASEE Systems Design Institute, 1972.

[7] J.D. Blacic, Mechanical properties of lunar materials under anhydrous, hard vacuum conditions: Applications of lunar glass structural components, in: Lunar Bases and Space Activities of the 21st Century, 1985: p. 487.

[8] A. Zocca, M. Fateri, D. Al-Sabbagh, J. Günster, Investigation of the sintering and melting of JSC-2A lunar regolith simulant, Ceram. Int. 46 (2020) 14097–14104. https://doi.org/10.1016/j.ceramint.2020.02.212.

[9] C. Montes, K. Broussard, M. Gongre, N. Simicevic, J. Mejia, J. Tham, E. Allouche, G. Davis, Evaluation of lunar regolith geopolymer binder as a radioactive shielding material for space exploration applications, Adv. Space Res. 56 (2015) 1212–1221. https://doi.org/10.1016/j.asr.2015.05.044.

[10] G. Corrias, R. Licheri, R. Orrù, G. Cao, Self-propagating high-temperature reactions for the fabrication of Lunar and Martian physical assets, Acta Astronaut. 70 (2012) 69–76. https://doi.org/10.1016/j.actaastro.2011.07.022.

[11] D. Karl, T. Duminy, P. Lima, F. Kamutzki, A. Gili, A. Zocca, J. Günster, A. Gurlo, Clay in situ resource utilization with Mars global simulant slurries for additive manufacturing and traditional shaping of unfired green bodies, Acta Astronaut. 174 (2020) 241–253. https://doi.org/10.1016/j.actaastro.2020.04.064.

[12] D. Karl, F. Kamutzki, P. Lima, A. Gili, T. Duminy, A. Zocca, J. Günster, A. Gurlo, Sintering of ceramics for clay in situ resource utilization on Mars, Open Ceramics. 3 (2020) 100008. https://doi.org/10.1016/j.oceram.2020.100008.

[13] L. Karacasulu, D. Karl, A. Gurlo, C. Vakifahmetoglu, Cold sintering as a promising ISRU technique: A case study of Mars regolith simulant, Icarus. 389 (2023) 115270.

[14] A.D. Roberts, D.R. Whittall, R. Breitling, E. Takano, J.J. Blaker, S. Hay, N.S. Scrutton, Blood, sweat, and tears: extraterrestrial regolith biocomposites with in vivo binders, Mater Today Bio. 12 (2021) 100136. https://doi.org/10.1016/j.mtbio.2021.100136.

[15] M.Z. Naser, Extraterrestrial construction materials, Prog. Mater. Sci. 105 (2019) 100577. https://doi.org/10.1016/j.pmatsci.2019.100577.

[16] R.W. Moses, D.M. Bushnell, Frontier in-situ resource utilization for enabling sustained human presence on mars, 2016.

[17] H.P. E, Q. Stephanie, Building a Lunar or Martian Launch Pad with In Situ Materials: Recent Laboratory and Field Studies, J Aerosp Eng. 26 (2013) 134–142. https://doi.org/10.1061/(ASCE)AS.1943-5525.0000205.

[18] T. Rousek, K. Eriksson, O. Doule, SinterHab, Acta Astronaut. 74 (2012) 98–111. https://doi.org/10.1016/j.actaastro.2011.10.009.

[19] A. Meurisse, J.C. Beltzung, M. Kolbe, A. Cowley, M. Sperl, Influence of Mineral Composition on Sintering Lunar Regolith, J Aerosp Eng. 30 (2017) 04017014. https://doi.org/10.1061/(ASCE)AS.1943-5525.0000721.

[20] L. Song, J. Xu, S. Fan, H. Tang, X. Li, J. Liu, X. Duan, Vacuum sintered lunar regolith simulant: Pore-forming and thermal conductivity, Ceram Int. 45 (2019) 3627–3633. https://doi.org/10.1016/j.ceramint.2018.11.023.

[21] R. Dou, W.Z. Tang, L. Wang, S. Li, W.Y. Duan, M. Liu, Y.B. Zhang, G. Wang, Sintering of lunar regolith structures fabricated via digital light processing, Ceram Int. 45 (2019) 17210–17215. https://doi.org/10.1016/j.ceramint.2019.05.276.

[22] P. Warren, N. Raju, H. Ebrahimi, M. Krsmanovic, S. Raghavan, J. Kapat, R. Ghosh, Effect of sintering temperature on microstructure and mechanical properties of molded Martian and Lunar regolith, Ceram Int. 48 (2022) 35825–35833. https://doi.org/10.1016/j.ceramint.2022.07.329.

[23] W. Han, L. Ding, L. Cai, J. Zhu, H. Luo, T. Tang, Sintering of HUST-1 lunar regolith simulant, Constr Build Mater. 324 (2022) 126655. https://doi.org/10.1016/j.conbuildmat.2022.126655.

[24] M. Fateri, A. Gebhardt, Process Parameters Development of Selective Laser Melting of Lunar Regolith for On-Site Manufacturing Applications, Int J Appl Ceram Technol. 12 (2015) 46–52. https://doi.org/10.1111/ijac.12326.

[25] V. Krishna Balla, L.B. Roberson, G.W. O'Connor, S. Trigwell, S. Bose, A. Bandyopadhyay, First demonstration on direct laser fabrication of lunar regolith parts, Rapid Prototyp J. 18 (2012) 451–457. https://doi.org/10.1108/13552541211271992.

[26] J.-C. Ginés-Palomares, M. Fateri, E. Kalhöfer, T. Schubert, L. Meyer, N. Kolsch, M. Brandić Lipińska, R. Davenport, B. Imhof, R. Waclavicek, M. Sperl, A. Makaya, J. Günster, Laser melting manufacturing of large elements of lunar regolith simulant for paving on the Moon, Sci Rep. 13 (2023) 15593. https://doi.org/10.1038/s41598-023-42008-1.

[27] K.W. Farries, P. Visintin, S.T. Smith, Direct laser sintering for lunar dust control: An experimental study of the effect of simulant mineralogy and process parameters on product strength and scalability, Constr Build Mater. 354 (2022) 129191. https://doi.org/10.1016/j.conbuildmat.2022.129191.

[28] A. Meurisse, A. Makaya, C. Willsch, M. Sperl, Solar 3D printing of lunar regolith, Acta Astronaut. 152 (2018) 800–810. https://doi.org/10.1016/j.actaastro.2018.06.063.

[29] S. Lim, J. Bowen, G. Degli-Alessandrini, M. Anand, A. Cowley, V. Levin Prabhu, Investigating the microwave heating behaviour of lunar soil simulant JSC-1A at different input powers, Sci Rep. 11 (2021) 2133. https://doi.org/10.1038/s41598-021-81691-w.

[30] Y.-J. Kim, B.H. Ryu, H. Jin, J. Lee, H.-S. Shin, Microstructural, mechanical, and thermal properties of microwave-sintered KLS-1 lunar regolith simulant, Ceram Int. 47 (2021) 26891–26897. https://doi.org/10.1016/j.ceramint.2021.06.098.

[31] L.A. Taylor, T.T. Meek, Microwave Sintering of Lunar Soil: Properties, Theory, and Practice, J Aerosp Eng. 18 (2005) 188–196. https://doi.org/10.1061/(ASCE)0893-1321(2005)18:3(188).

[32] T. Min, Manufacturing Construction Materials on Mars: A feasibility study on the use of Spark Plasma Sintering (SPS) for bulk manufacturing of a viable ISRU Mars construction material using regolith simulant (Master's thesis), Delft University of Technology (2022).

[33] W. Hoekman, Creating Structural Material From Martian Regolith Using Spark Plasma Sintering: Understanding the effect of additives and the possibility to lower the energy requirement (Master's thesis), Delft University of Technology (2022).

[34] X. Zhang, S. Gholami, M. Khedmati, B. Cui, Y.-R. Kim, Y.-J. Kim, H.-S. Shin, J. Lee, Spark plasma sintering of a lunar regolith simulant: effects of parameters on microstructure evolution, phase transformation, and mechanical properties, Ceram Int. 47 (2021) 5209–5220. https://doi.org/10.1016/j.ceramint.2020.10.100.

[35] R.K. Bordia, S.-J.L. Kang, E.A. Olevsky, Current understanding and future research directions at the onset of the next century of sintering science and technology, J Am Ceram Soc. 100 (2017) 2314–2352. https://doi.org/10.1111/jace.14919.

[36] M.P. Harmer, R.J. Brook, Fast firing-microstructural benefits, Trans. J. Br. Ceram. Soc. 80 (1981) 147–148.

[37] D.-H. Kim, C.H. Kim, Effect of Heating Rate on Pore Shrinkage in Yttria-doped Zirconia, J Am Ceram Soc. 76 (1993) 1877–1878. https://doi.org/10.1111/j.1151-2916.1993.tb06665.x.

[38] A. Leriche, F. Cambier, S. Hampshire, Sintering of Ceramics, in: Reference Module in Materials Science and Materials Engineering, Elsevier, 2017. https://doi.org/10.1016/B978-0-12-803581-8.10288-7.

[39] S.-J.L. Kang, What we should consider for full densification when sintering, Materials. 13 (2020) 3578.

[40] D. Hotza, D.E. García, R.H.R. Castro, Obtaining highly dense YSZ nanoceramics by pressureless, unassisted sintering, International Materials Reviews. 60 (2015) 353–375. https://doi.org/10.1179/1743280415Y.0000000005.

[41] K.M. Cannon, D.T. Britt, T.M. Smith, R.F. Fritsche, D. Batcheldor, Mars global simulant MGS-1: A Rocknest-based open standard for basaltic martian regolith simulants, Icarus. 317 (2019) 470–478. https://doi.org/10.1016/j.icarus.2018.08.019.

[42] D.L. Bish, et al., X-ray Diffraction Results from Mars Science Laboratory: Mineralogy of Rocknest at Gale Crater, Science (1979). 341 (2013). https://doi.org/10.1126/science.1238932.

[43] R. Danzer, W. Harrer, P. Supancic, T. Lube, Z. Wang, A. Börger, The ball on three balls test—Strength and failure analysis of different materials, J Eur Ceram Soc. 27 (2007) 1481–1485. https://doi.org/10.1016/j.jeurceramsoc.2006.05.034.

[44] M. Kądziołka-Gaweł, J. Nowak, M. Szubka, J. Klimontko, M. Wojtyniak, Thermal Decomposition of Siderite and Characterization of the Decomposition Products under O_2 and CO_2 Atmospheres, Minerals. 13 (2023) 1066.

[45] L.F. Adam, J.C. Bridges, C.C. Bedford, J.M.C. Holt, E. Rampe, M. Thorpe, K. Mason, R.C. Ewing, Synchrotron x-ray diffraction for sealed Mars Sample Return sample tubes, Meteorit Planet Sci. n/a (2023). https://doi.org/10.1111/maps.14105.

[46] M. Romero, J.M. Pérez, Relation between the microstructure and technological properties of porcelain stoneware. A review, Materiales de Construcción. 65 (2015) e065–e065.

[47] K.W. Farries, P. Visintin, S.T. Smith, P. van Eyk, Sintered or melted regolith for lunar construction: state-of-the-art review and future research directions, Constr Build Mater. 296 (2021) 123627. https://doi.org/10.1016/j.conbuildmat.2021.123627.

[48] H. Mostaghaci, R.J. Brook, Microstructure development and dielectric properties of fast-fired $BaTiO_3$ ceramics, J Mater Sci. 21 (1986) 3575–3580. https://doi.org/10.1007/BF00553803.

CHAPTER 10

FLASH AND REACTIVE FLASH SINTERING OF POTASSIUM SODIUM NİOBATE

The following chapter is written in the format of a manuscript to be submitted. In preparation

Abstract

Potassium sodium niobate was tried to densify via flash and reactive flash sintering process using different approaches (constant current mode). Since the single-step current approach led to lowly dense KNN ceramics with cavities. As such, flash sintering was applied to both KNN powders and a mixture of NN and KN powders using a gradual current increase step. After utilizing a multi-step current, the relative densities were enhanced up to around 90%. Additionally, higher current (e.g., 90 mA/mm^2) results in melting of KNN ceramics.

10.1. Introduction

The last 15 years have arguably been one of the most active periods for research in the field of sintering since the inception of sintering theories. In this process, many new techniques have been introduced to the literature, from low-temperature densification techniques by hydrothermal effects to sintering at high heating rates by utilizing electric current and field [1,2]. Perhaps the turning point that made these research active in this way may have been accidentally discovered flash sintering [3,4].

Flash sintering was introduced in 2010 by Raj's group at the University of Colorado [3,5,6]. Flash sintering has been employed in numerous materials systems so far. It usually provides lowering the sintering temperatures compared to conventional sintering, resulting in suppression of the grain growth [6,7]. In the flash sintering process, the specimen undergoes to Joule heating applying electric field to the green body. Once a specific temperature threshold is attained, sintering takes place rapidly within a few seconds. The process is characterized by a non-linear increase in conductivity just after the onset of the flash. Higher electric field strength correlates with a reduced flash temperature. Under voltage control, power dissipation is enhanced with decreasing the sample resistance which is a result (usually in ceramics) of an increase in temperature. The non-linear increase in the current in the sample is limited by the output of the power source. When the limit is reached, power supply switches to the current control mode. Subsequently, power dissipation reaches a quasi-steady-state rate depending on the reduction in resistance, ultimately resulting in a stable specimen temperature [7,8].

Potassium sodium niobate, $K_{0.5}Na_{0.5}NbO_3$ (KNN), has attracted attention as lead-free & environmentally-friendly piezoelectric material in recent years. Besides offering a relatively high Curie temperature ($T_c \cong 418$ °C), KNN has a satisfying large piezoelectric coefficient (d_{33} = 80 pC/N) when produced by conventional sintering [9,10]. The electrical properties of KNN are highly sensitive to the composition, this requires the maintenance of the desired stoichiometry during sintering to achieve the best electrical properties [11,12]. However, during solid-state sintering with even long dwell times, high densities cannot be obtained owing to problems such as the presence of volatilization of alkali elements, cubic grains that decelerated the densification, and high probability of secondary phase formation [13,14]. In addition, KNN ceramics have a narrow sintering window [7]. As a result of conventional sintering temperatures at around 1120°C, approaching KNN melting point (1140°C), leads to crystal structure defects and stoichiometry shift to different structures [15,16].

The main goal of the present study was to observe the applicability of such electric current-assisted techniques to produce KNN ceramics via flash sintering and reactive flash sintering processes. Therefore, the sintering of KNN powder and reactive sintering of KN and NN were carried out using flash sintering.

10.2. Experimental procedures

To synthesize potassium sodium niobate (KNN), potassium niobate (KN), sodium niobate (NN) powders, Nb_2O_5 (CAS#:12034–59-2, 99.9%, Sigma–Aldrich, USA), Na_2CO_3 (CAS#:497–18-8, ≥99%, Sigma Aldrich, USA), and K_2CO_3 (CAS#:584–08-7, ≥99.5%, Sigma Aldrich, USA) were weighed according to the stoichiometric ratios and mixed using a planetary ball mill in ethanol at 250 rpm for 24 h. After the slurries were dried, KNN powder for flash sintering was calcinated at 850 °C for 5 h with a heating rate of 5°C/min while KN and NN powders regarding reactive flash sintering were heat-treated at 700 °C for 1 h with a heating rate of 5°C/min. Finally, KNN powder was ball-milled to reduce particle size. Using the same procedure, KN and NN powder were mixed.

For flash and reactive flash sintering experiments, the dog bone specimens were pressed uniaxially at 300 MPa after the addition of 10 wt% distilled water. The cross-section of the dog-bone samples was around 3 x 1.5 mm^2, the electrode span was 20 mm.

The power supply was connected to the sample using two platinum wires, and placed into holes on opposite sides of the dog bone specimen. Conductive Pt-paste was used to improve the electrical contact between these platinum electrodes and the specimens.

A schematic representation of the flash sintering set-up utilized for this study is given in **Figure 10.1**. Various furnace temperature from 850 to 1075°C was used as an external heater source, eventually, the final experiments were carried out at 1075°C. Using a Glassman EW series 5 kV–120 mA DC power supply (Glassman EW series, TDK-Lambda, Villebon Courtaboeuf, France), a DC electric field of 1000 V/cm was employed. It was maintained at a constant value until the current limit value was reached. Generally, flash sintering requires a constant electric field applied to the body, along with a constant heating rate step. When the ceramic body becomes adequately conductive, a flash event takes place with a quick increase of current density; accordingly, the current flow must be cut-off to avoid melting. Herein, constant-current mode was also applied to the ceramics, causing a decrease in voltage. The current density was changed step-wise between 10 to 90 mA/mm^2. The current intensity and the voltage were monitored using a Keithley 2100 multimeter (Keithley Instruments Inc., USA). On reaching the selected current limit ($10mA/mm^2$- $90mA/mm^2$), the current flow was maintained for various times ranging from 1 min to 5 min and then shut down the system.

Relative density values of the specimens were determined using Archimedes' principle. For density measurements, only constant (linear) cross-section parts of the samples between electrodes were used. The morphology of the milled powder and the fracture surfaces of the specimens were analyzed by scanning electron microscopy (SEM, FEI Quanta 250 FEG, USA).

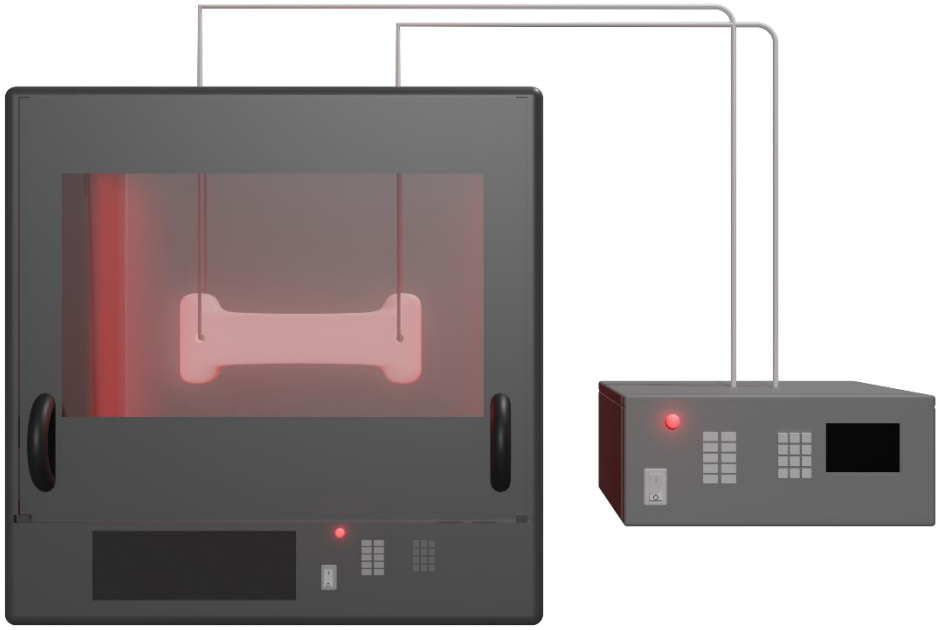

Figure 10.1. Schematic representation of flash sintering set-up utilized for this study.

10.3. Results and discussion

Relative density of around 80% were achieved as highest densification when KNN powder was directly used for single step flash sintering process under the conditions of 30-50 mA/mm^2 for 1 min. Then the samples were flash sintered at 10 mA/mm^2 for 5 min. Even though a relative density of 87.5% were achieved, the sample was about to melt. As such, different approaches were attempted to density KNN ceramics (**Table 10.1**). When the mixture of KN and NN were flash sintered at 3 step using different current adjustments. Using the multi-step current flow approach, around 91% relative density was reached after applying 10 mA/mm^2 for 1 min, 30 mA/mm^2 for 1 min, 50 mA/mm^2 for 1 min, respectively. For a comparison, KNN samples were flash-sintered utilizing the same step conditions, the relative density of sintered KNN was found to be around 88%.

But, when the dog bone-shaped green body obtained from the mixture of KN and NN was conventionally sintered, a relative density of 92% was achieved.

After the discovery of flash sintering, there have been many reports related to sintering of KNN. In the first study, the authors demonstrated that after flash sintering, a heterogeneous sintered structure reaching a relative density of 94% was found in the samples forming a compositional variation between the shell and the core. Subsequently, homogeneous composition was achieved after annealing at 1000 °C. In addition, compositional variations were attributed to grain boundary melting during the flash and resulting recrystallization as the sample cooled [7]. Villarinho's group carried out a series of flash sintering studies for KNN [17–21]. Similar to the results in this study, the initial results on the density found are similar to the results in this study [18,19]. After many process and procedure trials, the relative density values of the samples reached around 95% [17,18,20]. They also proposed that the mechanism for densification of KNN, leading to amorphization and particle sliding, could be current flowing via grain boundaries [17,18,21]. In addition, it was shown that KNN ceramics with remarkable densities reaching 99% can be produced by reactive flash sintering with potassium niobate and sodium niobate [22]. Lastly, flash sintering was also carried out using a parallel plate capacitor configuration, resulting in 98% densification and quite high dielectric permittivity [23].

Table 10.1. The sample's code and electric current schedule for flash sintering.

Sample code	Step 1	Step 2	Step 3	Relative density (%)
KNN	5 min @ 10 mA	-	-	87.5
KN+NN_10mA_20mA_30mA	1 min @ 10 mA	1 min @ 20 mA	1 min @ 30 mA	86.4
KN+NN_10mA_30mA_50mA	1 min @ 10 mA	1 min @ 30 mA	1 min @ 50 mA	90.9
KN+NN_10mA_40mA_70mA	1 min @ 10 mA	1 min @ 40 mA	1 min @ 70 mA	89.5
KN+NN_10mA_50mA_90mA	1 min @ 10 mA	1 min @ 50 mA	1 min @ 90 mA	87.6
KNN_10mA_30mA_50mA	1 min @ 10 mA	1 min @ 30 mA	1 min @ 50 mA	88
KNN_10mA_40mA_70mA	1 min @ 10 mA	1 min @ 40 mA	1 min @ 70 mA	87.9

SEM images obtained from the fracture surfaces of the flash-sintered samples produced with different starting materials and current conditions are shown in **Figure**

10.2. Using single-step current, the specimen produced at 50 mA/mm^2 for 1 min using KNN powder exhibited relatively porous with high cavities which is consistent with its relative density value. Directly, the application of high current to the samples led to the formation of such large cavities in all samples. On the other hand, by utilizing multi-step current approach, highly dense microstructures with relative densities of around 90% were formed, reducing the cavities and therefore porosity. It is worth noting that during the sintering of KNN powder starting in the same current range, abnormal grain growth was detected in the sample with a higher current step (40 and 70 mA/mm^2) while the sample produced with a lower current step (30 and 50 mA/mm^2) caused the samples to have a more homogeneous microstructure. It was shown that a homogeneous KNN microstructure can be obtained when sintered at lower sintering temperatures compared to higher temperatures due to abnormal grain growth frequently observed in KNN [24]. Besides, when a current step of 90 mA/mm^2 was applied, melting was observed in the sample. As such, the application of electric field-assisted sintering techniques to materials with a restricted sintering temperature range may provide difficulties because of melting temperatures.

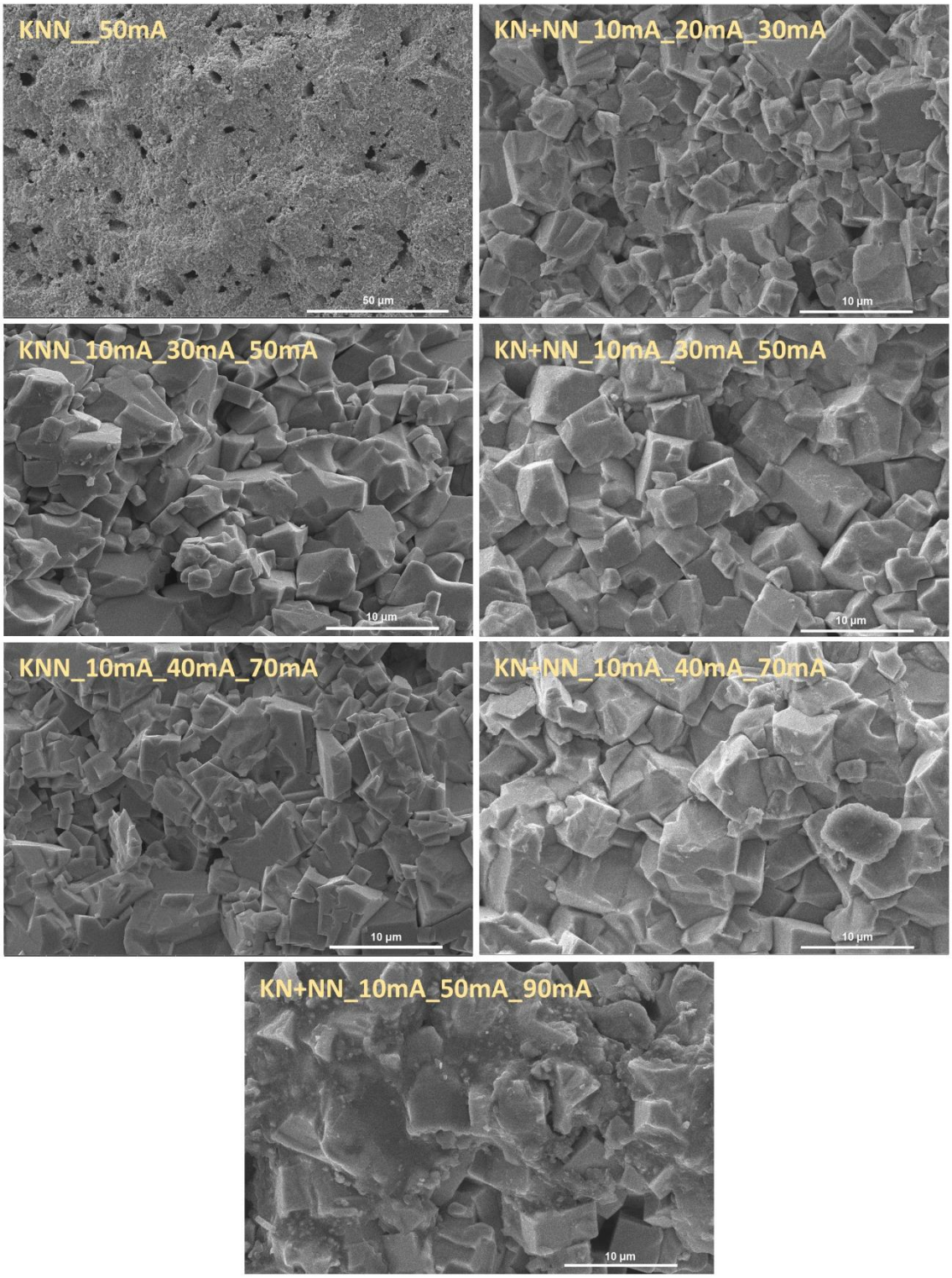

Figure 10.2. Fracture surface morphologies of flash-sintered specimens.

10.4. Conclusions

Potassium sodium niobate was attempted to densify via flash and reactive flash sintering process. Single step current approach resulted in lower densification with cavities. As such, with a gradual current increase, flash sintering was applied to both KNN powders and a mixture of NN and KN powders. After utilizing multi-step current, the relative densities were enhanced up to around 90%. Additionally, higher current (e.g., 90 mA/mm^2) led to the samples to melt. Although successful results can be found in the literature, such electric field-assisted sintering techniques may be challenging for materials with a narrow sintering temperature range due to melting temperatures.

References

[1] M. Biesuz, S. Grasso, V.M. Sglavo, What's new in ceramics sintering? A short report on the latest trends and future prospects, Curr. Opin. Solid State Mater. Sci. 24 (2020) 100868. https://doi.org/10.1016/j.cossms.2020.100868.

[2] O. Guillon, W. Rheinheimer, M. Bram, A Perspective on Emerging and Future Sintering Technologies of Ceramic Materials, Adv Eng Mater. 25 (2023) 2201870. https://doi.org/10.1002/adem.202201870.

[3] M. Cologna, B. Rashkova, R. Raj, Flash Sintering of Nanograin Zirconia in <5 s at 850°C, J. Am. Ceram. Soc. 93 (2010) 3556–3559. https://doi.org/10.1111/j.1551-2916.2010.04089.x.

[4] R. Raj, D.E. Wolf, C.N. Yamada, S.K. Jha, J.-M. Lebrun, On the confluence of ultrafast high-temperature sintering and flash sintering phenomena, Journal of the J. Am. Ceram. Soc. 106 (2023) 3983–3998. https://doi.org/10.1111/jace.19070.

[5] C.E.J. Dancer, Flash sintering of ceramic materials, Mater Res Express. 3 (2016) 102001. https://doi.org/10.1088/2053-1591/3/10/102001.

[6] M. Biesuz, V.M. Sglavo, Flash sintering of ceramics, J Eur Ceram Soc. 39 (2019) 115–143. https://doi.org/10.1016/j.jeurceramsoc.2018.08.048.

[7] G. Corapcioglu, M.A. Gulgun, K. Kisslinger, S. Sturm, S.K. Jha, R. Raj, Microstructure and microchemistry of flash sintered $K_{0.5}Na_{0.5}NbO_3$, J. Ceram. Soc. JAPAN 124 (2016) 321–328. https://doi.org/10.2109/jcersj2.15290.

[8] R. Raj, Joule heating during flash-sintering, J Eur Ceram Soc. 32 (2012) 2293–2301. https://doi.org/10.1016/j.jeurceramsoc.2012.02.030.

[9] L. Egerton, D.M. Dillon, Piezoelectric and dielectric properties of ceramics in the system potassium—sodium niobate, J. Am. Ceram. Soc. 42 (1959) 438–442.

[10] R.E. Jaeger, L. Egerton, Hot pressing of potassium-sodium niobates, Journal of the American Ceramic Society. 45 (1962) 209–213.

[11] C. Piskin, L. Karacasulu, M. Bortolotti, C. Vakifahmetoglu, Synthesis of potassium–sodium niobate (KNN) from NbO_2, Open Ceramics. 7 (2021) 100159. https://doi.org/10.1016/j.oceram.2021.100159.

[12] C. Piskin, L. Karacasulu, G. Ischia, M. Bortolotti, C. Vakifahmetoglu, Hydrothermal synthesis of potassium–sodium niobate powders, J. Am. Ceram. Soc. 105 (2022) 3809–3819. https://doi.org/10.1111/jace.18349.

[13] B. Malič, J. Koruza, J. Hreščak, J. Bernard, K. Wang, J.G. Fisher, A. Benčan, Sintering of lead-free piezoelectric sodium potassium niobate ceramics, Materials. 8 (2015) 8117–8146.

[14] M. Bah, R. Podor, R. Retoux, F. Delorme, K. Nadaud, F. Giovannelli, I. Monot-Laffez, A. Ayral, Real-Time Capturing of Microscale Events Controlling the Sintering of Lead-Free Piezoelectric Potassium-Sodium Niobate, Small. 18 (2022) 2106825. https://doi.org/10.1002/smll.202106825.

[15] R. López, F. González, M.P. Cruz, M.E. Villafuerte-Castrejon, Piezoelectric and ferroelectric properties of $K_{0.5}Na_{0.5}NbO_3$ ceramics synthesized by spray drying method, Mater Res Bull. 46 (2011) 70–74.

[16] L. Karacasulu, C. Vakifahmetoglu, Cold sintering assisted two-step sintering of potassium sodium niobate (KNN) ceramics, Materials Science and Engineering: B. 297 (2023) 116709. https://doi.org/10.1016/j.mseb.2023.116709.

[17] R. Serrazina, J.S. Dean, I.M. Reaney, L. Pereira, P.M. Vilarinho, A.M.O.R. Senos, Mechanism of densification in low-temperature FLASH sintered lead free potassium sodium niobate (KNN) piezoelectrics, J Mater Chem C Mater. 7 (2019) 14334–14341. https://doi.org/10.1039/C9TC03117K.

[18] R. Serrazina, A.M.O.R. Senos, L. Pereira, J.S. Dean, I.M. Reaney, P.M. Vilarinho, The Role of Particle Contact in Densification of FLASH Sintered Potassium Sodium Niobate, Eur J Inorg Chem. 2020 (2020) 3720–3728. https://doi.org/10.1002/ejic.202000458.

[19] R. Serrazina, C. Ribeiro, M.E. Costa, L. Pereira, P.M. Vilarinho, A.M.O.R. Senos, Particle characteristics' influence on FLASH sintering of potassium sodium niobate: A relationship with conduction mechanisms, Materials. 14 (2021) 1321.

[20] R. Serrazina, A. Tkach, L. Pereira, A.M.O.R. Senos, P.M. Vilarinho, Flash Sintered Potassium Sodium Niobate: High-Performance Piezoelectric Ceramics at Low Thermal Budget Processing, Materials. 15 (2022) 6603.

[21] R. Serrazina, P.M. Vilarinho, A.M.O.R. Senos, L. Pereira, I.M. Reaney, J.S. Dean, Modelling the particle contact influence on the Joule heating and temperature distribution during FLASH sintering, J Eur Ceram Soc. 40 (2020) 1205–1211. https://doi.org/10.1016/j.jeurceramsoc.2019.12.015.

[22] Y. Wu, X. Su, G. An, W. Hong, Dense $Na_{0.5}K_{0.5}NbO_3$ ceramics produced by reactive flash sintering of $NaNbO_3$-$KNbO_3$ mixed powders, Scr Mater. 174 (2020) 49–52. https://doi.org/10.1016/j.scriptamat.2019.08.035.

[23] İ. Şavklıyıldız, Ç. Okur, E.K. Akdoğan, Flash sintering and dielectric properties of $K_{0.5}Na_{0.5}NbO_3$, J. Am. Ceram. Soc. 105 (2022) 469–480. https://doi.org/10.1111/jace.18119.

[24] Y. Zhen, J.-F. Li, Abnormal Grain Growth and New Core–Shell Structure in (K,Na)NbO_3-Based Lead-Free Piezoelectric Ceramics, J. Am. Ceram. Soc. 90 (2007) 3496–3502. https://doi.org/10.1111/j.1551-2916.2007.01977.x.

CHAPTER 11

ULTRAFAST HIGH-TEMPERATURE SINTERING OF POTASSIUM SODIUM NİOBATE

The following chapter is written in the format of a manuscript to be submitted. In preparation

Abstract

A novel sintering method, ultrafast high-temperature sintering, was attempted to enhance the densification of KNN ceramics. Notably, a relative density of up to around 90% was achieved at a current flow of 16A for 1 min. KNN ceramics have a narrow sintering window due to the sintering temperature being close to the melting temperature, leading to high sensitivity to current. In addition, when UHS was utilized to produce KNN powders from only the starting materials, the fast synthesis was accomplished in a short time which might have prevented volatilization of the alkali materials.

11.1. Introduction

Potassium sodium niobate, $K_{0.5}Na_{0.5}NbO_3$ (KNN), has attracted attention as lead-free & environmental-friendly piezoelectric material in recent years. It exhibits a relatively high Curie temperature ($T_c \cong 418$ °C) and a substantial piezoelectric coefficient (d_{33} = 80 pC/N) in its conventionally sintered form [1–3]. The electrical properties of KNN are profoundly influenced by its composition, necessitating strict control over stoichiometry during the sintering process to achieve optimal electrical characteristics [4,5]. Nevertheless, challenges persist in achieving high densities during solid-state

sintering, despite prolonged dwell times, due to issues such as volatilization of alkali elements, hindrance by cubic grains impeding densification, and a possibility of secondary phase formation [3,6,7]. In addition, KNN ceramics have a narrow sintering window [8]. Solid-state sintering at temperatures around 1120°C, close to the KNN melting point (1140°C), often results in structural defects and deviations in stoichiometry, leading to different crystal structures [3,9].

Wang et al. introduced a novel unconventional sintering method in 2020, which is called Ultra-fast High-temperature Sintering (UHS) [10]. UHS enables the densification of monolithic ceramics by radiative heating (10^3-10^4 °C/min) under an inert atmosphere such as argon in extremely short times (10-300s). To achieve this, the green body is wrapped in graphite felts that have been quickly Joule-heated by an electric current passage [10–17]. Besides, utilizing this process, simultaneous synthesis and sintering of a variety of ceramic materials directly from the precursors as reactive UHS has been achieved [10,18–20].

The main aim of this study was to observe the implementation of such a joule heating-based sintering technique to produce KNN ceramics via ultrafast high-temperature sintering. Besides, the production of monolithic KNN ceramics from the starting materials (i.e., simultaneous synthesis and densification) were investigated.

11.2. Experimental procedures

Potassium sodium niobate (KNN) powders were synthesized using a solid-state synthesis route in order to use in the UHS process. Nb_2O_5 (CAS#:12034–59-2, 99.9%, Sigma–Aldrich, USA), Na_2CO_3 (CAS#:497–18-8, ≥99%, Sigma Aldrich, USA), and K_2CO_3 (CAS#:584–08-7, ≥99.5%, Sigma Aldrich, USA) stoichiometrically were weighed and ball-milled in an ethanol medium for 24 h. Then the obtained mixture was dried and calcined in an elevated furnace at 850°C for 5 h. KNN powder was then ball-milled again for 24h to reduce particle size. The milled KNN powders (≈ 0.18 g) were pressed uniaxially under a pressure of 100 MPa to obtain 8 mm disc-shaped pellets. In addition, the dried mixture (not calcined at 850°C) was pressed under the same conditions to use in the reactive UHS experiments. For UHS process, the felt was clamped between two copper electrodes with the distance between the two electrodes of 30 mm in order to

guarantee good electrical contact. Green pellets were inserted into the carbon felt with a size of 10-24x70x6 mm^3. UHS experiments were carried out in an argon-filled box. An electric current was applied to the felt using DC power supply (Agilent Technologies, model 6674A, Santa Clara, CA, USA). The applied electric current was increased starting from 10A up to 20A for varying times ranging from 15 sec to 2 min.

Relative densities of the samples were determined using Archimedes' principle. The morphology of fracture surfaces of the samples was observed by scanning electron microscopy (SEM, FEI Quanta 250 FEG, USA)). Crystallographic phases were identified using an X-ray diffractometer (XRD, Panalytical X'Pert PRO, The Netherlands) with a Copper anode X-Ray source (CuKα = 1.5406 Å at 40kV, 30 mA).

11.3. Results and discussion

The results of relative densities of the samples produced via UHS using different conditions such as dwell time and current for 24 mm-carbon felt are given in **Table 11.1**. Increasing from 16A to 17A for 30 s, the relative density of KNN pellets was enhanced from 73% to 81%. When 18A was employed in the system, the sample resulted in complete melting. However, the relative density of the UHSed compacts produced at 16A increased from 73% to 89% with increasing time from 30s to 60s. As such, the optimum current for producing KNN ceramics was found to be about 16A for 24 mm-carbon felt. However, the samples produced at this current for 90 and 120 seconds melted. It should be noted that the melting temperature of KNN is 1140°C [9]. Sintering of KNN is generally achieved at temperatures around 1100-1120°C, which is rather close to melting temperature of KNN [3].

Table 11.1. Relative densities of the samples produced via UHS using different conditions such as dwell time and current for 24 mm-carbon felt.

Duration (s)	Relative density (%)					
	15A	16A	17A	18A	19A	20A
15	56-60					66
30	-	73	81	M	M	M
45	-	84	M	M	M	M
60	73	89	M	M	M	M
90	-	M	M	M	M	M
120	75	M	M	M	M	M

* M: Melted

Fig. 11.1 shows the micrographs obtained from the fracture surfaces of UHSed KNN samples at different current conditions for 60 s. The sample produced at 16A appeared to have homogeneous morphology with smaller-grain sized structure. Additionally, the sample produced at 17 A had local melted regions due to the applied current.

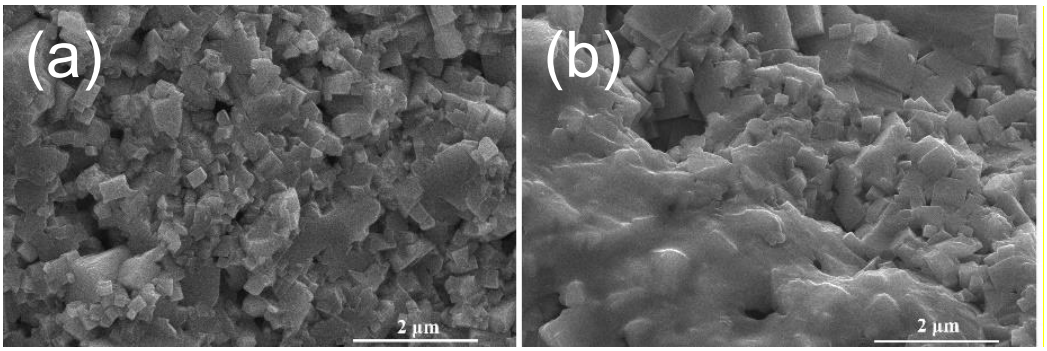

Figure 11.1. SEM images of the UHSed samples at different current conditions for 60 s, (a) 16A and (b) 17A.

X-ray diffraction patterns of the UHSed samples at different current conditions for 60s are shown in **Figure 11.2**. All samples were associated with KNN phase. XRD peaks split and became narrower and sharper as the current generally increased, and the

crystallinity increased. However, when 18A was applied to the system, the crystallinity decreased since the sample probably melted and solidified quickly.

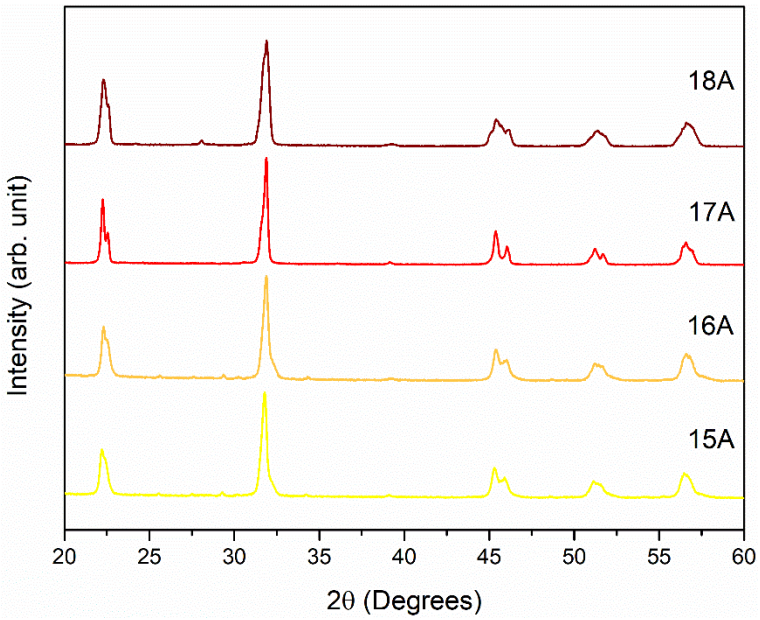

Figure 11.2. XRD pattern of the UHSed samples at different current conditions for 60 s.

In more recent work, $SrTiO_3$ ceramics were densified using 10 mm-width graphite felt via UHS [12]. In this regard, KNN ceramics were also tried to densify using 10 mm and 16 mm graphite felt. the samples prepared by UHS using 10 mm felt at the different currents (13A-16A) for 10 s were in the range of 59-64 %. However, blackening with local melted regions (the shape of the sample changed from a normal disc to an oval shape) was observed on the edges of the sample produced using 10 mm carbon felt. Therefore, smaller graphite felts might not be useful to sinter ceramics with lower melting temperatures. 16 mm-felt was also attempted to densify the pellets. The samples with a relative density of 80% were achieved using UHS at the conditions of 13A for 60s. Accordingly, it was found that 24 mm-felt was suited for UHS rather than 10- and 16-mm felts in terms of homogeneity and high density.

KNN ceramics have a narrow sintering window, which results in high sensitivity to current. This is because the melting temperature of KNN is very close to its sintering temperature [9]. Precise current control systems are required to densify KNN ceramics by UHS. As such, it is worth noting that the utilization and control of the UHS process

for materials with low melting temperatures or $T_s/T_m>0.9$ (e.g., T_s/T_m ratio of KNN is 0.98) pose challenges.

In addition to the ordinary sintering of KNN via UHS, KNN was attempted to sinter as "reactive processing" by UHS. However, specimens produced using the dried mixture of Na_2CO_3, K_2CO_3, and Nb_2O_5 (not calcinated) via reactive UHS resulted in either broken or misshapen due probably to the removal of CO_2 from starting carbonates and low melting temperature of K_2CO_3 and Na_2CO_3 [5]. However, the obtained results are promising since the process allows the production of KNN phase in a short time. XRD results of the ground samples produced at different currents are shown in **Figure 11.3**. All samples exhibited potassium sodium niobate phase with high crystallinity. As mentioned before, KNN has problems with volatilization of alkalis formation [3,6,7]. Since KNN powder may be produced in a short time via UHS route, UHS might prevent volatilization of the alkali materials. Further studies are required to investigate the influence of these conditions and the optimization of the process.

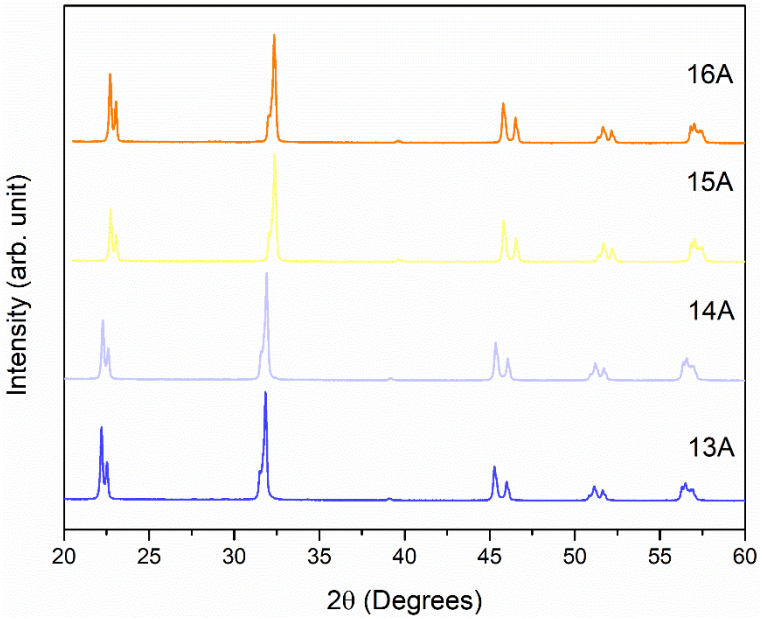

Figure 11.3. X-ray diffraction patterns of the samples produced using the dried mixture (not calcinated) at different currents for 60 s.

11.4. Conclusions

KNN ceramics were attempted to densify via a novel sintering technique, an ultrafast high-temperature sintering process. The highest relative density reaching 90% was achieved at a current flow of 16A for 1 min. Because KNN ceramics have a narrow sintering window due to close to their melting temperature, resulting in high sensitivity to the current. Besides, when the reaction was carried out in UHS from only the starting materials, it was also observed that the reaction of the starting materials into KNN was completed, resulting in the synthesis in a short time. The production of KNN powders via the UHS method might serve as a promising alternative compared to other powder synthesis techniques.

References

[1] L. Egerton, D.M. Dillon, Piezoelectric and dielectric properties of ceramics in the system potassium—sodium niobate, J. Am. Ceram. Soc. 42 (1959) 438–442.

[2] R.E. Jaeger, L. Egerton, Hot pressing of potassium-sodium niobates, J. Am. Ceram. Soc. 45 (1962) 209–213.

[3] L. Karacasulu, C. Vakifahmetoglu, Cold sintering assisted two-step sintering of potassium sodium niobate (KNN) ceramics, Mater. Sci. Eng. B. 297 (2023) 116709. https://doi.org/10.1016/j.mseb.2023.116709.

[4] C. Piskin, L. Karacasulu, M. Bortolotti, C. Vakifahmetoglu, Synthesis of potassium–sodium niobate (KNN) from NbO_2, Open Ceramics. 7 (2021) 100159. https://doi.org/10.1016/j.oceram.2021.100159.

[5] C. Piskin, L. Karacasulu, G. Ischia, M. Bortolotti, C. Vakifahmetoglu, Hydrothermal synthesis of potassium–sodium niobate powders, J. Am. Ceram. Soc. 105 (2022) 3809–3819. https://doi.org/10.1111/jace.18349.

[6] B. Malič, J. Koruza, J. Hreščak, J. Bernard, K. Wang, J.G. Fisher, A. Benčan, Sintering of lead-free piezoelectric sodium potassium niobate ceramics, Materials. 8 (2015) 8117–8146.

[7] M. Bah, R. Podor, R. Retoux, F. Delorme, K. Nadaud, F. Giovannelli, I. Monot-Laffez, A. Ayral, Real-Time Capturing of Microscale Events Controlling the

Sintering of Lead-Free Piezoelectric Potassium-Sodium Niobate, Small. 18 (2022) 2106825. https://doi.org/10.1002/smll.202106825.

[8] G. Corapcioglu, M.A. Gulgun, K. Kisslinger, S. Sturm, S.K. Jha, R. Raj, Microstructure and microchemistry of flash sintered $K_{0.5}Na_{0.5}NbO_3$, J. Ceram. Soc. JAPAN 124 (2016) 321–328. https://doi.org/10.2109/jcersj2.15290.

[9] R. López, F. González, M.P. Cruz, M.E. Villafuerte-Castrejon, Piezoelectric and ferroelectric properties of $K_{0.5}Na_{0.5}NbO_3$ ceramics synthesized by spray drying method, Mater Res Bull. 46 (2011) 70–74.

[10] C. Wang, W. Ping, Q. Bai, H. Cui, R. Hensleigh, R. Wang, A.H. Brozena, Z. Xu, J. Dai, Y. Pei, A general method to synthesize and sinter bulk ceramics in seconds, Science (1979). 368 (2020) 521–526.

[11] M. Ihrig, T.P. Mishra, W.S. Scheld, G. Häuschen, W. Rheinheimer, M. Bram, M. Finsterbusch, O. Guillon, $Li_7La_3Zr_2O_{12}$ solid electrolyte sintered by the ultrafast high-temperature method, J. Eur. Ceram. Soc. 41 (2021) 6075–6079.

[12] T.P. Mishra, S. Wang, C. Lenser, D. Jennings, M. Kindelmann, W. Rheinheimer, C. Broeckmann, M. Bram, O. Guillon, Ultra-fast high-temperature sintering of strontium titanate, Acta Mater. 231 (2022) 117918.

[13] M. Biesuz, A. Galotta, A. Motta, M. Kermani, S. Grasso, J. Vontorová, V. Tyrpekl, M. Vilémová, V.M. Sglavo, Speedy bioceramics: Rapid densification of tricalcium phosphate by ultrafast high-temperature sintering, Mater. Sci. and Eng. C. 127 (2021) 112246.

[14] J. Dong, V. Pouchly, M. Biesuz, V. Tyrpekl, M. Vilémová, M. Kermani, M. Reece, C. Hu, S. Grasso, Thermally-insulated ultra-fast high temperature sintering (UHS) of zirconia: A master sintering curve analysis, Scr Mater. 203 (2021) 114076.

[15] R.-X. Luo, M. Kermani, Z.-L. Guo, J. Dong, C.-F. Hu, F. Zuo, S. Grasso, B.-B. Jiang, G.-L. Nie, Z.-Q. Yan, Ultrafast high-temperature sintering of silicon nitride: A comparison with the state-of-the-art techniques, J. Eur. Ceram. Soc. 41 (2021) 6338–6345.

[16] M. Kermani, J. Dong, M. Biesuz, Y. Linx, H. Deng, V.M. Sglavo, M.J. Reece, C. Hu, S. Grasso, Ultrafast high-temperature sintering (UHS) of fine grained α-Al_2O_3, J. Eur .Ceram. Soc. 41 (2021) 6626–6633.

[17] R.-F. Guo, H.-R. Mao, Z.-T. Zhao, P. Shen, Ultrafast high-temperature sintering of bulk oxides, Scr Mater. 193 (2021) 103–107.

[18] Z.-T. Zhao, R.-F. Guo, H.-R. Mao, P. Shen, Effect of components on the microstructures and properties of rare-earth zirconate ceramics prepared by ultrafast high-throughput sintering, J. Eur. Ceram. Soc. 41 (2021) 5768–5773.

[19] H.-R. Mao, E.-T. Dong, S.-B. Jin, X.-M. Qiu, P. Shen, Ultrafast high-temperature synthesis and densification of high-entropy carbides, J. Eur. Ceram. Soc. 42 (2022) 4053–4065.https://doi.org/10.1016/j.jeurceramsoc.2022.03.054.

[20] R. Wang, W. Ping, C. Wang, Y. Liu, J. Gao, Q. Dong, X. Wang, Y. Mo, L. Hu, Computation-Guided Synthesis of New Garnet-Type Solid-State Electrolytes via an Ultrafast Sintering Technique, Adv. Mater. 32 (2020) 2005059. https://doi.org/10.1002/adma.202005059.

CHAPTER 12

ULTRAFAST HIGH-TEMPERATURE SINTERING OF YTTRIA-STABLIZED ZIRCONIA IN REACTIVE N_2 ATMOSPHERE

The following chapter is written in the format of a manuscript submitted to Acta Materialia.

Abstract

Ultrafast high-temperature sintering (UHS) has already been applied to different ceramic systems but no studies on possible reactions between the atmosphere and the material have been reported to date. In the present work, we investigated the behavior of 3YSZ upon UHS in nitrogen and argon atmosphere. It was observed that "*the atmosphere matters"*. Highly densified samples were achieved in both enviroments but densification and grain growth are significantly retarded in N_2. Moreover, the phase evolution is strongly atmosphere-dependent with the samples treated in Ar remaining tetragonal and those treated under nitrogen progressively reducing their tetragonality and eventually converting into cubic zirconia, and rock salt oxynitride. The results can be explained by the incorporation of nitrogen within the ZrO_2 lattice, leading to the formation of oxygen vacancy for charge compensation and consuming the free electrons produced by the oxide reduction in UHS (allowing the conversion of N_2 into N^{3-} ions). Besides structure and microstructure, the atmosphere can change the properties of UHS YSZ. Specifically, electrochemical impedance spectroscopy demonstrates that while the ionic bulk and grain boundary specific conductivity is not influenced by the sintering atmosphere, the grain boundaries' capacitive behavior strongly changes.

12.1. Introduction

In the decades, different sintering strategies that induce densification of ceramic materials with limited grain growth have been introduced [1–6]. Despite such non-conventional technologies refer to different approaches to enhance densification (electric fields and currents [7,8], electromagnetic radiations [9], solvent [6,10], pressure [11]) most of them share a common feature: they allow rapid hating of the ceramic body and examples include microwave sintering [12], fast firing [13], spark plasma sintering [2], blacklight sintering [14], ultrafast high-temperature sintering [15] and flash sintering [16,17].

In this context, particular interest has arisen from ultrafast high-temperature sintering (UHS) introduced by Wang et al. in 2020 [15]. UHS enables the densification of monolithic ceramics by radiative heating (10^3-10^4 K min^{-1}) under inert atmosphere, like argon, in extremely short times (10-300 s). To achieve this, the green body is placed within graphite felt [18] which is quickly Joule-heated by an electrical current flow [15,19–32]. In addition, simultaneous solid-state synthesis and sintering are possible in UHS using a mixture of different ceramic powders as precursors [15,28,29,32–35].

Due to its mechanical, thermal, and electrochemical properties, doped zirconia is used in a wide range of applications, such as cutting tools, dental implants, oxygen sensors, solid oxide fuel cells, and thermal barrier coatings [22,36]. Pure zirconia possesses three polymorphs, stable at different temperatures: monoclinic (T < 1170 °C), tetragonal (1170 < T < 2370 °C) and cubic (T > 2370 °C). Thelatter possesses the highest ionic conductivity and is employed in electrochemical devices, whereas the tetragonal phase is used for structural applications due to its high fracture toughness [22,37].

The stabilization of the cubic and tetragonal polymorphs at room temperature is usually achieved by doping with bivalent (CaO and MgO) or trivalent oxides (Y_2O_3, Sc_2O_3, and Yb_2O_3) [22,37]. Also anion doping is a practical approach in stabilizing the high-temperature polymorphs [38–40]. For instance, zirconia hot-pressed in N_2 atmosphere shows partial substitution of nitrogen (N^{3-}) for oxygen (O^{2-}) [37,41]. Besides hot pressing, nitridation of zirconia was observed in various heat treatments [38,39,42–46], microwave plasma processing [47], laser processing [48] and flash sintering [49] under a controlled atmosphere.

UHS has already been applied to YSZ [22,50]; nevertheless, the process were carried out in an inert Ar atmosphere, with no substantial reaction with the oxide. Besides the N-doping effect on phase stability, the sintering atmosphere can also impact the densification process and microstructure evolution, resulting in variable concentration, type, and mobility of both ionic and electronic defects [51–54].

Although reactive UHS was studied using solid precursors, it was not applied so far to obtain reactions or doping from a gas phase, as for zirconia sintered under N_2. The aim of the present work is to answer the following questions: "*Does UHS in N_2 impact the phase stability of sintered YSZ artifact? Does the atmosphere affect the microstructural evolution of YSZ?*". For this reason, the simultaneous sintering and nitriding of 3 mol% yttria-stabilized zirconia (3YSZ) upon UHS under N_2 atmosphere were explored here and the obtained materials were compared with those produced by more conventional UHS carried out in Ar.

12.2. Experimental procedures

3YSZ granulated powder (TZ-3YSB-E, Tosoh Corporation, Tokyo, Japan) was used in this work. Cylindrical pellets, 8 mm in diameter, were obtained by uniaxial pressing (300 MPa). Before UHS, the samples were debinded at 500°C in air for 30 min. The relative density of the green body was about 50% after debinding.

For the UHS process, a carbon felt (SGL Carbon Co., Germany) was clamped between two steel electrodes, resulting in an electrode span of 30 mm and a cross-section of 19x6 mm^2. The green pellets were introduced into the carbon felt through a small hole produced using a small spatula. The hole was closed with a felt fragment to prevent thermal gradients and reduce heat losses. UHS was carried out in a borosilicate flask filled with nitrogen or argon for "reactive" and "conventional" experiments, respectively. An electric current was applied to the felt using DC power supply (Agilent Technologies, model 6674A, Santa Clara, CA, USA), the power source always working in current control. Different currents were applied, ranging from 15 A up to 35 A, for different holding time (1 - 3 min). In order to estimate the temperature in the UHS system, finite element model (FEM) simulations were carried out using COMSOL Multiphysics software following two different approaches. In the former, called "full contact", an ideal

contact with the sample and no convection heat losses on the sample surfaces are assumed; in the second one, named "contactless", apertures and convective losses are considered. The real temperature is expected to be intermediate between those calculated by said two extreme scenarios. The details of the calibration procedures and the boundary conditions used for the numerical analysis are available in some previous works [30,31].

The density of the samples was determined using Archimedes' principle in a water medium. The relative density was calculated based on a theoretical density of 3-YSZ equal to (6.05 g cm^{-3}) [55].

The polished cross-sections of samples produced at ≥30A were thermally etched by UHS carried out at relatively low currents (24 A) under the atmosphere they were produced while the samples sintered at lower currents were thermally etched in a furnace. The cross-sections were observed by SEM (SUPRA V40, Carl-Zeiss, Germany) after being coated with Pt/Pd. Grain size measurements were carried out using the linear intercept method.

X-ray diffraction was carried out using an Italstructures IPD3000 diffractometer, with copper anode source (λ = 1.5406 Å, 40kV, 30mA) coupled to a collimating Goebel mirror on the primary beam side and a Dectris Mythen 1K detector on the diffracted beam side; Rietveld analysis was performed using the Maud software [56] by refining phase scale factors as well as lattice and average domain size parameters.

Raman measurements were carried out at room temperature using a micro-Raman spectrometer (Horiba Jobin-Yvon LabRam HR 800). The exciting radiation was provided by a He-Ne laser (λ_{exc} = 632.8 nm) operating at 6 mW with a spot size of about 1.5 μm. A narrow-band notch filter was used to cut the signal from the Rayleigh line to 200 cm^{-1}. The scattered radiation was filtered by using a grating with 600 lines mm^{-1}, and detected by a nitrogen-cooled CCD detector (1024×256 pixels).

Electrical Impedance Spectroscopy (EIS) measurements were performed in air using a Frequency Response Analyzer (MTZ35, Biologic, France) at 100 mV in the frequency range of 10-10^6 Hz. The obtained data were fitted using ZView software considering an equivalent circuit consisting of R-CPEs (Resistance-Fixed Phase Element) connected in series. Pt sputtered layers on the polished surfaces of the specimen were used as electrodes.

X-ray Photoelectron Spectroscopy (XPS) was carried out on a K alpha Thermo Scientific Spectrometer using an Al-Kα radiation. Angle-resolved measurements were

performed at take-off angle $\theta = 90°$ (e.g., normal to the sample surface). For the survey spectra, pass energy was fixed at 160 eV and at 40 eV for high resolution spectra. The background was calculated using the Shirley method and peaks were fitted using a Gaussian shape. A flood gun was also applied to avoid charge effects.

12.3. Results

The relative density evolution of 3YSZ is reported in **Fig. 12.1(a)** as a function of the UHS current and atmosphere. The density increases with the applied current, this reflecting the higher temperature achieved by the ceramic body, which exceeds 2000°C in the case of treatments under currents above 32.5 A. FEM simulations point out that the sample reaches the equilibrium within about 1 min (**Fig. 12.1(b,c))** the heating rates being well above 10^3 °C min^{-1}.

Well-densified bodies can be obtained within 1 min UHS treatments both in Ar and N_2 but the current needed to achieve full densification is substantially different in the two cases, 20 A in Ar and 25 A in N_2. In general, the samples treated in N_2 require a higher current to sinter if compared with those treated in Ar.

The densification of the YSZ artifacts by UHS is confirmed by SEM micrographs taken on polished and thermally etched cross-sections (**Fig. 12.2**, taken at the sample center). Samples sintered under Ar at 20 and 22.5A are already almost fully dense and show grain size of 0.24 ± 0.04 μm and 0.43 ± 0.15 μm, respectively. On the other hand, the samples treated under the same current under N_2 are still partially porous, in agreement with the density trend (**Fig. 12.1(a)**), and exhibit smaller grain size (0.11 ± 0.02 μm and 0.19 ± 0.06 μm under 20 and 22.5 A, respectively). It is worth noting that the sample produced in N_2 at 22.5 A possesses a grain size similar to the sample produced in Ar under 20 A, although the Ar-treated sample is much denser (**Fig. 12.1(a)**). The result suggests that treatments in Ar are more efficient in promoting densification over coarsening. When UHS is carried out at higher currents (≥30A), exaggerated grain growth occurs (one must note that the magnification increases 20 times in the different micrographs in **Fig. 12.2**). As expected, samples treated for 3 min are characterized by larger grains compared with those treated for 1 min (**Table 12.1**). Besides, the samples produced under Ar generally possess larger grains than under N_2 for the same sintering

conditions. Therefore, one can infer that the atmosphere (N_2 or Ar) has a fundamental impact on the microstructural evolution of YSZ during UHS.

We questioned whether these differences in densification and grain growth kinetics might originate from differences in the sample temperature under Ar and N_2 or form a reaction between nitrogen and YSZ, this causing a substantial modification of the defect chemistry. To exclude the first hypothesis, we checked the current needed to melt a small piece of copper within the UHS apparatus in Ar and N_2 and no statistically reproducible difference between the two atmospheres were detected. Hence, one can infer that thermal effects play a minor role and, consequently, some specific reactions between the oxide and the atmosphere must take place under N_2.

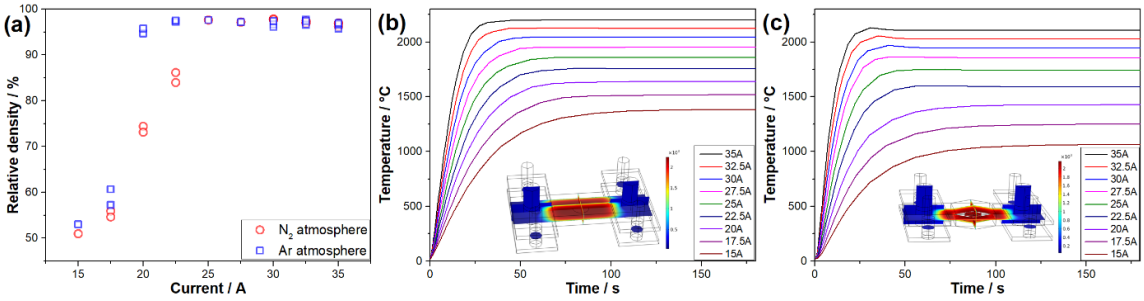

Figure 12.1. (a) Relative density of 3YSZ samples under Ar and N_2 atmosphere as a function of on current (each single point correspond to different sample); (b) full contact,and (c) contactless temperature simulation evolution upon UHS at different applied current.

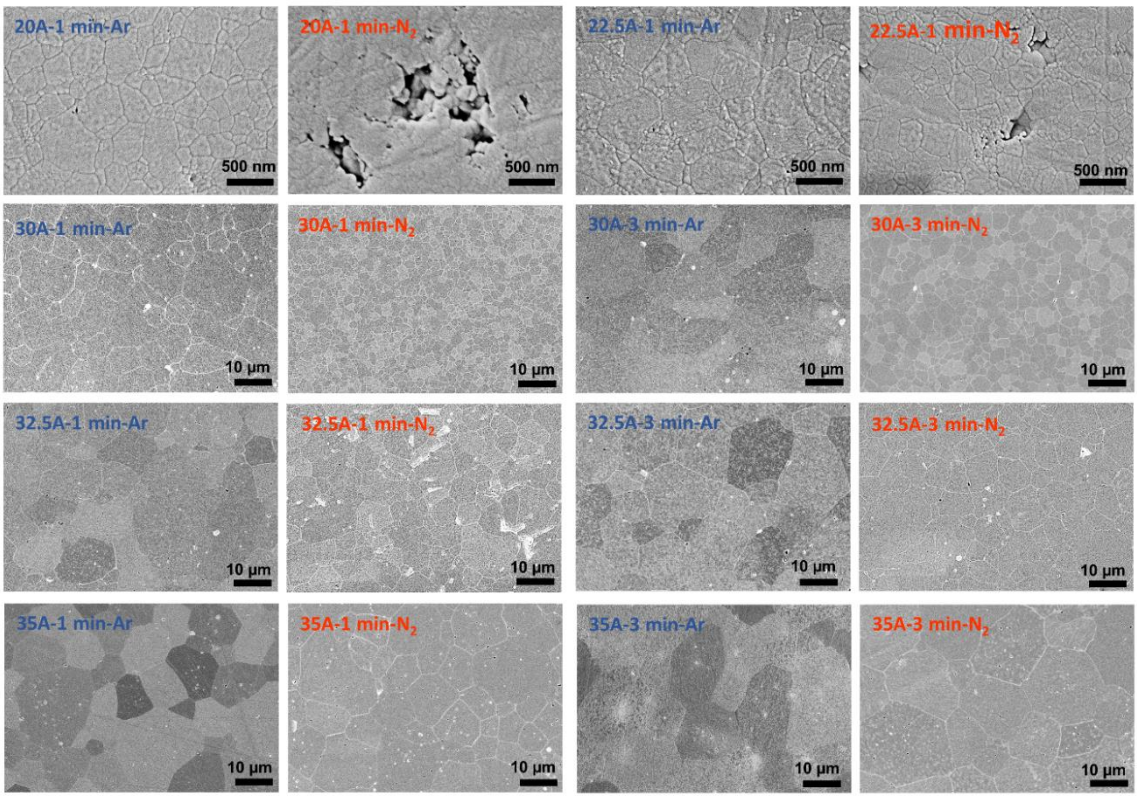

Figure 12.2. SEM micrographs of polished cross-section of the samples produced under different currents (A), dwell time (min) and environmental conditions (Ar or N_2).

Table 12.1. Grain size (in µm) after UHS under different currents/times in Ar and N_2.

Current / Time	Argon	Nitrogen
20A / 1 min	0.2±0.1	0.1±0.1
22.5A / 1 min	0.4±0.2	0.2±0.1
30A / 1 min	5.4±2.9	1.4±0.1
30A / 3 min	8.7±1.2	2.3±0.2
32.5A / 1 min	8.5±0.7	4.8±1.4
32.5A / 3 min	9.6±1.0	4.9±0.9
35A / 1 min	8.6±0.8	8.1±1.3
35A / 3 min	12.0±1.5	13.0±0.7

XRD was used to point out possible reactions between zirconia and N_2 (**Fig. 3**). As expected, all the samples produced under Ar show clear diffraction features related to t-ZrO_2 (PDF-2 Card 96-210-0389), this result being also consistent with previous work on UHS of additively-manufactured 3YSZ structures [31]. On the other hand, the samples produced under N_2 remain tetragonal only at the lowest currents, then convert into c-ZrO_2 (PDF-2 Card 00-027-0997). This can be detected by the disappearance of the peaks doublet at around $2\theta \approx 35°$ and 60° at ≈ 30 A. In the most severe UHS conditions, we also observe the appearance of a rock salt-structured phase. The complete quantitative analysis analysis is reported in **Fig. 12.4(a)**. The rock salt phase is consistent with ZrN (PDF-2 Card 00-035-0753), ZrO (PDF-2 Card 00-020-0684), or Zr(N,O) solid solution. These phases derive from FCC Zr lattice with the non-metals, either N and/or O, in the interstitial octahedral sites. It is not easy to differentiate between them by XRD since the lattice parameters are very similar to each other (0.4578 [57], 0.4577 [58] and 0.4580 nm [58] for ZrN, Zr(N,O) and ZrO, respectively). A certain uncertainness can also exist in the lattice parameter as a result of possible non-stoichiometry.

Furthermore, the Rietveld refinement of the patterns points out that tetragonality (**Fig. 12.4(b)**) of t-ZrO_2 progressively decreases from ≈1.014-1.015 to ≈1.09-1.10 as the current increases for UHS carried out in N_2 (note that the tetragonality was calculated only for samples where the amount of t-ZrO_2 was > 20%, the refinement being not reliable for lower tetragonal phase load).

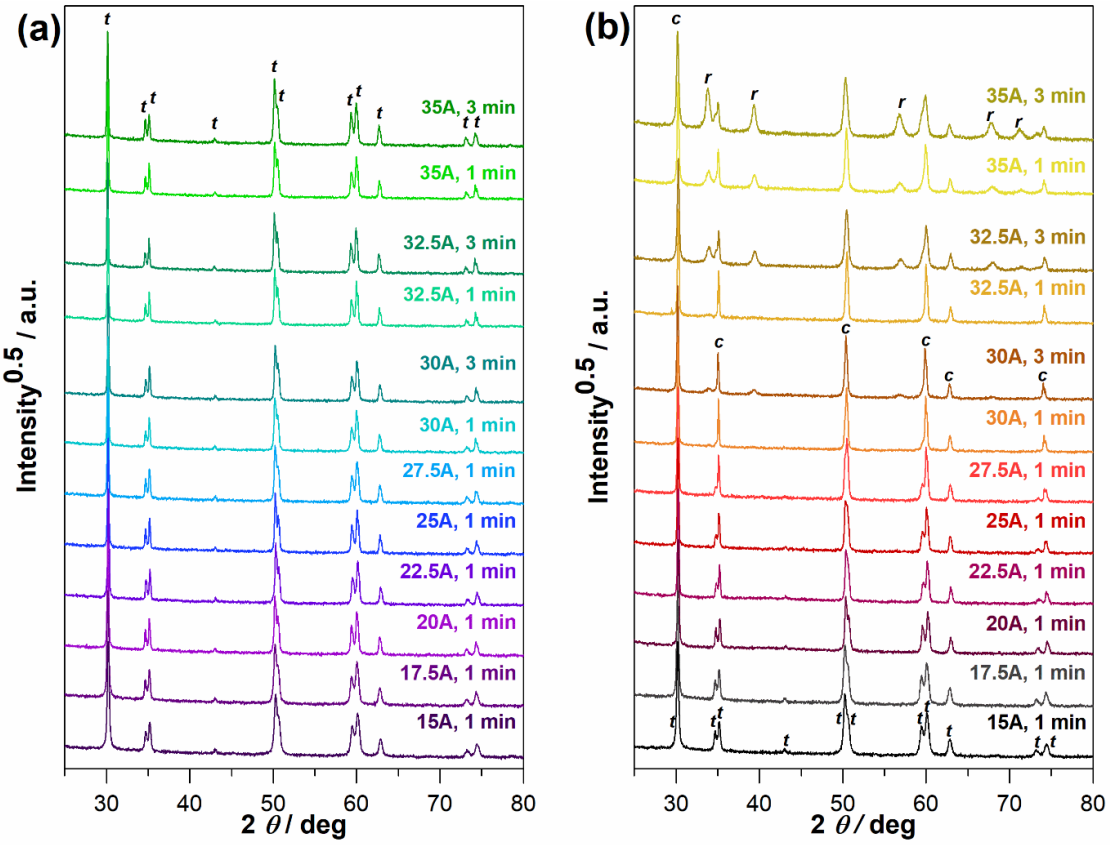

Figure 12.3. XRD patterns for 3YSZ samples sintered at different current and duration under (a) Ar atmosphere, (b) N_2 atmosphere. The peaks are indexed as follows: t = tetragonal zirconia, c = cubic zirconia, r = rock salt.

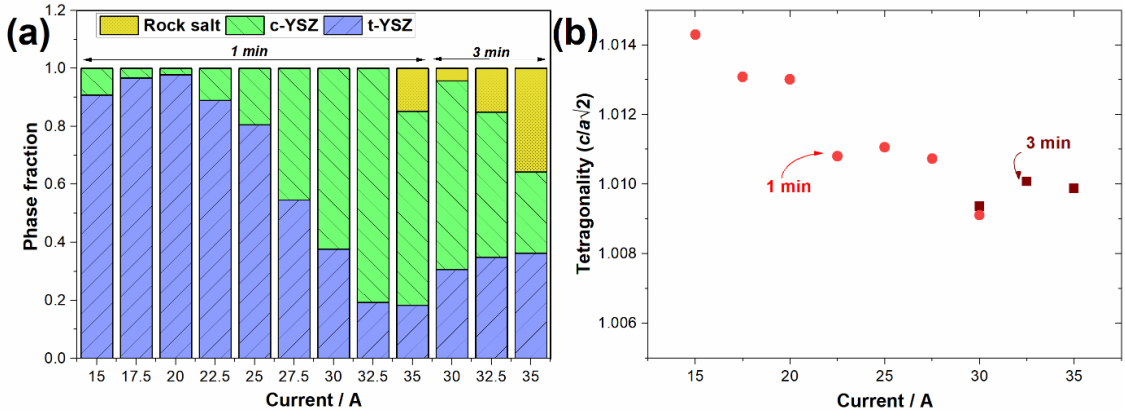

Figure 12.4. Rietveld-refined (a) phase composition and (b) tetragonality value as function of the current applied upon UHS carried out in N_2 atmosphere.

The phase evolution of the samples produced under N_2 was additionally investigated by Raman spectroscopy (**Fig. 5**). Raman is not very sensitive in differentiating between tetragonal and cubic zirconia but offers additional insight into the rock salt phase formation. The spectra for samples treated at lower currents (17.5 A and 20 A) show the typical feature of *t*-ZrO_2, with the 321, 467 cm^{-1} (E_g modes) and stronger 641 cm^{-1} peaks (A_{1g}) [59]. If the current exceeds 25-27.5 A in N_2, the spectra show clear features that can be ascribed to a rock salt phase, which becomes dominant under 30 A. These features include a shoulder at about 336 cm^{-1} (2TA), 390 cm^{-1} (TA+LA, weakly detected), the TO mode at about 460 cm^{-1} and the stronger LO mode at 500 cm^{-1}. The broad feature at higher frequencies (560-659 cm^{-1}) is dominated by the TO-LA and LO+LA modes [60]. The Raman spectra are in general consistent with the XRD findings with one main difference: the formation of the rock salt is already detected at 27.5 A or even 25 A by Raman, whereas it can be identified only above 30 A by XRD, such a difference being not surprising since Raman is certainly more sensitive to the sample surface.

If the spectra of the rock salt are analyzed in more detail, one can observe that (i) the main peak (≈460 cm^{-1}) shifts at higher wavenumbers when increasing the treatment time and current, (ii) the Raman features become broader and less defined. The result seems consistent with the evolution of the rock salt phase from O-rich to N-rich one, similarly to the spectra reported in the literature for YSZ flash sintered in Ar and N_2 [61].

The reaction between N_2 and YSZ is further confirmed by the fact that the sample coloration changes during UHS (**Fig. 12.6**). In Ar, YSZ remains white up to 17.5A, whereas at 20 A the oxide starts to darken, similarly to previous UHS results [31]. It can originate from carbon contamination or oxide reduction which introduces donor levels a fraction of electronvolts below the conduction band [62–64]. In the present work, no carbon contamination could originate from the binder burnout since the samples were pre-sintered before UHS. Contamination from the felt is possible, but this does not explain why the darkening onset in N_2 is delayed (between 22.5 A and 25 A). As a matter of fact, if the treating time or the current are increased, the darkening in Ar becomes more evident. On the other hand, the samples treated under N_2 at the highest currents turn goldish, acquiring a metallic aspect. Such gold-like coloration is a clear feature of ZrN or Zr(O,N) formation [58,65], the ZrO rock salt appearing as metallic dark grey [58].

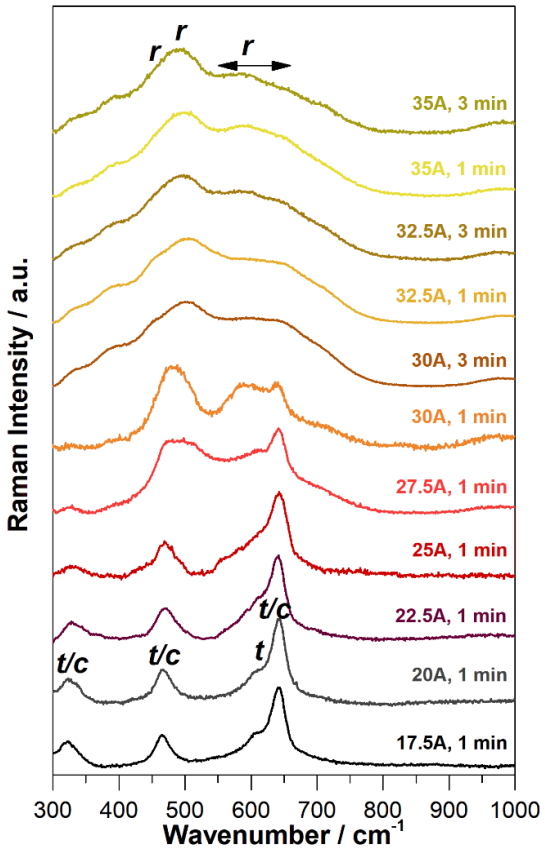

Figure 12.5. Raman spectra of samples sintered under N_2 atmosphere. The peaks are indexed as follows: t = tetragonal YSZ, r = rock salt.

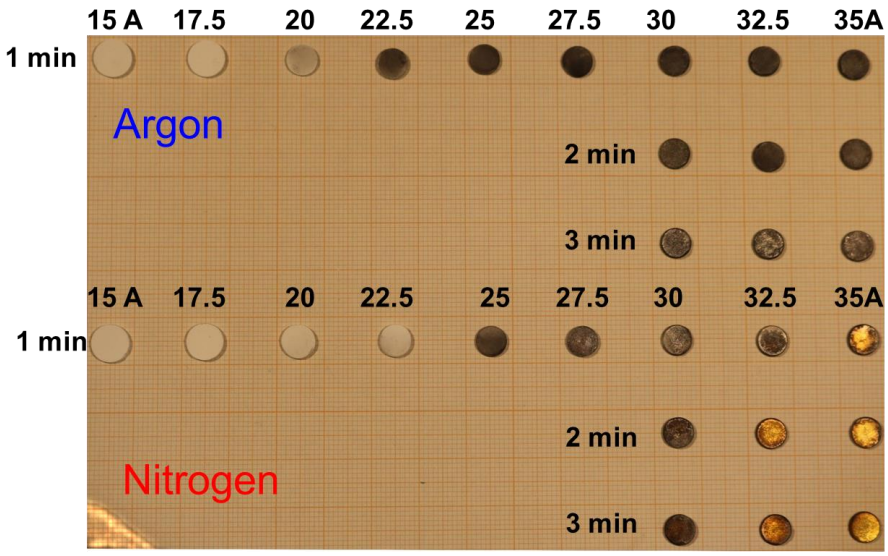

Figure 12.6. Image of the samples under different current, time, and atmospheric (Argon and Nitrogen) conditions.

XPS analyses were carried on two samples sintered in the same conditions (30 A – 1 min) under Ar and N_2. The high-resolution N1s spectrum reveals a clear presence of nitrogen in the sample treated under N_2, such contribution being totally missing in the Ar-processed sample (**Fig. 12.7**). Moreover, the position of this peak, with a maximum at 395.6 eV, is slightly lower than the expected 397.8 eV energy for a pure Zr-N bonding [66], very likely fitting with the expected value for oxynitride $(ZrO)\text{-}N^{3-}$ in ZrO_xN_y [66,67].

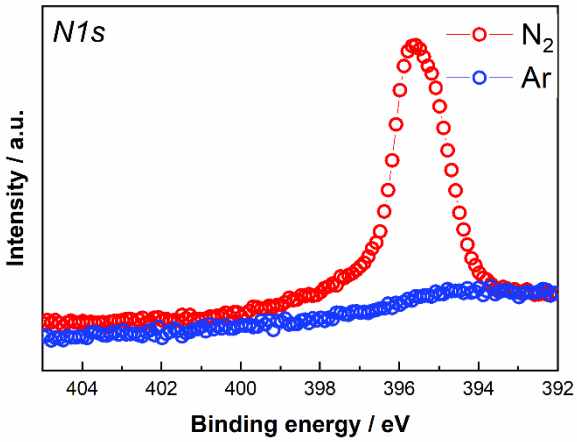

Figure 12.7. XPS spectrum of N1s for samples sintered in Ar and N_2 at 30 A – 1 min.

Zr3d spectrum was also collected on the same samples (**Fig. 12.8)**. Clear Zr3d contributions that differ mainly by the presence of lower energy contributions (<181 eV) in the N_2 sintered sample are identified. The datasets were fitted using 2 and 4 Gaussian contributions and the resulting peak positions are 181.57(1) and 183.94(1) eV for Ar-processed sample; these must be compared to181.58(3) and 183.89(1) eV for $Zr3d_{5/2}$ and $Zr3d_{3/2}$ contributions for N_2-sintered sample. All these are very close to the literature values found for Y-doped ZrO_2 (181.6 and 184.0 eV) [68].

In the case of the N_2 sintered sample, however, additional contributions were fitted at 178.5(1) and 180.2(3) eV, which can be attributed to Zr-N binding energies [67,69]. These XPS data, both in the case of Zr3d and N1s spectra, confirm the reactivity between ZrO_2 and N_2 to form oxynitride compounds, as detected by Raman spectroscopy and XRD.

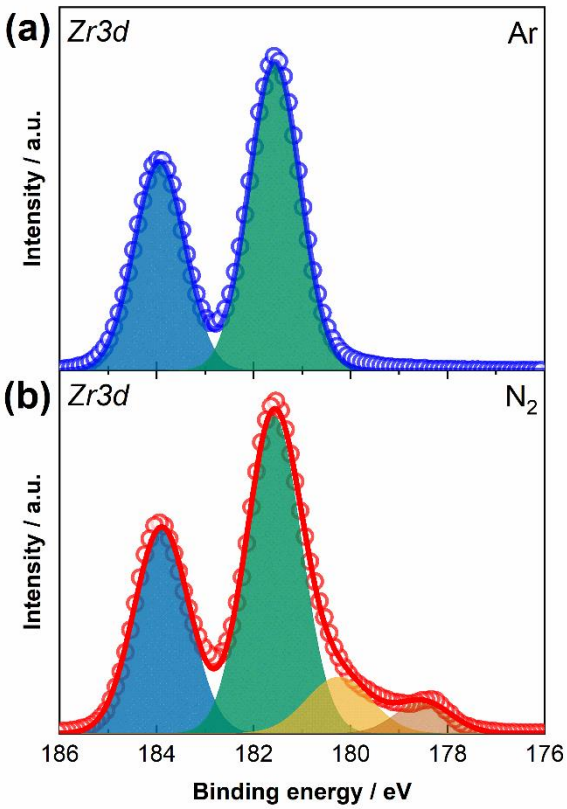

Figure 12.8. XPS spectrum of Zr3d for samples sintered at 30 A for 1 min in a) Ar and b) N_2.

Further sample analyses were carried out through AC impedance measurements (EIS) from 200°C to 400°C in air. **Fig. 12.9(a,b)** shows the EIS Nyquist plots of impedance measured at 300°C for samples sintered in Ar and N_2 at various currents. For all samples, two contributions (semi-circles) are observed. The higher frequency one (left side) can be associated with bulk, while the lower frequency one (right side) corresponds to grain boundaries. For samples sintered in Ar (**Fig. 12.9(a)**), the bulk contribution is similar, suggesting no major density evolution, as confirmed by the densification data in **Fig. 12.1(a)**. Conversely, the samples sintered in N_2 show a more important evolution of bulk contribution, with an impedance decrease visible between 20 A and 22.5 A. Concerning the GB contribution, it is similar for samples sintered at 20 A and 22.5 A in Ar and it almost disappears at 30 A. This is consistent with a net increase in grain size from 22.5 A to 30 A as shown in **Table 12.1**, with a grain size increase by more than one order of magnitude (from 0.4 µm to 5.4 µm). In the case of N_2, the evolution between 20

A and 22.5 A is consistent with the density difference and the spectrum becomes more complex at 30 A. Magnifications of such sample's dataset with two different fitting models are shown in **Fig. 12.9(c,d)**, where two contributions (R-CPE) are not sufficient for the fitting. A third one allows a better fit although its nature can not be identified on the basis of these measurements only, it seems consistent with the formation of a secondary rocksalt phase, namely Zr(O, N). In this dataset, contributions at low frequency (<10 Hz) are not considered since they relate to the electrode contribution instead of YSZ sample.

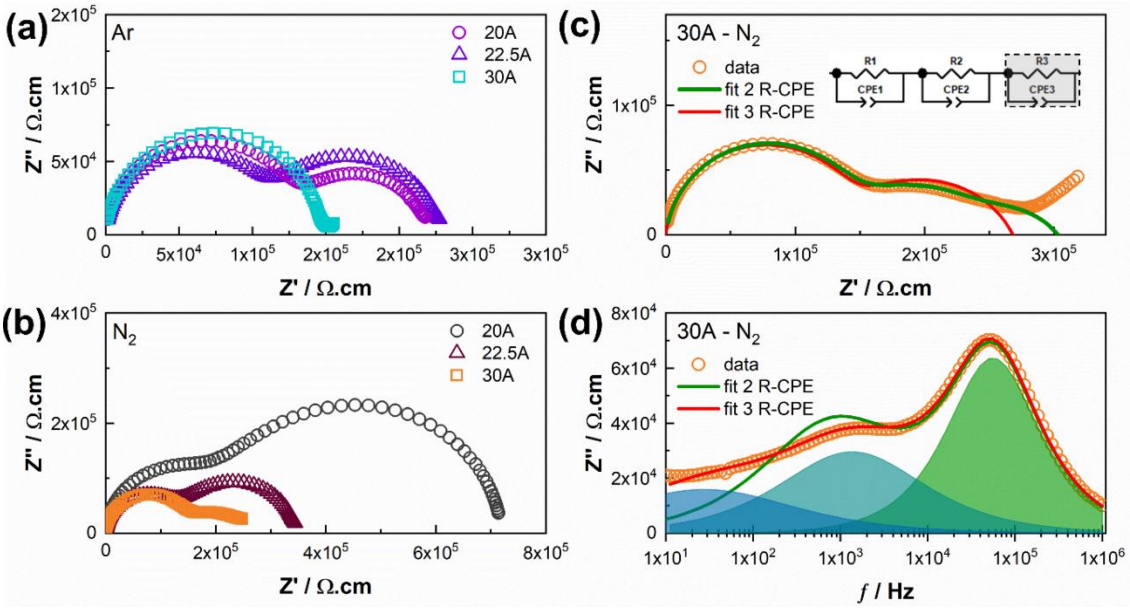

Figure 12.9. Nyquist plot of complex impedance (300°C, $10^2 < f < 10^6$ Hz) of samples sintered under different currents in (a) Ar and (b) N_2. The refined fit of data for the sample sintered at 30A-60s in N_2 with 2 and 3 R-CPE equivalent circuits, demonstrating (c) complex impedance Nyquist plot and d) imaginary part of impedance as a function of frequency, including deconvolution of 3 R-CPE fit.

According to the EIS data fitting, using two R-CPE contributions in series (for bulk and GB parts) for all other samples, the data for conductivity, relaxation frequency and capacitance were extracted and plotted in **Fig. 12.10**. First of all, for the Ar sintered

samples, the GB conductivity after sintering at 30 A is drastically increased (as highlighted in **Fig. 12.9a**). The activation energy (inset of **Fig. 12.10(a,d)**) for both bulk (b) and grain boundaries (GB) assumes similar values regardless the UHS atmosphere, with the bulk between 0.84 and 0.88 eV while GB are in the range 0.96 – 1.00 eV. The only exception is the grain boundary contribution for the samples sintered under 30 A, which shows a slightly lower activation energy ≈0.9 eV. These values must be handled with care since they reflect an uncertainty related to its meager contribution to impedance (see **Fig. 12.9a**). All relaxation frequencies are perfectly aligned both for bulk and GB contributions, confirming the similar nature of the relaxation phenomena. The good agreement between the relaxation behavior of the sample sintered in N_2 under 30 A, fitted with an additional contribution (**Fig. 12.9d**) and the other grain boundaries i.e., the measurements of the rest of the samples confirm the goodness of the fitting results. Finally, the bulk capacitances show temperature-independent values, similar for all samples (**Fig. 12.10(c,f)**). Conversely, one can notice the GB capacitance evolution with sintering conditions. This relates both to the microstructure evolution and grain boundary thicknesses (δ_{gb}), which can be calculated as [70,71]:

$$\delta_{gb} = \frac{C_b}{C_{gb}} G \tag{12.1}$$

where C_b and C_{gb} are equivalent capacitances of bulk and GB, respectively, and G the mean grain size.

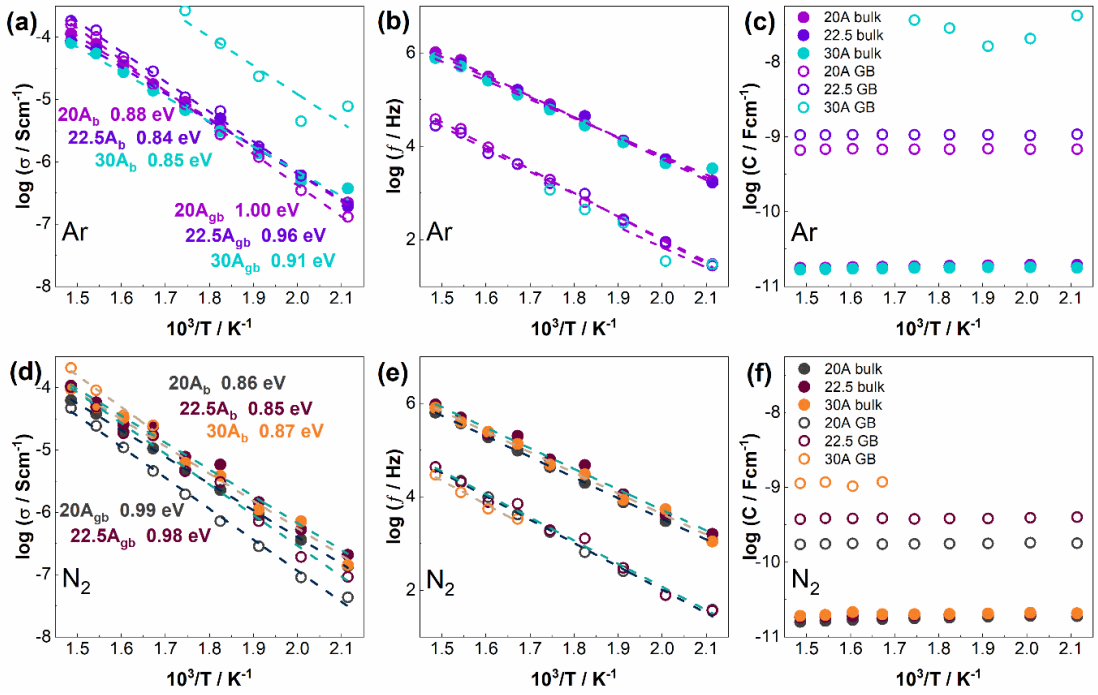

Figure 12.10. Data obtained from EIS measurements fits for samples produced in (a-c) Ar and (d-f) N_2 (a and d) conductivity, (b and e) relaxation frequency (c and f) equivalent capacitance.

The resulting data are plotted in **Fig. 12.11** for all samples. The specimens treated under N_2 at 20 and 22.5 A show a similar value of $\delta_{gb} \approx$ 9-11 nm, while that sintered under 30 A shows an apparent reduction < 3 nm. This value has to be taken carefully since the impedance fitting, by introducing a further addition overlapping the GB contribution, may be affected and lose precision. However, the trend is clear, leading to much smaller electrochemical GB thickness with respect to samples obtained under 20 A and 22.5 A. The samples sintered in Ar show a similar trend. Those sintered at 20 A and 22.5 A possess a similar δ_{gb} (≈6-7 nm), which is, however, lower than that was measured in N_2-processed materials. The sample sintered at 30 A shows a certain scatter, related to the very small GB resistivity, making fitting less precise compared to bulk contribution. Although the results are less clear if compared to the N_2 case, also in Ar there is a certain tendency for the grain boundary thickness to decrease from 22.5 (≈6-7 nm) to 30 A (≈2.5-6 nm).

Using the grain boundary thickness, one can calculate the GB specific conductivity to check whether the samples show a similar "intrinsic" conductivity or not. It is possible to figure it as [70]:

$$\sigma_{gb}^{sp} = \sigma_{gb} \frac{\delta_{gb}}{G} \tag{12.2}$$

where σ^{sp}_{gb} represents the specific GB conductivity. The data obtained for all samples, both in Ar and N_2, fit well, with similar conductivity of GB, in agreement with the literature data for 3YSZ produced by SPS at 1200°C for 180 min [70]. This confirms that both bulk and grain boundaries show a similar intrinsic conductivity in all samples and that the main difference lies in geometric variations of grain boundary thickness.

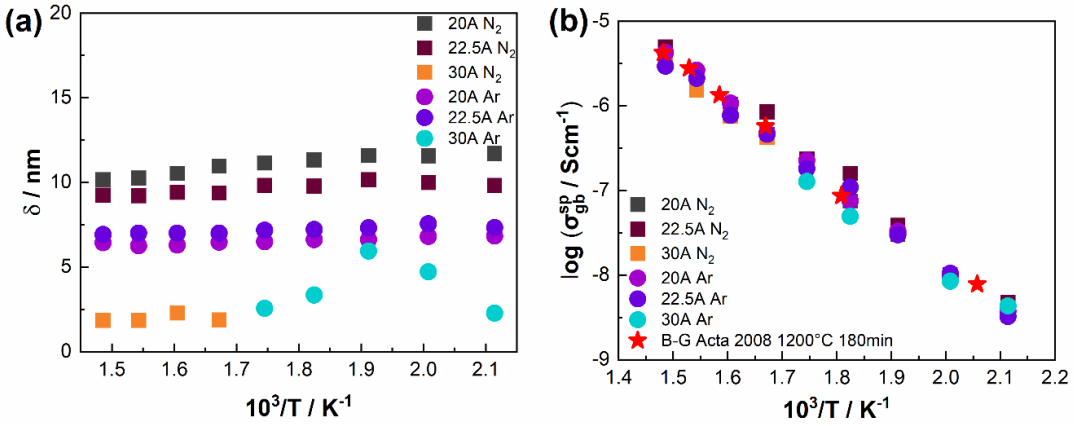

Figure 12.11. a) Grain boundary thickness and b) GB specific conductivity obtained from EIS data.

12.4. Discussion

The main outcome of this work is that the atmosphere plays a fundamental role when 3YSZ is processed by UHS. Substantial changes in terms of microstructural (**Figs 12.1 and 12.2**) and phase evolution (**Fig. 12.3**) were detected.

Ruling out thermal effects as major sources for the different microstructure, one can infer that YSZ reacts with N_2 thus determining a substantial modification of the defect chemistry and self-diffusion kinetics. The reaction between YSZ and nitrogen is further confirmed by the fact that after UHS one can observe that (i) t-ZrO_2 decreases its

tetragonality, (ii) c-ZrO_2 forms, (iii) a rock salt oxynitride is produced and (iv) the electrochemical grain boundary thickness varies. The formation of the rock salt phase is confirmed by Raman spectroscopy (**Fig. 12.5**) and XRD (**Fig. 12.3**), its oxynitride nature being detected by XPS (**Figs 12.7** and **12.8**) and corroborated by the chromatic alteration (**Fig. 12.6**) of the samples after UHS. The results resemble those obtained by Morisaki et al. [65] and, more recently, by Bechteler and Todd [58] in YSZ produced by flash sintering in N_2. In this latter case, the sample reduction was forced by the application of an electric current, herein by the high temperature combined with a highly reducing environment (presence of graphitic carbon).

Said structural features are typically accounted for by oxygen vacancy formation, which tends to stabilize the fluorite structure and reduce the tetragonal distortion of the lattice [72,73]. In fact, the formation of O vacancy in most cases is a result of doping with trivalent cations:

$$M_2O_3 \xrightarrow{ZrO_2} 2M'_{Zr} + V_{\ddot{O}} + 3O^x_O, \tag{12.3}$$

although, it could also originate from the doping of the anionic site with trivalent cations, like nitrogen:

$$2N_2 + 3O^x_O \xrightarrow{ZrO_2} 4N'_O + 2V_{\ddot{O}} + 3O_2 \tag{12.4}$$

Therefore, N^{3-} anionic site doping has an effect analogous to Y^{3+} cationic site doping. If one looks at the literature, 3YSZ sintered under conventional conditions possess a tetragonality of about 1.014, this value being in good agreement with the samples treated at the lowest currents. The tetragonality in the present work is as low as 1.009, which corresponds to Y-doping between 4 and 5 mol%. The “additional doping” effect must derive here from the reaction with the atmosphere. If the current and the UHS time increase further, a heavy reduction occurs, leading to the formation of the rock salt phase.

Two reactions —reduction and nitridation— are required to convert tetragonal zirconia into cubic zirconia and then oxynitride. The first one takes place also in Ar and can be written as:

$$C + O_O^x \xrightarrow{ZrO_2} CO + V_O^{\cdot\cdot} + 2e' \quad (12.5)$$

where C can come from the felt. Native reduction is also possible:

$$2O_O^x \xrightarrow{ZrO_2} O_2 + 2V_O^{\cdot\cdot} + 4e' \quad . \quad (12.6)$$

As such, UHS under Ar and N_2 atmosphere causes the formation of oxygen vacancies and free electrons. One must note that both reactions move to the right at high temperature due to the evolution of a gas phase. However, due to the high and negative formation energy of ZrO_2, the reactions can not proceed to the right "forever". It is important to remember that zirconia lies below CO in the Ellingham diagram even at 2300°C; therefore, in standard conditions, its total reduction to metallic zirconium is not possible [74].

On the other hand, the electrons created by **Eq. 12.5** and **12.6** can react with N_2, reducing it into nitrogen ions, which can be incorporated in the YSZ lattice (as previously reported in the literature [65,75]):

$$3V_O^{\cdot\cdot} + 6e' + N_2 \xrightarrow{ZrO_2} V_O^{\cdot\cdot} + 2N_O' \quad (12.7)$$

Such reaction removes the electrons (and, partially, the oxygen vacancies), which are the product of **Eq. 12.5** and **12.6**; therefore, it allows them to prosecute and move further to the products. The overall reaction in nitrogen can be written as:

$$3C + N_2 + 3O_O^x \xrightarrow{ZrO_2} 3CO + V_O^{\cdot\cdot} + 2N_O' \quad (12.8)$$

or

$$2N_2 + 6O_O^x \xrightarrow{ZrO_2} 2V_O^{\cdot\cdot} + 4N_O' + 3O_2 \quad (12.9)$$

In summary, one can infer that the presence of N_2 in the UHS atmosphere (i) allows the formation of a higher amount of oxygen vacancies compared to Ar as they are stabilized by the net negative charge on the nitrogen dopants, and (ii) the conditions are

"less reducing" in the sense that the free electrons from **Eqs 12.5** and **12.6** are partially consumed by **Eq. 12.7** and are not available to reduce the average oxidation state of cations. This is testified by the fact that the overall reactions (**Eqs 12.8** and **12.9**) do not contain any free electrons on the right side and do not involve any change in the oxidation state of the cations.

The abovementioned reactions perfectly match the experimental results: the formation of extra oxygen vacancy through the reaction in **Eqs 12.8** and **12.9** are in agreement with a reduction of the cell tetragonality and with the stabilization of the fluorite cubic structure. Indeed, when reactions in **Eqs 12.8** and **12.9** move to the right, approaching the solubility limit of N in YSZ, rock salt oxynitride precipitates [43].

The defect reactions also explain why blackening is observed at higher currents in N_2 if compared with Ar (**Fig. 12.7**). YSZ darkening is associated with the visible light absorption by free electrons, Zr^{3+} (Zr'_{Zr}), F (V_O) and F^+ ($V_O^{\cdot}$) centers which form through the following reactions:

$$Zr_{Zr}^{x} + e' \longrightarrow Zr'_{Zr} \tag{12.10}$$

$$V_O^{\cdot\cdot} + 2e' \longrightarrow V_O^{\cdot} + e' \longrightarrow V_O \tag{12.11}$$

Zr'_{Zr} represents a donor state located only 0.2 eV below the conduction band edge. F and F^+ centers represent deeper levels, about 2 eV below the conduction band [64], but can still absorb most of the visible light (≈1.7-2.7 eV). Indeed, the free electron consumption by nitrogen reduction (**Eq. 12.7**) hinders reactions in **Eqs 12.10** and **12.11** by reducing the concentration of one of the reagents. On the other hand, **Eq. 12.7** causes the formation of N'_O which is an acceptor level laying 2.8 eV above the valence band edge [76] thus being optically inactive in the visible spectrum.

The effect of the atmosphere on the phase evolution appears therefore consistent and robust. It is less straightforward the reason why we observe a substantial change in the densification and grain growth kinetics in different atmospheres (**Figs 12.1** and **12.2**). Although the conclusion is not definitive, one can point out that there is already solid literature evidencing the beneficial effect of reducing conditions on mass transport, especially referred to as grain growth, in fluorite-structured ceramics [77–81]. For instance, Dong [81] reported a decrease in the energy barrier for Zr diffusion in YSZ

along the [1 1 0] direction from 4.31 to 3.17 eV for the unreduced Zr^{4+} and reduced Zr^{3+} cations, respectively. In a recent paper, Martin et al. [82] have aslo shown the beneficial effect of reducing conditions on sintering of YSZ. In the UHS experiments carried out in the present work, the treatments in Ar are more reducing than those in N_2: the free electrons are consumed to reduce nitrogen and, therefore, are not available for the reaction in **Eq. 12.10,** which allows the formation of Zr^{3+}. Hence, one can infer as a possible explanation that the reduction-induced boosting effect on densification observed in Ar cannot be reproduced to the same extent in nitrogen.

Along with these observations, impedance data show that the bulk ionic conductivity is not affected by the atmosphere, and the measured values are substantially consistent with what is expected from the literature [74]. Nevertheless, the grain boundaries show an important modification of their capacitive behavior. In particular, N_2 atmosphere seems to promote thicker grain boundaries (9-11 nm) than Ar (6-7 nm) at least under "moderate" UHS conditions, i.e., 20 A and 22.5 A (**Fig. 12.11**). This suggests once again that N_2 interacts with the material even at relatively low UHS currents. Despite the result could seem in partial contradiction with XRD data (not showing a substantial formation of c-ZrO_2 at such currents), one should bear in mind that EIS provides resistivity information and, therefore, it is highly sensitive to phases present in the grain boundaries (the difference between GB specific conductivity and bulk conductivity is around 1.5 order of magnitude). Consequently, it is susceptible to what happens in GB interfaces, including chemical or structural changes that cannot be detected by XRD or Raman spectroscopy.

The grain boundary specific conductivities are similar for all samples, comparable with literature data (**Fig. 12.11**). This confirms that the difference between samples relies essentially on the grain boundary thickness. One can additionally observe that the grain boundary thickness measured in samples processed here in Ar is not far different from what was reported for the same 3YSZ powder consolidated by flash sintering [83] and flash-SPS [70] (≈ 5 nm); this suggests some similarities in terms of grain boundary formation and local defect chemistry for all these techniques. However, the difference between UHS in N_2 and Ar points out that the similarities between said techniques do not originate from the rapid heating/cooling, only, but must probably account also for additional effects. We could speculate that the heavily reducing conditions generated by flash and UHS in Ar (already discussed that UHS in N_2 is "less reducing") play a role.

Furthermore, when UHS moves to more “severe” currents, one observes a substantial decrease in the electrochemical grain boundary thickness, which can reflect a higher ordering of the structure and/or a reduction of the grain boundary space charge potentials. The samples sintered under 30 A show, in any case, a remarkable effect, with an increase of ionic conductivity and a substantially negligible blocking effect at the grain boundaries.

12.5. Conclusion

The UHS atmosphere impacts both microstructural and phase evolution of YSZ. In N_2, highly densified samples can be obtained at 25 A, whereas in the Ar atmosphere densification is anticipated at around 20 A. A similar trend is shown also in terms of grain growth. While the samples treated under Ar always remain tetragonal, a reduction of the cell tetragonality occurs first and then the stabilization of cubic zirconia and eventually the formation of a rock salt oxynitride is observed in specimens processed under N_2.

The results can be explained by assuming the incorporation of nitrogen in the ZrO_2 lattice which was further confirmed by XPS. The anionic solid solution results in the formation of oxygen vacancies for charge compensation which stabilize cubic zirconia and reduce the tetragonality of t-ZrO_2. Furthermore, molecular N_2 reduction to N^{3-} ions incorporated in the lattice can also explain the different chromatic alteration of the specimen and, at least partially, the delayed densification under N_2.

In addition to the phase and microstructural evolution, UHS in dissimilar atmospheres leads to different electrochemical properties of YSZ at the grain boundaries and specifically to different electrochemical grain boundary thickness.

References

[1] R.K. Bordia, S.-J.L. Kang, E.A. Olevsky, Current understanding and future research directions at the onset of the next century of sintering science and technology, J. Am. Ceram. Soc. 100 (2017) 2314–2352. https://doi.org/10.1111/jace.14919.

[2] S. Grasso, Y. Sakka, G. Maizza, Electric current activated/assisted sintering (ECAS): a review of patents 1906–2008, Sci. Technol. Adv. Mater. 10 (2009) 053001.

[3] O. Guillon, J. Gonzalez-Julian, B. Dargatz, T. Kessel, G. Schierning, J. Räthel, M. Herrmann, Field-Assisted Sintering Technology/Spark Plasma Sintering: Mechanisms, Materials, and Technology Developments, Adv. Eng. Mater. 16 (2014) 830–849. https://doi.org/10.1002/adem.201300409.

[4] M. Biesuz, S. Grasso, V.M. Sglavo, What's new in ceramics sintering? A short report on the latest trends and future prospects, Curr. Opin. Solid State Mater. Sci. 24 (2020) 100868. https://doi.org/10.1016/j.cossms.2020.100868.

[5] M. Bram, A.M. Laptev, T.P. Mishra, K. Nur, M. Kindelmann, M. Ihrig, J.G. Pereira da Silva, R. Steinert, H.P. Buchkremer, A. Litnovsky, F. Klein, J. Gonzalez-Julian, O. Guillon, Application of Electric Current-Assisted Sintering Techniques for the Processing of Advanced Materials, Adv. Eng. Mater. 22 (2020) 2000051. https://doi.org/10.1002/adem.202000051.

[6] C. Vakifahmetoglu, L. Karacasulu, Cold sintering of ceramics and glasses: A review, Curr. Opin. Solid State Mater. Sci. 24 (2020) 100807. https://doi.org/10.1016/j.cossms.2020.100807.

[7] R. Orrù, R. Licheri, A.M. Locci, A. Cincotti, G. Cao, Consolidation/synthesis of materials by electric current activated/assisted sintering, Mater. Sci. Eng. R. 63 (2009) 127–287. https://doi.org/10.1016/j.mser.2008.09.003.

[8] O. Guillon, C. Elsässer, O. Gutfleisch, J. Janek, S. Korte-Kerzel, D. Raabe, C.A. Volkert, Manipulation of matter by electric and magnetic fields: Toward novel synthesis and processing routes of inorganic materials, Materials Today. 21 (2018) 527–536. https://doi.org/10.1016/j.mattod.2018.03.026.

[9] M. Biesuz, T. Saunders, D. Ke, M.J. Reece, C. Hu, S. Grasso, A review of electromagnetic processing of materials (EPM): Heating, sintering, joining and forming, J. Mater. Sci. Technol. 69 (2021) 239–272. https://doi.org/10.1016/j.jmst.2020.06.049.

[10] J. Guo, R. Floyd, S. Lowum, J.-P. Maria, T. Herisson de Beauvoir, J.-H. Seo, C.A. Randall, Cold Sintering: Progress, Challenges, and Future Opportunities, Annu. Rev. Mater. Res. 49 (2019) 275–295. https://doi.org/10.1146/annurev-matsci-070218-010041.

[11] Z.A. Munir, U. Anselmi-Tamburini, M. Ohyanagi, The effect of electric field and pressure on the synthesis and consolidation of materials: A review of the spark plasma sintering method, J. Mater. Sci. 41 (2006) 763–777. https://doi.org/10.1007/s10853-006-6555-2.

[12] D. Agrawal, 9 - Microwave sintering of ceramics, composites and metal powders, in: Z.Z. Fang (Ed.), Sintering of Advanced Materials, Woodhead Publishing, 2010: pp. 222–248. https://doi.org/10.1533/9781845699949.2.222.

[13] M.N. Rahaman, Ceramic processing and sintering, CRC press, 2017.

[14] L. Porz, M. Scherer, D. Huhn, L.-M. Heine, S. Britten, L. Rebohle, M. Neubert, M. Brown, P. Lascelles, R. Kitson, D. Rettenwander, L. Fulanovic, E. Bruder, P. Breckner, D. Isaia, T. Frömling, J. Rödel, W. Rheinheimer, Blacklight sintering of ceramics, Mater. Horiz. 9 (2022) 1717–1726. https://doi.org/10.1039/D2MH00177B.

[15] C. Wang, W. Ping, Q. Bai, H. Cui, R. Hensleigh, R. Wang, A.H. Brozena, Z. Xu, J. Dai, Y. Pei, A general method to synthesize and sinter bulk ceramics in seconds, Science (1979). 368 (2020) 521–526.

[16] M. Biesuz, V.M. Sglavo, Flash sintering of ceramics, J. Eur. Ceram. Soc. 39 (2019) 115–143. https://doi.org/10.1016/j.jeurceramsoc.2018.08.048.

[17] M. Yu, S. Grasso, R. Mckinnon, T. Saunders, M.J. Reece, Review of flash sintering: materials, mechanisms and modelling, Advances in Applied Ceramics. 116 (2017) 24–60. https://doi.org/10.1080/17436753.2016.1251051.

[18] C. Vakifahmetoglu, L. Karacasulu, Cold sintering of ceramics and glasses: A review, Curr. Opin. Solid State Mater. Sci. 24 (2020) 100807. https://doi.org/10.1016/j.cossms.2020.100807.

[19] M. Ihrig, T.P. Mishra, W.S. Scheld, G. Häuschen, W. Rheinheimer, M. Bram, M. Finsterbusch, O. Guillon, $Li_7La_3Zr_2O_{12}$ solid electrolyte sintered by the ultrafast high-temperature method, J. Eur. Ceram. Soc. 41 (2021) 6075–6079.

[20] T.P. Mishra, S. Wang, C. Lenser, D. Jennings, M. Kindelmann, W. Rheinheimer, C. Broeckmann, M. Bram, O. Guillon, Ultra-fast high-temperature sintering of strontium titanate, Acta Mater. 231 (2022) 117918.

[21] M. Biesuz, A. Galotta, A. Motta, M. Kermani, S. Grasso, J. Vontorová, V. Tyrpekl, M. Vilémová, V.M. Sglavo, Speedy bioceramics: Rapid densification of tricalcium

phosphate by ultrafast high-temperature sintering, Mater. Sci. Eng. C. 127 (2021) 112246.

[22] J. Dong, V. Pouchly, M. Biesuz, V. Tyrpekl, M. Vilémová, M. Kermani, M. Reece, C. Hu, S. Grasso, Thermally-insulated ultra-fast high temperature sintering (UHS) of zirconia: A master sintering curve analysis, Scr Mater. 203 (2021) 114076.

[23] R.-X. Luo, M. Kermani, Z.-L. Guo, J. Dong, C.-F. Hu, F. Zuo, S. Grasso, B.-B. Jiang, G.-L. Nie, Z.-Q. Yan, Ultrafast high-temperature sintering of silicon nitride: A comparison with the state-of-the-art techniques, J. Eur. Ceram. Soc. 41 (2021) 6338–6345.

[24] M. Kermani, J. Dong, M. Biesuz, Y. Linx, H. Deng, V.M. Sglavo, M.J. Reece, C. Hu, S. Grasso, Ultrafast high-temperature sintering (UHS) of fine grained α-Al_2O_3, J. Eur. Ceram. Soc. 41 (2021) 6626–6633.

[25] R.-F. Guo, H.-R. Mao, Z.-T. Zhao, P. Shen, Ultrafast high-temperature sintering of bulk oxides, Scr Mater. 193 (2021) 103–107.

[26] A. Alemayehu, M. Biesuz, K.Y. Javan, A. Tkach, P.M. Vilarinho, V.M. Sglavo, V. Tyrpekl, Ultrafast high-temperature sintering of gadolinia-doped ceria, J. Eur. Ceram. Soc. 43 (2023) 4837–4843. https://doi.org/10.1016/j.jeurceramsoc.2023.04.025.

[27] S. Wang, T.P. Mishra, Y. Deng, L. Balice, A. Kaletsch, M. Bram, C. Broeckmann, Electric Current-Assisted Sintering of 8YSZ: A Comparative Study of Ultrafast High-Temperature Sintering and Flash Sintering, Adv. Eng. Mater. 25 (2023) 2300145. https://doi.org/10.1002/adem.202300145.

[28] Y. Zhao, H. Li, Y. Zu, Y. Wang, X. Fu, W. Zhou, G. Chen, (MgCoNiCuZn)O with particular microstructure and distinctive electrochemical performance prepared using ultrafast high-temperature sintering, J. Eur. Ceram. Soc. 43 (2023) 7573–7580. https://doi.org/10.1016/j.jeurceramsoc.2023.07.062.

[29] R.-F. Guo, H.-R. Mao, P. Shen, Ultra-fast high-temperature synthesis and densification of high-entropy diborides and diboride-carbide ceramics, J. Eur. Ceram. Soc. 43 (2023) 5763–5773. https://doi.org/10.1016/j.jeurceramsoc.2023.05.042.

[30] E. De Bona, C. Manière, V.M. Sglavo, M. Biesuz, Ultrafast high-temperature sintering (UHS) of ZrB_2-based materials, J. Eur. Ceram. Soc. 44 (2024) 567–573. https://doi.org/10.1016/j.jeurceramsoc.2023.09.007.

[31] S. Bhandari, C. Manière, F. Sedona, E. De Bona, V.M. Sglavo, P. Colombo, L. Fambri, M. Biesuz, G. Franchin, Ultra-rapid debinding and sintering of additively manufactured ceramics by ultrafast high-temperature sintering, J. Eur. Ceram. Soc. 44 (2024) 328–340. /https://doi.org/10.1016/j.jeurceramsoc.2023.08.040.

[32] T. Che, H.-R. Mao, R.-F. Guo, P. Shen, Ultrafast synthesis and pressureless densification of multicomponent nitride and carbonitride ceramics, Ceram. Int. 49 (2023) 31530–31538. https://doi.org/10.1016/j.ceramint.2023.07.104.

[33] Z.-T. Zhao, R.-F. Guo, H.-R. Mao, P. Shen, Effect of components on the microstructures and properties of rare-earth zirconate ceramics prepared by ultrafast high-throughput sintering, J. Eur. Ceram. Soc. 41 (2021) 5768–5773.

[34] H.-R. Mao, E.-T. Dong, S.-B. Jin, X.-M. Qiu, P. Shen, Ultrafast high-temperature synthesis and densification of high-entropy carbides, J. Eur. Ceram. Soc. 42 (2022) 4053–4065. https://doi.org/10.1016/j.jeurceramsoc.2022.03.054.

[35] R. Wang, W. Ping, C. Wang, Y. Liu, J. Gao, Q. Dong, X. Wang, Y. Mo, L. Hu, Computation-Guided Synthesis of New Garnet-Type Solid-State Electrolytes via an Ultrafast Sintering Technique, Advanced Materials. 32 (2020) 2005059. https://doi.org/10.1002/adma.202005059.

[36] A. Flaureau, A. Weibel, G. Chevallier, C. Estournès, Study of the densification and grain growth mechanisms occurring during spark plasma sintering of different submicronic yttria-stabilized zirconia powders, J. Eur. Ceram. Soc. 41 (2021) 3581–3594. https://doi.org/10.1016/j.jeurceramsoc.2021.01.032.

[37] P. Aldebert, J.-P. Traverse, Structure and Ionic Mobility of Zirconia at High Temperature, J. Am. Ceram. Soc. 68 (1985) 34–40. https://doi.org/10.1111/j.1151-2916.1985.tb15247.x.

[38] T.-J. Chung, H. Song, G.-H. Kim, D.-Y. Kim, Microstructure and Phase Stability of Yttria-Doped Tetragonal Zirconia Polycrystals Heat Treated in Nitrogen Atmosphere, J. Am. Ceram. Soc. 80 (1997) 2607–2612. https://doi.org/10.1111/j.1151-2916.1997.tb03163.x.

[39] M. Lerch, Nitridation of Zirconia, J. Am. Ceram. Soc. 79 (1996) 2641–2644. https://doi.org/10.1111/j.1151-2916.1996.tb09028.x.

[40] Y.-K. Paek, J.-H. Ahn, G.-H. Kim, S.-J.L. Kang, Effect of Nitrogen Atmosphere on the Densification of a 3-mol%-Yttria-Doped Zirconia, J. Am. Ceram. Soc. 85 (2002) 1631–1633. https://doi.org/10.1111/j.1151-2916.2002.tb00327.x.

[41] N. Claussen, R. Wagner, L.J. Gauckler, G. Petzow, Nitride-Stabilized Cubic Zirconia, J. Am. Ceram. Soc. 61 (1978) 369–370.

[42] Y. Cheng, D.P. Thompson, Nitrogen-Containing Tetragonal Zirconia, J. Am. Ceram. Soc. 74 (1991) 1135–1138. https://doi.org/10.1111/j.1151-2916.1991.tb04355.x.

[43] Y.-B. Cheng, D.P. Thompson, Role of Anion Vacancies in Nitrogen-Stabilized Zirconia, J. Am. Ceram. Soc. 76 (1993) 683–688. https://doi.org/10.1111/j.1151-2916.1993.tb03660.x.

[44] T.-J. Chung, J.-S. Lee, D.-Y. Kim, H. Song, Surface Nitridation of Yttria-Doped Tetragonal Zirconia Polycrystals (Y-TZP): Microstructural Evolution and Kinetics, J. Am. Ceram. Soc. 82 (1999) 3193–3199. https://doi.org/10.1111/j.1151-2916.1999.tb02223.x.

[45] T.-J. Chung, J.-S. Lee, D.-Y. Kim, G.-H. Kim, H. Song, Morphology and Phase Stability of Nitrogen–Partially Stabilized Zirconia (N-PSZ), J. Am. Ceram. Soc. 84 (2001) 172–178. https://doi.org/10.1111/j.1151-2916.2001.tb00626.x.

[46] A. Feder, J. Alcalá, L. Llanes, M. Anglada, Microstructure, mechanical properties and stability of nitrided Y-TZP, J. Eur. Ceram. Soc. 23 (2003) 2955–2962. https://doi.org/10.1016/S0955-2219(03)00307-8.

[47] R. Milani, R.P. Cardoso, T. Belmonte, C.A. Figueroa, C.A. Perottoni, J.E. Zorzi, G. V Soares, I.J.R. Baumvol, Nitriding of yttria-stabilized zirconia in atmospheric pressure microwave plasma, J. Mater. Res. 24 (2009) 2021–2028. https://doi.org/10.1557/jmr.2009.0245.

[48] Y.P. Kathuria, Laser surface nitriding of yttria stabilized tetragonal zirconia, Surf Coat Technol. 201 (2007) 5865–5869. https://doi.org/10.1016/j.surfcoat.2006.10.041.

[49] T. Kurachi, Y. Yamashita, T. Tokunaga, H. Yoshida, T. Yamamoto, Suppression of nitridation of yttria-doped zirconia during flash sintering, J. Am. Ceram. Soc. 103 (2020) 3002–3007. https://doi.org/10.1111/jace.16990.

[50] J. Wu, M. Kermani, D. Zhu, J. Li, Y. Lin, C. Hu, S. Grasso, Carbon free ultra-fast high temperature sintering of translucent zirconia, Scr. Mater. 210 (2022) 114476. https://doi.org/10.1016/j.scriptamat.2021.114476.

[51] R.F. Walker, Mechanism of Material Transport During Sintering, J. Am. Ceram. Soc. 38 (1955) 187–197. https://doi.org/10.1111/j.1151-2916.1955.tb14928.x.

[52] R.L. Coble, Sintering Alumina: Effect of Atmospheres, J. Am. Ceram. Soc. 45 (1962) 123–127. https://doi.org/10.1111/j.1151-2916.1962.tb11099.x.

[53] S.K. Roy, Effects of Atmosphere on Sintering of Alumina, Trans. Indian Ceram. Soc. 54 (1995) 190–196. https://doi.org/10.1080/0371750X.1995.10804718.

[54] S.-J.L. Kang, What we should consider for full densification when sintering, Materials. 13 (2020) 3578.

[55] A.F.S. Marques, F.A.P. Loureiro, N. Sahoo, J.R.O.F. Marques, M.F.B. da Cruz, A.D.S.P. da Mata, J. Caramês, F.S.C.P. da Silva, Ó.S.N. Carvalho, Nd-YAG Laser Texturing of Zirconia Implant Surfaces, Lasers in Manufacturing and Materials Processing. 10 (2023) 1–18. https://doi.org/10.1007/s40516-022-00191-5.

[56] M. Bortolotti, L. Lutterotti, G. Pepponi, Combining XRD and XRF analysis in one Rietveld-like fitting, Powder Diffr. 32 (2017) S225–S230. https://doi.org/DOI: 10.1017/S0885715617000276.

[57] W. Bao, S. Robertson, J.-X. Liu, G.-J. Zhang, F. Xu, H. Wu, Structural integrity and characteristics at lattice and nanometre levels of ZrN polycrystalline irradiated by 4 MeV Au ions, J. Eur. Ceram. Soc. 38 (2018) 4373–4383. https://doi.org/10.1016/j.jeurceramsoc.2018.05.013.

[58] C. Bechteler, R.I. Todd, Lattice modification of ZrO2-δ and formation of rocksalt structure ZrO and Zr(O,N) after DC electrical loading of 3YSZ, J. Eur. Ceram. Soc. (2023). https://doi.org/10.1016/j.jeurceramsoc.2023.09.014.

[59] A.P. Naumenko, N.I. Berezovska, M.M. Biliy, O. V Shevchenko, Vibrational analysis and Raman spectra of tetragonal zirconia, Phys. Chem. Solid State. 9 (2008) 121–125.

[60] J.-M. Costantini, G. Gutierrez, G. Lelong, M. Guillaumet, Md.M. Rahman, K. Yasuda, Raman spectroscopy study of damage in swift heavy ion-irradiated ceramics, J. Raman Spectrosc. 53 (2022) 1614–1624. https://doi.org/10.1002/jrs.6414.

[61] C. Bechteler, R.I. Todd, Investigation about the electrochemical reduction in 3YSZ, related phase transition and consequences, ArXiv Preprint ArXiv:2307.03557. (2023).

[62] M. Biesuz, L. Pinter, T. Saunders, M. Reece, J. Binner, V.M. Sglavo, S. Grasso, Investigation of electrochemical, optical and thermal effects during flash sintering of 8YSZ, Materials. 11 (2018) 1214.

[63] J. Janek, C. Korte, Electrochemical blackening of yttria-stabilized zirconia – morphological instability of the moving reaction front, Solid State Ion. 116 (1999) 181–195. https://doi.org/10.1016/S0167-2738(98)00415-9.

[64] C. Gionco, M.C. Paganini, E. Giamello, R. Burgess, C. Di Valentin, G. Pacchioni, Paramagnetic Defects in Polycrystalline Zirconia: An EPR and DFT Study, Chemistry of Materials. 25 (2013) 2243–2253. https://doi.org/10.1021/cm400728j.

[65] N. Morisaki, H. Yoshida, K. Matsui, T. Tokunaga, K. Sasaki, T. Yamamoto, Synthesis of zirconium oxynitride in air under DC electric fields, Appl. Phys. Lett. 109 (2016) 083104. https://doi.org/10.1063/1.4961624.

[66] I. Milošev, H.-H. Strehblow, M. Gaberšček, B. Navinšek, Electrochemical Oxidation of ZrN Hard (PVD) Coatings Studied by XPS, Surface and Interface Analysis. 24 (1996) 448–458.

[67] P. Carvalho, J.M. Chappé, L. Cunha, S. Lanceros-Méndez, P. Alpuim, F. Vaz, E. Alves, C. Rousselot, J.P. Espinós, A.R. González-Elipe, Influence of the chemical and electronic structure on the electrical behavior of zirconium oxynitride films, J. Appl. Phys. 103 (2008) 104907. https://doi.org/10.1063/1.2927494.

[68] D. Majumdar, D. Chatterjee, X-ray photoelectron spectroscopic studies on yttria, zirconia, and yttria-stabilized zirconia, J. Appl. Phys. 70 (1991) 988–992. https://doi.org/10.1063/1.349611.

[69] I. Takano, S. Isobe, T.A. Sasaki, Y. Baba, Nitrogenation of various transition metals by N+2-ion implantation, Appl. Surf. Sci. 37 (1989) 25–32. https://doi.org/10.1016/0169-4332(89)90970-7.

[70] T. Hérisson de Beauvoir, Z. Ghomari, G. Chevallier, A. Flaureau, A. Weibel, C. Elissalde, F. Mauvy, R. Chaim, C. Estournès, Flash Spark Plasma Sintering of 3YSZ: Modified sintering pathway and impact on grain boundary formation, J. Eur. Ceram. Soc. 41 (2021) 7762–7770. https://doi.org/10.1016/j.jeurceramsoc.2021.08.013.

[71] G. Bernard-Granger, C. Guizard, S. Surblé, G. Baldinozzi, A. Addad, Spark plasma sintering of a commercially available granulated zirconia powder—II. Microstructure after sintering and ionic conductivity, Acta Mater. 56 (2008) 4658–4672. https://doi.org/10.1016/j.actamat.2008.05.031.

[72] J.A. Krogstad, M. Lepple, Y. Gao, D.M. Lipkin, C.G. Levi, Effect of Yttria Content on the Zirconia Unit Cell Parameters, J. Am. Ceram. Soc. 94 (2011) 4548–4555. https://doi.org/10.1111/j.1551-2916.2011.04862.x.

[73] P. Vult von Steyern, E. Bruzell, L. Vos, F.S. Andersen, A. Ruud, Sintering temperature accuracy and its effect on translucent yttria-stabilized zirconia: Flexural strength, crystal structure, tetragonality and light transmission, Dental Materials. 38 (2022) 1099–1107. https://doi.org/10.1016/j.dental.2022.04.023.

[74] M.J. Balart, J.B. Patel, F. Gao, Z. Fan, Grain Refinement of Deoxidized Copper, Metallurgical and Materials Transactions A. 47 (2016) 4988–5011. https://doi.org/10.1007/s11661-016-3671-8.

[75] R. Marchand, Y. Laurent, J. Guyader, P. L'Haridon, P. Verdier, Nitrides and oxynitrides: Preparation, crystal chemistry and properties, J. Eur. Ceram. Soc. 8 (1991) 197–213. https://doi.org/10.1016/0955-2219(91)90096-I.

[76] I. Valov, V. Rührup, R. Klein, T.-C. Rödel, A. Stork, S. Berendts, M. Dogan, H.-D. Wiemhöfer, M. Lerch, J. Janek, Ionic and electronic conductivity of nitrogen-doped YSZ single crystals, Solid State Ion. 180 (2009) 1463–1470. https://doi.org/10.1016/j.ssi.2009.09.003.

[77] S.-W. Kim, S.G. Kim, J.-I. Jung, S.-J.L. Kang, I.-W. Chen, Enhanced Grain Boundary Mobility in Yttria-Stabilized Cubic Zirconia under an Electric Current, J. Am. Ceram. Soc. 94 (2011) 4231–4238. https://doi.org/10.1111/j.1551-2916.2011.04800.x.

[78] Y. Dong, H. Wang, I.-W. Chen, Electrical and hydrogen reduction enhances kinetics in doped zirconia and ceria: I. grain growth study, J. Am. Ceram. Soc. 100 (2017) 876–886. https://doi.org/10.1111/jace.14615.

[79] Y. Dong, I.-W. Chen, Electrical and hydrogen reduction enhances kinetics in doped zirconia and ceria: II. Mapping electrode polarization and vacancy condensation in YSZ, J. Am. Ceram. Soc. 101 (2018) 1058–1073. https://doi.org/10.1111/jace.15274.

[80] Y. Dong, L. Qi, A. Alvarez, J. Li, I.-W. Chen, Enhanced mobility of cations and anions in the redox state: The polaronium mechanism, Acta Mater. 232 (2022) 117941. https://doi.org/10.1016/j.actamat.2022.117941.

[81] Y. Dong, Redox enhanced slow ion kinetics in oxide ceramics, J. Am. Ceram. Soc. 107 (2024) 1905–1916. https://doi.org/10.1111/jace.19441.

[82] E. Martin, U.C. Chung, M. Duttine, M.A. Dourges, G. Clermont, C. Labrugère, S. Fourcade, D. Michau, C. Estournès, T. Hérisson de Beauvoir, F. Mauvy, V. Jubera, M. Maglione, G. Goglio, C. Elissalde, Defect chemistry to trigger zirconia densification at low temperatures by Spark Plasma Sintering, Open Ceramics. 17 (2024) 100518. https://doi.org/10.1016/j.oceram.2023.100518.

[83] J.-C. M'Peko, J.S.C. Francis, R. Raj, Impedance Spectroscopy and Dielectric Properties of Flash Versus Conventionally Sintered Yttria-Doped Zirconia Electroceramics Viewed at the Microstructural Level, J. Am. Ceram. Soc. 96 (2013) 3760–3767. https://doi.org/10.1111/jace.12567.

CHAPTER 13

A CRITICAL EVALUATION AND COMPARISON OF CURRENT SINTERING TECHNIQUES

Table 13.1 summarizes comparison of current sintering techniques used in terms of materials characteristics, sintering parameters, easiness, and applicability. When considering embodied energy, encompassing all energy expended in the processes associated with ceramic body production, cold sintering techniques, in other word “firing without fire” emerge in cases where a liquid is used to enhance densification.[97]

For cold sintering process, despite existing material limitations, primarily concerning low yield stress and soluble compounds, as well as constraints related to achievable shapes, a significant milestone has been attained in producing dense components below 400°C. However, the industrial scaling of such technologies faces critical difficulties due to batch processing, excessive high pressures (approximately 300-500 MPa), and small sample sizes. Although processing time is limited (from a few minutes to a few hours), the productivity may remain relatively low compared to conventional sintering methods. Despite all this, promising studies on the feasibility of scaling up CSP for industrial applications are still ongoing.[28,98] It is believed that continuous liquid-assisted consolidation techniques will emerge within the forthcoming years. If the mentioned scenario materializes, a rapid transition from laboratory experimentation to industrial implementation under the actual paradigm shift of 'firing without fire' will be anticipated.[97] Besides, the constraints related to complex shapes in cold sintering process may be expected to be solved in the next years similar to the solutions developed strategies in spark plasma sintering.[99,100]

Table 13.1. Comparison of current sintering techniques used within the scope of dissertation, modified from.[77,97]

	Cold sintering	RHLPD	Fast firing	Flash sintering	UHS
Materials	Oxides	Oxides	Oxides	Oxides Carbides Nitrides Borides Metals	Oxides Carbides Nitrides Borides Metals
Temperature range	<400°C	<600°C[a)]	<2000°C[b)]	<1768°C[c)]	<3000 °C
Sintering time	Few hours	Few days	Few minutes	Few seconds	Few seconds
Applied pressure	<1 GPa	None	None	None[e)]	None
Heating rates	1-20 °C/min	1-20 °C/min	10^2-10^3 °C/min	10^3 -10^4°C/min	10^3 -10^4°C/min
Sample size	<2 cm	<5 cm	<5 cm	< 2 cm	<2.5 cm
Sample geometry	Simple shapes	Simple and complex samples	Simple and complex samples	Simple shapes (Disc, dogbone, and rod)	Thin, small samples, rather complex geometries
Atmosphere	Any	Any	Mostly air	Mostly air	Mostly inert
Heating source	Heating jacket	Oven or heating jacket	Heating element	AC/DC power source + external heater	Graphite felt heated by AC/DC power source
Sintering device	Hydraulic press, FAST/SPS	Autoclave	Furnace	Chamber furnace, tubular kiln	Atmosphere-controlled chamber
Industrial application	Not yet	Not yet	Widely used	Very early state	Not yet but promising

a) Maximum operation temperature of currently available high pressure/high temperature vessels
b) Maximum operation temperature of currently available heating elements
c) Melting temperature of Pt electrodes
d) Below around melting temperature of carbon and tungsten
e) For disc-shaped specimens optional pressure possible.

It is important to note that the efficiency of the cold sintering process depends on factors such as particle size, agglomeration, and surface chemistry, etc.[74] When examining materials sintered via cold methods (those that do not need post-annealing), it can be stated that the selection of materials for the cold sintering process requires factors such as ionic bonding characteristics, including bonding potential and bonding strength.[22] Furthermore, similar to the study of cold sintering of KNN, cold sintering acts as a compaction process causing an increase in densification up to around 80%; however, it requires additional annealing at elevated temperatures to obtain high densification and the desired properties.[77] As such, it can be considered as an intermediate densifying tool for enhancing the final densification and the resultant properties. Besides, one of the challenging points is that such perovskite or other ternary oxides may result in incongruent dissolution under cold sintering process conditions, affecting the properties of the materials.[101–104] It is also important to emphasize that despite being less frequently discussed, the punches and dies utilized for cold sintering (made from working steel), experience wear over time, particularly in corrosive environments such as caustic conditions.[24,105]

Another cold sintering technique, rHLPD, facilitates simultaneous synthesis and densification by filling pores during the reaction period in the presence of a liquid phase. Due to reasons such as the requirement for a positive molar volume change, grain growth, and hydrothermal considerations, the application of this method appears limited to specific material systems. Owing to its synthesis capabilities, it holds significant promise for ternary or quaternary oxides (e.g., perovskites, spinels, garnets, etc.). But, within the context of kinetic and thermodynamic variables in such a method, the possibility of hydrothermal liquid phase densification (HLPD) or solvothermal liquid phase densification (SLPD) for binary oxides without reactivity may be feasible (e.g., filling the pores of porous ZnO pellets in the presence of a liquid phase used for the potential hydro/solvothermal synthesis of ZnO). Although it has not been tested yet, rHLPD may be a useful tool in condensing complex shapes due to uniaxial pressure not being applied. The sample sizes that can be produced by the rHLPD method theoretically depend on the vessel dimensions in which the reaction takes place and the practical limitation in this regard may be determined by the thermodynamics and kinetic variables of the rHLPD. As seen, the carried-out reactions ($BaTiO_3$, and $SrTiO_3$) were quite slow, taking days compared to other techniques. Besides, carbon capture and sequestration were also

attempted by utilization of rHLPD.[106] One drawback of this method is that in cases where the reaction involves intermediate phases or when the starting material has a high degree of solubility, it may pose challenges in maintaining the pellet's monolithic structure and achieving the desired product. For instance, several attempts were made to densify KNN materials using this method, but undesirable results were observed in reactions involving KOH and NaOH solutions with NbO_2 and Nb_2O_5 sources, similar to the observed intermediate hexaniobate phase in the hydrothermal synthesis of KNN.[107,108]

Compared to field-assisted techniques that enable much faster heating rates, fast-firing process requiring simpler equipment is adopted as the most suitable for industrial applications. In industrial applications (e.g., tile industry), production is possible even with larger sample geometries, consequently, thickness might be a potential limiting factor [37]. Additionally, exceeding 2000°C can be challenging due to the limitations of existing heating elements.[109] While there are various studies on oxide materials, research involving non-oxide materials is limited due to specific furnace requirements (e.g., atmosphere-controlled furnaces).[110] The performance of this technique on covalently bonded ceramic materials remains a subject of curiosity.

Although flash sintering necessitates a furnace, the temperature typically remains significantly under 1000°C in most cases. However, specific scenarios, such as with α-Al_2O_3, may demand elevated temperatures above 1000°C.[97,111,112] Nevertheless, these temperatures are several hundred degrees lower than those employed in conventional sintering. Moreover, the component is electrically heated through the Joule effect, narrowing the gap between the actual temperature in flash sintering and that of conventional sintering. It is worth noting that the material must have some conductivity to achieve the critical power dissipation of around 10-100 mW/mm^3 required to trigger the flash.[113,114] A significant advantage of flash sintering lies in its limited processing duration and thermal concentration within the ceramic; this enables the processing of materials with a consolidation temperature even higher than the maximum temperature allowed by the furnace used.[115] Although the melting temperature of Pt electrode is specified as the maximum operating temperature of the system, this value can often be exceeded during the process because Pt is well conductive and removes the much faster than the sample.[116] The utilization of thermal insulators to prevent thermal distribution (thermally insulated FS) further enhances the efficiency of the process.[81,97]

Despite being a significant advanced sintering technique with low-cost equipment, presents a challenging process from the preparation of samples to the final product. Limitations in sample geometries, difficulties in preparing suitable samples, and possible problems during sintering are among the reasons for the complexity of this process. Although dog bone shapes are quite complex and have limited use in applications, they are the best sample geometry for flash sintering. Because this shape can easily pass through the thinner section and conductivity development can be carefully monitored, it minimizes the problems associated with current concentration during flash sintering.[17] However, the probability of scrap material extraction (e.g., scrap in dogbone-shaped materials) is higher compared to other processes. This is due to the removal requirement of unsintered regions, except for the areas where the electric current passes through the linear region, following flash sintering. To overcome such problems, contactless flash sintering was introduced, which allows the use of electric arcs, cold plasma, and conductive flame instead of Pt electrodes.[117–121] In this way, such flash sintering systems will lead to the emergence of new opportunities. However, it should be noted that a limitation of this method is the high cost of such electrodes. Although there are first attempts at industrial applications of flash sintering, it might seem this technique remains at the laboratory scale unless relevant developments occur.[77]

Due to its simplicity and adaptability, UHS has great potential and works utilizing graphite felt heaters in direct contact with ceramic green bodies. Due to the absence of a large furnace chamber and the low thermal mass of the installation, very high heating rates (e.g., ~1000°C/min) can easily be achieved. However, UHS needs an oxygen-deficient environment to prevent degradation of graphite felt. As well as accomplishing smaller grain sized structures, UHS can allow obtaining microstructures and properties that resemble those achieved through conventional sintering within reduced time.[62,77] The scale-up studies of UHS carried out since its introduction in 2020 truly demonstrate the potential industrial applicability of this process.[62,122] Additionally, possible carbon contamination can be prevented by using tungsten heaters instead of graphite felt.[123] To homogenize the temperature distribution of the system and reduce the heat loss thermal insulation material can be utilized.[63] One of the most challenging aspects of this technique is temperature measurement during sintering in a short time with a high heating rate. For instance, a metal shield on the thermocouple tip can cause a substantial reduction in the measured temperature. Because the existing metal shield has more thermally

conductivity with orders of magnitude than the graphite felt, it enables the removal of heat from the tip region. Therefore, data obtained from such thermocouples must be approached with caution.[116] As noticed, in the UHS of ZrO_2 study, the determination of temperature was simulated by FEM.

As stated, UHS must be performed in an oxygen-free environment such as Argon, vacuum [124], or Nitrogen (as performed in this study). It should be noted that the mentioned atmospheres may impact or change the structure of the material, either reducing the material or reacting with the material as with YSZ study.

The most important issue that should be recommended in such electric field-assisted sintering techniques with high heating rates is the determination of the ratio of the sintering temperatures of the materials to those of melting temperatures (T_s/T_m). For instance, the sintering temperature of KNN, whose sintering was attempted in this thesis study, is found to be at around 1120°C, while its melting temperature is 1140°C.[95,125] This causes unsuccessful results in such techniques where temperature control is difficult. Although there are successful results in the literature regarding the sintering of KNN materials using these methods[126–130], there will always be a question mark about the repeatability of the samples. Therefore, KNN has a T_s/T_m ratio of 0.98, and based on this value, it can be deduced properly that the materials with Ts/Tm < 0.8-0.9 for such sintering methods unless more precise temperature control is developed.

In this context, the algorithm for current sintering techniques shown in Figure 13.1 was developed. It presents a general perspective for sintering applications to achieve target properties. Besides, an algorithm for rHLPD is also shown in Figure 13.2 since it offers a different concept due to the different dynamics of the system. Of course, expecting these algorithms to work perfectly always isn't realistic. However, the recommendations provided for the employed sintering techniques will prove beneficial for future research.

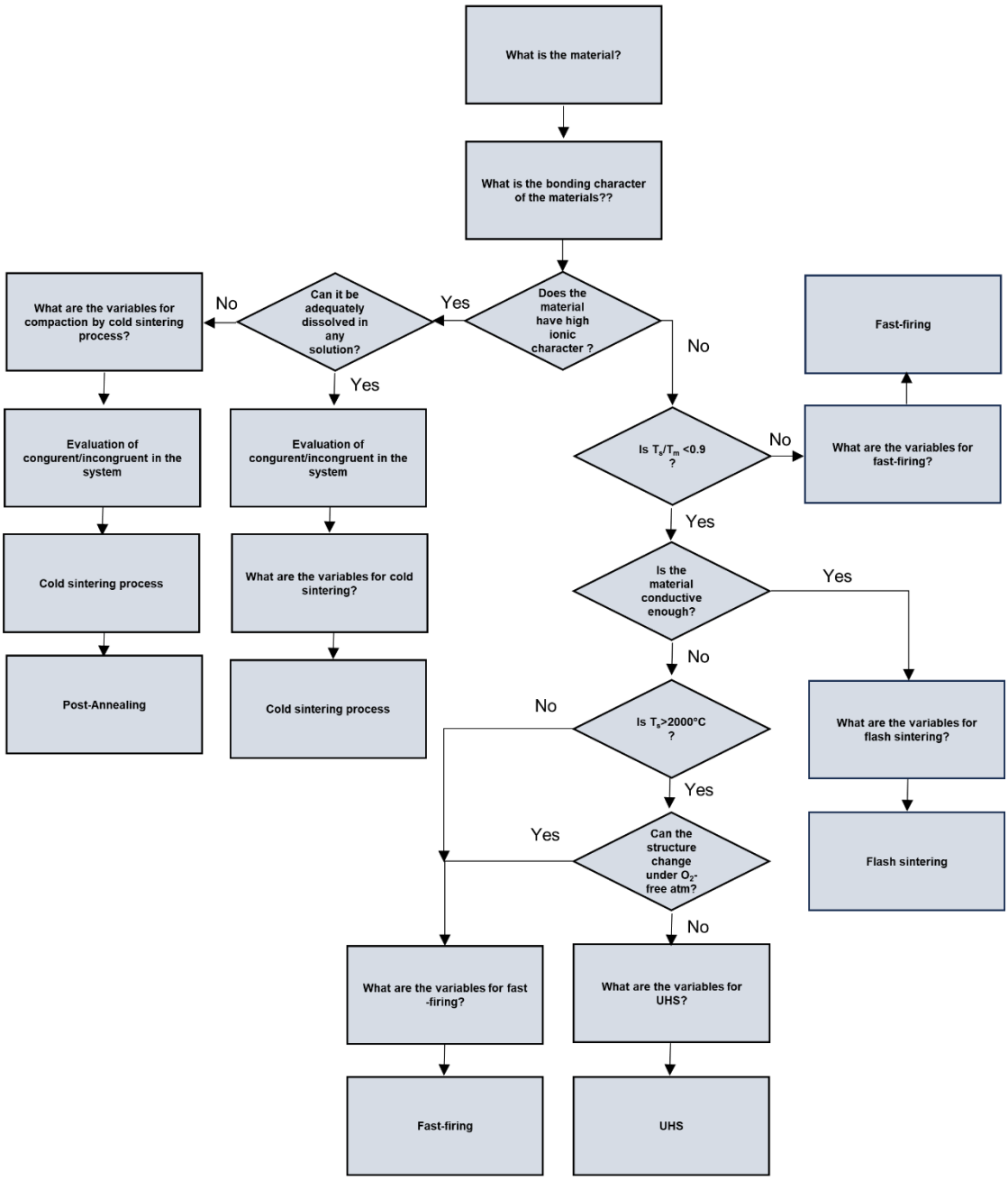

Figure 13.1. Proposed algorithm for current sintering technique, including cold sintering, fast-firing, Flash sintering, and UHS.

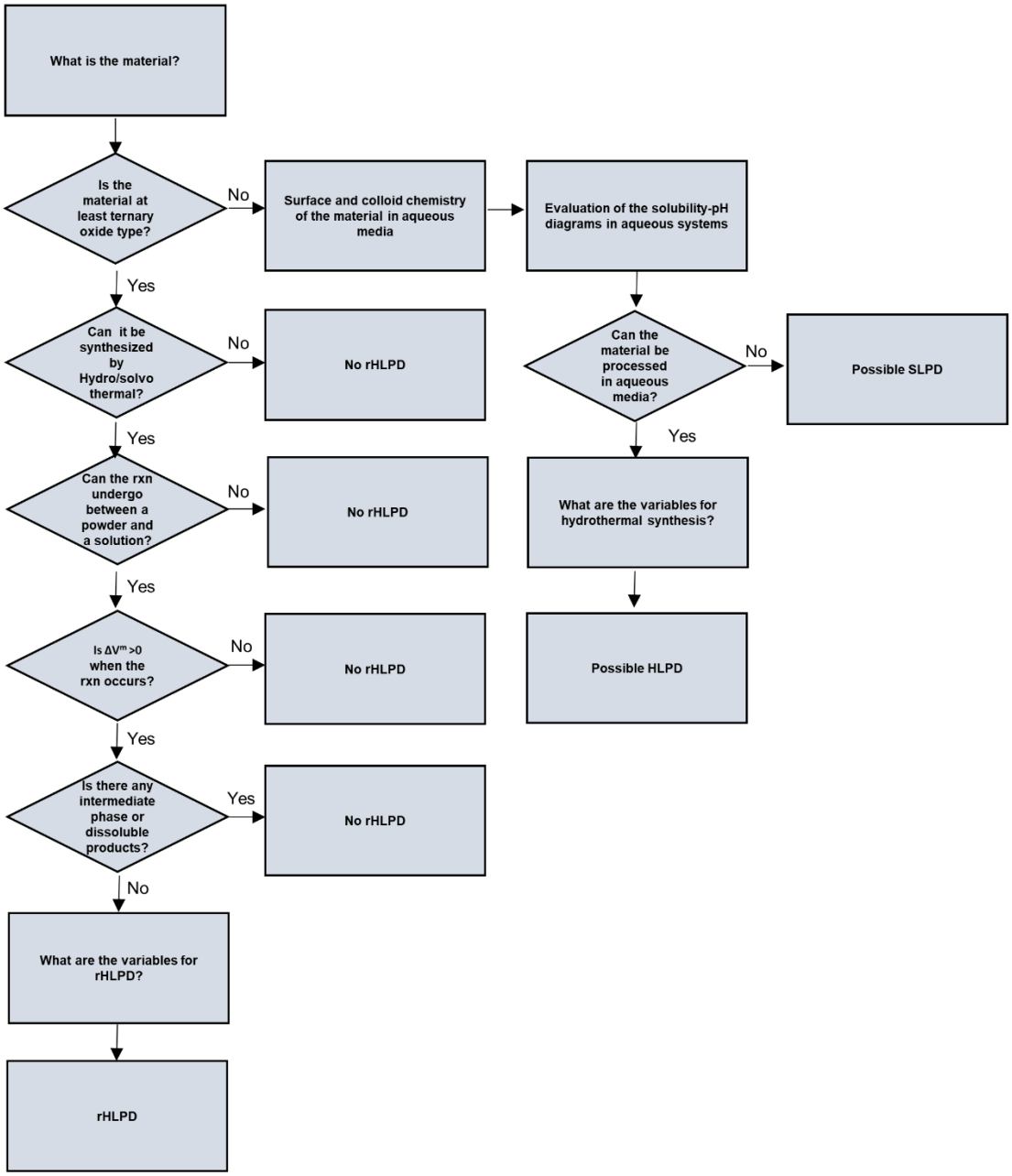

Figure 13.2. Proposed algorithm for rHLPD, including possible opportunities, modified from.[76] (Rxn: Reaction; $AV^m>0$: Positive molar volume change).

CHAPTER 14

CONCLUSIONS AND PERSPECTIVES

The utility of different sintering techniques ranging from low temperature densification methods to production techniques with high heating rates for various ceramic materials was demonstrated comparing with the literature, conventional sintering or conventional procedures of the sintering processes used.

CSP, which is one of the low-temperature densification techniques, has its roots dating back to the 1970s, and with the latest developments in the technique, it has become an extremely simple method for densification using basic equipment. It was demonstrated successful densification of recycled glass powders and Mars regolith simulants by utilizing NaOH to dissolve, while in the case of KNN ceramics, despite attempting to use various liquid phases and parameters, low densification was achieved, necessitating an annealing procedure. The efficiency of the cold sintering process depends on the solubility characteristics of the material to be sintered. Furthermore, similar to cold sintering procedure of KNN, CSP can be considered as an intermediate densifying tool for enhancing the final densification and the resultant properties in the future. Additionally, as mentioned in the introduction section, it is worth noting that a standardized diffusion mechanism for cold sintering has yet to be identified. It is believed that further in-depth investigations will be necessary in the future to address this issue.

Another low-temperature densification technique, namely rHLPD, remains an open field for development, with a significant scientific knowledge gap. This approach, based on filling pores in the material using reactive capabilities rather than sintering and shrinkage, holds promise, especially for components with three-dimensional complex shapes and/or near-net-shaped products. As mentioned before, one of the challenges is that the carried-out reactions for $BaTiO_3$, and $SrTiO_3$ were quite slow, taking days. Even the kinetic of $SrTiO_3$ was slower than that of $BaTiO_3$.

Fast firing, also can be said as ancient UHS, is an extremely practical technique used in the industry. Although it is a common technique for industry, ongoing research is required for the production and industrial scale-up of various technical ceramics. Since compared to conventional sintering, it is evident that microstructure control can be more easily achieved. So far, in terms of ease of use and infrastructure, fast firing can be considered the sintering process with a great potential for industrial utilization. Besides, while fast firing is indeed explained by diffusion mechanisms (e.g., surface diffusion vs. grain boundary diffusion or lattice diffusion) proposed for solid-state sintering, it can be also considered to be a useful method for materials with a glassy phase (e.g., Mars simulant), which might lead to somehow aiding viscous flow.

Although considered an advanced sintering method utilizing basic equipment, it poses substantial challenges throughout the process, spanning from sample preparation to the obtainment of the end product. Challenges arise due to constraints in sample geometries, complexities in sample preparation, and potential issues encountered during flash sintering process, contributing to the complex nature of this technique. While industrial scaling attempts have been made, it is not anticipated to be feasible soon. Because it might seem this method remains at the laboratory scale unless relevant developments (i.e., contactless flash sintering) happen.

The recently introduced UHS process in the literature is believed to be a great candidate for sintering a wide range of materials. Its potential for industrial scale-up places it as one of the strongest candidates against conventional sintering and fast firing. Furthermore, as a contribution to the UHS process, an investigation was conducted to address the question of whether the atmosphere matters in diffusion, i.e. sintering. In this regard, UHS experiments were conducted in a nitrogen atmosphere instead of an argon atmosphere which is a typical atmosphere for UHS. The results unequivocally demonstrate that the atmosphere significantly influences the sintering process and, consequently, the final product. Additionally, the most significant challenge observed is the narrow sintering window for some materials due to melting temperatures being close to sintering temperatures, as seen in materials like KNN. Lastly, temperature measurement during the process is one of the most challenging aspects of this technique.

In a general conclusion, every ceramic material might not guaranteed to yield successful results in all sintering processes. It should be noted that each sintering process takes place in distinct sintering mechanisms. The selection of the appropriate sintering

method and conditions should be based on an evaluation of the specific material's characteristics (e.g., bonding characteristics, diffusion ability, electrical conductivity, sintering temperature, and melting temperature of the material, etc) and the desired properties in the final product. This entails a comprehensive understanding of the material's behavior and the careful optimization of sintering parameters, such as temperature, pressure, and atmosphere, to ensure the desired microstructure and properties are achieved. In conclusion, this dissertation highlights the need for a material-specific approach to sintering processes, acknowledging the multifaceted nature of ceramics and the diversity of sintering mechanisms. Therefore, this understanding of the interaction between ceramic materials and sintering processes is essential for advancing the field of ceramic science.

REFERENCES

(1) Walker, R. F. Mechanism of Material Transport During Sintering. *J. Am. Ceram. Soc.* **1955**, *38* (6), 187–197. https://doi.org/10.1111/j.1151-2916.1955.tb14928.x.

(2) Rahaman, M. N. *Ceramic Processing and Sintering*; CRC press, **2017**.

(3) Rahaman, M. N. *Sintering of Ceramics*; CRC press, **2007**.

(4) German, R. M. *Sintering Theory and Practice*; Wiley, **1996**.

(5) Vakifahmetoglu, C.; Karacasulu, L. Cold Sintering of Ceramics and Glasses: A Review. *Curr. Opin. Solid State Mater. Sci.* **2020**, *24* (1), 100807. https://doi.org/10.1016/j.cossms.2020.100807.

(6) Bordia, R. K.; Kang, S.-J. L.; Olevsky, E. A. Current Understanding and Future Research Directions at the Onset of the next Century of Sintering Science and Technology. *J. Am. Ceram. Soc.* **2017**, *100* (6), 2314–2352. https://doi.org/https://doi.org/10.1111/jace.14919.

(7) German, R. M. History of Sintering: Empirical Phase. *Powder Metallurgy* **2013**, *56* (2), 117–123. https://doi.org/10.1179/1743290112Y.0000000025.

(8) Kang, S.-J. L. *Sintering: Densification, Grain Growth and Microstructure*; Elsevier, **2004**.

(9) Chiang, Y.-M.; Birnie, D. P.; Kingery, W. D. Physical Ceramics: Principles for Ceramic Science and Engineering, John Wiley & Sons, **1997**.

(10) Leriche, A.; Hampshire, S.; Cambier, F. Control of the Microstructure in Ceramics. In *Encyclopedia of Materials: Technical Ceramics and Glasses*; Pomeroy, M., Ed.; Elsevier: Oxford, **2021**; pp 349–366. https://doi.org/10.1016/B978-0-12-818542-1.00017-5.

(11) Munir, Z. A.; Anselmi-Tamburini, U.; Ohyanagi, M. The Effect of Electric Field and Pressure on the Synthesis and Consolidation of Materials: A Review of the Spark Plasma Sintering Method. *J. Mater. Sci.* **2006**, *41* (3), 763–777. https://doi.org/10.1007/s10853-006-6555-2.

(12) Garay, J. E. Current-Activated, Pressure-Assisted Densification of Materials. *Annu. Rev. Mater. Res.* **2010**, *40* (1), 445–468. https://doi.org/10.1146/annurev-matsci-070909-104433.

(13) Sutton, W. H. Microwave Processing of Ceramics - An Overview. *MRS Online Proceedings Library* **1992**, *269* (1), 3–20. https://doi.org/10.1557/PROC-269-3.

(14) Katz, J. D. Microwave Sintering of Ceramics. *Annual Review of Materials Science* **1992**, *22* (1), 153–170. https://doi.org/10.1146/annurev.ms.22.080192.001101.

(15) Oghbaei, M.; Mirzaee, O. Microwave versus Conventional Sintering: A Review of Fundamentals, Advantages and Applications. *J. Alloys Compd.* **2010**, *494* (1), 175–189. https://doi.org/10.1016/j.jallcom.2010.01.068.

(16) Yu, M.; Grasso, S.; Mckinnon, R.; Saunders, T.; Reece, M. J. Review of Flash Sintering: Materials, Mechanisms and Modelling. *Advances in Applied Ceramics* **2017**, *116* (1), 24–60. https://doi.org/10.1080/17436753.2016.1251051.

(17) Biesuz, M.; Sglavo, V. M. Flash Sintering of Ceramics. *J Eur Ceram Soc* 2019, *39* (2), 115–143. https://doi.org/10.1016/j.jeurceramsoc.2018.08.048.

(18) Guo, H.; Baker, A.; Guo, J.; Randall, C. A. Protocol for Ultralow-Temperature Ceramic Sintering: An Integration of Nanotechnology and the Cold Sintering Process. *ACS Nano* **2016**, *10* (11), 10606–10614.

(19) Guo, H.; Guo, J.; Baker, A.; Randall, C. A. Hydrothermal-Assisted Cold Sintering Process: A New Guidance for Low-Temperature Ceramic Sintering. *ACS Appl. Mater. Interfaces* **2016**, *8* (32), 20909–20915. https://doi.org/10.1021/acsami.6b07481.

(20) Sohrabi Baba Heidary, D.; Lanagan, M.; Randall, C. A. Contrasting Energy Efficiency in Various Ceramic Sintering Processes. *J. Eur. Ceram. Soc.* **2018**, *38* (4), 1018–1029. https://doi.org/10.1016/j.jeurceramsoc.2017.10.015.

(21) Guo, J.; Guo, H.; Baker, A. L.; Lanagan, M. T.; Kupp, E. R.; Messing, G. L.; Randall, C. A. Cold Sintering: A Paradigm Shift for Processing and Integration of Ceramics. *Angewandte Chemie International Edition* **2016**, *55* (38), 11457–11461. https://doi.org/10.1002/anie.201605443.

(22) Grasso, S.; Biesuz, M.; Zoli, L.; Taveri, G.; Duff, A. I.; Ke, D.; Jiang, A.; Reece, M. J. A Review of Cold Sintering Processes. *Advances in Applied Ceramics* **2020**, *119* (3), 115–143. https://doi.org/10.1080/17436753.2019.1706825.

(23) Galotta, A.; Sglavo, V. M. The Cold Sintering Process: A Review on Processing Features, Densification Mechanisms and Perspectives. *J. Eur. Ceram. Soc.* **2021**, *41* (16), 1–17. https://doi.org/10.1016/j.jeurceramsoc.2021.09.024.

(24) Karacasulu, L.; Ogur, E.; Piskin, C.; Vakifahmetoglu, C. Cold Sintering of Soda-Lime Glass. *Scr. Mater.* **2021**, *192*, 111–114. https://doi.org/10.1016/j.scriptamat.2020.10.015.

(25) Guo, H.; Baker, A.; Guo, J.; Randall, C. A. Cold Sintering Process: A Novel Technique for Low-Temperature Ceramic Processing of Ferroelectrics. *J. Am. Ceram. Soc* **2016**, *99* (11), 3489–3507. https://doi.org/10.1111/jace.14554.

(26) Gonzalez-Julian, J.; Neuhaus, K.; Bernemann, M.; Pereira da Silva, J.; Laptev, A.; Bram, M.; Guillon, O. Unveiling the Mechanisms of Cold Sintering of ZnO at 250 °C by Varying Applied Stress and Characterizing Grain Boundaries by Kelvin Probe Force Microscopy. *Acta Mater.* **2018**, *144*, 116–128. https://doi.org/10.1016/j.actamat.2017.10.055.

(27) Galotta, A.; Giust, E.; Bortolotti, M.; Sorarù, G. D.; Sglavo, V. M.; Biesuz, M. Cold Sintering of Diatomaceous Earth. *J. Am. Ceram. Soc.* **2021**, *104* (9), 4329–4340. https://doi.org/10.1111/jace.17863.

(28) Jabr, A.; Jones, H. N.; Argüelles, A. P.; Trolier-McKinstry, S.; Randall, C.; Bermejo, R. Scaling up the Cold Sintering Process of Ceramics. *J. Eur. Ceram. Soc.* **2023**, *43* (12), 5319–5329. https://doi.org/10.1016/j.jeurceramsoc.2023.04.061.

(29) Riman, R. E.; Atakan, V. Method of Hydrothermal Liquid Phase Sintering of Ceramic Materials and Products Derived Therefrom, US Patent 8,313,802. **2012**.

(30) Vakifahmetoglu, C.; Anger, J. F.; Atakan, V.; Quinn, S.; Gupta, S.; Li, Q.; Tang, L.; Riman, R. E. Reactive Hydrothermal Liquid-Phase Densification (RHLPD) of Ceramics - A Study of the $BaTiO_3$ [TiO_2] Composite System. *J. Am. Ceram. Soc.* **2016**, *99* (12), 3893–3901. https://doi.org/10.1111/jace.14468.

(31) Karacasulu, L.; Tokkan, M.; Bortolotti, M.; Ischia, G.; Adem, U.; Vakifahmetoglu, C. Electrical Characteristics of Low Temperature Densified Barium Titanate. *Ceram. Int.* **2020**, *46* (10), 16670–16676. https://doi.org/10.1016/j.ceramint.2020.03.240.

(32) Harmer, M.P.; Brook, R.J. Fast Firing-Microstructural Benefits. *Trans. J. BR. Ceram. Soc.* **1981**, *80*, 147–148.

(33) Bijalwan, V.; Prajzler, V.; Erhart, J.; Velazquez, J. J.; Galusek, D.; Maca, K. Rapid Pressureless Sintering of Barium Titanate–Based Piezoceramics and Their Electromechanical Harvesting Performance. *J. Am. Ceram. Soc.* **2022**, *105* (11), 6886–6897. https://doi.org/10.1111/jace.18602.

(34) Kim, D.-H.; Kim, C. H. Effect of Heating Rate on Pore Shrinkage in Yttria-Doped Zirconia. *J. Am. Ceram. Soc.* **1993**, *76* (7), 1877–1878. https://doi.org/10.1111/j.1151-2916.1993.tb06665.x.

(35) Leriche, A.; Cambier, F.; Hampshire, S. Sintering of Ceramics. In *Reference Module in Materials Science and Materials Engineering*; Elsevier, **2017**. https://doi.org/10.1016/B978-0-12-803581-8.10288-7.

(36) Kang, S.-J. L. What We Should Consider for Full Densification When Sintering. *Materials* **2020**, *13* (16), 3578.

(37) Hotza, D.; García, D. E.; Castro, R. H. R. Obtaining Highly Dense YSZ Nanoceramics by Pressureless, Unassisted Sintering. *International Materials Reviews* **2015**, *60* (7), 353–375. https://doi.org/10.1179/1743280415Y.0000000005.

(38) Moertel, H. Porcelain for Fast Firing. *Ceramurgia International* **1977**, *3* (2), 65–69. https://doi.org/10.1016/0390-5519(77)90032-1.

(39) Berenshtein, P. I. Fast Single Firing of Ceramic Tiles. *Glass and Ceramics* **1976**, *33* (1), 36–38. https://doi.org/10.1007/BF00702046.

(40) Viswabaskaran, V.; Gnanam, F. D. Development of Fast Firing Vitreous Sanitaryware. *Transactions of the Indian Ceramic Society* **2000**, *59* (4), 105–108. https://doi.org/10.1080/0371750X.2000.10799942.

(41) García, D. E.; Seidel, J.; Janssen, R.; Claussen, N. Fast Firing of Alumina. *J. Eur. Ceram. Soc.* **1995**, *15* (10), 935–938. https://doi.org/10.1016/0955-2219(95)00071-2.

(42) García, D. E.; Hotza, D.; Janssen, R. Building a Sintering Front through Fast Firing. *Int. J. Appl. Ceram. Technol.* **2011**, *8* (6), 1486–1493. https://doi.org/10.1111/j.1744-7402.2011.02609.x.

(43) Possamai, T. S.; Oba, R.; Nicolau, V. P.; Hotza, D.; García, D. E. Numerical Simulation of the Fast Firing of Alumina in a Box Furnace. *J. Am. Ceram. Soc.* **2012**, *95* (12), 3750–3757. https://doi.org/10.1111/j.1551-2916.2012.05432.x.

(44) Prajzler, V.; Salamon, D.; Maca, K. Pressure-Less Rapid Rate Sintering of Pre-Sintered Alumina and Zirconia Ceramics. *Ceram. Int.* **2018**, *44* (9), 10840–10846. https://doi.org/10.1016/j.ceramint.2018.03.132.

(45) Mostaghaci, H.; Brook, R. J. Microstructure Development and Dielectric Properties of Fast-Fired $BaTiO_3$ Ceramics. *J. Mater. Sci.* **1986**, *21* (10), 3575–3580. https://doi.org/10.1007/BF00553803.

(46) Zhu, W.; Wang, C. C.; Akbar, S. A.; Asiaie, R. Fast-Sintering of Hydrothermally Synthesized $BaTiO_3$ Powders and Their Dielectric Properties. *J. Mater. Sci.* **1997**, *32* (16), 4303–4307. https://doi.org/10.1023/A:1018663621241.

(47) Bologna Alles, A.; Vanalstine, R.; Schulze, W. Dielectric Properties and Aging of Fast-Fired Barium Titanate. *Latin American applied research* **2005**, *35* (1), 29–35.

(48) Dias, A. Microstructural Evolution of Fast-Fired Nickel–Zinc Ferrites from Hydrothermal Nanopowders. *Mater. Res. Bull.* **2000**, *35* (9), 1439–1446. https://doi.org/10.1016/S0025-5408(00)00337-8.

(49) Kim, B.-C.; Lee, J.-H.; Kim, J.-J.; Lee, H. Y.; Lee, J.-S. Densification of Nanocrystalline ITO Powders in Fast Firing: Effect of Specimen Mass and Sintering Atmosphere. *Mater. Res. Bull.* **2005**, *40* (2), 395–404. https://doi.org/10.1016/j.materresbull.2004.10.006.

(50) Reis, S. L.; Muccillo, E. N. S. Microstructure and Electrical Conductivity of Fast Fired Sr- and Mg-Doped Lanthanum Gallate. *Ceram. Int.* **2016**, *42* (6), 7270–7277. https://doi.org/10.1016/j.ceramint.2016.01.121.

(51) Landin, S. M.; Schulze, W. A. Rapid Sintering of Stoichiometric Zinc-Modified Lead Magnesium Niobate. *J. Am. Ceram. Soc.* **1990**, *73* (4), 913–918. https://doi.org/10.1111/j.1151-2916.1990.tb05135.x.

(52) Landin, S. M.; Schulze, W. A. Rapid Thermal Processing of $Pb(Mg_{0.7}Zn_{0.3})_{1/3}Nb_{2/3}O_3$ Multilayer Ceramic Capacitors. *J. Am. Ceram. Soc.* **1990**, *73* (4), 909–912. https://doi.org/10.1111/j.1151-2916.1990.tb05134.x.

(53) Bowen, C. R.; Open, J.; Fitzmaurice, J.; Mahon, S. Fast Firing of Electroceramics. *Ferroelectrics* **1999**, *228* (1), 159–166. https://doi.org/10.1080/00150199908226133.

(54) Seal, A.; Mazumder, R.; Sen, A.; Maiti, H. S. Fast Firing of Lead Zirconate Titanate Ceramics at Low Temperature. *Mater. Chem. Phys.* **2006**, *97* (1), 14–18. https://doi.org/10.1016/j.matchemphys.2005.05.038.

(55) Gómez, S. Y.; da Silva, A. L.; Gouvêa, D.; Castro, R. H. R.; Hotza, D. Nanocrystalline Yttria-Doped Zirconia Sintered by Fast Firing. *Mater. Lett* **2016**, *166*, 196–200. https://doi.org/10.1016/j.matlet.2015.12.042.

(56) Prajzler, V.; Průša, S.; Maca, K. Rapid Pressure-Less Sintering of Fine Grained Zirconia Ceramics: Explanation and Elimination of a Core-Shell Structure. *J. Eur. Ceram. Soc.* **2019**, *39* (16), 5309–5319. https://doi.org/10.1016/j.jeurceramsoc.2019.07.053.

(57) Ji, W.; Parker, B.; Falco, S.; Zhang, J. Y.; Fu, Z. Y.; Todd, R. I. Ultra-Fast Firing: Effect of Heating Rate on Sintering of 3YSZ, with and without an Electric Field. *J. Eur. Ceram. Soc.* **2017**, *37* (6), 2547–2551. https://doi.org/10.1016/j.jeurceramsoc.2017.01.033.

(58) García, D. E.; Wendorff, J.; Janssen, R.; Claussen, N. Fast Firing of Reaction-Bonded Aluminium Oxide RBAO Composites. *J. Mater. Sci.* **1995**, *30* (20), 5121–5124. https://doi.org/10.1007/BF00356058.

(59) Cologna, M.; Rashkova, B.; Raj, R. Flash Sintering of Nanograin Zirconia in <5 s at 850°C. *J. Am. Ceram. Soc.* **2010**, *93* (11), 3556–3559. https://doi.org/10.1111/j.1551-2916.2010.04089.x.

(60) Dancer, C. E. J. Flash Sintering of Ceramic Materials. *Mater. Res. Express* **2016**, *3* (10), 102001. https://doi.org/10.1088/2053-1591/3/10/102001.

(61) Jones, G. M.; Biesuz, M.; Ji, W.; John, S. F.; Grimley, C.; Manière, C.; Dancer, C. E. J. Promoting Microstructural Homogeneity during Flash Sintering of Ceramics through Thermal Management. *MRS Bull.* **2021**, *46* (1), 59–66. https://doi.org/10.1557/s43577-020-00010-2.

(62) Wang, C.; Ping, W.; Bai, Q.; Cui, H.; Hensleigh, R.; Wang, R.; Brozena, A. H.; Xu, Z.; Dai, J.; Pei, Y. A General Method to Synthesize and Sinter Bulk Ceramics in Seconds. *Science (1979)* **2020**, *368* (6490), 521–526.

(63) Dong, J.; Pouchly, V.; Biesuz, M.; Tyrpekl, V.; Vilémová, M.; Kermani, M.; Reece, M.; Hu, C.; Grasso, S. Thermally-Insulated Ultra-Fast High Temperature Sintering (UHS) of Zirconia: A Master Sintering Curve Analysis. *Scr. Mater.* **2021**, *203*, 114076.

(64) Biesuz, M.; Galotta, A.; Motta, A.; Kermani, M.; Grasso, S.; Vontorová, J.; Tyrpekl, V.; Vilémová, M.; Sglavo, V. M. Speedy Bioceramics: Rapid Densification of Tricalcium Phosphate by Ultrafast High-Temperature Sintering. *Materials Science and Engineering: C* **2021**, *127*, 112246.

(65) Luo, R.-X.; Kermani, M.; Guo, Z.-L.; Dong, J.; Hu, C.-F.; Zuo, F.; Grasso, S.; Jiang, B.-B.; Nie, G.-L.; Yan, Z.-Q. Ultrafast High-Temperature Sintering of Silicon Nitride: A Comparison with the State-of-the-Art Techniques. *J. Eur. Ceram. Soc.* **2021**, *41* (13), 6338–6345.

(66) Kermani, M.; Dong, J.; Biesuz, M.; Linx, Y.; Deng, H.; Sglavo, V. M.; Reece, M. J.; Hu, C.; Grasso, S. Ultrafast High-Temperature Sintering (UHS) of Fine Grained α-Al_2O_3. *J. Eur. Ceram. Soc.* **2021**, *41* (13), 6626–6633.

(67) Guo, R.-F.; Mao, H.-R.; Zhao, Z.-T.; Shen, P. Ultrafast High-Temperature Sintering of Bulk Oxides. *Scr. Mater.* **2021**, *193*, 103–107.

(68) Zhao, Z.-T.; Guo, R.-F.; Mao, H.-R.; Shen, P. Effect of Components on the Microstructures and Properties of Rare-Earth Zirconate Ceramics Prepared by Ultrafast High-Throughput Sintering. *J. Eur. Ceram. Soc.* **2021**, *41* (11), 5768–5773.

(69) Lin, Y.; Luo, N.; Quattrocchi, E.; Ciucci, F.; Wu, J.; Kermani, M.; Dong, J.; Hu, C.; Grasso, S. Ultrafast High-Temperature Sintering (UHS) of $Li_{1.3}Al_{0.3}Ti_{1.7}(PO_4)_3$. *Ceram. Int.* **2021**, *47* (15), 21982–21987.

(70) Ihrig, M.; Mishra, T. P.; Scheld, W. S.; Häuschen, G.; Rheinheimer, W.; Bram, M.; Finsterbusch, M.; Guillon, O. $Li_7La_3Zr_2O_{12}$ Solid Electrolyte Sintered by the Ultrafast High-Temperature Method. *J. Eur. Ceram. Soc.* **2021**, *41* (12), 6075–6079.

(71) Sada, T.; Ndayishimiye, A.; Fan, Z.; Fujioka, Y.; Randall, C. A. Surface Modification of $BaTiO_3$ with Catechol Surfactant and Effects on Cold Sintering. *J. Appl. Phys.* **2021**, *129* (18), 184102. https://doi.org/10.1063/5.0049905.

(72) Ranjbar, N.; Kashefi, A.; Maheri, M. R. Hot-Pressed Geopolymer: Dual Effects of Heat and Curing Time. *Cem. Concr. Compos.* **2018**, *86*, 1–8. https://doi.org/10.1016/j.cemconcomp.2017.11.004.

(73) Sada, T.; Fan, Z.; Ndayishimiye, A.; Tsuji, K.; Bang, S. H.; Fujioka, Y.; Randall, C. A. In Situ Doping of $BaTiO_3$ and Visualization of Pressure Solution in Flux-Assisted Cold Sintering. *J. Am. Ceram. Soc.* **2021**, *104* (1), 96–104. https://doi.org/10.1111/jace.17461.

(74) Ndayishimiye, A.; Bang, S. H.; Spiers, Christopher. J.; Randall, C. A. Reassessing Cold Sintering in the Framework of Pressure Solution Theory. *J. Eur. Ceram. Soc.* **2023**, *43* (1), 1–13. https://doi.org/10.1016/j.jeurceramsoc.2022.09.053.

(75) Kingery, W. D. Densification during Sintering in the Presence of a Liquid Phase. I. Theory. *J. Appl. Phys.* **1959**, *30* (3), 301–306.

(76) Suvaci, E.; Özel, E. Hydrothermal Synthesis. In *Encyclopedia of Materials: Technical Ceramics and Glasses*; Pomeroy, M., Ed.; Elsevier: Oxford, **2021**; pp 59–68. https://doi.org/10.1016/B978-0-12-803581-8.12096-X.

(77) Guillon, O.; Rheinheimer, W.; Bram, M. A Perspective on Emerging and Future Sintering Technologies of Ceramic Materials. *Adv. Eng. Mater.* **2023**, *25* (18), 2201870. https://doi.org/10.1002/adem.202201870.

(78) Ji, W.; Zhang, J.; Wang, W.; Fu, Z.; Todd, R. I. The Microstructural Origin of Rapid Densification in 3YSZ during Ultra-Fast Firing with or without an Electric Field. *J. Eur. Ceram. Soc.* **2020**, *40* (15), 5829–5836. https://doi.org/10.1016/j.jeurceramsoc.2020.07.027.

(79) Zhang, J.; Meng, F.; Todd, R. I.; Fu, Z. The Nature of Grain Boundaries in Alumina Fabricated by Fast Sintering. *Scr. Mater.* **2010**, *62* (9), 658–661. https://doi.org/10.1016/j.scriptamat.2010.01.019.

(80) Salamon, D.; Kalousek, R.; Zlámal, J.; Maca, K. Role of Conduction and Convection Heat Transfer during Rapid Crack-Free Sintering of Bulk Ceramic with Low Thermal Conductivity. *J. Eur. Ceram. Soc.* **2016**, *36* (12), 2955–2959. https://doi.org/10.1016/j.jeurceramsoc.2015.11.034.

(81) Biesuz, M.; Dong, J.; Fu, S.; Liu, Y.; Zhang, H.; Zhu, D.; Hu, C.; Grasso, S. Thermally-Insulated Flash Sintering. *Scr. Mater.* **2019**, *162*, 99–102. https://doi.org/10.1016/j.scriptamat.2018.10.042.

(82) Biesuz, M.; Saunders, T.; Ke, D.; Reece, M. J.; Hu, C.; Grasso, S. A Review of Electromagnetic Processing of Materials (EPM): Heating, Sintering, Joining and Forming. *J. Mater. Sci. Technol.* **2021**, *69*, 239–272. https://doi.org/10.1016/j.jmst.2020.06.049.

(83) Cao, C.; Mücke, R.; Guillon, O. Effect of AC Field on Uniaxial Viscosity and Sintering Stress of Ceria. *Acta Mater.* **2020**, *182*, 77–86. https://doi.org/10.1016/j.actamat.2019.10.035.

(84) Guillon, O.; De Souza, R. A.; Mishra, T. P.; Rheinheimer, W. Electric-Field-Assisted Processing of Ceramics: Nonthermal Effects and Related Mechanisms. *MRS Bull.* **2021**, *46* (1), 52–58. https://doi.org/10.1557/s43577-020-00008-w.

(85) Dong, Y. Redox Enhanced Slow Ion Kinetics in Oxide Ceramics. *J. Am. Ceram. Soc.* **2023**. https://doi.org/10.1111/jace.19441.

(86) Wang, S.; Mishra, T. P.; Deng, Y.; Balice, L.; Kaletsch, A.; Bram, M.; Broeckmann, C. Electric Current-Assisted Sintering of 8YSZ: A Comparative Study of Ultrafast High-Temperature Sintering and Flash Sintering. *Adv. Eng. Mater.* **2023**, *25* (18), 2300145. https://doi.org/10.1002/adem.202300145.

(87) Chaim, R. On the Kinetics of Liquid-Assisted Densification during Flash Sintering of Ceramic Nanoparticles. *Scr. Mater.* **2019**, *158*, 88–90. https://doi.org/10.1016/j.scriptamat.2018.08.029.

(88) Chaim, R. Liquid Film Capillary Mechanism for Densification of Ceramic Powders during Flash Sintering. *Materials* **2016**, *9* (4), 280. https://doi.org/10.3390/ma9040280.

(89) Holland, T. B.; Anselmi-Tamburini, U.; Quach, D. V; Tran, T. B.; Mukherjee, A. K. Effects of Local Joule Heating during the Field Assisted Sintering of Ionic Ceramics. *J. Eur. Ceram. Soc.* **2012**, *32* (14), 3667–3674. https://doi.org/10.1016/j.jeurceramsoc.2012.02.033.

(90) Raj, R. Joule Heating during Flash-Sintering. *J. Eur. Ceram. Soc.* **2012**, *32* (10), 2293–2301. https://doi.org/10.1016/j.jeurceramsoc.2012.02.030.

(91) Ibn-Mohammed, T.; Randall, C. A.; Mustapha, K. B.; Guo, J.; Walker, J.; Berbano, S.; Koh, S. C. L.; Wang, D.; Sinclair, D. C.; Reaney, I. M. Decarbonising Ceramic Manufacturing: A Techno-Economic Analysis of Energy Efficient Sintering Technologies in the Functional Materials Sector. *J. Eur. Ceram. Soc.* **2019**, *39* (16), 5213–5235. https://doi.org/10.1016/j.jeurceramsoc.2019.08.011.

(92) Zapata-Solvas, E.; Gómez-García, D.; Domínguez-Rodríguez, A.; Todd, R. I. Ultra-Fast and Energy-Efficient Sintering of Ceramics by Electric Current Concentration. *Sci. Rep.* **2015**, *5* (1), 8513. https://doi.org/10.1038/srep08513.

(93) Sohrabi Baba Heidary, D.; Lanagan, M.; Randall, C. A. Contrasting Energy Efficiency in Various Ceramic Sintering Processes. *J. Eur. Ceram. Soc.* **2018**, *38* (4), 1018–1029. https://doi.org/10.1016/j.jeurceramsoc.2017.10.015.

(94) Karacasulu, L.; Karl, D.; Gurlo, A.; Vakifahmetoglu, C. Cold Sintering as a Promising ISRU Technique: A Case Study of Mars Regolith Simulant. *Icarus* **2023**, *389*, 115270.

(95) Karacasulu, L.; Vakifahmetoglu, C. Cold Sintering Assisted Two-Step Sintering of Potassium Sodium Niobate (KNN) Ceramics. *Materials Science and Engineering: B* **2023**, *297*, 116709. https://doi.org/10.1016/j.mseb.2023.116709.

(96) Karacasulu, L.; Kartal, U.; Icin, O.; Bortolotti, M.; Biesuz, M.; Vakifahmetoglu, C. Formation of Monolithic $SrTiO_3$-TiO_2 Ceramic Heterostructures by Reactive Hydrothermal Sintering. *J. Eur. Ceram. Soc.* **2023**, *43* (15), 6982–6988. https://doi.org/10.1016/j.jeurceramsoc.2023.07.012.

(97) Biesuz, M.; Grasso, S.; Sglavo, V. M. What's New in Ceramics Sintering? A Short Report on the Latest Trends and Future Prospects. *Curr. Opin. Solid State Mater. Sci* **2020**, *24* (5), 100868. https://doi.org/10.1016/j.cossms.2020.100868.

(98) Bang, S. H.; Tsuji, K.; Ndayishimiye, A.; Dursun, S.; Seo, J.-H.; Otieno, S.; Randall, C. A. Toward a Size Scale-up Cold Sintering Process at Reduced Uniaxial Pressure. *J. Am. Ceram. Soc.* **2020**, *103* (4), 2322–2327. https://doi.org/10.1111/jace.16976.

(99) Manière, C.; Durand, L.; Weibel, A.; Chevallier, G.; Estournès, C. A Sacrificial Material Approach for Spark Plasma Sintering of Complex Shapes. *Scr. Mater.* **2016**, *124*, 126–128. https://doi.org/10.1016/j.scriptamat.2016.07.006.

(100) Manière, C.; Nigito, E.; Durand, L.; Weibel, A.; Beynet, Y.; Estournès, C. Spark Plasma Sintering and Complex Shapes: The Deformed Interfaces Approach.

Powder Technol. **2017**, *320*, 340–345. https://doi.org/10.1016/j.powtec.2017.07.048.

(101) Guo, H.; Baker, A.; Guo, J.; Randall, C. A. Cold Sintering Process: A Novel Technique for Low-Temperature Ceramic Processing of Ferroelectrics. *J. Am. Ceram. Soc.* **2016**, *99* (11), 3489–3507. https://doi.org/10.1111/jace.14554.

(102) Ma, J.; Li, H.; Wang, H.; Lin, C.; Wu, X.; Lin, T.; Zheng, X.; Yu, X. Composition, Microstructure and Electrical Properties of $K_{0.5}Na_{0.5}NbO_3$ Ceramics Fabricated by Cold Sintering Assisted Sintering. *J. Eur. Ceram. Soc.* **2019**, *39* (4), 986–993. https://doi.org/10.1016/j.jeurceramsoc.2018.11.044.

(103) Kamani, M.; Yourdkhani, A.; Poursalehi, R.; Sarraf-Mamoory, R. Studying the Cold Sintering Process of Zinc Ferrite as an Incongruent Dissolution System. *International Journal of Ceramic Engineering & Science* **2019**, *1* (3), 125–135. https://doi.org/10.1002/ces2.10018.

(104) Huang, Y.; Huang, K.; Zhou, S.; Lin, C.; Wu, X.; Gao, M.; Zhao, C.; Fang, C. Influence of Incongruent Dissolution-Precipitation on 8YSZ Ceramics during Cold Sintering Process. *J. Eur. Ceram. Soc.* **2022**, *42* (5), 2362–2369. https://doi.org/10.1016/j.jeurceramsoc.2021.12.072.

(105) Biesuz, M.; Taveri, G.; Duff, A. I.; Olevsky, E.; Zhu, D.; Hu, C.; Grasso, S. A Theoretical Analysis of Cold Sintering. *Advances in Applied Ceramics* **2020**, *119* (2), 75–89. https://doi.org/10.1080/17436753.2019.1692173.

(106) Li, Q.; Gupta, S.; Tang, L.; Quinn, S.; Atakan, V.; Riman, R. E. A Novel Strategy for Carbon Capture and Sequestration by RHLPD Processing. *Front Energy Res.* **2016**, *3*, 53.

(107) Piskin, C.; Karacasulu, L.; Bortolotti, M.; Vakifahmetoglu, C. Synthesis of Potassium–Sodium Niobate (KNN) from NbO_2. *Open Ceramics* **2021**, *7*, 100159. https://doi.org/10.1016/j.oceram.2021.100159.

(108) Piskin, C.; Karacasulu, L.; Ischia, G.; Bortolotti, M.; Vakifahmetoglu, C. Hydrothermal Synthesis of Potassium–Sodium Niobate Powders. *J. Am. Ceram. Soc.* **2022**, *105* (6), 3809–3819. https://doi.org/10.1111/jace.18349.

(109) Carter, C. B.; Norton, M. G. *Ceramic Materials: Science and Engineering*; Springer, **2007**.

(110) Dole, S. L.; Prochazka, S.; Doremus, R. H. Microstructural Coarsening During Sintering of Boron Carbide. *J. Am. Ceram. Soc.* **1989**, *72* (6), 958–966. https://doi.org/10.1111/j.1151-2916.1989.tb06252.x.

(111) Biesuz, M.; Sglavo, V. M. Flash Sintering of Alumina: Effect of Different Operating Conditions on Densification. *J. Eur. Ceram. Soc.* **2016**, *36* (10), 2535–2542. https://doi.org/10.1016/j.jeurceramsoc.2016.03.021.

(112) Cologna, M.; Francis, J. S. C.; Raj, R. Field Assisted and Flash Sintering of Alumina and Its Relationship to Conductivity and MgO-Doping. *J. Eur. Ceram.*

Soc. **2011**, *31* (15), 2827–2837. https://doi.org/10.1016/j.jeurceramsoc.2011.07.004.

(113) Raj, R. Analysis of the Power Density at the Onset of Flash Sintering. *J. Am. Ceram. Soc.* **2016**, *99* (10), 3226–3232. https://doi.org/10.1111/jace.14178.

(114) Prado, M. O.; Biesuz, M.; Frasnelli, M.; Benedetto, F. E.; Sglavo, V. M. Viscous Flow Flash Sintering of Porous Silica Glass. *J. Non Cryst. Solids* **2017**, *476*, 60–66. https://doi.org/10.1016/j.jnoncrysol.2017.09.024.

(115) Zapata-Solvas, E.; Bonilla, S.; Wilshaw, P. R.; Todd, R. I. Preliminary Investigation of Flash Sintering of SiC. *J. Eur. Ceram. Soc.* **2013**, *33* (13), 2811–2816. https://doi.org/10.1016/j.jeurceramsoc.2013.04.023.

(116) Biesuz, M.; Karacasulu, L.; Vakifahmetoglu, C.; Sglavo, V. M. On the Temperature Measurement during Ultrafast High-Temperature Sintering (UHS): Shall We Trust Metal-Shielded Thermocouples? *J. Eur. Ceram. Soc.* **2023**, in press. https://doi.org/10.1016/j.jeurceramsoc.2023.11.061.

(117) Saunders, T.; Grasso, S.; Reece, M. J. Ultrafast-Contactless Flash Sintering Using Plasma Electrodes. *Sci. Rep.* **2016**, *6* (1), 27222. https://doi.org/10.1038/srep27222.

(118) Johnson, S. L.; Venugopal, G.; Hunt, A. T. Flame-Assisted Flash Sintering: A Noncontact Method to Flash Sinter Coatings on Conductive Substrates. *J. Am. Ceram. Soc.* **2018**, *101* (2), 536–541. https://doi.org/10.1111/jace.15218.

(119) Dong, J.; Wang, Z.; Zhao, X.; Biesuz, M.; Saunders, T.; Zhang, Z.; Hu, C.; Grasso, S. Contactless Flash Sintering Based on Cold Plasma. *Scr. Mater.* **2020**, *175*, 20–23. https://doi.org/10.1016/j.scriptamat.2019.08.039.

(120) Jones, G. M.; Biesuz, M.; Ji, W.; John, S. F.; Grimley, C.; Manière, C.; Dancer, C. E. J. Promoting Microstructural Homogeneity during Flash Sintering of Ceramics through Thermal Management. *MRS Bull.* **2021**, *46* (1), 59–66. https://doi.org/10.1557/s43577-020-00010-2.

(121) Jalali, S. I. A.; Raj, R. Touch-Free Flash Sintering with Magnetic Induction within a Reactor Activated by the Usual Flash Method. *J. Am. Ceram. Soc.* **2022**, *105* (11), 6517–6522. https://doi.org/10.1111/jace.18601.

(122) Zuo, F.; Wang, Q.; Yan, Z.-Q.; Kermani, M.; Grasso, S.; Nie, G.-L.; Jiang, B.-B.; He, F.-P.; Lin, H.-T.; Wang, L.-G. Upscaling Ultrafast High-Temperature Sintering (UHS) to Consolidate Large-Sized and Complex-Shaped Ceramics. *Scr. Mater.* **2022**, *221*, 114973. https://doi.org/10.1016/j.scriptamat.2022.114973.

(123) Wu, J.; kermani, M.; Zhu, D.; Li, J.; Lin, Y.; Hu, C.; Grasso, S. Carbon Free Ultra-Fast High Temperature Sintering of Translucent Zirconia. *Scr. Mater.* **2022**, *210*, 114476. https://doi.org/10.1016/j.scriptamat.2021.114476.

(124) Mondal, S.; Lombard, J. D. S.; Gollapudi, S.; Tallon, C.; Li, J.-F.; Viehland, D. Ultrafast High-Temperature Sintering of ZrB_2. *J. Am. Ceram. Soc.* **2024**, *107,* 11-15. https://doi.org/10.1111/jace.19445.

(125) López, R.; González, F.; Cruz, M. P.; Villafuerte-Castrejon, M. E. Piezoelectric and Ferroelectric Properties of $K_{0.5}Na_{0.5}NbO_3$ Ceramics Synthesized by Spray Drying Method. *Mater. Res. Bull.* **2011**, *46* (1), 70–74.

(126) Serrazina, R.; Dean, J. S.; Reaney, I. M.; Pereira, L.; Vilarinho, P. M.; Senos, A. M. O. R. Mechanism of Densification in Low-Temperature FLASH Sintered Lead Free Potassium Sodium Niobate (KNN) Piezoelectrics. *J. Mater. Chem. C Mater.* **2019**, *7* (45), 14334–14341. https://doi.org/10.1039/C9TC03117K.

(127) Serrazina, R.; Senos, A. M. O. R.; Pereira, L.; Dean, J. S.; Reaney, I. M.; Vilarinho, P. M. The Role of Particle Contact in Densification of FLASH Sintered Potassium Sodium Niobate. *Eur. J. Inorg. Chem.* **2020**, *2020* (39), 3720–3728. https://doi.org/10.1002/ejic.202000458.

(128) Serrazina, R.; Tkach, A.; Pereira, L.; Senos, A. M. O. R.; Vilarinho, P. M. Flash Sintered Potassium Sodium Niobate: High-Performance Piezoelectric Ceramics at Low Thermal Budget Processing. *Materials* **2022**, *15* (19), 6603.

(129) Şavklıyıldız, İ.; Okur, Ç.; Akdoğan, E. K. Flash Sintering and Dielectric Properties of $K_{0.5}Na_{0.5}NbO_3$. *J. Am. Ceram. Soc.* **2022**, *105* (1), 469–480. https://doi.org/10.1111/jace.18119.

(130) Wu, Y.; Su, X.; An, G.; Hong, W. Dense $Na_{0.5}K_{0.5}NbO_3$ Ceramics Produced by Reactive Flash Sintering of $NaNbO_3$-$KNbO_3$ Mixed Powders. *Scr. Mater.* **2020**, *174*, 49–52. https://doi.org/10.1016/j.scriptamat.2019.08.035.

VITA

Levent Karacasulu

Education

Ph.D. - Materials Science and Engineering, İzmir Institute of Technology, 2023

M.Sc. - Materials Science and Engineering, Anadolu University, 2018

B.Sc. - Materials Science and Engineering, Anadolu University, 2016

B.Sc. - Environmental Engineering, Anadolu University, 2016

Appointments

- Research & Teaching Assistant - Materials Science and Engineering, İzmir Institute of Technology, 2018-
- Visiting researcher - Industrial Engineering, University of Trento, 2022-2023

Other publications

Piskin, C., **Karacasulu, L.**, Ischia, G., Bortolotti, M., & Vakifahmetoglu, C. (2022). Hydrothermal synthesis of potassium–sodium niobate powders. Journal of the American Ceramic Society, 105(6), 3809–3819.

Piskin, C., **Karacasulu, L.**, Bortolotti, M., & Vakifahmetoglu, C. (2021). Synthesis of potassium–sodium niobate (KNN) from NbO_2. Open Ceramics, 7, 100159.

Günkaya, Z., **Karacasulu, L.**, Evliyaoğlu, G., Çiftçi, M. (2018). Life Cycle Assessment of Marble Plate Production. Süleyman Demirel University Journal of Natural and Applied Sciences, 22(2), 521-528.

Özkan, A., Günkaya, Z., Tok, G., **Karacasulu, L.**, Metesoy, M., Banar, M., Kara, A. (2016). "Life Cycle Assessment and Life Cycle Cost Analysis of Magnesia Spinel Brick Production", Sustainability, 8, 662.